Development of strategies for electrochemiluminescence enhancement

Sara Knežević

THÈSE PRÉSENTÉE

POUR OBTENIR LE GRADE DE

DOCTEUR DE L'UNIVERSITÉ DE BORDEAUX

ÉCOLE DOCTORALE DES SCIENCES CHIMIQUES

SPÉCIALITÉ CHIMIE-PHYSIQUE

par **Sara KNEŽEVIĆ**

DEVELOPPEMENT DE STRATEGIES POUR L'AMELIORATION DE L'ELECTROCHIMILUMINESCENCE

DEVELOPMENT OF STRATEGIES FOR ELECTROCHEMILUMINESCENCE ENHANCEMENT

Sous la direction du **Professeur Neso SOJIC**

Soutenue le 11 octobre 2024

Membres du jury :

Mme LAGROST Corinne	Directeur de recherche, CNRS, Université de Rennes, France	Présidente du jury
M. POLO Federico	Professeur, Ca' Foscari University of Venice, Italie	Rapporteur
M. DICK Jeffrey	Professeur, Purdue University, Etats Unis	Rapporteur
M. KANOUFI Frédéric	Directeur de recherche, CNRS, Université Paris Cité, France	Examinateur
M. BOUFFIER Laurent	Directeur de recherche, CNRS, Université de Bordeaux, France	Examinateur
M. SOJIC Neso	Professeur, Bordeaux INP, France	Directeur de thèse

Abstract

Electrochemiluminescence (ECL), is the light emission process that occurs when an excited state of a luminophore is populated through a highly exergonic redox reaction of electrogenerated species. It has emerged as a prominent transducing technique in biosensing due to its robustness, biocompatibility, and user-friendly nature. The orthogonality of the electrochemical trigger and the optical readout distinguishes it from classic microscopy and electrochemical techniques, and, owing to its near-zero background, remarkable sensitivity, and absence of photobleaching and phototoxicity it is rapidly evolving into a powerful electrochemical/optical microscopy. However, ECL is limited by relatively low light intensities, rapid signal decay, and spatial confinement to the micrometric region near the electrode surface, which can limit its practical application. In this context, our goal is to improve the ECL method by amplifying the ECL emission and extending its duration in space and time, both of which significantly depend on understanding and improving the efficiency of the underlying mechanisms for ECL generation. Thus, we investigate mechanistic pathways and kinetics within ECL systems by analysing current and ECL intensity and resolving its spatial distribution using ECL microscopy. Additionally, we employ finite element simulations to complement the experimental data, providing deeper insights into the systems under study. Based on these insights, we develop strategies to enhance ECL generation efficiency by improving specific reaction steps or introducing additional pathways to populate the luminophore's excited state.

Résumé

L'électrochimiluminescence (ECL) est le processus d'émission de lumière qui se produit lorsqu'un état excité d'un luminophore est peuplé par une réaction d'oxydo-réduction hautement exergonique d'espèces électrogénées. Elle s'est imposée comme une technique de transduction de premier plan dans le domaine de la biodétection en raison de sa robustesse, de sa biocompatibilité et de sa facilité d'utilisation. L'orthogonalité du déclenchement électrochimique et de la lecture optique la distingue de la microscopie classique et des techniques électrochimiques. En raison de son bruit de fond quasi nul, de sa sensibilité remarquable et de l'absence de photoblanchiment et de phototoxicité, elle évolue rapidement pour devenir un nouveau type de microscopie électrochimique/optique. Cependant, l'ECL est limitée par des intensités lumineuses relativement faibles, une décroissance rapide du signal et un confinement spatial dans une région micrométrique adjacente de la surface de l'électrode, ce qui peut limiter son application pratique. Dans ce contexte, notre objectif est d'améliorer la méthode ECL en amplifiant l'émission ECL et en prolongeant sa durée dans l'espace et dans le temps, ce qui dépend considérablement de la compréhension et de l'amélioration de l'efficacité des mécanismes sous-jacents de la génération ECL. Nous étudions donc les voies mécanistiques et la cinétique au sein des systèmes ECL en analysant l'intensité du courant et de l'ECL, et en résolvant sa distribution spatiale à l'aide de la microscopie ECL. En outre, nous utilisons des simulations par éléments finis pour compléter les données expérimentales, ce qui permet de mieux comprendre le système étudié. Sur la base de ces informations, nous développons des stratégies pour améliorer l'efficacité de la génération ECL en améliorant des étapes de réaction spécifiques ou en introduisant des voies supplémentaires pour peupler l'état excité du luminophore.

Résumé de la thèse

L'électrochimiluminescence (ECL) est le processus d'émission de lumière qui se produit lorsqu'un luminophore est excité lors d'une réaction d'oxydo-réduction hautement exergonique d'espèces générées au niveau de l'éléctrode.[1–3] L'ECL a progressivement évolué d'une curiosité de laboratoire à une technique bioanalytique puissante, commercialisée avec succès pour les diagnostics cliniques.[4,5] Les applications actuelles de l'ECL vont de la détection sensible et de la quantification de divers biomarqueurs (anticorps, médicaments, hormones, protéines virales, marqueurs tumoraux, *etc.*[6]) à l'étude *operando* de la réactivité chimique à proximité des surfaces d'électrodes,[4,7–17] dans des espaces confinés,[18–23] aux interfaces[24–28] et les sites catalytiques.[29–33]

Les performances analytiques de la méthode ECL reposent sur l'orthogonalité du déclenchement électrochimique et de la lecture optique. Ainsi, l'ECL fournit des informations utiles, faradiques (courant) et optiques (émission de lumière), sur le système étudié. Cependant, alors que les mesures de courant donnent une mesure globale du flux d'électrons à travers l'électrode de travail, la lumière produite peut être résolue spatialement pour donner une image résolue spatialement des événements. Par conséquent, combinée à la microscopie optique, l'ECL devient une puissante méthode d'imagerie capable de visualiser les objets qui participent, entravent ou modifient les réactions ECL à proximité de la surface de l'électrode.[31,34] En outre, la cartographie de la distribution de l'ECL offre une quantité considérable d'informations, au-delà de la simple mesure de son intensité globale, un paramètre clé pour comprendre les processus dynamiques ou démêler des situations mécanistiques complexes dans divers domaines.

Outre le fait qu'elle fournit davantage d'informations sur le système observé (courbes courant/potentiel et intensités de luminescence), l'ECL présente une faible limite de détection, un bruit de fond quasi nul, un rapport signal/bruit élevé et une bonne résolution spatio-temporelle. Cependant, l'ECL est limitée par des intensités lumineuses relativement faibles, une décroissance rapide du signal et un confinement spatial dans une région micrométrique adjacente à la surface de l'électrode, ce qui peut limiter son application pratique.[35,36] Dans ce contexte, notre objectif est d'améliorer la méthode ECL en amplifiant l'émission ECL et en prolongeant sa durée dans l'espace et dans le temps, ce qui dépend

considérablement de la compréhension et de l'amélioration de l'efficacité des mécanismes sous-jacents de la génération ECL..[9,36] Nous étudions donc les voies mécanistiques et la cinétique au sein des systèmes ECL en analysant l'intensité du courant et de l'ECL, et en résolvant sa distribution spatiale à l'aide de la microscopie ECL. En outre, nous utilisons des simulations par éléments finis pour compléter les données expérimentales, ce qui permet de mieux comprendre le système étudié. Sur la base de ces informations, nous développons des stratégies pour améliorer l'efficacité de la génération ECL en améliorant des étapes de réaction spécifiques ou en introduisant des voies supplémentaires pour peupler l'état excité du luminophore.

Le chapitre I présente le contexte théorique général de l'électrochimie et de la photophysique nécessaire pour comprendre les phénomènes ECL. Il décrit différents systèmes et configurations ECL, ainsi que les aspects mécanistiques de la génération ECL, qui sont nécessaires pour examiner et discuter de manière critique le travail contenu dans la suite de la thèse. Enfin, ce premier chapitre présente brièvement l'état de l'art dans le domaine de l'ECL, en donnant une perspective sur les avancées récentes et les tendances de la recherche.

Le système modèle pour la majorité des applications ECL utilise $[Ru(bpy)_3]^{2+}$ comme luminophore et la tri-*n*-propylamine (TPrA) comme coréactif sacrificiel. Il s'agit de l'un des systèmes ECL les plus étudiés, tant sur le plan expérimental que théorique, et il est donc bien caractérisé (d'un point de vue mécanistique et cinétique).[4,36–38] En bref, si $[Ru(bpy)_3]^{2+}$ et TPrA diffusent librement en solution, ils peuvent subir une oxydation hétérogène à un potentiel d'électrode approprié et réagir par un mécanisme d'oxydation-réduction pour peupler l'état excité $[Ru(bpy)_3]^{2+*}$. Toutefois, si l'électrode est polarisée à un potentiel suffisant pour oxyder la TPrA mais pas le $[Ru(bpy)_3]^{2+}$, ou si l'oxydation directe du $[Ru(bpy)_3]^{2+}$ est entravée d'une autre manière (c'est-à-dire si le $[Ru(bpy)_3]^{2+}$ est utilisé pour marquer un objet isolant), la génération de l'ECL dépendra de la cascade de réactions impliquant des radicaux TPrA transitoires (**figure 1A**). Dans ce dernier cas, l'efficacité de la génération d'ECL est limitée par la courte demi-vie des $TPrA^{\bullet+}$, ce qui limite l'épaisseur de la couche émettrice d'ECL et le signal ECL.[4] Pour surmonter cette limitation, des recherches approfondies se sont concentrées sur l'orientation de la voie réactionnelle, par le développement de nanomatériaux,[22,39–41] luminophores,[42–47] ou de coréactifs,[48–51] aux propriétés améliorées. Toutefois, comme indiqué

précédemment, le succès de ces approches d'optimisation dépend fortement d'une compréhension mécanistique complète de ce système ECL.[14,36–38,52,53]

Dans le **chapitre II**, nous explorons les mécanismes à l'origine de l'amplification de l'ECL à faible potentiel dans ce système modèle de coréactif ECL lors de l'ajout d'un complexe redox d'Ir(III) soluble dans l'eau - tris(2-(*2-pyridinyl-κN*)-4-sulfonate phényl-κC)iridium(III) ($[Ir(sppy)_3]^{3-}$, voir **figure 1E**).[15,16,54] La cascade de réactions redox qui suit l'oxydation électrochimique du médiateur Ir(III), du coréactif et du luminophore produit les états électroniques excités $[Ru(bpy)_3]^{2+*}$ et $[Ir(sppy)_3]^{3-*}$, qui émettent de la lumière (à λmax = 620 nm et 515 nm, respectivement) lors de leurs relaxations. Notre approche repose sur la construction d'un modèle de simulation par éléments finis et i) la reproduction des tracés expérimentaux du courant en fonction du potentiel (i-E) et de l'intensité de l'ECL en fonction du potentiel (IECL-E) pour optimiser les paramètres thermodynamiques et cinétiques dans le modèle de simulation ; ii) la variation des paramètres cinétiques dans le modèle pour explorer les propriétés de ce système et d'autres systèmes de luminophores mixtes dans un espace de paramètres raisonnablement large et/ou analyser la contribution d'étapes réactionnelles spécifiques dans le schéma mécanistique total et étudier leurs interactions avec les autres voies mécanistiques.

Grâce à des méthodes électrochimiques, à la spectroscopie et à la simulation par éléments finis, nous démontrons que l'émission ECL à faible potentiel est régie par trois réactions cinétiquement limitantes, qui modulent le rapport de concentration des espèces radicalaires. Les réactions d'oxydation facilitées par l'Ir(III) conduisent à la production de radicaux TPrA (**figure 1D**) et d'états excités $[Ru(bpy)_3]^{2+*}$ (**figure 1C**), ce qui renforce l'intensité de l'ECL. Inversement, la réaction de $[Ir(sppy)_3]^{2-}$ avec les radicaux $TPrA^{\bullet}$ (**figure 1B**) entraine l'extinction de l'ECL de Ru. Enfin, nous avons étudié l'interaction entre les étapes clés de la réaction, mettant en évidence que les propriétés redox du médiateur dictent le comportement de l'ECL : le début de l'ECL et le potentiel de crête, ainsi que l'intensité maximale et l'extension spatiale de la couche émettrice de lumière. Le modèle développé aide donc à la fois à comprendre et à prédire la dynamique de l'ECL en présence de médiateurs redox ayant des propriétés redox distinctes, manifestant le potentiel pour des systèmes ECL sur mesure avec des performances améliorées dans les applications analytiques, d'imagerie et biomédicales.

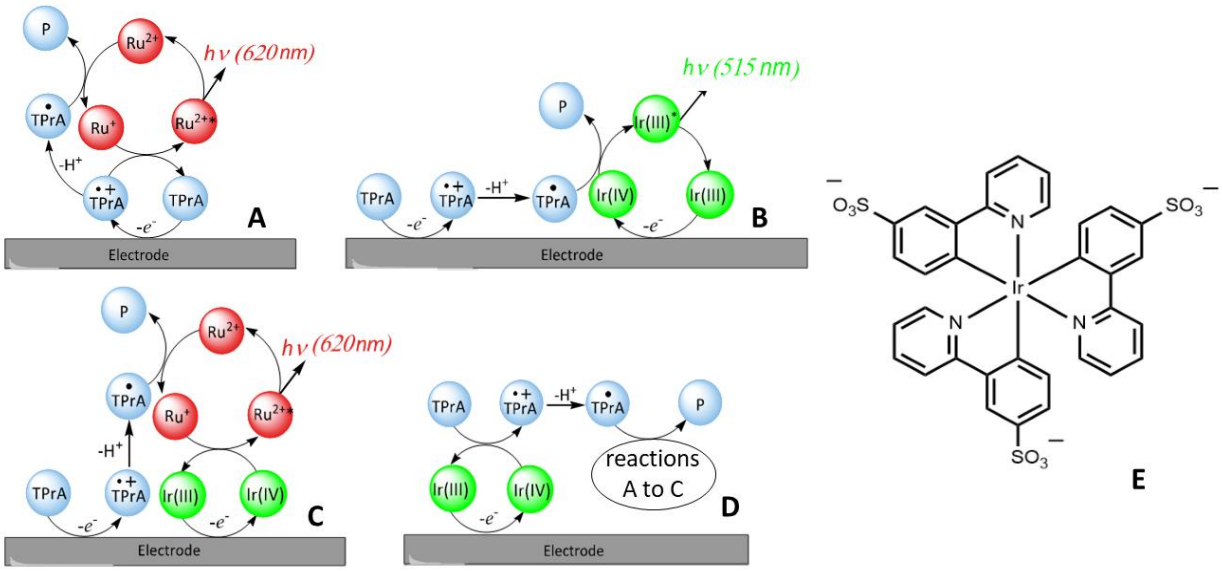

Figure 1. Schémas de la **(A)** voie ECL conventionnelle "à distance", **(B)** voie directe vers l'ECL $[Ir^{III}(sppy)]_3^{3-}$, **(C)** voie ECL améliorée "à médiation redox" et **(D)** catalyse redox (oxydation catalytique de TPrA par $[Ir^{IV}(sppy)]_3^{2-}$). Ru^{2+}, Ir(III) et TPrA représentent respectivement le luminophore $[Ru(bpy)_3]^{2+}$, le médiateur redox $[Ir^{III}(sppy)]_3^{3-}$ et la tri-*n*-propylamine. **(E)** Structure chimique du complexe $[Ir(sppy)_3]^{3-}$.

Les tests ECL commerciaux reposent généralement sur un système ECL conventionnel comprenant de la TPrA comme coréactif et $[Ru(bpy)_3]^{2+}$ comme luminophore. [6] Ces tests utilisent souvent une conception sandwich à base de billes, où les biomarqueurs cibles sont piégés entre une bille magnétique recouverte d'un anticorps de capture et un anticorps de détection marqué avec l'émetteur $[Ru(bpy)_3]^{2+}$. Dans le **chapitre III,** nous décrivons une amélioration remarquable de l'ECL de $[Ru(bpy)_3]^{2+}$ dans les immunodosages à base de microbilles en introduisant le complexe redox-actif $[Ir(sppy)_3]^{3-}$ (**figure 1E**) dans la solution contenant du TPrA. Nous avons obtenu une augmentation par un facteur 70,9 à des potentiels anodiques faibles (0,9 V) et 2,9 fois plus à des potentiels anodiques modérés (1,2 V) (histogramme de la **figure 2G**). Nous avons contrôlé la réponse ECL de billes de polystyrène individuelles (**figure 2A-F**), confirmant ainsi expérimentalement que les mécanismes décrits au **chapitre II** (voir **figure 1**) sont réalisables lorsque $[Ru(bpy)_3]^{2+}$ est utilisé comme marqueur luminescent (Ru@PS), car elles contribuent à l'amélioration ECL observée dans la configuration à base de billes.

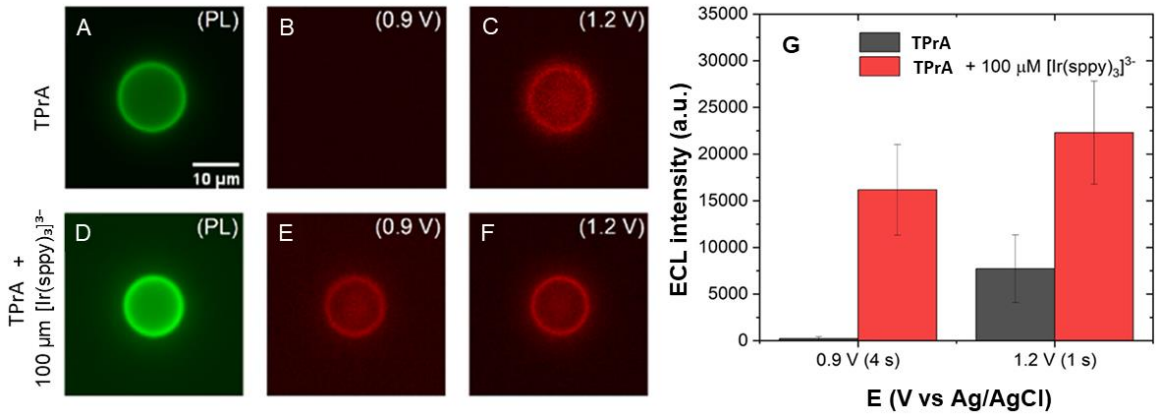

Figure 2. Images représentatives, en vue de dessus, de billes Ru@PS uniques de 12 µm en utilisant le mode PL (**(A** et **D)**, échelle d'intensité 0-65 000) et ECL (**(B** et **C)**, échelle de contraste 0-12 000, **(E** et **F)**, échelle de contraste 0 à 45 000). **(A-C)** Obtenu en présence de 0,1 M TPrA, **(D-F)** ou 0,1 M TPrA et 100 µM $[Ir(sppy)_3]^{3-}$ **: (B** et **E)** 0,9 V, **(C** et **F)** 1,2 V. **(G)** Intensités ECL dans 0.1 M TPrA (colonnes grises) et 0,1 M TPrA avec 100 µM $[Ir(sppy)_3]^{3-}$ (colonnes rouges) à 0,9 et 1,2 V. Mêmes conditions expérimentales que dans **(A-F)**.

Nous avons également étendu l'application de ce système ECL pour permettre l'imagerie cellulaire bimodale (**figure 3**). En général, la microscopie ECL est réalisée dans l'un des deux modes: ECL "positif" ou ECL "négatif" (ou "ombre"). Dans le mode ECL positif (PECL) les entités émettrices d'ECL étudiées (par exemple, des micro- ou nanoparticules, des cellules marquées ou des billes pour l'immunodétection) sont vues comme des objets brillants sur un fond sombre, comme dans le cas des billes de la **figure 2**, ce qui est similaire aux images obtenues en fluorescence.[34,55] Inversement, dans le mode ECL négatif (SECL), les objets isolants (cellules, organites, microparticules ou empreintes digitales) entravent le flux de diffusion des réactifs ECL et sont visualisés comme des objets sombres sur un fond clair. [56,57] Pour cette étude, nous avons cultivé les cellules à la surface de l'électrode, marqué les membranes cellulaires avec l'émetteur $[Ru(bpy)_3]^{2+}$ (SA@Ru) et les avons immergées dans une solution contenant à la fois du TPrA et le complexe $[Ir(sppy)_3]^{3-}$. Le succès du marquage des membranes cellulaires a été confirmé par microscopie à épifluorescence (**figure 3A**). Ensuite, nous avons appliqué un potentiel électrochimique et capturé simultanément des images PECL et SECL de cellules individuelles (**Figure 3B** et **3C**, respectivement) résultant de la luminescence rouge simultanée des étiquettes $[Ru(bpy)_3]^{2+}$ et de la luminescence verte de $[Ir(sppy)_3]^{3-}$ en solution. Les émissions ECL des deux luminophores ont ensuite été résolues spectralement et spatialement,

ce qui a permis d'obtenir deux images des mêmes cellules. La PECL montre la distribution des étiquettes $[Ru(bpy)_3]^{2+}$ attachées à la membrane cellulaire, et la SECL reflète l'entrave à la diffusion locale des réactifs ECL par chaque cellule. En perspective, cette approche bénéficie de signaux amplifiés qui peuvent réduire considérablement les limites de détection en (immuno)détection ECL. En outre, lorsqu'elle est appliquée à l'imagerie ECL, elle permet de mieux comprendre les systèmes (biologiques) observés.

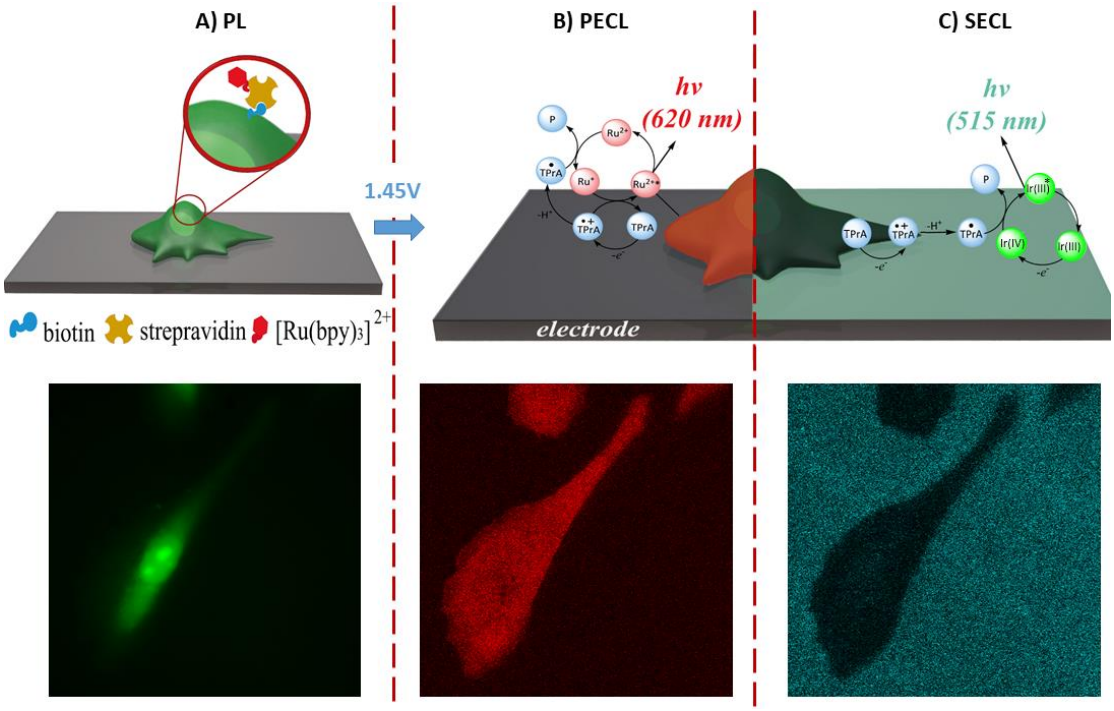

Figure 3. (Haut) Représentation schématique de l'imagerie bimodale d'une cellule immobilisée sur une électrode de carbone vitreux (GCE) : **(A)** PL, **(B)** PECL, et **(C)** SECL. Mécanismes des modes PECL (voie hétérogène impliquant principalement le TPrA dissous et l'étiquette SA@Ru immobilisée sur la cellule) et SECL (voie homogène impliquant uniquement $[Ir(sppy)_3]^{3-}$ et le TPrA dissous). Ru^{2+} et Ir(III) représentent l'étiquette ECL SA@Ru et $[[Ir(sppy)_3]^{3-}$, respectivement. (Bas) La même cellule CHO-K1 a été imagée par **(A)** PL, **(B)** PECL et **(C)** SECL. Barre d'échelle : 30 µm.

Le **chapitre IV** étudie l'amélioration de la couche émissive ECL dans le système ECL luminol/H_2O_2 et son extension spatiale et temporelle. Le luminol (et ses dérivés) émet de la lumière lors de son oxydation en présence de H_20_2 dans des solutions aqueuses alcalines,

l'intensité lumineuse dépendant linéairement de la concentration de H_2O_2[58–63] Le mécanisme de génération de l'ECL est complexe et implique l'oxydation du luminol pour produire des radicaux diazaquinone (L). [9,64] Ces radicaux réagissent ensuite avec l'anion peroxyde d'hydrogène (HO_2^-) ou d'autres espèces réactives de l'oxygène (ROS), à savoir les radicaux hydroxyles ($OH^\bullet$) et les radicaux superoxydes ($O_2^{\bullet-}$), produits lors de la décomposition de H_2O_2 , de l'oxydation de l'eau,[65,66] ou la réduction de l'oxygène dissous,[64,67] Ils finissent par occuper l'état excité et émettent de la lumière bleue lors de la désintégration.[9,64,68]

Nous avons mis en œuvre une approche expérimentale simple impliquant la génération électrochimique de bulles de gaz à la surface d'une anode pour augmenter l'émission ECL du dérivé du luminol L-012. Tout d'abord, nous avons analysé l'évolution du courant et de l'intensité de l'ECL en balayant le potentiel de l'électrode de 0 V à 3 V dans des solutions contenant L-012 et H_2O_2, en utilisant du KCl et du KNO_3 comme électrolyte support. Cette analyse a confirmé que dans la solution contenant du chlorure, les bulles produites à des potentiels d'électrode élevés sont principalement constituées de chlore. En revanche, des bulles d'oxygène se forment en l'absence de chlorures dissous. Lors de la dissolution, le chlore réagit avec l'eau pour donner de l'hypochlorite (ClO^-). La présence d'hypochlorite à l'interface entre la phase aqueuse et les bulles générées électrochimiquement peuvent oxyder de manière homogène L-012[8,59]ce qui entraîne une amélioration significative de l'ECL. Par la suite, nous avons imagé la distribution de l'ECL dans des solutions contenant L-012 et H_2O_2 avec du KCl et du KNO_3 comme électrolyte support. Nous avons polarisé une microélectrode en or à un faible potentiel de 0,7 V (où aucune bulle ne se forme) et à des potentiels élevés de 2,4 V et 3,0 V (**figure 4 A-F**). Les images ECL à 0,7 V (**figures 4A** et **D**) montrent que l'ECL est confinée à la surface de la microélectrode. En revanche, les images capturées à des potentiels élevés révèlent une émission ECL provenant de l'interface gaz/liquide, suggérant l'implication de réactions chimiques à la surface de la bulle (c'est-à-dire l'oxydation homogène de L-012 par l'hypochlorite, mais aussi la production de ROS pendant l'évolution de l'oxygène en l'absence de chlorures). En outre, l'effet « couronne » des bulles [24,69] augmente les taux de réaction d'oxydation à l'interface électrode/gaz/électrolyte, assurant la génération d'une quantité abondante de ROS à la fois en présence et en l'absence de chlorures dissous. Les ROS réagissent ensuite avec le L-012 oxydé, produisant son état excité et entraînant une émission ECL accrue et durable (jusqu'à 145 s) à la surface de la bulle.

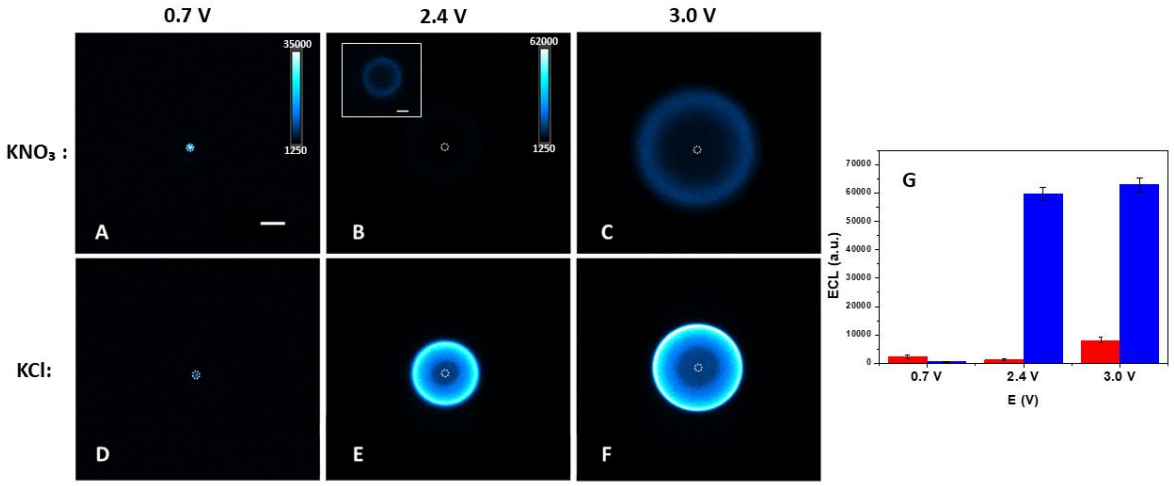

Figure 4. (**A-F**) et (**H-K**) Images de l'émission ECL au niveau de la microélectrode d'or dans la solution PBS 0,2 M (pH 8) contenant 0,5 M H_2O_2, 0,42 mM L-012 et 50 mM **(A-C)** KNO_3 ou **(D-F** et **H-K)** KCl. Le potentiel de l'électrode a été réglé à **(A** et **D)** 0,7 V, **(B** et **E)** 2,4 V et **(C** et **F)** 3 V vs Ag/AgCl pendant 20 s. Les images ECL en fausses couleurs (**A** et **D)** et (**B**, **C**, **E** et **F**) ont été codées avec les échelles d'intensité lumineuse 1200-35000 (montrées en **A**) et 1200-62000 (montrées en **B**), respectivement. L'image en médaillon dans **(B)** a été codée avec la gamme d'intensité 1200-10000. Le cercle en pointillé matérialise le disque d'or de la microélectrode. Barre d'échelle : 50 µm. **(G)** L'intensité moyenne de l'ECL en présence de l'électrolyte support KNO_3 50 mM (en rouge) ou KCl 50 mM (en bleu) lors de l'application d'impulsions chronoampérométriques de 0,7 V, 2,4 V et 3 V par rapport à Ag/AgCl. Les valeurs de l'histogramme représentent la moyenne des expériences pour chaque condition, comme le montrent les images **(A-F)**, réalisées en trois exemplaires en présence (en bleu) et en l'absence de Cl^- (en rouge). Les barres d'erreur indiquent ±1 écart-type par rapport à la moyenne.

En présence de chlore électrogénéré, nous avons observé une augmentation de 51,8 fois de l'intensité de l'ECL à 2,4 V et une augmentation de 7,8 fois à 3 V par rapport aux signaux produits dans les mêmes conditions dans la solution contenant du KNO_3 comme électrolyte support. De plus, l'intensité ECL est 127,6 fois plus élevée à 2,4 V par rapport à l'ECL à faible potentiel (à 0,7 V) dans la même solution d'électrolyte (**figure 4G**). Notamment, une fois que la bulle de Cl_2 est générée, l'ECL est émise à l'interface gaz/liquide même en l'absence d'un potentiel appliqué. Par conséquent, après s'être détachée de l'électrode, la bulle agit probablement comme un réservoir d'espèces oxydantes, initiant des réactions d'oxydo-

réduction et produisant une émission ECL tout en se déplaçant dans la solution. Pour le confirmer, nous avons suivi la formation d'une bulle et son détachement ultérieur de l'électrode, lorsque la bulle a été propulsée vers le haut de la solution (voir les images ECL dans les **figures 5A-D** et les profils d'intensité dans la **figure 5E**).

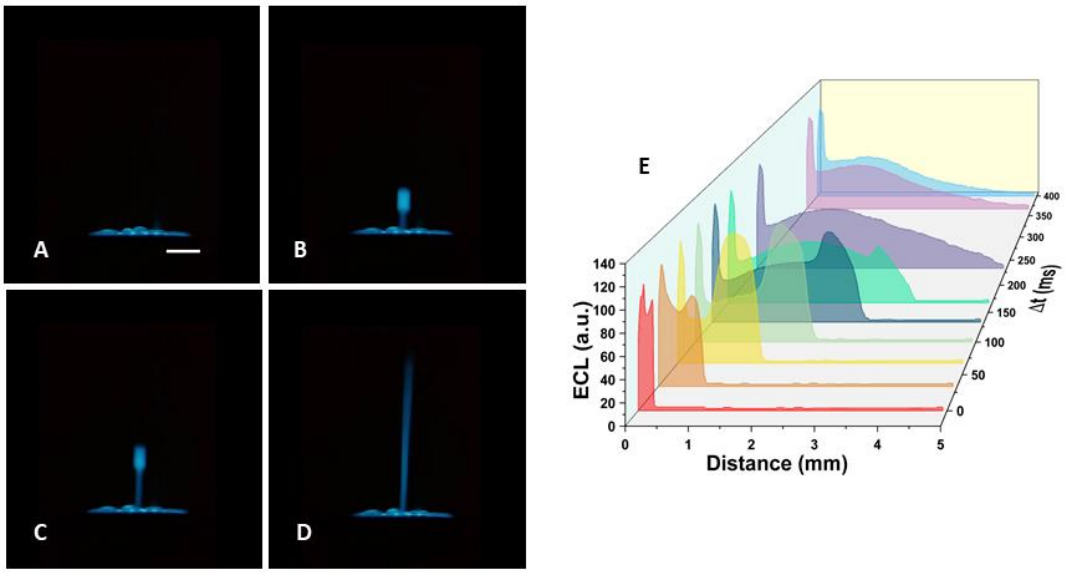

Figure 5. Images ECL **(A-D)** montrant la trajectoire d'une bulle de Cl_2 générée par électrochimie à différents moments (0 ms, 67 ms, 100 ms et 367 ms, respectivement) après son détachement de la surface de l'électrode de carbone vitreux pendant un balayage en voltampérométrie cyclique de 0 V à 3 V à une vitesse de balayage de 0,1 V s^{-1} . Barre d'échelle 1 mm. **(E)** Extension spatiale de l'émission ECL suite au détachement d'une bulle de Cl_2 de la surface de l'électrode (les images correspondantes sont montrées dans **(A-D)**). La propagation de l'ECL jusqu'à 5 mm de l'électrode indique la possibilité d'une formation retardée des espèces radicalaires réactives lors de la dissolution du gaz emprisonné dans la bulle.

Cette émission, due à la production (électro)chimique *in situ* d'oxydants, s'est étendue jusqu'à 5 mm de la surface de l'électrode après le détachement des bulles. Alors que l'ECL est généralement limitée aux processus se déroulant à proximité immédiate (quelques micromètres) de l'électrode, notre méthode étend son application aux phénomènes se produisant à grande distance (jusqu'à plusieurs millimètres) de la surface de l'électrode. Cette ECL générée à distance et de longue durée ouvre des perspectives pour analyser les processus dynamiques en solution normalement inaccessibles aux méthodes ECL traditionnelles.

Références

1 Z. Liu, W. Qi and G. Xu, *Chem. Soc. Rev.*, 2015, **44**, 3117–3142.
2 N. Sojic, Ed., *Analytical Electrogenerated Chemiluminescence: From Fundamentals to Bioassays*, Royal Society of Chemistry, London, UK, 2020.
3 A. J. Bard, Ed., *Electrogenerated Chemiluminescence*, CRC Press, Boca Raton, 2004.
4 A. Zanut, A. Fiorani, S. Canola, T. Saito, N. Ziebart, S. Rapino, S. Rebeccani, A. Barbon, T. Irie, H.-P. Josel, F. Negri, M. Marcaccio, M. Windfuhr, K. Imai, G. Valenti and F. Paolucci, *Nat. Commun.*, 2020, **11**, 2668.
5 H. Yang, J. K. Leland, D. Yost and R. J. Massey, *Nat Biotechnol*, 1994, **12**, 193–194.
6 E. Faatz, A. Finke, H.-P. Josel, G. Prencipe, S. Quint and M. Windfuhr, *Analytical Electrogenerated Electroluminescence*, 2019, 443–470.
7 M. Sentic, M. Milutinovic, F. Kanoufi, D. Manojlovic, S. Arbault and N. Sojic, *Chem. Sci.*, 2014, **5**, 2568–2572.
8 U. Isacsson, J. Kowalewska and G. Wettermark, *J. Inorg. Nucl. Chem.*, 1978, **40**, 1653–1656.
9 P. Zhou, S. Hu, W. Guo and B. Su, *Fundam. Res.*, 2022, **2**, 682–687.
10 J. E. Dick, C. Renault, B.-K. Kim and A. J. Bard, *Angew. Chem. Int. Ed.*, 2014, **53**, 11859–11862.
11 F.-R. F. Fan and A. J. Bard, *Nano Lett.*, 2008, **8**, 1746–1749.
12 Y. Wang, W. Guo, Q. Yang and B. Su, *J. Am. Chem. Soc.*, 2020, **142**, 1222–1226.
13 N. S. Adamson, A. G. Theakstone, L. C. Soulsby, E. H. Doeven, E. Kerr, C. F. Hogan, P. S. Francis and L. Dennany, *Chem. Sci.*, 2021, **12**, 9770–9777.
14 W.-X. Fu, P. Zhou, W.-L. Guo and B. Su, *Adv. Sens. Energy Mater.*, 2022, **1**, 100028.
15 E. Kerr, S. Knezevic, P. S. Francis, C. F. Hogan, G. Valenti, F. Paolucci, F. Kanoufi and N. Sojic, *ACS Sens.*, 2023, **8**, 933–939.
16 A. Fracassa, C. I. Santo, E. Kerr, S. Knežević, D. J. Hayne, P. S. Francis, F. Kanoufi, N. Sojic, F. Paolucci and G. Valenti, *Chem. Sci.*, 2024, **15**, 1150–1158.
17 M. Belotti, M. M. T. El-Tahawy, M. Garavelli, M. L. Coote, K. S. Iyer and S. Ciampi, *Anal. Chem.*, 2023, **95**, 9779–9786.
18 J.-H. Han, E. Lee, S. Park, R. Chang and T. D. Chung, *J. Phys. Chem. C*, 2010, **114**, 9546–9553.
19 P. A. Defnet and B. Zhang, *ChemElectroChem*, 2020, **7**, 252–259.
20 Y. Wang, R. Jin, N. Sojic, D. Jiang and H. Chen, *Angew. Chem. Int. Ed.*, 2020, **59**, 10416–10420.
21 S. Voci, A. Ismail, P. Pham, J. Yu, A. Maziz, F. Mesnilgrente, L. Reynaud, T. Livache, P. Mailley, A. Buhot, T. Leichle, A. Kuhn, L. Leroy, A. Bouchet-Spinelli and N. Sojic, *J. Electrochem. Soc.*, 2020, **167**, 137509.
22 P. Nikolaou, G. Valenti and F. Paolucci, *Electrochim. Acta*, 2021, **388**, 138586.
23 W. Guo, P. Zhou, L. Sun, H. Ding and B. Su, *Angew. Chem. Int. Ed.*, 2021, **60**, 2089–2093.
24 Y. B. Vogel, C. W. Evans, M. Belotti, L. Xu, I. C. Russell, L.-J. Yu, A. K. K. Fung, N. S. Hill, N. Darwish, V. R. Gonçales, M. L. Coote, K. Swaminathan Iyer and S. Ciampi, *Nat. Commun.*, 2020, **11**, 6323.
25 M. W. Glasscott and J. E. Dick, *J. Phys. Chem. Lett.*, 2020, **11**, 4803–4808.
26 M. W. Glasscott, S. Voci, P. J. Kauffmann, A. I. Chapoval and J. E. Dick, *Langmuir*, 2021, **37**, 2907–2912.
27 S. Voci, K. J. Vannoy and J. E. Dick, *J. Colloid Interface Sci.*, 2024, **661**, 853–860.
28 B. R. Layman and J. E. Dick, *J. Am. Chem. Soc.*, 2024, **146**, 707–713.
29 Y. Chen, D. Zhao, J. Fu, X. Gou, D. Jiang, H. Dong and J.-J. Zhu, *Anal. Chem.*, 2019, **91**, 6829–6835.
30 M.-M. Chen, C.-H. Xu, W. Zhao, H.-Y. Chen and J.-J. Xu, *Chem. Commun.*, 2020, **56**, 3413–3416.
31 M.-M. Chen, C.-H. Xu, W. Zhao, H.-Y. Chen and J.-J. Xu, *J. Am. Chem. Soc.*, 2021, **143**, 18511–18518.

32 H. Zhu, D. Jiang and J.-J. Zhu, *Chem. Sci.*, 2021, **12**, 4794–4799.
33 J. Dong, Y. Xu, Z. Zhang and J. Feng, *Angew. Chem. Int. Ed.*, 2022, **61**, e202200187.
34 G. Valenti, S. Scarabino, B. Goudeau, A. Lesch, M. Jović, E. Villani, M. Sentic, S. Rapino, S. Arbault, F. Paolucci and N. Sojic, *J. Am. Chem. Soc.*, 2017, **139**, 16830–16837.
35 C. Ma, Y. Cao, X. Gou and J.-J. Zhu, *Anal. Chem.*, 2020, **92**, 431–454.
36 S. Rebeccani, A. Zanut, C. I. Santo, G. Valenti and F. Paolucci, *Anal. Chem.*, 2022, **94**, 336–348.
37 W. Miao, J.-P. Choi and A. J. Bard, *J. Am. Chem. Soc.*, 2002, **124**, 14478–14485.
38 E. Daviddi, A. Oleinick, I. Svir, G. Valenti, F. Paolucci and C. Amatore, *ChemElectroChem*, 2017, **4**, 1719–1730.
39 A. Fiorani, J. P. Merino, A. Zanut, A. Criado, G. Valenti, M. Prato and F. Paolucci, *Curr. Opin. Electrochem.*, 2019, **16**, 66–74.
40 S. Kesarkar, S. Valente, A. Zanut, F. Palomba, A. Fiorani, M. Marcaccio, E. Rampazzo, G. Valenti, F. Paolucci and L. Prodi, *J. Phys. Chem. C*, 2019, **123**, 5686–5691.
41 P. Dai, C. Liu, C. Xie, J. Ke, Y. He, L. Wei, L. Chen and J. Jin, *Anal Bioanal Chem*, 2020, **412**, 1375–1384.
42 A. Abdussalam and G. Xu, *Anal Bioanal Chem*, 2022, **414**, 131–146.
43 F. Rizzo, F. Polo, G. Bottaro, S. Fantacci, S. Antonello, L. Armelao, S. Quici and F. Maran, *J. Am. Chem. Soc.*, 2017, **139**, 2060–2069.
44 G. J. Barbante, E. H. Doeven, E. Kerr, T. U. Connell, P. S. Donnelly, J. M. White, T. Lópes, S. Laird, D. J. D. Wilson, P. J. Barnard, C. F. Hogan and P. S. Francis, *Eur. J. Chem.*, 2014, **20**, 3322–3332.
45 D. Bruce and M. M. Richter, *Anal. Chem.*, 2002, **74**, 1340–1342.
46 L. Chen, D. J. Hayne, E. H. Doeven, J. Agugiaro, D. J. D. Wilson, L. C. Henderson, T. U. Connell, Y. H. Nai, R. Alexander, S. Carrara, C. F. Hogan, P. S. Donnelly and P. S. Francis, *Chem. Sci.*, 2019, **10**, 8654–8667.
47 M. A. Haghighatbin, S. E. Laird and C. F. Hogan, *Curr. Opin. Electrochem.*, 2018, **7**, 216–223.
48 S. A. Kitte, C. Wang, S. Li, Y. Zholudov, L. Qi, J. Li and G. Xu, *Anal Bioanal Chem*, 2016, **408**, 7059–7065.
49 H. Xing, Q. Zhai, X. Zhang, J. Li and E. Wang, *Anal. Chem.*, 2018, **90**, 2141–2147.
50 C. V. Raju and S. S. Kumar, *Chem. Commun.*, 2017, **53**, 6593–6596.
51 F. Yuan, M. I. Halawa, X. Ma, A. Abdussalam, B. Lou and G. Xu, *ChemElectroChem*, 2020, **7**, 4239–4244.
52 J. Ding, P. Zhou and B. Su, *ChemElectroChem*, 2022, **9**, e202200236.
53 O. V. Klymenko, I. Svir and C. Amatore, *ChemPhysChem*, 2013, **14**, 2237–2250.
54 E. Kerr, D. J. Hayne, L. C. Soulsby, J. C. Bawden, S. J. Blom, E. H. Doeven, L. C. Henderson, C. F. Hogan and P. S. Francis, *Chem. Sci.*, 2022, **13**, 469–477.
55 S. Voci, B. Goudeau, G. Valenti, A. Lesch, M. Jović, S. Rapino, F. Paolucci, S. Arbault and N. Sojic, *J. Am. Chem. Soc.*, 2018, **140**, 14753–14760.
56 H. Ding, P. Zhou, W. Fu, L. Ding, W. Guo and B. Su, *Angew. Chem. Int. Ed.*, 2021, **60**, 11769–11773.
57 H. Ding, W. Guo and B. Su, *Angew. Chem. Int. Ed.*, 2020, **59**, 449–456.
58 N. Harvey, *J. Phys. Chem.*, 1929, **33**, 1456–1459.
59 J. Arnhold, S. Mueller, K. Arnold and E. Grimm, *J. Biolumin. Chemilumin.*, 1991, **6**, 189–192.
60 H. Cui, W. Wang, C.-F. Duan, Y.-P. Dong and J.-Z. Guo, *Eur. J. Chem.*, 2007, **13**, 6975–6984.
61 M. Guo, D. Du, J. Wang, Y. Ma, D. Yang, M. A. Haghighatbin, J. Shu, W. Nie, R. Zhang, Z. Bian, L. Wang, Z. J. Smith and H. Cui, *Chem. Biomed. Imaging*, 2023, **1**, 179–185.
62 F. Han, H. Jiang, D. Fang and D. Jiang, *Anal. Chem.*, 2014, **86**, 6896–6902.
63 R. He, H. Tang, D. Jiang and H. Chen, *Anal. Chem.*, 2016, **88**, 2006–2009.
64 W. Xu, Y. Wu, X. Wang, Y. Qin, H. Wang, Z. Luo, J. Wen, L. Hu, W. Gu and C. Zhu, *Angew. Chem. Int. Ed.*, 2023, **62**, e202304625.
65 M. Xi, Z. Wu, Z. Luo, L. Ling, W. Xu, R. Xiao, H. Wang, Q. Fang, L. Hu, W. Gu and C. Zhu, *Angew. Chem. Int. Ed.*, 2023, **62**, e202302166.

66 W. Liang, M. Wang, C. Ma, J. Wang, C. Zhao and C. Hong, *Small*, 2024, **20**, 2306473.
67 N. Gao, G. Ren, M. Zhang and L. Mao, *J. Am. Chem. Soc.*, 2024, **146**, 3836–3843.
68 H. Xia, X. Zheng, J. Li, L. Wang, Y. Xue, C. Peng, Y. Han, Y. Wang, S. Guo, J. Wang and E. Wang, *J. Am. Chem. Soc.*, 2022, **144**, 7741–7749.
69 L. Qiu and R. G. Cooks, *Angew. Chem. Int. Ed.*, 2024, **63**, e202400118.

Table of contents

List of abbreviations

Abbreviation	Meaning
BPO	benzoyl peroxide
CA	chronoamperometry
CCD	charge coupled device
CER	chlorine evolution reaction
CHO	Chinese hamster ovary
CL	chemiluminescence
CNTs	carbon nanotubes
CV	cyclic voltammetry
DBAE	dibutylaminoethanol
DC	direct current
DNA	deoxyribonucleic acid
ECL	electrochemiluminescence
EM-CCD	electron multiplied charge coupled device
ET	electron transfer
Fc	ferrocene
FOWA	foot of the wave analysis
fps	frame per second
FRET	Förster resonance energy transfer
GC	glassy carbon
HOMO	highest occupied molecular orbital
IL	inter ligand (charge transfer)
LED	light emitting diode
LMCT	ligand to metal charge transfer
LUMO	lowest occupied molecular orbital
MC	metal centred (charge transfer)
MLCT	metal to ligand charge transfer
NADH	nicotinamide adenine dinucleotide
OER	oxygen evolution reaction

PECL	positive electrochemiluminescence (imaging)
PL	photoluminescence
PMT	photomultiplier tube
QDs	quantum dots
RNA	ribonucleic acid
ROI	region of interest
Ru@PS	polystyrene bead decorated with $[Ru(bpy)_3]^{2+}$ emitter
Sa@Ru	streptavidin modified (covalently labelled) with $[Ru(bpy)_3]^{2+}$
SECL	shadow electrochemiluminescence (imaging)
SECM	scanning electrochemical microscopy
STED	stimulated emission depletion
SUSHI	super resolution shadow imaging
TOF	turnover frequency
TPrA	tri-*n*-propylamine

List of symbols

Symbol	Meaning
$E_{A\ /A^{\bullet-}}$	reduction potential (in the general case)
$E_{B^{\bullet+}/B}$	oxidation potential (in the general case)
C	concentration
c	speed of light
E	electrode potential
$E^0_{A/B}$	standard potential of the substrate/product redox couple
$E^0_{P/Q}$	standard potential of the catalyst redox couple
F	Faraday constant
h	Planck constant
i	current
i^0_p	peak current of the catalyst in the absence of the substrate
i_p	peak current
k_b	Boltzmann constant
$k_{b\ (n)}$	electron transfer rate constant for the backward reaction
$k_{f\ (n)}$	electron transfer rate constant for the forward reaction
Q	charge
R	normal gas constant
S_0	singlet ground state
S_1	first excited singlet state
T	temperature
t	time
T_0	triplet ground state
T_1	first excited triplet state
ΔE	energy difference between the frontier orbitals
ΔG*	activation free energy
ΔG^0	Gibbs free energy
ΔH	enthalpy

ΔS	entropy
λ	reorganisation energy
λ_{ab}	absorption wavelength
λ_{em}	emission wavelength
ν	frequency
ϕ_{em}	emission quantum yield

Preface

People have always been captivated by beauty and elegance, whether it is the vivid spectacle of fireworks, the graceful movements of dance, the intricate designs of art, or the melodies of music. This fascination with aesthetics transcends the arts and seeps through every aspect of our lives. Our pursuit of beauty is even reflected in the way we approach and appreciate science, where the harmony of a well-designed experiment or the beauty of a result can be as compelling as any artistic masterpiece. Often, it is this very elegance of certain ideas, methods, and approaches that drives scientific curiosity and leads to innovation.

Electrochemiluminescence (ECL) is a field that uniquely blends the control and precision of electrochemistry with the sensitivity and resolution of luminescence. This synergy creates a captivating interplay of light and darkness which dynamically evolves in space and time, painting a vivid and detailed view of local (and global) (electro)chemical reactivity. Thus, apart from its remarkable beauty, ECL stands out for its elegance in revealing complex molecular interactions and reaction dynamics, seamlessly providing profound practical and fundamental insights into the systems under study.

It is no surprise that this electrochemical method has found a wide range of applications. It is invaluable in fundamental studies of physicochemical phenomena, the development of sensitive biological assays, material science, and even biological imaging. However, intrinsic downsides of ECL, which can limit its practical application, are low light emission intensity, rapid signal decay, and spatial confinement to the micrometric region near the electrode surface. In this context, the scope of this thesis revolves around improving the ECL method by amplifying the emission intensity and extending its duration in space and time. To do so, we investigate the underlying ECL reactivity and utilize the obtained mechanistic insights to improve the efficiency of specific reaction steps and/or to introduce additional mechanistic pathways to obtain brighter and long-lasting light emission.

Chapter I presents the general theoretical background of electrochemistry and photophysics required to understand the ECL phenomena. It describes different ECL systems and configurations, as well as the mechanistic aspects of ECL generation, which are necessary to critically examine and discuss the work contained in the remainder of the thesis. Finally,

this first chapter briefly presents the state of the art in the field of ECL, giving a perspective on recent advances and research trends.

Chapter II explores the mechanisms underlying ECL amplification in the $[Ru(bpy)_3]^{2+}$/TPrA coreactant system when an Ir(III) redox mediator is added to the reaction mixture. In this work, we employed electrochemical analysis, spectroscopic investigation, and finite element simulation to elucidate how the redox mediator critically modulates ECL efficiency by controlling the mechanisms and kinetics of radical species production and decay. Our approach was to develop a numerical simulation model that can reproduce experimental electrochemical and spectroscopic data, allowing us to evaluate key kinetic parameters and gain deeper mechanistic insights into the system. Data obtained from this model confirm the pivotal role of redox catalysis in enhancing ECL, demonstrating how the redox mediator efficiently triggers ECL reactions at low anodic overpotentials by homogeneously oxidizing both TPrA and $[Ru(bpy)_3]^{+}$. Moreover, beyond merely replicating experimental results, this model also serves as a predictive tool, enabling us to explore how individual reaction steps contribute to the overall mechanism. By varying the specific thermodynamic and kinetic parameters within the model, we investigate the interplay between different pathways in ECL systems employing redox mediators with distinct properties. This predictive capability holds significant potential for guiding the rational design of ECL reagents and mediators, ultimately leading to customized systems with optimized and enhanced ECL properties.

Chapter III describes a remarkable ECL enhancement (of 70.9-fold) in a bead-based immunoassay setup, which uses Ru-emitter as a luminescent label, upon adding Ir(III) redox mediator into the TPrA-containing electrolyte solution. Using ECL microscopy, we monitored the intensity and spatial distribution of ECL emission at individual Ru-labelled polystyrene beads, thus experimentally confirming the catalytic enhancement pathways, studied in Chapter II, are also relevant in this heterogeneous setup where $[Ru(bpy)_3]^{2+}$ does not undergo direct oxidation at the electrode surface. These pathways involve the direct oxidation of the Ir(III) complex which subsequently oxidises ECL reagents, thus improving the overall ECL efficiency by reducing the dependence of ECL reactions on the sluggish electrochemical oxidation of TPrA and by minimizing the reliance on transient $TPrA^{\bullet+}$ radicals to produce the luminophore's excited state. Consequently, coreactant ECL in the presence of redox mediators

has substantial potential to advance ECL immunosensing by improving its sensitivity and lowering detection limits, which could facilitate earlier and less invasive disease diagnostics.

Additionally, we extend the application of this ECL system with a redox mediator to enable bimodal imaging of cells. To do so, we used the concurrent red luminescence of $[Ru(bpy)_3]^{2+}$, employed for membrane labelling (light-emitting object on a dark background - PECL), and green luminescence of Ir(III) mediator in solution (non-emissive object shadowing the background luminescence - SECL). ECL emissions of the two luminophores were then spectrally and spatially resolved, yielding two micrographs of the same cells, where PECL shows the distribution of the $[Ru(bpy)_3]^{2+}$ labels attached to the cellular membrane, and SECL reflects the local diffusional hindrance of the ECL reagents by each cell. This bimodal approach can provide more information about the observed cells compared with the classically used ECL and fluorescence microscopy techniques, opening new prospects for sensitive and multidimensional ECL bioimaging.

Chapter IV investigates the ECL of the luminol/H_2O_2 system at the interfaces of electrogenerated chlorine and oxygen bubbles, revealing a remarkable 127.6-fold enhancement in ECL emission at the surface of a chlorine bubble compared to that at a microelectrode. Notably, this enhanced ECL extends up to several millimetres from the electrode, demonstrating for the first time that ECL can reach into the bulk solution instead of being confined to the vicinity of the electrode. We explore the mechanisms behind this phenomenon by studying the evolution of current and ECL intensity with electrode potential and by using ECL microscopy to resolve the underlying ECL reactivity in space and time. These investigations, conducted both in chloride-containing and chloride-free electrolyte solutions, demonstrate the effects of the gas/liquid interface on electrochemical reactivity. The accumulation of hydroxyl radicals at the bubble's interface (i.e. corona effect of a bubble) leads to locally enhanced ECL of luminol, while higher ECL intensities in the presence of chlorides prove the involvement of electrogenerated chlorine species in the ECL reactions. Therefore, this work not only reveals important mechanistic information about ECL at the interface of chlorine and oxygen gas bubbles but also enhances ECL emission and extends it in space and time, providing a valuable tool for studying the reactivity at interfaces and in solution.

Chapter I:
What is ECL?

Chapter I: What is ECL?

1.1 Introduction

Electrogenerated chemiluminescence, also referred to as electrochemiluminescence (ECL), is the light emission process that occurs when an excited state of a luminophore is populated through a highly exergonic redox reaction of electrogenerated species.[1–3] As its name suggests, it is initiated electrochemically, i.e. via a heterogeneous electron-transfer reaction, leading to the conversion of reactants into their radical ions at the electrode surface. This step triggers a cascade of chemical reactions in solution between the reactive radical intermediates that finally undergo a highly exergonic homogeneous electron-transfer to produce the electronically excited state of a luminophore. It subsequently relaxes to its ground state by emitting a photon in a process known as luminescence.[4]

Luminescence refers to any light-emitting phenomenon that is not caused by the rise in temperature. It is a "cold" light emission appearing as a product of the radiative decay of an electronically excited state of an atom, molecule or material to its lower energy (ground) state. This means that, for the luminescence to occur, the electrons within the atom or a molecule must first absorb energy to move to higher energy levels (i.e. become excited). Depending on the nature of the excitation process, one can classify luminescence phenomena into different types, as shown in **Table 1.1**.[5]

The term photoluminescence (PL) implies that electronic excitation is a consequence of photon absorption. Depending on the nature of processes following light absorption, it is possible to distinguish two types of PL: fluorescence and phosphorescence (see section **1.3**). Fluorescence techniques, characterised by a strong emission, ease of use and precise control over the experimental conditions (i.e. excitation energy, spatial and temporal resolution) became invaluable for the majority of imaging and spectroscopic applications.[6,7]

Chemiluminescence (CL),[8] on the other hand, does not require an external light source for excitation, as it is a product of the energy released in a chemical reaction. As this energetic reaction typically takes place in the bulk solution, CL emission depends on the fluid flow and diffusion of the reacting species, thus lacking precise control over the reaction conditions. ECL is a specific case of CL, where the reactive radicals involved in energetic chemical reactions are formed at the surface of a working electrode. Owing to the initial electrochemical step,

ECL has several advantages when compared to CL, including precise spatial and temporal control over signal generation.[1–3] In contrast to CL and ECL, electroluminescence is related to the highly energetic recombination of electrons and holes in a semiconducting material, usually under a strong electric field. This process is responsible for the light emission at the p-n junction of two semiconductors in the light-emitting diodes (LEDs).[9]

Naturally, there are other highly energetic phenomena (unrelated to ECL) that can cause light emission. Some of the examples are i) Bioluminescence, which is another case of chemiluminescence where exergonic biochemical reactions take place inside living organisms. ii) Crystaloluminescence and iii) lyoluminescence, which utilise the energy released during the crystallisation and dissolution of crystals, respectively. iv) Mechanoluminescence, which occurs due to bending, stretching, crushing, or other mechanical stress imposed upon the material. v) Radioluminescence and vi) Sonoluminescence, initiated by the high energy radiation, and implosion of gas cavitations generated by the ultrasound, respectively. Regardless of the source of excitation, all luminescence phenomena follow the same photophysical principles, which will be discussed later.

Table 1.1. Types of luminescence according to the excitation source

Luminescence type	Excitation source
Photoluminescence → fluorescence / phosphorescence	absorption of photons
Chemiluminescence	chemical reaction
Bioluminescence	biochemical reaction in a living organism
Electroluminescence	recombination of electrons and holes in a material
Electrochemiluminescence	electrochemical reaction
Mechanoluminescence	mechanical stress
Crystaloluminescence	crystallization
Lyoluminescence	dissolution of a crystal
Sonoluminescence	imploding bubbles in a liquid excited by sound
Radioluminescence (scintilation)	high-energy particles or radiation

1.2 Brief history of ECL

Light emission during electrolysis was first reported in the late 1920s by Dafford and Harvey independently.[10,11] Dafford[10] observed luminescence at both the cathode and the anode when applying high voltages of 500 V and 1500 V in solutions of Grignard compounds in anhydrous ether. Harvey,[11] on the other hand, studied the light emission of 5-amino-2,3-dihydrophthalazine-1,4-dione (luminol) at the surface of an anode in alkaline aqueous solutions at ca. 2.4 V. He suggested using this phenomenon for the detection of reactive oxygen species, which remained one of its applications to this day. While the mechanism and application of luminol's ECL are discussed later, it is worth mentioning that chemical reactions that provide energy for the luminophore's excitation in this ECL system (as well as the one containing Grignard compounds) involve bond-breaking (or atom transfer) reactions.

However, ECL emission produced in the energetic electron-transfer reactions [12–15], reported in the late 1960s, remains one of the breakthrough events in the ECL field. The first experiments of this kind were documented by Hercules in 1964[12] and they involved the simultaneous electrochemical production of positively and negatively charged radical ions of hydrocarbons (i.e. rubrene, pyrene and anthracene) in dry aprotic solvents (e.g. dimethylformamide and acetonitrile). Following the generation at metal electrode surfaces, the oppositely charged radical ions reacted in a rapid and highly exergonic electron-transfer reaction - ionic annihilation, leading to the ECL emission. This comprehensive study investigated the as-obtained radicals and their lifetimes, as well as the possible mechanistic pathways for their reaction. It also tested several different electrode configurations and experimental setups for the simultaneous generation of different radical ions, the most important ones involving the application of direct current (DC) to the two closely spaced Pt electrodes, and cycling of the electrode potential at high-frequencies (i.e. 10 Hz). Subsequent studies,[13,14] which used cyclic voltammetry (CV) to analyse the anodic and cathodic electron transfer processes in these aromatic systems, confirmed the ionic annihilation nature of the highly energetic chemical step. This pioneering work was important for the field of ECL because it laid the fundamentals that facilitated the development of the annihilation ECL. But, more importantly, it provided additional experimental evidence that radical ions can be

generated (electrochemically) by a transfer of a single electron, contradicting the popular belief (at the time) that electrons in chemical reactions move only in pairs. Marcus theoretically addressed these phenomena during the 1950s and 1960s, devising the electron-transfer theory,[16] which explains curious redox reactivity in various fields of chemical research, including the generation of chemiluminescence following an electron-transfer reaction.[17]

In 1972, Tokel and Bard[18] successfully obtained ECL by annihilation of ion radicals of tris(2,2'-bipyridine)ruthenium(II) dichloride ($[Ru(bpy)_3]Cl_2$) in the acetonitrile solution, demonstrating that ECL upon electron transfer is not exclusive to aromatic hydrocarbons. At this point, electron-transfer reactions and ECL were well investigated and understood both theoretically and experimentally, facilitating further generalization of these phenomena and extension of their applications. Specifically, works from the late 1970s to 1990s demonstrate that the exergonic electron transfer between two different compounds - luminophore and coreactant, can produce luminescence. In these early works, (electro)chemiluminescence was successfully emitted by mixtures of $[Ru(bpy)_3]^{2+}$ and oxalate,[19,20] peroxydisulfate[21] and different aliphatic amines[22], of which the most practically useful one is tri-*n*-propylamine (TPrA)[23]. This discovery had major implications on the ECL, allowing its use in aqueous solutions at a single (cathodic or anodic) applied potential, simplifying the ECL experimental setups and allowing the light to be generated using the conventional electrochemical techniques (i.e. cyclic voltammetry and chronoamperometry). This led to accelerated progress in the ECL field, where $[Ru(bpy)_3]^{2+}$/TPrA became a model ECL luminophore/coreactant system, used nowadays for the majority of ECL applications.

1.3 Fundamentals of photophysiscs

As described above, luminescence phenomena involve the excitation of electrons within an atom or a molecule to a higher energy level, followed by their subsequent transition to the original low energy (i.e. ground) state, accompanied by light emission.

Quantum mechanics treats electrons as waves, describing the electronic structure using wavefunctions called orbitals, that have distinct energies, shapes (orbital angular momentum), and spatial orientations (angular momentum), all denoted by their specific

quantum numbers. This theory provides a model that can explain chemical reactivity and spectroscopic properties of molecules, consequently imposing a set of rules (selection rules) describing electron configurations and possible electron transitions, which are relevant for studying luminescence phenomena. In a very simplified representation, one can imagine that, in a molecule's ground state, electrons (that have a magnetic spin of either + ½ or - ½) occupy the lowest energy orbitals in pairs. Since, according to Pauli's exclusion principle, two electrons within a molecule cannot be identical (i.e. with the same quantum numbers), electrons populating the same orbital have opposite magnetic spins. Therefore, when all the electrons are paired, which is the case for most of the organic molecules in their ground state, the total spin equals 0, resulting in a spin multiplicity (2S + 1) of 1. Such a ground state is referred to as a singlet state (S_0). However, in some cases, molecules can have unpaired electrons in their ground state. A characteristic example is a molecule of oxygen, which has a triplet ground state configuration (T_0) with two unpaired electrons.

Typically, the lowest energy transition occurs between the highest occupied molecular orbital (HOMO) and the lowest unoccupied molecular orbital (LUMO), adhering to selection rules based on orbital symmetry and conservation of electron magnetic spin. This transition is induced when the absorbed energy matches the HOMO–LUMO gap, satisfying the resonance condition. In the context of photon absorption (and emission), this condition is expressed as:

$$\Delta E = E_2 - E_1 = h\upsilon = \frac{hc}{\lambda} \qquad (1.1)$$

where ΔE is the energy difference between the frontier orbitals (E_2 and E_1, respectively), corresponding to the amount of energy absorbed (or emitted) during a reaction. h is a Planck constant, ν is the frequency, c is the speed of light and $\lambda_{ab}/\lambda_{em}$ is the wavelength of the absorbed/emitted light.

Figure 1.1 shows a Jablonski diagram, which is useful for intuitively visualizing the photophysical processes and their respective kinetics or lifetimes. It shows the singlet ground state (S_0) and two electronically excited states with the lowest energy: the singlet (S_1) and the triplet (T_1), their names referring to the spin multiplicity. Notably, triplet states are always lower in energy than their corresponding singlet states of the same electronic configuration,

which is related to the electromagnetic interactions between the electrons and nuclei. The diagram also shows the vibrational energy levels, appearing due to the oscillation of the atoms along the chemical bonds, while the rotational fine structure is omitted.

According to the Boltzmann distribution, the most probable thermal energy of molecules in equilibrium corresponds to the lowest vibronic level of their ground state (S_0). Thus, following the photon absorption, electronic excitation (blue line) from the lowest vibronic level of S_0 to different vibronic levels of S_1 (first excited state of the same multiplicity) occurs on a timescale of a femtosecond. This transition is so rapid that, per the Franck-Condon principle, there is no displacement of the nuclei, implying that immediately upon excitation the configuration and energy of a luminophore molecule are the same as in the ground state but with a very different electronic configuration. A fast vibrational relaxation on a timescale of picoseconds, follows the excitation, bringing the electron to the lowest vibronic level of the excited state. During this event, vibrational energy is dissipated as heat (kinetic or thermal energy), mostly to the surrounding medium, reorganising the configuration of the molecule and its solvation sphere to match the new electronic configuration.

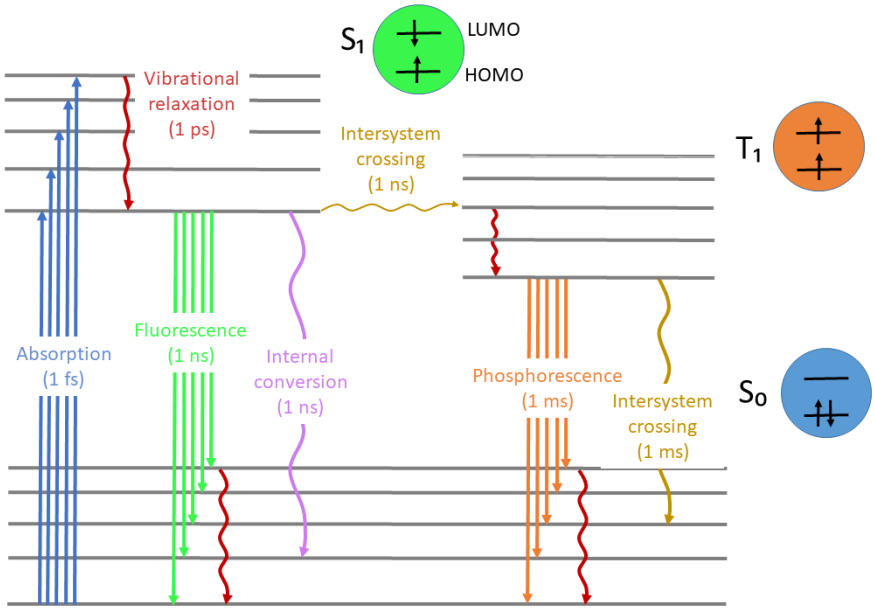

Figure 1.1 Jablonski diagram illustrating the typical photophysical processes in molecules following photoexcitation, accompanied by a schematic depiction of the electron configuration of the frontier orbitals for each electronic state. The provided time constants offer an indication of the order of magnitude of the typical duration of each process.

The molecule stays in this state for long enough that it can react with other compounds (quenchers) in energy transfer or electron transfer interactions, while itself undergoing a non-radiative decay to the ground state. However, these processes are not included in the Jablonski diagram and will be discussed later. Alternatively, several competitive deactivation processes, namely fluorescence, internal conversion and intersystem crossing, can occur from the excited state. All of these competing processes are fast, lasting several nanoseconds. The only radiative process amongst those is fluorescence, which involves a decay to vibrational levels of the ground state accompanied by the emission of a photon. Fluorescence emission has lower energy than the excitation light since some of the energy is dissipated during the relaxation of vibronic levels, and this difference in the absorption and emission band maxima is called Stokes Shift. Conversely, in processes alternative to fluorescence, the electron can return to the ground state by a non-radiative transition called internal conversion, or transfer (also non-radiatively) to a vibronic level of the same energy within the T_1 state. The latter transition is named intersystem crossing and is forbidden since it involves two electronic states of different multiplicities, violating the conservation of spin. However, this forbidden transition can happen due to interactions between the orbital magnetic moment and the spin magnetic moment (i.e the spin-orbit coupling), which is particularly pronounced in the presence of heavy atoms (e.g. in transition metal complexes that contain highly charged nuclei). The as-formed triplet state can subsequently undergo a radiative relaxation to the S_0 ground state, and the emission process in this case is called phosphorescence. Since it involves forbidden transitions, phosphorescence usually occurs on a longer timescale (in milliseconds) and has a lower intensity than fluorescence. Additionally, since the triplet state is lower in energy, Stokes shift is more pronounced for the phosphorescence phenomena. Phosphorescence competes with the non-radiative transition (intersystem crossing) from T_1 to S_0, which is a dominant process at room temperature and typically takes place within several milliseconds. Finally, two triplet states can interact in a triplet-triplet annihilation, leading to an excited singlet state that can subsequently undergo chemical reactions or relax to the ground state via fluorescence or internal conversion. The comparison between the ECL and photoluminescence spectra may indicate whether the same electronic state is reached by both excitation modes.

Apart from its electronic structure and spectral properties, an important intrinsic property of a luminophore's excited state is its emission quantum yield (ϕ_{em}). Quantum yield defines the ratio between the photons emitted and photons absorbed by a fluorophore, indicating the relative rates of fluorescence (or phosphorescence) and all the non-radiative processes that compete with emission. Since it is a ratio, the numerical value of quantum yield is between 0 and 1. For example, the quantum yield of $[Ru(bpy)_3]^{2+}$ is 0.063 in deaerated water solutions, while it slightly changes in different media or in the presence of oxygen.[24] Another common way to express the quantum yield in photoluminescence is as the emission strength of the investigated compound relative to another (reference) fluorescence compound of a known quantum yield for the identic experimental parameters (excitation wavelength, excitation and emission slit widths, photomultiplier voltage, etc.). $[Ru(bpy)_3]^{2+}$ is commonly used as a standard in the determination of quantum yields of transition-metal complexes.

1.4 Fundamentals of electrochemistry

Since heterogeneous electron transfer initiates the ECL reactions, it is clear that electrochemistry plays a crucial part in the ECL process. Although electrochemical systems require a minimum of two electrodes to enable the flow of electrons, adhering to the principle of charge conservation, the primary focus in electrochemistry typically revolves around controlling and analysing processes at one of the electrodes, referred to as the working electrode. These processes, fundamental to electrochemistry, involve an exchange of electrons between the electrode and redox-active species in the solution and can be discussed in terms of oxidation or reduction events at the electrode-electrolyte interface.[25] Whether a compound will oxidise or reduce at this interface depends on the relative energies of its valent electrons and the electrons within the Fermi level of the electrode material. Thus, the electrode potential, which is effectively a measure of the electron energy, is a key thermodynamic parameter for an electrochemical reaction, with the equilibrium potential expressed by the Nernst equation.

If the electron energies within the electrode are manipulated (if the potential is imposed externally) by using a potentiostat, they can reach a certain threshold value at which

the electrochemical reactions initiate. Polarizing the electrode negatively increases the electron energies, eventually reaching levels high enough for electrons to transfer from the electrode to the vacant LUMO orbital, reducing the redox species in the solution. Conversely, applying positive potentials decreases the electron energy levels, facilitating the transfer of electrons from the HOMO orbitals of dissolved molecules to the surface of the electrode, leading to the oxidation of the molecules. Therefore, the electrode potential (E) controls the direction and rate of heterogeneous electron transfers. Notably, the ability of redox species to undergo (simple) redox reactions (i.e their redox potential) depends on the energies of their frontier orbitals. The lower the LUMO, the easier the molecule will receive an electron and undergo reduction, while more energetic HOMO orbitals facilitate easier oxidation. Hence, the same orbitals govern the molecule's electrochemical and photophysical properties, determining its ECL behaviour.

Apart from the electrode potential, an important parameter in electrochemical measurements is the current (i) flowing through the circuit between the working and counter electrodes. According to Faraday's law, the amount of charge transferred during the electrochemical reaction is proportional to the amount of reactants transformed at the electrode. Consequently, the current arising from the redox reactions amounts to the rate of the heterogeneous electron transfer ($i = dQ/dt$), and as such can be used to determine the rates of (electro)chemical reactions. Thus, electrochemical measurements are a valuable tool for studying both the thermodynamics and kinetics of heterogeneous electron transfer and chemical steps preceding or following the electrochemical reaction. These aspects are demonstrated and discussed for homogeneous electrocatalysis in **Chapter 2**.

A usual way of presenting electrochemical data is as current versus time (i-t) or current versus potential (i-E) plots. The former representation is more common when applying pulses of constant potential, in which case the current corresponds to the evolution of the concentration of electroactive species near the electrode surface with time. Chronoamperometry (CA) is a common electrochemical technique based on applying constant potential, often used for triggering coreactant ECL emission in sensing or imaging applications.

On the other hand, the plot following the evolution of current with potential provides deeper insights into the dynamics of the processes taking place at the electrode-electrolyte

interface, proving more useful for analysing (electro)chemical reactivity. The instrumental methods used in this case involve imposing an electrode potential which systematically changes over time across a broad range of values, a typical example being cyclic voltammetry (CV).[26] In CV, the electrode potential is continuously swept, starting from a point where no electrochemical reactions occur and progressing to potentials where the oxidation (or reduction) of dissolved redox species begins. Following the redox reaction in the forward scan, the direction of potential scanning is reversed, enabling the reduction (or oxidation) of the electrogenerated species.

In a standard CV experiment, the i-E curve is characterised by distinct oxidation and reduction peaks. The positions and shapes of these current peaks are related to the concentration and redox potentials of the electroactive molecules, as well as their diffusion coefficients, the number of exchanged electrons and the rates of involved electron transfer reactions. Thus, the key parameters in a CV measurement are the peak current, the peak potential, the half-wave potential and the half-current potential. Additionally, as the rate of potential scanning dictates the duration of a CV experiment, it is often useful, especially when studying the kinetic parameters of an electrochemical reaction, to conduct multiple CV experiments with different scan rates. In the context of ECL, CV measurements are frequently coupled with light detection, facilitating the investigation of underlying mechanistic pathways in coreactant ECL systems (see **Chapter 2**).

1.4.1 Bridging electrochemistry and photochemistry

As discussed earlier, both the spectral and redox properties of molecules are determined by the relative energies of their frontier orbitals. This section seeks to establish a clear connection between photophysics and electrochemistry by illustrating the relationship between the (electrochemical and spectroscopic) HOMO-LUMO gap and the redox reactivities of both the ground and excited electronic states. Importantly, although electrochemical and spectroscopic plots for $[Ru(bpy)_3]^{2+}$, which is a model luminophore in ECL applications, were used as an example in the following considerations, the same principles extend to the study of photoelectrochemical behaviour of other compounds.

Figure 1.2A shows a typical CV of $[Ru(bpy)_3]^{2+}$ in acetonitrile in the presence of the supporting electrolyte. Scanning the potentials in an anodic direction reveals a reversible

oxidation of the metal centre at 0.88 V vs ferrocene (Fc/Fc^+ redox couple), indicating a one-electron transfer to form $[Ru(bpy)_3]^{3+}$. Conversely, a cathodic scan shows three reversible reduction waves. These waves correspond to the successive one-electron reductions of each of the three ligands, generating $[Ru(bpy^{\bullet-})(bpy)_2]^+$, $[Ru(bpy^{\bullet-})_2(bpy)]$ and $[Ru(bpy^{\bullet-})_3]^-$ radical ions, respectively.

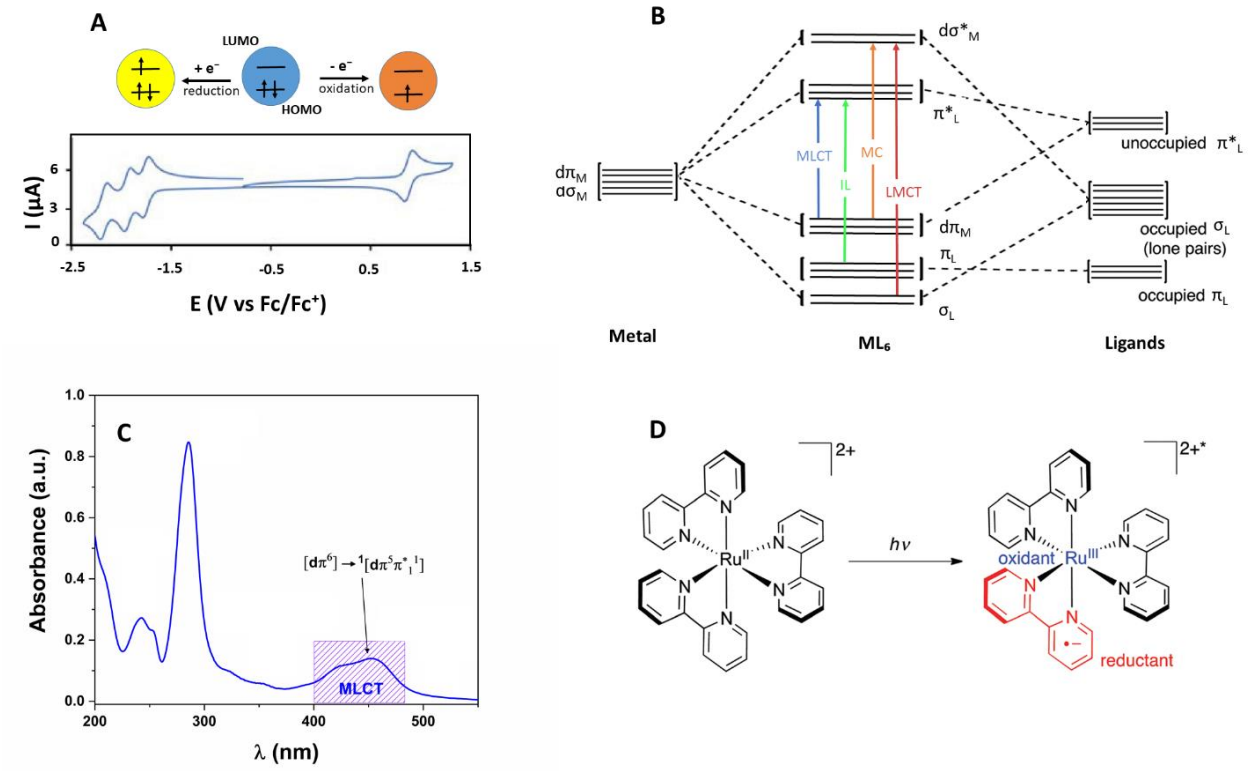

Figure 1.2 (A) Shematic representation of the electronic configuration of frontier orbitals upon oxidation and reduction and a CV of 5 mM $[Ru(bpy)_3]^{2+}$ solution in acetonitrile containing 0.1 M tetrabutylammonium hexafluorophosphate supporting electrolyte. Reproduced from [27]. **(B)** Simplified molecular orbital diagram of an octahedral transition metal complex with π-acceptor ligands (i.e $Ru(bpy)_3]^{2+}$). Possible types of electronic transitions from the ground to the first excited electronic state — metal to ligand (MLCT), interligand (IL), metal-centred (MC) and ligand to metal charge transfer (LMCT) — are indicated by the arrows. Reproduced from [28] **(C)** Electronic absorption spectrum of $[Ru(bpy)_3]^{2+}$ in water at ambient temperature, with MLCT band highlighted in the purple hatched region. Reproduced from [29]. **(D)** Schematics depicting the charge separation following the electronic excitation of the $Ru(bpy)_3]^{2+}$ luminophore. Reproduced from [28].

The CV experiment provides information on the ground state oxidation and reduction potentials of the investigated complex. Furthermore, it allows to indirectly estimate its HOMO-LUMO by subtracting the reduction potential (corresponding to the population of the LUMO orbital) from the oxidation potential (correlated with vacating the HOMO orbital).[30–33] For the $[Ru(bpy)_3]^{2+}$ complex, the electrochemical HOMO-LUMO gap equals ~2.62 eV and corresponds to an electron transition during a metal-to-ligand charge transfer (MLCT, see molecular orbital diagram in **Figure 1.2B**) as the oxidation predominantly takes place on the metal centre, while the reduction involves the ligands.

Alternatively, the energy difference between the excited and ground state can be estimated from spectroscopic information. The UV-VIS spectrum of $[Ru(bpy)_3]^{2+}$ is characterised by a wide absorption band at ca. 450 nm (**Figure 1.2C**). This band corresponds to the electron transition between the lowest vibrational level of the ground state and the first excited state (MLCT). Thus, the optical HOMO-LUMO gap can be determined based on the absorption edges of $[Ru(bpy)_3]^{2+}$, which is the onset value of absorption in the direction of longer wavelengths. Calculated as $\Delta E = hc/\lambda$,[30,31,33] it equals ~ 2.56 eV, corresponding well to the electrochemically determined value. Notably, these considerations about HOMO-LUMO energies enable the prediction of spectral and electrochemical behaviour resulting from stabilization or destabilization of the luminophores' frontier orbitals due to changes in chemical or electronic structure.

Furthermore, assuming that all the excited state energy is available as free energy, it is possible to estimate the redox potentials of the excited states from the available spectroscopic and electrochemical data as the difference between the redox potential of the ground state and the energy required for the electron excitation.

Equations *1.2* and *1.3* describe the reduction and oxidation potentials of the $[Ru(bpy)_3]^{2+*}$ first excited state, respectively, predicting that the excited molecule will be a better electron acceptor and a better electron donor compared to the ground state.

$$E_{[Ru(bpy)_3]^{+/2+*}} = E_{[Ru(bpy)_3]^{+/2+}} + \Delta E \qquad (1.2)$$

$$E_{[Ru(bpy)_3]^{2+*/3+}} = E_{[Ru(bpy)_3]^{2+/3+}} - \Delta E \qquad (1.3)$$

Notably, the electron excitation can be perceived as simultaneous photo-induced oxidation of the metal centre and reduction of the ligand, yielding the species with changed distribution of charge density compared to the ground state (**Figure 1.2D**). This implies the potential usefulness of photoexcitation for facilitating (or catalysing) chemical reactions, or inversely, the possibility of producing electronically excited states in highly energetic reactions.

In the former case, when light appears on the side of the reactants, the reactions are classified as photochemical (or photocatalytic). Photochemical reactions usually do not involve radiative decay of the excited species. Instead, they harness the energy of light, benefiting from the altered polarization and redox potentials of the excited molecule caused by charge redistribution during the electron excitation. This energy is then used to facilitate the formation or cleavage of chemical bonds (chemical reactions) or electron transfer (redox reactions). Without photoexcitation, photochemical reactions would not proceed as they are usually either endergonic or have a high activation energy.

Conversely, the phenomena where the light is a product of an exergonic chemical reaction are called chemiluminescence. This work focuses on specific cases of CL which are initiated by a heterogeneous electron transfer (ECL) and they will be described in detail in the following sections.

1.5 Energetic and kinetic requirements for light-producing redox processes

ECL is a process that involves the interplay of electric, chemical, and light energy, serving as a bridge between photochemistry and electrochemistry. Its underlying mechanism involves the application of suitable electrode potentials to initiate heterogeneous redox reactions at the surface of the working electrode. This initial step transforms reactants (luminophore, coreactant or both) into their radical ions, triggering a series of chemical reactions which can be highly exergonic. If the change in free energy (or rather enthalpy) during a chemical reaction surpasses the energy of the luminophore's first excited (singlet or triplet) state, it will lead to the luminophore's excitation, followed by the emission of visible light upon decay. While bond-breaking or atom transfer reactions fulfil the necessary

energetic criteria, this section will be restricted to discussing the exergonic electron transfer reactions, which are dominant in modern ECL applications.

Suppose that the molecules A and B (which can principally be of the same compound) undergo reversible electrochemical oxidation and reduction, respectively, yielding their radical ions. The as-formed opposite radical ions $A^{\bullet-}$ and $B^{\bullet+}$ can subsequently react in a strongly exergonic electron-transfer reaction (ionic annihilation) and the free energy (or enthalpy) released during this process can be estimated as:

$$\Delta G = \Delta H - T\Delta S = E_{A\,/A^{\bullet-}} - E_{B^{\bullet+}/B} \qquad (1.4)$$

where $E_{A\,/A^{\bullet-}}$ and $E_{B^{\bullet+}/B}$ are reduction and oxidation potentials (in V) of $B/B^{\bullet-}$ and $A/A^{\bullet+}$ redox couples, respectively, G is the Gibbs free energy (in eV), ΔH is enthalpy (in eV), T is the temperature (in K) and S is entropy (in eV K^{-1} mol^{-1}).

Generally, the redox potentials of electrogenerated radicals are accessible via cyclic voltammetry. However, in ECL with the coreactant, chemical transformations of the coreactant follow the electrochemical step yielding its radicals. Coreactant radicals act as potent electron donors (or acceptors), undergoing energetically favourable redox reactions with the luminophore (sections **1.6.1.2.** and **1.8.2.**). The redox potentials of these reactive species cannot be determined by CV but can be inferred from more elaborate experimental approaches and calculations.[34–38] Importantly, the reaction enthalpy can be calculated according to equation *3.1* regardless of the nature of the redox species involved. The entropic term TΔS for usual laboratory conditions can be neglected or used as a fixed value of 0.1 eV.[39,40]

Comparing ΔH with the energy of the emitted photons (ΔE, calculated from the emission wavelength in the fluorescence spectrum) can serve as a good estimate if the investigated ECL system is energy sufficient or not and indicate its relative ECL efficiency compared to other systems with similar underlying mechanistic pathways and quantum yields. This relationship can be graphically visualised by assigning each luminophore its specific coordinates based on its redox potential and maximal emission wavelength on a corresponding E(V) versus λ(nm) plot.[41–43] This representation, called "ECL wall of energy sufficiency", was first reported for a series of iridium-based inorganic complexes by Hogan

and co-workers.[41] The thermodynamic requirement for electroexcitation, expressed as the linear equation ΔG (or ΔH) = ΔE, divides the resulting plot into two regions: energy insufficient and energy sufficient, thus providing simple visual means for quick comparison of ECL efficiency in a set of luminophores that undergo the same (or comparable) ECL mechanism. An example of such a graph is presented in **Figure 1.3**, with the grey zone (on the left) in which ECL is thermodynamically forbidden and the white zone (on the right) where the ECL reactions are thermodynamically feasible. According to equation *1.1* these thermodynamic criteria, depending on the emission wavelength, are between 2 eV and 3 eV for most of the luminophores. For example, the energetic threshold is ca. 2.0 V for the red (620 nm), 2.48 eV for green (500 nm) and 2.75 eV for blue emission (450 nm).

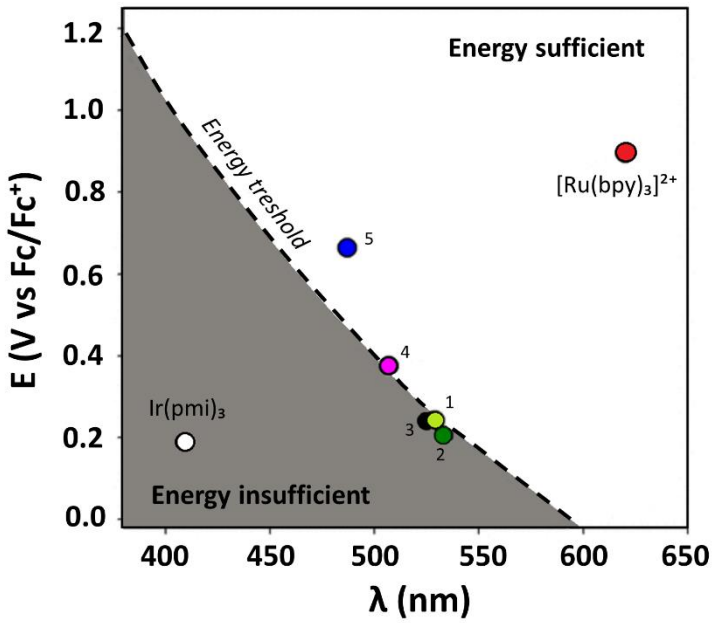

Figure 1.3 Graphic representation of the energetic sufficiency of a coreactant reaction for different emission wavelengths when the TPrA is used as a coreactant. Compounds 1 to 5 are different cyclometalated Ir(III) complexes, while $[Ru(bpy)_3]^{2+}$ and $Ir(pmi)_3$ are given as reference examples of energy-sufficient and energy-insufficient systems, respectively. Reproduced from [41].

Analogous to photoluminescence, a crucial aspect of ECL phenomena is their yield (i.e ECL efficiency). The emission in ECL, as in other luminescence processes, depends on the likelihood of radiative versus non-radiative decay of excited states—the luminophore's quantum yield. However, the electron excitation process in ECL is less straightforward

compared to PL and is initiated and controlled through multiple electrochemical and chemical steps, each having limited efficiency. Consequently, ECL efficiency can be expressed as a sum of two main factors: i) the efficiency of the generation of the excited state and ii) the efficiency of the light emission from that state.

Both thermodynamic (reaction enthalpy) and kinetic parameters (reaction rate) dictate the energetic feasibility of ECL-producing reactions and the extent to which the excited state is populated relative to the ground state, respectively. The electron transfer reaction leading to the excited state must occur rapidly to prevent the dissipation of reaction energy to the vibrational and rotational levels and surrounding solvent molecules. Additionally, the lifetimes of intermediate radical species play a significant role in shaping the ECL emission, while the chemical structure of the luminophore influences the efficiency of the emission. As all of these factors are inherently bound to the intrinsic properties of the participants in ECL reactions, careful selection of luminophores (and coreactants) and tuning their underlying ECL mechanistic pathways is crucial for improving the efficiency of the ECL process. A good electroluminophore should be a good emitter (have a high quantum yield), be stable and soluble in commonly used solvents, and have convenient thermodynamic (i.e HOMO-LUMO) properties such as redox potentials and energies of the excited and the ground state. Furthermore, the reaction steps should be sufficiently exergonic and proceed at fast rates.

In fact, these exergonic electron transfers occur at rates comparable to the time scale of vibrational transitions, demonstrating the Franc codon principle. According to the Franck-Condon principle, when this fast electron transition occurs, there is no time for the nuclei to move and consequently, the molecule would find itself in the wrong high-energy environment of solvent molecules, where its charge is not compatible with the position and dipole orientation of its surroundings. This situation is true for the photo-induced, vertical electron transition, where the as-formed high energy state is relaxed by vibrationally dissipating the excess energy to its environment. However, in a redox reaction (where no external energy is involved), such manifestation of Franck-Condon's principle would violate energy conservation. To satisfy both of those fundamental principles, a theory elucidating electron transfers was developed by Rudolph Marcus in the 1960s.

1.5.1 Electron tranfer theory

According to Marcus' theory,[16] to conserve the total energy, electron transfer is preceded by fluctuations in various nuclear coordinates, such as variations in bond lengths and orientation of solvent molecules, as well as any other coordinates that have different probable distributions in the reactant and product molecules. During these fluctuations, the nuclear coordinates reach a state (which can be referred to as a transition state) in which they resemble the coordinates of neither the reactant, nor the product, but are in between the two (**Figure 1.4**). At this configuration, electron transfer can occur and is followed by the relaxation to the coordinates of the products, satisfying both Franc Condon and energy conservation principles.

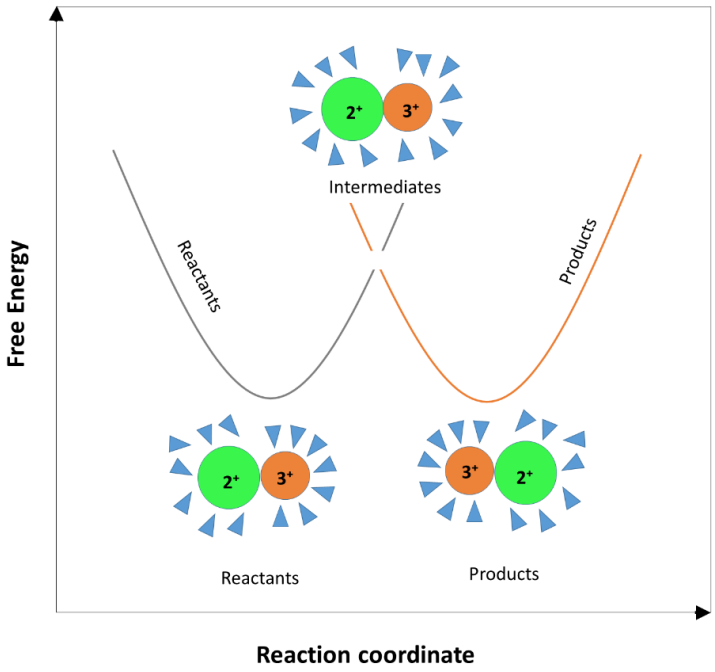

Figure 1.4. Schematic representation of the typical arrangement of solvent molecules surrounding reactants and products in the electron transfer between the two ions of the same atom (i.e. $Fe^{2+/3+}$). In the transition state, the environment of the ions does not correspond neither to the one of the reactants nor the one of the products.

The kinetics of such electron transfer will depend on the activation energy necessary to overcome the energy barrier and reach the transition state. This relation can be expressed in the form of Arrhenius equation:

$$k = Ae^{\frac{-\Delta G^*}{k_b T}} \qquad (1.5)$$

where k is the electron transfer rate, A is the constant that depends on the nature of the electron transfer reaction (e.g. if it is bimolecular or intramolecular), k_b is Boltzmann constant, T is the temperature (in K) and ΔG* is the activation free energy, which equals to:

$$\Delta G^* = \frac{\lambda}{4}\left(1 + \frac{\Delta G^0}{\lambda}\right)^2 \qquad (1.6)$$

Naturally, ΔG* depends on the free energy of the electron transfer reaction (ΔG^0), but it also depends on the reorganization term (λ), which encompasses differences in equilibrium bond lengths of each reacting species in its initial and final electronic states (vibrational term, λ_i) and differences in equilibrium orientation polarization of solvent molecules in these electronic states (solvation term, λ_0). The work terms (ω_r and ω_p), which are involved in bringing the reactants of bimolecular reactions together and in separating the reaction products, also contribute to the energy of the activation barrier, but can be neglected and thus are omitted from equation *1.6*.

The parabolic plots depicted in **Figures 1.5A** and **1.5B** result from changes in the free energies of reactants and products, involving their environments, along the reaction coordinate. They offer a clear visualization of trends predicted by equations *1.5* and *1.6*. These plots exhibit a split near their intersection point, which is attributed to electronic coupling and the coupling between electronic and nuclear motion. The width of the splitting indicates the strength of the coupling that facilitates electron transfer, while the position of the intersection along the free energy axes reflects the height of the energy barrier (ΔG*).

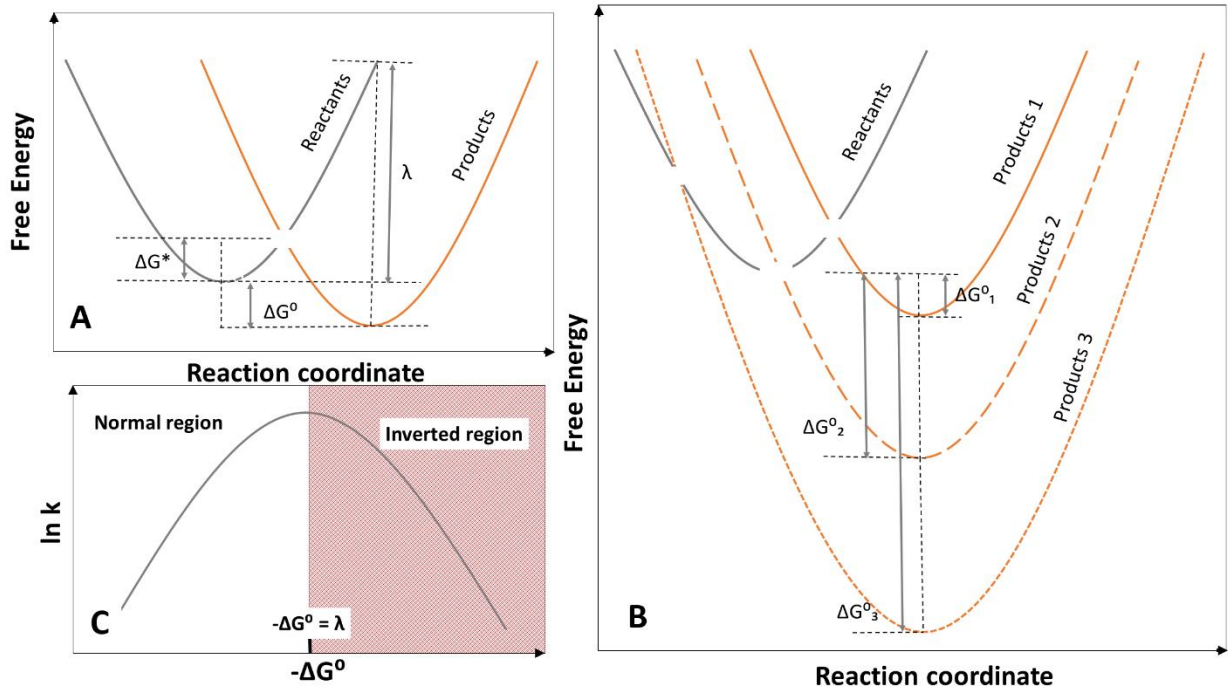

Figure 1.5. (A) Graphic displaying the free energy of reactants and products as a function of the reaction coordinate. The scheme also depicts the three key parameters: activation free energy (ΔG*), Gibbs free energy (ΔG^0) and reorganization energy (λ). **(B)** Schematic representation of the influence of the change in the ΔG^0 of products on the ΔG*. **(C)** Relationship between the logarithm of the rate constant (ln k) and $-\Delta G^0$ of the reaction products that separates the so-called "normal" from the "inverted" Marcus regions. Reproduced from [16].

As indicated by equation *1.6*, **Figure 1.5B** shows the changes in the activation free energy as the free energy of the products becomes increasingly negative. At first, as the free energy of the products decreases from ΔG^0_1 (solid line) to ΔG^0_2 (dashed line), the ΔG* decreases. This trend represents a typical behaviour for the majority of chemical reactions when the likely nuclear configurations at the intersection region (including the solvent orientations) represent a compromise between stable coordinate configurations of the reactants and those of the products. The situation illustrated by the dashed line is a specific (borderline) case when the value of ΔG^0 equals -λ. For this value of ΔG^0, there is no energy barrier for the electron transfer (ΔG* = 0). However, for more negative values of ΔG^0, configurations at the intersection become increasingly different from stable configurations of both reactants and products, leading to a rapid increase in activation free energy with the

further decrease in the products' free energy to ΔG^0_3 (dotted line). Thus, the region between the dashed and dotted line is termed an "inverted" or "abnormal" Marcus region, as opposed to the "normal" region shown between the solid line and the dashed line. Consequently, as per equation *1.5*, electron transfer kinetics increases with decreasing ΔG^0 until reaching $\Delta G^0 = -\lambda$, beyond which the trend changes and the electron transfer kinetics starts to decrease with free energy's further decrease. This behaviour is illustrated in the k vs $-\Delta G^0$ plot in **Figure 1.5C**. This plot divided in half by a line passing through $-\Delta G^0 = \lambda$ into a "normal" region (on the left) and an "inverted" region (on the right).

In the inverted region, the kinetics of reactions leading to the ground state of the product are low. However, if the values of reorganisation energy leading to the ground and the excited state are similar and if the excited state of the product is accessible, the reactions leading to the formation of an excited state will occur rapidly (**Figure 1.6**).[16,17] This prediction based on Marcus' theory elucidates the mechanism and kinetics of electron transfer reactions that lead to ECL phenomena, in which there is a significant difference in rates favouring the formation of an excited state over the ground state. These kinetic considerations explain the influence that changes in the luminophore's structure have on the formation of the excited state via exergonic electron transfer, as these changes influence the energies of both the ground and excited states (as explained in section **1.5**).

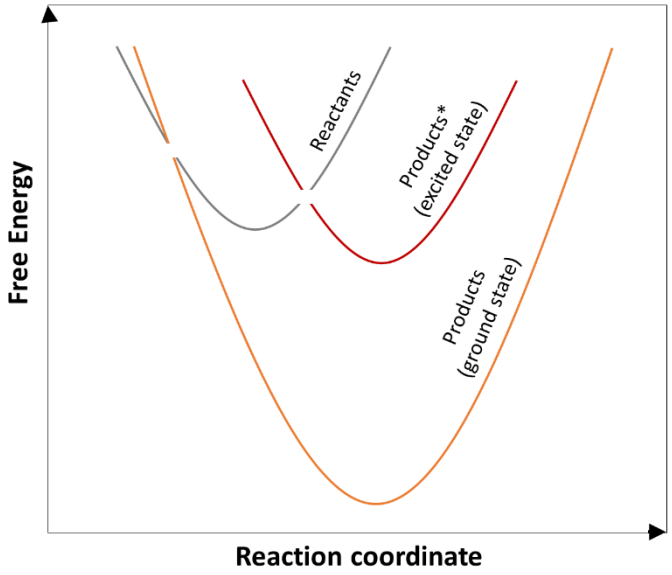

Figure 1.6. Graphic displaying the favoured formation of an electronically excited state of the products when $-\Delta G^0 > \lambda$ for the formation of the ground state of the products. This phenomenon prevents the observation of the inverse region. Reproduced from [16].

Notably, all the remarks made so far apply to homogeneous electron transfer reactions. Most electron transfers under typical electrochemical conditions involve transitions between the frontier orbitals of the ground state of a chemical compound and a one-electron orbital within the Fermi level of the electrode. While equations *1.5* and *1.6* remain applicable for describing the mechanism and kinetics of such electrochemical electron transfers, the free energy of the electrode cannot be represented by a single parabolic curve, but rather by multiple free-energy surfaces within which each curve, shifted vertically from the others, reflects different electron energies. In highly exothermic electrode processes, where electron transfer from an ion to the electrode occurs, numerous potential-energy surfaces emerge, each allowing the electron to occupy a high unoccupied orbital of the metal, typically near the top of the unfilled half of the conduction band. The broad conduction band in metals facilitates the reduction of exothermicity through electron transfer into such unfilled levels. Similarly, in highly exothermic electron transfers from an electrode to a molecule or ion in solution, the electron can alleviate the exothermicity by transferring from lower levels in the filled half of the conduction band. Consequently, even in the case of highly energetic heterogeneous electron transfers, their exothermicity can be reduced due to the substantial widths of the conduction band from which the electron transfer could proceed, resulting in a small ΔG^0. Therefore, generating the excited electronic states of the luminophore in heterogeneous electron transfer reactions is usually unfeasible as it cannot compete with processes involving the formation of the luminophore's ground state and an excited state of the electrode. This explains the necessity of the homogeneous electron transfer steps in ECL mechanistic routes.

1.6 Mechanisms of ECL reactions

As previously discussed, ECL is a specific type of chemiluminescence initiated through a heterogeneous electron transfer. It includes multiple chemical steps, culminating in a highly exergonic event, which ultimately leads to light emission. Therefore, ECL processes can be categorized based on the nature of this exergonic step, which may involve either a homogeneous electron transfer or an atom transfer (bond-breaking) reaction. This section

aims to elucidate both of these highly energetic processes, highlighting their similarities and differences, and providing examples of prevalent ECL systems that benefit from such reactions.

1.6.1 Electron transfer involving the luminophore

In this mechanism, the excited electronic state (of the luminophore) is produced via the exergonic homogeneous electron transfer involving the luminophore. The thermodynamic and kinetic requirements, as well as the mechanism of such processes, were a subject of discussion in the previous sections and will not be repeated here. However, it is important to notice that these electron transfers are reversible if not followed by a chemical reaction. Thus, a luminophore participating in an exergonic redox reaction returns to its initial state after emitting a photon (i.e., it is regenerated), allowing it to reenter the new ECL mechanistic cycle.

In general, ECL systems that involve homogeneous electron transfer can be classified into two main groups, annihilation and coreactant systems, depending on the composition of the reaction mixture and, consequently, the underlying mechanistic routs.

1.6.1.1 Annihilation ECL

The annihilation pathway involves a simultaneous generation of radical anions and cations of the (same or distinct) luminophore molecules, which can be designated as A and B (equations 1.7 and 1.8). The as-formed oppositely charged radical ions then react in a rapid electron-transfer reaction (ionic annihilation) that is always strongly exergonic and its enthalpy can be approximated according to *1.4*. If the liberated energy is sufficiently high, an excitation of one of the reaction partners occurs, followed by a fluorescence emission (equations *1.9a* and *b* and *1.10a* and *b)*. This energy-sufficient route is called a singlet route, or S-route.

$$A + e^- \rightleftarrows A^{\bullet -} \qquad (1.7)$$

$$B \rightleftarrows B^{\bullet +} + e^- \qquad (1.8)$$

$$A^{\bullet -} + B^{\bullet +} \rightarrow {}^1A^* + B \qquad \text{when E } ({}^1A^*) < \text{E } ({}^1B^*) \qquad (1.9a)$$

or

$A^{\bullet-} + B^{\bullet+} \rightarrow A + {}^1B^*$ when E ($^1A^*$) > E ($^1B^*$) (*1.9b*)

${}^1A^* \rightarrow A + h\nu$ or ${}^1B^* \rightarrow B + h\nu$ (*1.10a* and *1.10b*)

However, if the change in enthalpy during ionic annihilation does not surpass the energy of the luminophore's first excited singlet state (calculated from its emission wavelength according to *1.1*), it can lead to a population of a triplet state (equations *1.11a* and *b*). Even though this state is typically non-emissive (unless phosphorescence occurs), triplet-triplet recombination[44,45] can lead to populating a corresponding singlet state (equations *1.12a* and *b*) that emits a photon according to *1.10*. This „energy deficient " pathway is then called a triplet or T-route.

$A^{\bullet-} + B^{\bullet+} \rightarrow {}^3A + B$ when E (^3A) < E (^3B) (*1.11a*)

or

$A^{\bullet-} + B^{\bullet+} \rightarrow A + {}^3B$ when E (^3A) > E (^3B) (*1.11b*)

${}^3A + {}^3A \rightarrow A + {}^1A^*$ (*1.12a*)

or

${}^3B + {}^3B \rightarrow B + {}^1B^*$ (*1.12b*)

Finally, if the enthalpy of the exergonic electron transfer step is lower than the triplet state energy, the excitation does not occur. In this case, the luminophore's ground state is formed and the excess energy dissipates as thermal energy.

Apart from the S and T routes, in specific cases when the formation of ionic pairs is favourable, usually in non-polar media or in the absence of electrolyte, the ionic annihilation can result in the formation of excited dimers (excimers, equation *1.13*)[46,47] or excited complexes (exciplexes, equation *1.14*).[48,49] This pathway is called an E-route. Typically, compounds involved in the E route are aromatic hydrocarbons, such as anthracen[46] and pyrene.[47] The emission of these species is characterized by a broad band at longer wavelengths compared to the emission of their corresponding monomers.

$A^{\bullet-} + A^{\bullet+} \rightarrow A_2^*$ (*1.13*)

$A^{\bullet-} + B^{\bullet+} \rightarrow (AB)^*$ (*1.14*)

Principally, any ECL luminophore capable of being excited trough exergonic electron transfer can participate in ionic-annihilation reactions, assuming that its oxidised and reduced states can be reached electrochemically and are stable in the given experimental conditions. However, only a limited number of luminophores fulfill these criteria.

Annihilation ECL systems are relatively simple, involving only the electrolyte, solvent and luminophore. The oppositely charged radical ions of the luminophore are usually generated either by alternating the potential of the working electrode between positive and negative values or by using two oppositely polarized and closely placed electrodes. It is noteworthy that the stability of the generated radical ions, as they have to diffuse and interact, significantly influences the overall efficiency of annihilation ECL. This, coupled with the relatively narrow potential window of water, insufficient to form stable $A^{\bullet -}$ and $B^{\bullet +}$ species at most electrode materials, necessitates the use of dry organic solvents (typically DMF or acetonitrile) for annihilation ECL experiments. Moreover, due to electroactivity and the quenching effect of oxygen, solutions usually need to be degassed before conducting annihilation ECL.

These experimental constraints render excitation by ionic annihilation unsuitable for many biological and analytical applications, restricting its practical utility. To address this challenge, the majority of contemporary ECL applications rely on sacrificial species referred to as "coreactants."

1.6.1.2 Coreactant ECL

ECL with a coreactant involves a reversible redox reaction of a luminophore at the working electrode, while simultaneously, the coreactant molecule undergoes irreversible oxidation (or reduction) at the same electrode and potential. The resulting coreactant radical ion then spontaneously dissociates into a stable ion and a highly reactive nucleophilic (or electrophilic) radical. Acting as potent oxidants (or reductants), these coreactant radicals engage in an exergonic redox reaction with the radical ions of the luminophore, leading to the excitation of the luminophore and subsequent light emission. Thus, the role of the coreactant is to provide energetic radicals capable of reacting with the luminophore to populate its excited state. It serves as a sacrificial molecule that irreversibly transforms during an ECL cycle, as the chemical (typically bond-breaking) step is involved in the formation of its

reactive radicals, while the luminophore molecule is usually regenerated after each ECL cycle. Consequently, to achieve stable ECL emission, coreactants must be used in excess.

Introducing coreactants has allowed for generating light upon applying a single moderate electrode potential, enabling ECL applications in aqueous solutions and making this method suitable for (bio)analytical applications. Furthermore, because all the participants of the ECL process react on the same electrode, the use of coreactants ensures strong ECL emission regardless of the stability of the luminophore's radical ions, even in cases where the annihilation pathway is not efficient. However, for coreactants to facilitate efficient ECL, they must meet several requirements. They need to be non-toxic, stable, and soluble in the reaction media, have moderate to low redox potentials, generate radicals with sufficiently long lifetimes, exhibit fast electron transfer kinetics, and, specifically, not react with the luminophore's excited state (i.e., they should not quench ECL emission).

Depending on the initial electrode polarization, the corresponding coreactant ECL mechanisms are typically termed oxidative reduction and reductive oxidation, depending on whether the reactive species are initially oxidized or reduced on the electrode. The most commonly used coreactants in the oxidative reductive pathway are oxalate and aliphatic amines such as TPrA, NADH and DBAE, while the predominantly used coreactants for reductive oxidation are peroxydisulfate and benzoyl peroxide (BPO). Principally, the most useful coreactant system employs $[Ru(bpy)_3]^{2+}$ as a luminophore and TPrA as a coreactant. It stands out for its ability to trigger ECL not only through the oxidation of both reaction participants, but also through the selective oxidation of either the coreactant alone or, in rare instances, solely the luminophore. This property allows its application in various experimental setups: i) where both reagents can diffuse freely in solution, ii) where only the coreactant is present in the solution while the luminophore is used to label the object under investigation. As such, it is used in commercial ECL immunoassays[50] and for the majority of ECL imaging applications involving single biological objects.[51] Therefore, a detailed description of its underlying mechanistic pathways will be provided here, while more information about other relevant luminophore and coreactant species will be given in **section 1.8.2**.

ECL of $[Ru(bpy)_3]^{2+}$/TPrA can be generated through the 'homogeneous' (oxidative-reductive route), so called because the luminophore and the coreactant are free in solution. In this case, direct electrooxidation of the luminophore occurs generally at the electrode

surface, followed by electron transfer between its oxidized state ($[Ru(bpy)_3]^{3+}$) and a potent reductant ($TPrA^{\bullet}$) formed from the oxidation and deprotonation of TPrA (**Figure 1.7A**). This leads to the population of luminophore's excited state, resulting in ECL emission.[52] Another ECL pathway, important for bioanalysis and microscopy, is called the 'heterogeneous' or 'remote' route (**Figure 1.7B**), which implies that the luminophore is not oxidized directly by the electrode. This is the case, for instance, when the luminophore is immobilized on a non-conducting entity such as an insulating polystyrene bead or a living cell. Nevertheless, this pathway can also occur when $[Ru(bpy)_3]^{2+}$ is free in solution, by applying potentials sufficient to oxidize the coreactant but not the luminophore. Under both of these conditions, $[Ru(bpy)_3]^{2+}$ is not oxidized at the electrode surface. Instead, all the redox reactions leading to ECL emission must be initiated by the electrogenerated TPrA radicals. The heterogeneous oxidation of TPrA yields $TPrA^{\bullet+}$ radical cation, a moderately strong oxidant that undergoes spontaneous and rapid deprotonation, forming a strongly reducing $TPrA^{\bullet}$ radical. $TPrA^{\bullet}$ reduces $[Ru(bpy)_3]^{2+}$ to $[Ru(bpy)_3]^{+}$, and ECL is produced upon its subsequent reaction with the radical cation $TPrA^{\bullet+}$.[53] Generally, the only oxidant in the $[Ru(bpy)_3]^{2+}$/TPrA coreactant system operating through the 'remote' route (**Figure 1.7B**) is the short-lived $TPrA^{\bullet+}$ (with a half-life of ~200 μs).[52–54] This mechanistic pathway enables $[Ru(bpy)_3]^{2+}$ derivatives to be used as labels, rendering this coreactant system indispensable in biological assays and ECL imaging.[50,55–57] **Figure 1.7C** shows the "catalytic" route[53] involving homogeneous oxidation of TPrA by $[Ru(bpy)_3]^{3+}$. Apart from the homogeneous oxidation of TPrA, the pathway follows the same mechanistic route as an oxidative reductive pathway. However, homogeneous catalysis enables the generation of reactive coreactant radicals far from the electrode surface, expanding the thickness of the ECL emitting layer and enhancing the spatial resolution of the ECL method.[58,59] Furthermore, this pathway allows for the analysis of cells using intracellular molecules (such as NADH and DNA) as coreactants,[60] bypassing the need for their direct electrooxidation.

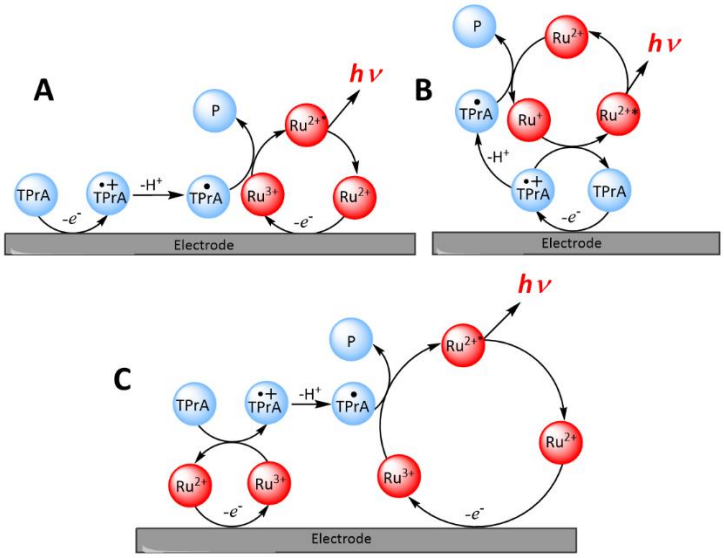

Figure 1.7. Schematics of the **(A)** 'homogeneous' (oxidative-reductive) route, **(B)** conventional 'remote' ECL route, **(C)** redox catalysis (catalytic oxidation of TPrA by $[Ru(bpy)_3]^{3+}$). Ru^{2+}, and TPrA represent the $[Ru(bpy)_3]^{2+}$ luminophore, and tri-*n*-propylamine, respectively.

1.6.2 Atom transfer or bond breaking within the luminophore's frame

Even though the electron transfer induced excitation dominates in the modern ECL applications, the first ECL systems were based on the highly exergonic intramolecular bond breaking reactions, that were energetic enough to populate the luminophore's excited state. [10,11] In contrast to the previously described cases, where the luminophore regenerates after undergoing energetic electron transfer, the luminophores employed in the ECL process involving atom transfer can emit a photon only once, after which their chemical structure is irreversibly changed. Typical examples of such luminophores are luminol, luciferine, lucigenin (bis-N-methylacridinium nitrate), and acridinium esters. Luminol and its derivatives are currently the most widely used ECL compounds belonging to this family of electrochemiluminophores, [42,61] because they produce bright luminescence at low applied potentials, with intensity linearly dependent on the H_2O_2 concentration.[11,62,63] Therefore, since H_2O_2 is a common byproduct in enzymatic reactions and is released by stressed cells, the luminol/H_2O_2 system is widely used in biosensing. [64]

Luminol (and its derivatives) emits light upon either homogeneous (i.e. by hypochlorites, chlorine, ferricyanides, permanganates) oxidation or heterogeneous oxidation (at the surface of an anode) in the presence of H_20_2 in aqueous alkaline solutions. The

mechanism of this (electro)chemiluminescence generation is complex and depends on the solution's composition and pH value. In the general case, it involves luminol's oxidation to yield diazaquinone intermediate radicals ($L^{\bullet -}$) (see **Figure 1.8**).[65,66] These radicals subsequently react with hydrogen peroxide anion (HO_2^-) or reactive oxygen species (ROS), namely hydroxyl radicals ($OH^\bullet$) and superoxide radicals ($O_2^{\bullet -}$), produced during H_2O_2 decomposition, water oxidation,[67,68] or reduction of dissolved oxygen,[66,69] ultimately yielding the 3-aminophthalate (AP^{2-*}) in an excited state, which is populated through an O–O bond cleavage in the endoperoxide form (LO_2^{2-}). It subsequently undergoes a radiative decay followed by a blue light emission.

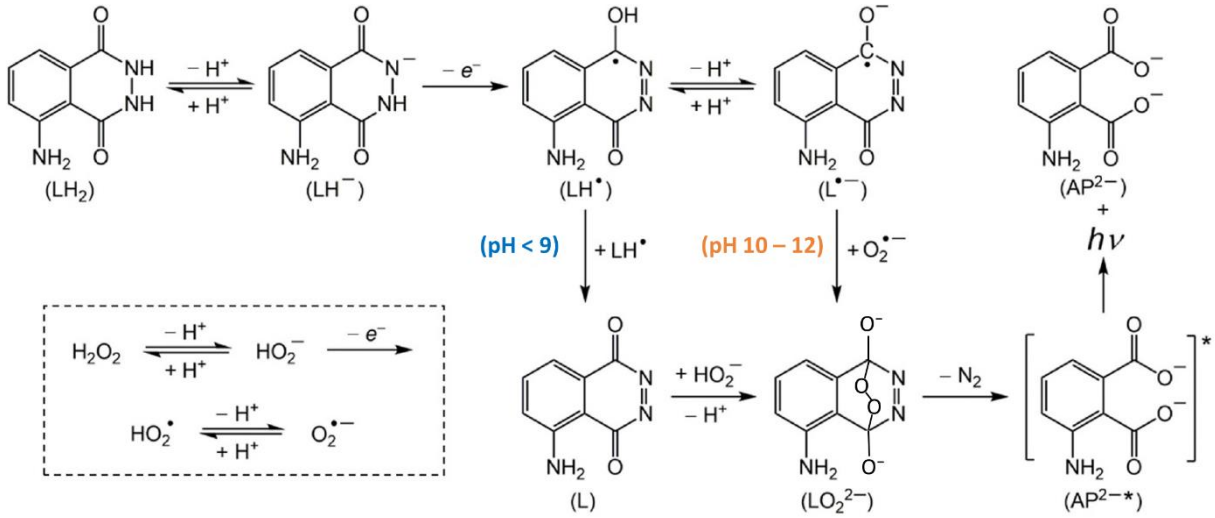

Figure 1.8. Schematics depicting the mechanistic pathway of ECL generation in the luminol/H_2O_2 system at low and high pH. Reproduced from [65].

1.7 ECL quenching and sensitising

When discussing the photophysical properties of the luminophores, we highlighted that radiative decay is only one of the possible ways for the electronically excited molecule to relax to its ground state. Apart from dissipating the energy through multiple vibrational states and to the surrounding solvent as thermal energy, the electronically excited states can also undergo chemical reactions. As the excited molecules are better oxidants and reductants compared to their ground states, they can enter a redox reaction with other electroactive species in solution, undergoing oxidative or reductive quenching. This reaction can sometimes be useful as excited compounds can serve as catalysts, and such reactions are classified as

photocatalytic reactions. However, it is more common to use photoexcitation as opposed to electroexcitation of the luminophore for such catalytic processes. Thus, in the context of ECL, redox reactivity of the excited state is an undesirable process that causes ECL quenching and decreases the overall efficiency of the ECL system.

Apart from electron transfer, an excited compound can participate in an energy transfer. The characteristic example of this is triplet-triplet annihilation (equation *1.12*) leading to an emissive singlet state. Another possibility is an energy transfer to the compound that has a lower triplet energy than the electrochemically excited luminophore, but has a higher quantum yield, leading to a stronger luminescence emission (equation *1.15*).

$$A^* + Q \rightarrow A + Q^* \qquad \text{E(Q)} < \text{E(A)} \qquad (1.15)$$

In this case, the compound Q, which is called a sensitizer, is a better emitter than A and sensitized ECL is observed at the wavelength typical for Q. Thus, the change of λ upon the addition of Q is proof of the energy transfer. Energy transfer from a luciferase enzyme to another luminescent protein with high QY provides strong and stable bioluminescence in marine organisms.

On the other hand, if the compound Q is not able to emit light, the relaxation of its excited state proceeds in a non-radiative way and ECL quenching due to energy transfer occurs. If the molecule Q undergoes a chemical reaction during this non-radiative decay, the overall process can be considered a photochemical reaction. The typical example of such a quencher is trans-Stilben which, after its excitation to a triplet state, undergoes a non-radiative isomerization to cis-Stilben.[70,71]

The common requirement for an energy transfer to occur is a spectral overlap between the emission band of the donor (A) and the absorption band of the acceptor (Q), which is simply a manifestation of the energy conservation principle. While an energy transfer can proceed through light emission from A that is absorbed by Q, it more commonly occurs via a non-radiative mechanism. Specifically, either Förster resonance energy transfer (FRET) or Dexter energy transfer.[28] FRET has a dipolar nature as it involves coupling of the transition moment dipoles of A and Q.[72] This means that the overlap of molecular orbitals of the two interacting molecules is not necessary, allowing this energy transfer to occur at relatively large

distances, on a scale from 1 to 10 nm. However, the rate constant of FRET depends on the relative orientation of the dipoles and, similarly to other dipole-dipole interactions, decreases with the R^6, where R is the distance between the A and Q.

Conversely, the Dexter mechanism can formally be considered as an electron exchange reaction, involving a simultaneous two-electron transfer.[73] Its electron transfer nature implies that, unlike FRET, it is not limited by the resonance energy requirement and depends only on the relative energies of the frontier orbitals of A and Q. However, due to the necessity of an orbital overlap for an electron exchange, this process can take place only within the electron tunnelling distance (1-3 nm), meaning that the reacting molecules have to be in contact. One of the examples of the Dexter mechanism is luminescence quenching of many transition metal complexes by triplet oxygen,[74] which is why the majority of photophysical measurements involving $[Ru(bpy)_3]^{2+}$ are performed in degassed solutions.

1.8 Participants in ECL reactions

Unrelated to its underlying reactivity, the main component of all ECL systems is the luminophore. Annihilation systems, for instance, consist of only the luminophore compound, solvent and supporting electrolyte. However, due to the practical limitations of these systems, the majority of ECL applications today take advantage of sacrificial coreactant species that help produce ECL emissions in mild experimental conditions. This section aims to give a brief overview of the main classes of luminophores and the most extensively used coreactants.

1.8.1 Luminophores

Historically, the first compounds used for ECL were Grignard reagents[10] and luminol[11]. Since then, as the field evolved, many other molecules with luminescence properties have been investigated or specifically developed for ECL applications. Generally, depending on their structure, they can be classified into three major groups: metal complexes (inorganic luminophores), organic luminophores and nanoparticles.

A typical representative of the first class is the model luminophore in ECL applications – $[Ru(bpy)_3]^{2+}$. The photophysical and electrochemical properties of this luminophore have already been discussed in section **1.4.1** and the same discussion can be extrapolated to the

other metal complexes, as they are usually characterised by the MLCT transition. The excited state of $[Ru(bpy)_3]^{2+}$ can be considered a triplet in multiplicity, but due to spin-orbit coupling a strong photoluminescence occurs with a maximum at ca. 620 nm. Moreover, functionalization of bipyridine moieties in $[Ru(bpy)_3]^{2+}$ enables its covalent binding to biological molecules (e.g. biotin and streptavidin), allowing for it to act as a label for biological imaging and biodiagnostic applications. However, due to the low ligand-field splitting energies of the Ru(II) ion, it is not easy to tune the spectral properties of this complex, limiting Ru-based dyes to the red part of the spectrum.

In recent years, Ir(III) complexes have emerged as promising alternatives to traditional Ru(II) luminophores for analytical applications of ECL. Contrary to Ru(II), Ir(III) ion has a high ligand-field splitting energy, which enables its emission to be fine-tuned, resulting in a huge number of structurally similar complexes with very different electrochemical and spectral properties. Ir(III) complexes emit bright ECL with TPrA as a coreactant and exhibit ECL emissions into the blue region of the visible spectrum.[41,75–83] Apart from Ir(III) and Ru(II), most of the other transition metals and some of the lanthanides can be utilised as metal centres in the inorganic luminophores. Furthermore, extensive research into multiplexed ECL systems – examining combinations of luminophores, specifically of Ru(II) and Ir(III) metal chelates, has demonstrated the ability to potentially and, or, spectrally resolve the ECL emissions from solutions containing combinations of such complexes.[84–89] This approach enables fine-tuning the emission wavelength by simply varying the applied electrode potential. In addition to those mixed luminophore systems, complexes containing two distinct metal centres have been investigated. These complexes usually combine a metal centre that is an efficient electroluminophore and another centre that can be excited through FRET. This is the case for the binuclear complex with Ir(III) and Eu centres, which allows for using a narrow emission band of Eu.[90]

Although most current ECL applications employ metal complexes, organic luminophores are still studied due to their high luminescence quantum yields and relatively straightforward relation between their structure and the energy of their frontier orbitals. Historically, anthracene, perylene, rubrene, and their derivatives have been extensively studied[12–14] and, even today, most classic organic luminophores are polyaromatic (and often heterocyclic) hydrocarbons. A major advantage of organic luminophores is a possibility to

tune their spectral and electrochemical properties in a chemically intuitive manner by introducing electron-withdrawing (or electron-donating) substituents to stabilize (or destabilize) their frontier orbitals, respectively. Examples of this include a series of substituted aromatic compounds (phenols or heterocyclic aromatic rings) linked by a spirobifluorene bridge.[91,92] However, a drawback of the majority of organic luminophores is their poor solubility in water, necessitating the use of dry organic (and degassed) solvents. Efforts are being made to overcome this problem by introducing polar substituents.

Finally, different nanomaterials can be used as ECL luminophores. Most of the ECL applications use nanomaterials obtained through one of the two common approaches: i) doping a hydrophobic and inert material, which can be either silica-based or made out of an organic polymer, with organic or metal complex ECL luminophores,[93–96] ii) synthesizing an electroactive material that can luminescence. Quantum dots (QDs) are a distinguished example of the latter, with their electronic (and thus ECL) properties primarily controlled by the particle size and the nature of their surface states. Quantum dots can be synthesised from different starting materials, the typical ones being chalcogenide-based (CdSe, CdS, ZnSe)[97,98] and carbon-based materials (carbon, graphene, carbon nitride).[99,100] Moreover, atomically precise noble metal clusters constituted only by a few atoms were successfully investigated as ECL luminophores.[101,102]

1.8.2 Coreactants

Coreactants are specific sacrificial species that produce a strong reductant (or oxidant) in a chemical transformation which follows an initial oxidation (or reduction) step. As such, they are involved in the so-called oxidative-reductive (or reductive-oxidative) ECL systems. Therefore, important characteristics of coreactants are their redox potentials and the redox potentials of their degradation products, which are usually either neutral radicals or ion radicals, as well as the lifetimes of their radicals.

Typical coreactants in oxidative-reductive systems include oxalate and alkylamines (i.e TPrA, DBAE, and NADH). The oxalate ion was the first coreactant used in ECL.[19,20] Upon oxidation, it forms a radical anion that breaks down into carbon dioxide and $CO2^{\bullet-}$. This radical anion is a potent reductant that reacts with the oxidized state of the luminophore to populate its excited state, following a general oxidative-reductive mechanism.

Similarly, alkylamines heterogeneously oxidise to their corresponding cation radicals, which subsequently undergo deprotonation at the αC atom to form highly reactive neutral radicals (as discussed in section **1.6.1.2.**), implying that ECL reactivity of different alkylamines depends on the electronic environment of the αC and (consequently) acidity of the α-H atom. For example, DBAE undergoes oxidation and deprotonation more easily than TPrA due to the proximity of an electron-withdrawing OH group to the αC.[103] Furthermore, tertiary amines generally exhibit better ECL properties than secondary and primary amines and aliphatic amines perform better than aromatic ones. These examples highlight the important influence of the electronic environment (via both inductive and resonance effects) on the stability of the coreactant radical intermediates.

In reductive-oxidative pathways, the most important coreactants are peroxydisulfate and benzoyl peroxide (BPO).[104–106] Upon reduction, these coreactants form anion radicals that spontaneously undergo homolytic cleavage of the O-O bond, generating an anion and a neutral radical. The neutral radical acts as a potent oxidant, capable of reacting with the reduced state of the luminophore to populate its excited state via the reductive-oxidative route.

1.9 ECL applications

Historically, ECL has progressively evolved from a lab curiosity to a process allowing us to investigate the Marcus inverted region and the very energetic electron transfer reactions in organic solvents.[16] With the discovery of ECL emission using sacrificial coreactant species in water, ECL has become a powerful bioanalytical technique that is successfully commercialized for clinical diagnostics.[54,107] It is used for the sensitive detection and quantification of various biomarkers (antibodies, drugs, hormones, viral proteins, tumor markers, *etc.*) in human body fluids.[50] Furthermore, ECL is very efficient for *operando* studying chemical reactivity near electrode surfaces,[54,56,62,65,108–115] in confined spaces,[116–121] at interfaces[122–126] and catalytic sites.[127–131]

Given that ECL does not require any external light for excitation (except, photo-induced ECL), the commonly used ECL setup is relatively simple. It typically involves a three-electrode system connected to a potentiostat and a photodetector which, depending on the

specific application can be a photomultiplier tube (PMT), an optic fibre, spectrophotometer or a camera.

The analytical performances of the ECL method are based on the orthogonality of the electrochemical trigger and the optical readout. Thus, ECL provides useful faradaic (current) and optical information (light emission) about the investigated system. However, while the current measurements yield a global flow of electrons through the working electrode, the light can be spatially resolved to provide insight into single events. Consequently, combined with optical microscopy, ECL transformed into a powerful imaging method capable of visualizing objects that participate in, impede, or otherwise alter the ECL reactions near the electrode surface.[55,129] Thus, successful ECL imaging methods rely on a profound understanding of the underlying electrochemical, photochemical and chemical reactivities, and their implementation to resolve single (biological) objects, and, in specific cases, even single molecules.[57,110,122,126,131–138] Additionally, mapping the distribution of ECL offers a considerable amount of information beyond merely measuring its overall intensity, proving invaluable for understanding dynamic processes or unravelling complex mechanistic situations in various fields.

1.9.1 ECL biosensing

ECL has emerged as a prominent transducing technique in biosensing due to its robustness, biocompatibility, and user-friendly nature. However, the growing demand for devices with enhanced analytical properties and higher complexity and multiplexing drives continuous innovation.[139]

Many ECL bioanalytical applications are based on the luminol ECL enhancement in the presence of hydrogen peroxide. In such analysis, ECL intensity is linearly dependent on the concentration of H_2O_2, prompting the analysis of hydrogen peroxide efflux from cells using ECL imaging.[140] By coupling the luminol ECL system with different enzymatic reactions that generate hydrogen peroxide, a variety of biomolecules can be determined. For instance, cholesterol oxidases react with active cholesterol on cell membranes, producing hydrogen peroxide and enhancing ECL intensity.[141] Exploring the intracellular molecules provides abundant information, allowing one to unveil the life process. By integrating porous Pt deposit at the tip of a nanopipette, wireless BPE was prepared. Upon the insertion of the

nanopipette, intracellular molecules were electrochemically sorted into the nanopipette and reacted with a luminol derivative and oxidases inside the nanopipette, producing bipolar ECL signals.[118] Wireless analysis of intracellular hydrogen peroxide, glucose and enzyme activity was achieved. In addition, some biomolecules with amine moieties such as DNA and RNA can act as the coreactants of $[Ru(bpy)_3]^{2+}$.[60] To generate ECL, these intracellular biomolecules react with electrogenerated $[Ru(bpy)_3]^{3+}$ to drive the ECL reactions. Accordingly, intracellular structures that contain most intracellular DNA and RNA including nucleolus, and endoplasmic reticulum were identified. This bio-coreactant-enhanced ECL microscopy provides a new method for studying intracellular biomolecules and structures.

Furthermore, employing ECL imaging techniques to resolve emitted light allows for parallel processing and detection without the complicated connections in the array, providing a unique method for high-density biosensing. For example, to fulfil the need for high-throughput analysis in molecular biology and genomics, a nanoneedle array with a very high density of more than 10^3 spots/mm^2 was developed for ECL bioanalysis. Due to enhanced mass transfer of reagents, localized ECL signals at the tip of nanoneedles were observed. By further embedding oxidases in the Nafion-coated electrode surface, substrates of corresponding enzymes can be quantified in the presence of luminol.[142] Large arrays of electrodes can be further powered using wireless bipolar electrochemistry and read out by ECL imaging.[143,144]

1.9.1.1 Sandwich immunoassays

Immunosensing of biomarkers in human fluids is one of the major bioanalytical applications of ECL.[50] Successfully-commercialized immunoassays are based on an ECL readout in a bead-based sandwich-like format, where target biomarkers are trapped between a capture antibody, that is attached on a magnetic non-conductive bead, and a detection antibody, decorated with a $[Ru(bpy)_3]^{2+}$ emitter. Following the incubation steps, the beads are drawn to the electrode surface using a magnet, and the ECL is triggered by applying a suitable electrode potential. The resulting emission corresponds to the concentration of the target protein, allowing for the quantification of biomarker levels based on luminescent intensity.[50] However, enhancing signal intensity in these bead-based (i.e. heterogeneous) immunoassays is crucial for improving sensitivity, which directly impacts detection limits and

the ability to detect biomarkers early in disease progression. Therefore, ongoing efforts focus on amplifying ECL intensity to elevate assay sensitivity.

1.9.2 ECL imaging of single cells

Single-cell analysis has emerged as a fundamental tool in biomedical research, earning significant attention in ECL microscopy over the past decade. Owing to the nature of the ECL processes, two complementary approaches toward ECL imaging of cells (and other biological entities) have emerged. They can be distinguished as "positive" and "negative" (or "shadow") ECL. In positive ECL (PECL), the luminophore-labelled cells are viewed as bright objects against a dark background, which is similar to the images obtained using classic photoluminescence (PL) techniques (i.e. fluorescence, phosphorescence). Initially influenced by the paradigm of fluorescence imaging, wherein cells are typically labelled with fluorescent probes, researchers have explored the application of ECL luminophores for cell surface labelling. In 2017, Valenti et al. introduced a novel single-cell PECL imaging approach employing the ECL strategy.[55] In this method, CHO-K1 cells were attached to the working electrode surface. The luminophore $[Ru(bpy)_3]^{2+}$ was immobilized to the cell membrane protein via a biotin-streptavidin linkage, leading to ECL emission upon interaction with electrogenerated TPrA radicals. The visual contrast between areas of cells with luminophores and the luminophore-free electrode surface accurately delineated the attachment positions of single cells at the interface. Following mitigation of the TPrA permeability issue at the cell-electrode interface, this strategy showcased enhanced delineation of single-cell outlines compared to fluorescence imaging, thus earning the designation of surface-confined ECL microscopy.[145]

Conversely, in the negative ECL mode (SECL), the cells adhering to the electrode hinder the diffusional flux of the ECL reagents and are imaged as dark objects against a bright background. This imaging mode possesses label-free characteristics, offering distinct advantages in monitoring dynamic changes in morphology of living cells. Ding et al. utilized the ECL- strategy to illustrate the adhesion of individual living cells on electrode surfaces.[58] ECL generated by freely diffusing luminophores provides clear visual contrast between cell adhesion sites at the electrode interface and non-contact regions, selectively revealing spatial distribution of cell-matrix adhesion and motion information during collective migration. Moreover, by adjusting luminophore and/or co-reactant concentrations, the thickness of ECL

emission layer could be controlled to match spatial positions of different cell connections, comprehensively presenting morphological heterogeneity of individual living cells from bottom to top.[59] It is noteworthy that ECL can modulate the height of the emission layer by altering the concentration of molecules within the system.[65,121,146]

In recent years, ECL microscopy has gradually entered into the realm of smaller biological entities with sub-micron dimensions, by successfully imaging single mitochondria using SECL[147]. Furthermore, single-bacteria imaging was achieved in both positive and negative ECL modes, by modulating the contrast from SECL to PECL by absorption of the $[Ru(bpy)_3]^{2+}$ dye on the bacterial surface.[148] Finally, imaging single ECL photons[132] or molecules[57] was reported simultaneously in 2021 and has been utilized since for imaging cells and single entities such as gold microplates, magnetic beads (in immunosensing) and bacteria.[131,148,149]

1.10 Conclusion

Although it began as a scientific curiosity without significant practical applications, the field of ECL has evolved into a multidisciplinary domain with important and ever-expanding applications in various scientific and industrial fields, including physics, biology, medicine, and material science. ECL stands out as a powerfull technique owing to its excellent sensitivity and selectivity, low background noise, and precise spatiotemporal control over signal generation. However, low ECL intensity remained the method's intrinsic limitation. To address this challenge, numerous strategies have focused on enhancing ECL through the development of more efficient luminophores,[75,81,92,150–152], coreactants,[153–156] or nanomaterials.[96,120,157,158]. However, developing general strategies for enhancing ECL properties requires a thorough understanding of the physicochemical principles of ECL generation and the underlying reaction mechanisms within ECL systems. This introducing section brings electrochemistry and photophysics togeather to lay out the general principles necessary to comprehend this multidisciplinary field. The fundamental considerations presented here are essential for understanding the specific strategies aimed at enhancing ECL efficiency within $[Ru(bpy)_3]^{2+}$/TPrA and luminol/H_2O_2 coreactant systems, which will be discussed in the following chapters.

References

1 Z. Liu, W. Qi and G. Xu, *Chem. Soc. Rev.*, 2015, **44**, 3117–3142.
2 N. Sojic, Ed., *Analytical Electrogenerated Chemiluminescence: From Fundamentals to Bioassays*, Royal Society of Chemistry, London, UK, 2020.
3 A. J. Bard, Ed., *Electrogenerated Chemiluminescence*, CRC Press, Boca Raton, 2004.
4 X. Gou, Z. Xing, C. Ma and J.-J. Zhu, *Chem. Biomed. Imaging*, 2023, **1**, 414–433.
5 In *Molecular Fluorescence*, John Wiley & Sons, Ltd, 2012, pp. 1–30.
6 T. Itoh, *Chem. Rev.*, 2012, **112**, 4541–4568.
7 J. W. Lichtman and J.-A. Conchello, *Nat Methods*, 2005, **2**, 910–919.
8 U. Isacsson and G. Wettermark, *Anal. Chim. Acta*, 1974, **68**, 339–362.
9 U. Mitschke and P. Bäuerle, *J. Mater. Chem.*, 2000, **10**, 1471–1507.
10 R. T. Dufford, D. Nightingale and L. W. Gaddum, *J. Am. Chem. Soc.*, 1927, **49**, 1858–1864.
11 N. Harvey, *J. Phys. Chem.*, 1929, **33**, 1456–1459.
12 D. M. Hercules, *Science*, 1964, **145**, 808–809.
13 R. E. Visco and E. A. Chandross, *J. Am. Chem. Soc.*, 1964, **86**, 5350–5351.
14 K. S. V. Santhanam and A. J. Bard, *J. Am. Chem. Soc.*, 1965, **87**, 139–140.
15 D. M. Hercules and F. E. Lytle, *J. Am. Chem. Soc.*, 1966, **88**, 4745–4746.
16 R. A. Marcus, *Angew. Chem. Int. Ed. Engl*, 1993, **32**, 1111–1121.
17 R. A. Marcus, *J. Chem. Phys.*, 1965, **43**, 2654–2657.
18 N. E. Tokel and A. J. Bard, *J. Am. Chem. Soc.*, 1972, **94**, 2862–2863.
19 M.-M. Chang, T. Saji and A. J. Bard, *J. Am. Chem. Soc.*, 1977, **99**, 5399–5403.
20 I. Rubinstein and A. J. Bard, *J. Am. Chem. Soc.*, 1981, **103**, 512–516.
21 H. S. White and A. J. Bard, *J. Am. Chem. Soc.*, 1982, **104**, 6891–6895.
22 J. B. Noffsinger and N. D. Danielson, *Anal. Chem.*, 1987, **59**, 865–868.
23 J. K. Leland and M. J. Powell, *J. Electrochem. Soc.*, 1990, **137**, 3127.
24 H. Ishida, S. Tobita, Y. Hasegawa, R. Katoh and K. Nozaki, *Coord. Chem. Rev.*, 2010, **254**, 2449–2458.
25 A. J. Bard, L. R. Faulkner and H. S. White, *Electrochemical Methods: Fundamentals and Applications*, John Wiley & Sons, 2022.
26 J. Heinze, *Angew. Chem. Int. Ed. Engl*, 1984, **23**, 831–847.
27 D. van der Westhuizen, K. G. von Eschwege and J. Conradie, *Electrochim. Acta*, 2019, **320**, 134540.
28 D. M. Arias-Rotondo and J. K. McCusker, *Chem. Soc. Rev.*, 2016, **45**, 5803–5820.
29 E. Kerr, D. J. Hayne, L. C. Soulsby, J. C. Bawden, S. J. Blom, E. H. Doeven, L. C. Henderson, C. F. Hogan and P. S. Francis, *Chem. Sci.*, 2022, **13**, 469–477.
30 Y. Zhou, Q. He, Y. Yang, H. Zhong, C. He, G. Sang, W. Liu, C. Yang, F. Bai and Y. Li, *Adv. Funct. Mater.*, 2008, **18**, 3299–3306.
31 R. E. Aderne, B. G. A. L. Borges, H. C. Ávila, F. von Kieseritzky, J. Hellberg, M. Koehler, M. Cremona, L. S. Roman, C. Moyses Araujo, M. L. M. Rocco and C. F. N. Marchiori, *Mater. Adv.*, 2022, **3**, 1791–1803.
32 J. Sworakowski, J. Lipiński and K. Janus, *Org. Electron.*, 2016, **33**, 300–310.
33 J. Sworakowski, *Synth. Met.*, 2018, **235**, 125–130.
34 R. Y. Lai and A. J. Bard, *J. Phys. Chem. A*, 2003, **107**, 3335–3340.
35 D. D. M. Wayner, D. J. McPhee and D. Griller, *J. Am. Chem. Soc.*, 1988, **110**, 132–137.
36 Elias. Papaconstantinou, *Anal. Chem.*, 1975, **47**, 1592–1595.
37 E. Papaconstantinou, *J. Chem. Soc., Faraday Trans. 1*, 1982, **78**, 2769–2772.
38 P. S. Rao and E. Hayon, *J. Am. Chem. Soc.*, 1974, **96**, 1287–1294.
39 A. J. Bard, in *Electrogenerated Chemiluminescence*, CRC Press, 2004.
40 J. Ludvík, *J. Solid State Electrochem.*, 2011, **15**, 2065–2081.

41 B. D. Stringer, L. M. Quan, P. J. Barnard, D. J. D. Wilson and C. F. Hogan, *Organometallics*, 2014, **33**, 4860–4872.
42 E. Kerr, E. H. Doeven, D. J. D. Wilson, C. F. Hogan and P. S. Francis, *Analyst*, 2016, **141**, 62–69.
43 H. Li, S. Voci, A. Wallabregue, C. Adam, G. M. Labrador, R. Duwald, I. Hernández Delgado, S. Pascal, J. Bosson, J. Lacour, L. Bouffier and N. Sojic, *ChemElectroChem*, 2017, **4**, 1750–1756.
44 A. Weller and K. Zachariasse, *Chem. Phys. Lett.*, 1971, **10**, 197–200.
45 J. D. Debad, J. C. Morris, V. Lynch, P. Magnus and A. J. Bard, *J. Am. Chem. Soc.*, 1996, **118**, 2374–2379.
46 A. Weller and K. Zachariasse, *Chem. Phys. Lett.*, 1971, **10**, 590–594.
47 B. Fleet, G. F. Kirkbright and C. J. Pickford, *J. Electroanal. Chem. Interf. Electrochem.*, 1971, **30**, 115–121.
48 S.-M. Park and R. A. Caldwell, *J. Electrochem. Soc.*, 1977, **124**, 1859.
49 R. Ziebig, H.-J. Hamann, W. Jugelt and F. Pragst, *J. Lumin.*, 1980, **21**, 353–366.
50 E. Faatz, A. Finke, H.-P. Josel, G. Prencipe, S. Quint and M. Windfuhr, , DOI:10.1039/9781788015776-00443.
51 S. Knezevic, L. Bouffier, B. Liu, D. Jiang and N. Sojic, *Curr. Opin. Electrochem.*, 2022, 101096.
52 S. Rebeccani, A. Zanut, C. I. Santo, G. Valenti and F. Paolucci, *Anal. Chem.*, 2022, **94**, 336–348.
53 W. Miao, J.-P. Choi and A. J. Bard, *J. Am. Chem. Soc.*, 2002, **124**, 14478–14485.
54 A. Zanut, A. Fiorani, S. Canola, T. Saito, N. Ziebart, S. Rapino, S. Rebeccani, A. Barbon, T. Irie, H.-P. Josel, F. Negri, M. Marcaccio, M. Windfuhr, K. Imai, G. Valenti and F. Paolucci, *Nat. Commun.*, 2020, **11**, 2668.
55 G. Valenti, S. Scarabino, B. Goudeau, A. Lesch, M. Jović, E. Villani, M. Sentic, S. Rapino, S. Arbault, F. Paolucci and N. Sojic, *J. Am. Chem. Soc.*, 2017, **139**, 16830–16837.
56 M. Sentic, M. Milutinovic, F. Kanoufi, D. Manojlovic, S. Arbault and N. Sojic, *Chem. Sci.*, 2014, **5**, 2568–2572.
57 Y. Liu, H. Zhang, B. Li, J. Liu, D. Jiang, B. Liu and N. Sojic, *J. Am. Chem. Soc.*, 2021, **143**, 17910–17914.
58 H. Ding, W. Guo and B. Su, *Angew. Chem. Int. Ed.*, 2020, **59**, 449–456.
59 H. Ding, P. Zhou, W. Fu, L. Ding, W. Guo and B. Su, *Angew. Chem. Int. Ed.*, 2021, **60**, 11769–11773.
60 C. Ma, S. Wu, Y. Zhou, H. Wei, J. Zhang, Z. Chen, J. Zhu, Y. Lin and W. Zhu, *Angew. Chem. Int. Ed.*, 2021, **60**, 4907–4914.
61 M. Mayer, S. Takegami, M. Neumeier, S. Rink, A. Jacobi von Wangelin, S. Schulte, M. Vollmer, A. G. Griesbeck, A. Duerkop and A. J. Baeumner, *Angew. Chem. Int. Ed.*, 2018, **57**, 408–411.
62 U. Isacsson, J. Kowalewska and G. Wettermark, *J. Inorg. Nucl. Chem.*, 1978, **40**, 1653–1656.
63 J. Arnhold, S. Mueller, K. Arnold and E. Grimm, *J. Biolumin. Chemilumin.*, 1991, **6**, 189–192.
64 R. He, H. Tang, D. Jiang and H. Chen, *Anal. Chem.*, 2016, **88**, 2006–2009.
65 P. Zhou, S. Hu, W. Guo and B. Su, *Fundam. Res.*, 2022, **2**, 682–687.
66 W. Xu, Y. Wu, X. Wang, Y. Qin, H. Wang, Z. Luo, J. Wen, L. Hu, W. Gu and C. Zhu, *Angew. Chem. Int. Ed.*, 2023, **62**, e202304625.
67 M. Xi, Z. Wu, Z. Luo, L. Ling, W. Xu, R. Xiao, H. Wang, Q. Fang, L. Hu, W. Gu and C. Zhu, *Angew. Chem. Int. Ed.*, 2023, **62**, e202302166.
68 W. Liang, M. Wang, C. Ma, J. Wang, C. Zhao and C. Hong, *Small*, 2024, **20**, 2306473.
69 N. Gao, G. Ren, M. Zhang and L. Mao, *J. Am. Chem. Soc.*, 2024, **146**, 3836–3843.
70 C. K. Chien, H. C. Wang, M. Szwarc, A. J. Bard and K. Itaya, *J. Am. Chem. Soc.*, 1980, **102**, 3100–3104.
71 L. R. Faulkner and D. J. Freed, *J. Am. Chem. Soc.*, 1971, **93**, 3565–3568.
72 H. C. Cheung, in *Topics in Fluorescence Spectroscopy: Principles*, ed. J. R. Lakowicz, Springer US, Boston, MA, 2002, pp. 127–176.
73 D. L. Dexter, *J. Chem. Phys.*, 1953, **21**, 836–850.

74 C. Grewer and H.-D. Brauer, *J. Phys. Chem.*, 1994, **98**, 4230–4235.
75 D. Bruce and M. M. Richter, *Anal. Chem.*, 2002, **74**, 1340–1342.
76 L. Flamigni, A. Barbieri, C. Sabatini, B. Ventura and F. Barigelletti, in *Photochemistry and Photophysics of Coordination Compounds II*, eds. V. Balzani and S. Campagna, Springer, Berlin, Heidelberg, 2007, pp. 143–203.
77 S. Zanarini, M. Felici, G. Valenti, M. Marcaccio, L. Prodi, S. Bonacchi, P. Contreras-Carballada, R. M. Williams, M. C. Feiters, R. J. M. Nolte, L. De Cola and F. Paolucci, *Eur. J. Chem.*, 2011, **17**, 4640–4647.
78 J. M. Fernandez-Hernandez, E. Longhi, R. Cysewski, F. Polo, H.-P. Josel and L. De Cola, *Anal. Chem.*, 2016, **88**, 4174–4178.
79 L. Yu, Z. Huang, Y. Liu and M. Zhou, *J. Organomet. Chem.*, 2012, **718**, 14–21.
80 E. Kerr, E. H. Doeven, G. J. Barbante, T. U. Connell, P. S. Donnelly, D. J. D. Wilson, T. D. Ashton, F. M. Pfeffer and P. S. Francis, *Eur. J. Chem.*, 2015, **21**, 14987–14995.
81 G. J. Barbante, E. H. Doeven, E. Kerr, T. U. Connell, P. S. Donnelly, J. M. White, T. Lópes, S. Laird, D. J. D. Wilson, P. J. Barnard, C. F. Hogan and P. S. Francis, *Eur. J. Chem.*, 2014, **20**, 3322–3332.
82 B. Newman, L. Chen, L. C. Henderson, E. H. Doeven, P. S. Francis and D. J. Hayne, *Front. Chem.*
83 A. Kapturkiewicz, *Anal. Bioanal. Chem.*, 2016, **408**, 7013–7033.
84 E. Kerr, E. H. Doeven, G. J. Barbante, C. F. Hogan, D. J. Bower, P. S. Donnelly, T. U. Connell and P. S. Francis, *Chem. Sci.*, 2015, **6**, 472–479.
85 E. Kerr, E. H. Doeven, G. J. Barbante, C. F. Hogan, D. J. Hayne, P. S. Donnelly and P. S. Francis, *Chem. Sci.*, 2016, **7**, 5271–5279.
86 E. H. Doeven, E. M. Zammit, G. J. Barbante, C. F. Hogan, N. W. Barnett and P. S. Francis, *Angew. Chem. Int. Ed.*, 2012, **51**, 4354–4357.
87 E. H. Doeven, G. J. Barbante, E. Kerr, C. F. Hogan, J. A. Endler and P. S. Francis, *Anal. Chem.*, 2014, **86**, 2727–2732.
88 W. Guo, H. Ding, C. Gu, Y. Liu, X. Jiang, B. Su and Y. Shao, *J. Am. Chem. Soc.*, 2018, **140**, 15904–15915.
89 B. D. Muegge and M. M. Richter, *Anal. Chem.*, 2004, **76**, 73–77.
90 B. D. Stringer, L. M. Quan, P. J. Barnard and C. F. Hogan, *ChemPhotoChem*, 2018, **2**, 27–33.
91 H. Li, J. Daniel, J.-B. Verlhac, M. Blanchard-Desce and N. Sojic, *Eur. J. Chem.*, 2016, **22**, 12702–12714.
92 F. Rizzo, F. Polo, G. Bottaro, S. Fantacci, S. Antonello, L. Armelao, S. Quici and F. Maran, *J. Am. Chem. Soc.*, 2017, **139**, 2060–2069.
93 S. Zanarini, E. Rampazzo, L. D. Ciana, M. Marcaccio, E. Marzocchi, M. Montalti, F. Paolucci and L. Prodi, *J. Am. Chem. Soc.*, 2009, **131**, 2260–2267.
94 A. Zanut, F. Palomba, M. Rossi Scota, S. Rebeccani, M. Marcaccio, D. Genovese, E. Rampazzo, G. Valenti, F. Paolucci and L. Prodi, *Angew. Chem. Int. Ed.*, 2020, **59**, 21858–21863.
95 S. Kesarkar, E. Rampazzo, A. Zanut, F. Palomba, M. Marcaccio, G. Valenti, L. Prodi and F. Paolucci, *Curr. Opin. Electrochem.*, 2018, **7**, 130–137.
96 S. Kesarkar, S. Valente, A. Zanut, F. Palomba, A. Fiorani, M. Marcaccio, E. Rampazzo, G. Valenti, F. Paolucci and L. Prodi, *J. Phys. Chem. C*, 2019, **123**, 5686–5691.
97 Z. Cao, Y. Shu, H. Qin, B. Su and X. Peng, *ACS Cent. Sci.*, 2020, **6**, 1129–1137.
98 N. Myung, Z. Ding and A. J. Bard, *Nano Lett.*, 2002, **2**, 1315–1319.
99 L.-L. Li, J. Ji, R. Fei, C.-Z. Wang, Q. Lu, J.-R. Zhang, L.-P. Jiang and J.-J. Zhu, *Adv. Funct. Mater.*, 2012, **22**, 2971–2979.
100 L. Zheng, Y. Chi, Y. Dong, J. Lin and B. Wang, *J. Am. Chem. Soc.*, 2009, **131**, 4564–4565.
101 K. N. Swanick, M. Hesari, M. S. Workentin and Z. Ding, *J. Am. Chem. Soc.*, 2012, **134**, 15205–15208.
102 M. Hesari, M. S. Workentin and Z. Ding, *ACS Nano*, 2014, **8**, 8543–8553.
103 X. Liu, L. Shi, W. Niu, H. Li and G. Xu, *Angew. Chem. Int. Ed.*, 2007, **46**, 421–424.

104 D. L. Akins and R. L. Birke, *Chem.l Phys. Lett.*, 1974, **29**, 428–435.
105 A. Fiorani, null Irkham, G. Valenti, F. Paolucci and Y. Einaga, *Anal Chem*, 2018, **90**, 12959–12963.
106 H. S. White, W. G. Becker and A. J. Bard, *J. Phys. Chem.*, 1984, **88**, 1840–1846.
107 H. Yang, J. K. Leland, D. Yost and R. J. Massey, *Nat Biotechnol*, 1994, **12**, 193–194.
108 J. E. Dick, C. Renault, B.-K. Kim and A. J. Bard, *Angew. Chem. Int. Ed.*, 2014, **53**, 11859–11862.
109 F.-R. F. Fan and A. J. Bard, *Nano Lett.*, 2008, **8**, 1746–1749.
110 Y. Wang, W. Guo, Q. Yang and B. Su, *J. Am. Chem. Soc.*, 2020, **142**, 1222–1226.
111 N. S. Adamson, A. G. Theakstone, L. C. Soulsby, E. H. Doeven, E. Kerr, C. F. Hogan, P. S. Francis and L. Dennany, *Chem. Sci.*, 2021, **12**, 9770–9777.
112 W.-X. Fu, P. Zhou, W.-L. Guo and B. Su, *Adv. Sens. Energy Mater.*, 2022, **1**, 100028.
113 E. Kerr, S. Knezevic, P. S. Francis, C. F. Hogan, G. Valenti, F. Paolucci, F. Kanoufi and N. Sojic, *ACS Sens.*, 2023, **8**, 933–939.
114 A. Fracassa, C. I. Santo, E. Kerr, S. Knežević, D. J. Hayne, P. S. Francis, F. Kanoufi, N. Sojic, F. Paolucci and G. Valenti, *Chem. Sci.*, , DOI:10.1039/D3SC06357G.
115 M. Belotti, M. M. T. El-Tahawy, M. Garavelli, M. L. Coote, K. S. Iyer and S. Ciampi, *Anal. Chem.*, 2023, **95**, 9779–9786.
116 J.-H. Han, E. Lee, S. Park, R. Chang and T. D. Chung, *J. Phys. Chem. C*, 2010, **114**, 9546–9553.
117 P. A. Defnet and B. Zhang, *ChemElectroChem*, 2020, **7**, 252–259.
118 Y. Wang, R. Jin, N. Sojic, D. Jiang and H. Chen, *Angew. Chem. Int. Ed.*, 2020, **59**, 10416–10420.
119 S. Voci, A. Ismail, P. Pham, J. Yu, A. Maziz, F. Mesnilgrente, L. Reynaud, T. Livache, P. Mailley, A. Buhot, T. Leichle, A. Kuhn, L. Leroy, A. Bouchet-Spinelli and N. Sojic, *J. Electrochem. Soc.*, 2020, **167**, 137509.
120 P. Nikolaou, G. Valenti and F. Paolucci, *Electrochim. Acta*, 2021, **388**, 138586.
121 W. Guo, P. Zhou, L. Sun, H. Ding and B. Su, *Angew. Chem. Int. Ed.*, 2021, **60**, 2089–2093.
122 Y. B. Vogel, C. W. Evans, M. Belotti, L. Xu, I. C. Russell, L.-J. Yu, A. K. K. Fung, N. S. Hill, N. Darwish, V. R. Gonçales, M. L. Coote, K. Swaminathan Iyer and S. Ciampi, *Nat. Commun.*, 2020, **11**, 6323.
123 M. W. Glasscott and J. E. Dick, *J. Phys. Chem. Lett.*, 2020, **11**, 4803–4808.
124 M. W. Glasscott, S. Voci, P. J. Kauffmann, A. I. Chapoval and J. E. Dick, *Langmuir*, 2021, **37**, 2907–2912.
125 S. Voci, K. J. Vannoy and J. E. Dick, *J. Colloid Interface Sci.*, 2024, **661**, 853–860.
126 B. R. Layman and J. E. Dick, *J. Am. Chem. Soc.*, 2024, **146**, 707–713.
127 Y. Chen, D. Zhao, J. Fu, X. Gou, D. Jiang, H. Dong and J.-J. Zhu, *Anal. Chem.*, 2019, **91**, 6829–6835.
128 M.-M. Chen, C.-H. Xu, W. Zhao, H.-Y. Chen and J.-J. Xu, *Chem. Commun.*, 2020, **56**, 3413–3416.
129 M.-M. Chen, C.-H. Xu, W. Zhao, H.-Y. Chen and J.-J. Xu, *J. Am. Chem. Soc.*, 2021, **143**, 18511–18518.
130 H. Zhu, D. Jiang and J.-J. Zhu, *Chem. Sci.*, 2021, **12**, 4794–4799.
131 J. Dong, Y. Xu, Z. Zhang and J. Feng, *Angew. Chem. Int. Ed.*, 2022, **61**, e202200187.
132 J. Dong, Y. Lu, Y. Xu, F. Chen, J. Yang, Y. Chen and J. Feng, *Nature*, 2021, **596**, 244–249.
133 Y. Lu, X. Huang, S. Wang, B. Li and B. Liu, *ACS Nano*, 2023, **17**, 3809–3817.
134 C. Cui, R. Jin, D. Jiang, J. Zhang and J. Zhu, *Research*, , DOI:10.34133/2021/1742919.
135 R. Pan, K. Hu, D. Jiang, U. Samuni and M. V. Mirkin, *J. Am. Chem. Soc.*, 2019, **141**, 19555–19559.
136 M. Belotti, M. M. T. El-Tahawy, L.-J. Yu, I. C. Russell, N. Darwish, M. L. Coote, M. Garavelli and S. Ciampi, *Angew. Chem. Int. Ed.*, 2022, **61**, e202209670.
137 B. R. Layman and J. E. Dick, *J. Phys. Chem. Lett.*, 2023, **14**, 8151–8156.
138 S. Voci, T. B. Clarke and J. E. Dick, *Chem. Sci.*, 2023, **14**, 2336–2341.

139 A. Barhoum, Z. Altintas, K. S. S. Devi and R. J. Forster, *Nano Today*, 2023, **50**, 101874.
140 J. Zhang, H. Ding, S. Zhao, D. Jiang and H.-Y. Chen, *Electrochem.Comm.*, 2019, **98**, 38–42.
141 J. Zhou, G. Ma, Y. Chen, D. Fang, D. Jiang and H. Chen, *Anal. Chem.*, 2015, **87**, 8138–8143.
142 J. Zhang, J. Zhou, C. Tian, S. Yang, D. Jiang, X.-X. Zhang and H.-Y. Chen, *Anal. Chem.*, 2017, **89**, 11399–11404.
143 K.-F. Chow, F. Mavré, J. A. Crooks, B.-Y. Chang and R. M. Crooks, *J. Am. Chem. Soc.*, 2009, **131**, 8364–8365.
144 B.-Y. Chang, K.-F. Chow, J. A. Crooks, F. ço Mavré, R. M. Crooks, B.-Y. Chang, K.-F. Chow, J. A. Crooks, F. co Mavre and R. M. Crooks, *Analyst*, 2012, **137**, 2827–2833.
145 S. Voci, B. Goudeau, G. Valenti, A. Lesch, M. Jović, S. Rapino, F. Paolucci, S. Arbault and N. Sojic, *J. Am. Chem. Soc.*, 2018, **140**, 14753–14760.
146 A. Fiorani, D. Han, D. Jiang, D. Fang, F. Paolucci, N. Sojic and G. Valenti, *Chem. Sci.*, 2020, **11**, 10496–10500.
147 Y. Ma, C. Colin, J. Descamps, S. Arbault and N. Sojic, *Angew. Chem. Int. Ed.*, 2021, **60**, 18742–18749.
148 Y. Zhou, J. Dong, P. Zhao, J. Zhang, M. Zheng and J. Feng, *J. Am. Chem. Soc.*, 2023, **145**, 8947–8953.
149 W. Zhu, J. Dong, G. Ruan, Y. Zhou and J. Feng, *Angew. Chem. Int. Ed.*, 2023, **62**, e202214419.
150 A. Abdussalam and G. Xu, *Anal Bioanal Chem*, 2022, **414**, 131–146.
151 L. Chen, D. J. Hayne, E. H. Doeven, J. Agugiaro, D. J. D. Wilson, L. C. Henderson, T. U. Connell, Y. H. Nai, R. Alexander, S. Carrara, C. F. Hogan, P. S. Donnelly and P. S. Francis, *Chem. Sci.*, 2019, **10**, 8654–8667.
152 M. A. Haghighatbin, S. E. Laird and C. F. Hogan, *Curr. Opin. Electrochem.*, 2018, **7**, 216–223.
153 S. A. Kitte, C. Wang, S. Li, Y. Zholudov, L. Qi, J. Li and G. Xu, *Anal Bioanal Chem*, 2016, **408**, 7059–7065.
154 H. Xing, Q. Zhai, X. Zhang, J. Li and E. Wang, *Anal. Chem.*, 2018, **90**, 2141–2147.
155 C. V. Raju and S. S. Kumar, *Chem. Commun.*, 2017, **53**, 6593–6596.
156 F. Yuan, M. I. Halawa, X. Ma, A. Abdussalam, B. Lou and G. Xu, *ChemElectroChem*, 2020, **7**, 4239–4244.
157 A. Fiorani, J. P. Merino, A. Zanut, A. Criado, G. Valenti, M. Prato and F. Paolucci, *Curr. Opin. Electrochem.*, 2019, **16**, 66–74.
158 P. Dai, C. Liu, C. Xie, J. Ke, Y. He, L. Wei, L. Chen and J. Jin, *Anal Bioanal Chem*, 2020, **412**, 1375–1384.

Chapter II:
Using Redox Mediators for ECL Enhancement: Theoretical Considerations

Chapter II: Using Redox Mediators for ECL Enhancement: Theoretical Considerations

2.1 Introduction

Starting from pure scientific curiosity at the beginning of the 20th century, ECL has evolved into a contemporary analytical technique with a wide range of applications. This method features high specificity and sensitivity, nearly zero background signal and excellent spatial and temporal resolution, but is limited by relatively low emission intensities. Consequently, strategies to enhance overall ECL performance typically focus on amplifying ECL signal intensity. For most practical applications, this is achieved by varying and calibrating experimental parameters or synthesising more efficient ECL emitters (luminophores[1–6] or nanomaterials[7–10]). However, while useful for specific purposes, these experimental approaches are not general–parameters optimised for a specific ECL system and application can rarely be extended to other ECL systems or applications. Furthermore, the optimisation process is often laborious and time-consuming, without yielding fundamental insights or significant advancements in the investigated system.

A more rational approach involves investigating ECL systems' underlying reactivity and physicochemical characteristics. This leads to a better understanding of the factors that influence the reaction system as a whole, as well as its individual parts, allowing for the optimisation of the ECL efficiency in a general way, which applies to different ECL systems and experimental setups, and having the potential to open new research questions. Additionally, it eliminates the need for a trial-and-error approach to testing different experimental conditions and allows for the rational design of suitable ECL emitters. However, this is not to say that meticulous experimentation is unimportant, but rather that it should be designed (and conducted) in a manner that yields meaningful information about the system. Moreover, equally important theoretical considerations can complement such experiments, providing deeper insights into the studied system.

Regardless of the system under investigation, all ECL reaction mechanisms involve an initial electrochemical step followed by a cascade of chemical steps, most of which are

extremely rapid (diffusion-limited) bimolecular reactions in solution.[11,12] To fully describe an ECL process and study its underlying reactivity, one must analyse the evolution of ECL emission intensity and the electrochemical current during an experiment. While these two descriptors reflect the same overall mechanistic process, they exhibit different sensitivities to distinct reaction steps. The current reflects the total flux of electroactive species at the electrode, offering insights into the thermodynamics and kinetics of the electrochemical reactions, as well as the potential involvement of catalytic reactions or other chemical transformations coupled with the initial electron transfer (ET) step. Conversely, ECL emission is a product of the formation of electronically excited species and can, therefore, provide information about the intricate interplay between different homogeneous steps that influence the rate, magnitude, and spatial distribution of the luminophore's excited state production. Evaluation of these experimental descriptors can be performed by carefully analysing the plots of current and ECL intensity versus time (or potential), whether the potential of a working electrode is being kept constant or changing in a predictable manner. Additionally, ECL imaging offers valuable insights into the stability of ECL species and the dominant mechanistic pathways by mapping the spatial distribution of ECL emission.

In typical ECL systems (and, more generally, during electrochemical reactions), the mass transfer (i.e., diffusion) and (electro)chemical processes proceed at extremely different rates and, consequently, over very different temporal and spatial scales. While the diffusion layer of freely diffusing species can extend up to few hundreds of micrometres into the solution, limited by natural convection,[13–17] (electro)chemical transformations of reacting species cause rapid fluctuations in their concentration profiles, resulting in narrow reaction zones - from several tens of nanometres to several micrometres. For instance, rapid reaction rates (and short lifetimes of reacting species) confine the generation of the electronically excited state of a luminophore to extremely thin reaction zones near the electrode surface, and its concentration remains exceedingly low due to its fast depletion via radiative decay. Analysing the evolution of concentration profiles of various reactive species during the ECL reactions can offer valuable insights into the processes occurring in the reaction mixture. However, while the local intensity (i.e. concentration) and spatial distribution of photon emission can be resolved using ECL microscopy[18–22] or self-interference spectroscopy,[23] localising the concentration profiles of other reaction species can be challenging.

2.1.1 The use of finite element simulations

Detailed simulation of the ECL system, using general-purpose Finite Element software such as COMSOL Multiphysics, or other standard simulation packages like KISSA, Digielch, or Digisim, can serve as an invaluable tool to complement the experimental data and help analyse the parameters of the system that are difficult to follow experimentally (ie. lifetimes of reactive species, their concentration profiles and rate constants of homogeneous steps).[12,24]

However, simulating ECL reactivity within complex coreactant systems is often challenging due to the need to simultaneously resolve phenomena across drastically different spatial, temporal, and concentration scales. These phenomena include fast homogeneous and heterogeneous steps causing steep concentration gradients near the electrode surface and across narrow reaction fronts within comparably wide diffusion profiles. Consequently, a reliable model must compute all of these processes with satisfactory precision. Fortunately, it is possible to address these challenges in a single simulation, but constructing the simulation mesh to ensure accurate simulation of varying concentration profiles, while not being overly computationally demanding, is difficult.[12] However, knowing and predefining the localisation of the most dramatic concentration gradients (near the electrode surface, but also in solution) allows for adjusting the mesh density—dense near the electrode, labelled objects, phase interfaces, or in solution where steep concentration gradients occur, and sparse in the bulk solution, where the concentrations of species are constant.

Furthermore, the system's geometry can be depicted in the simulation model as 1D, 2D, or 3D (**Figure 2.1**).

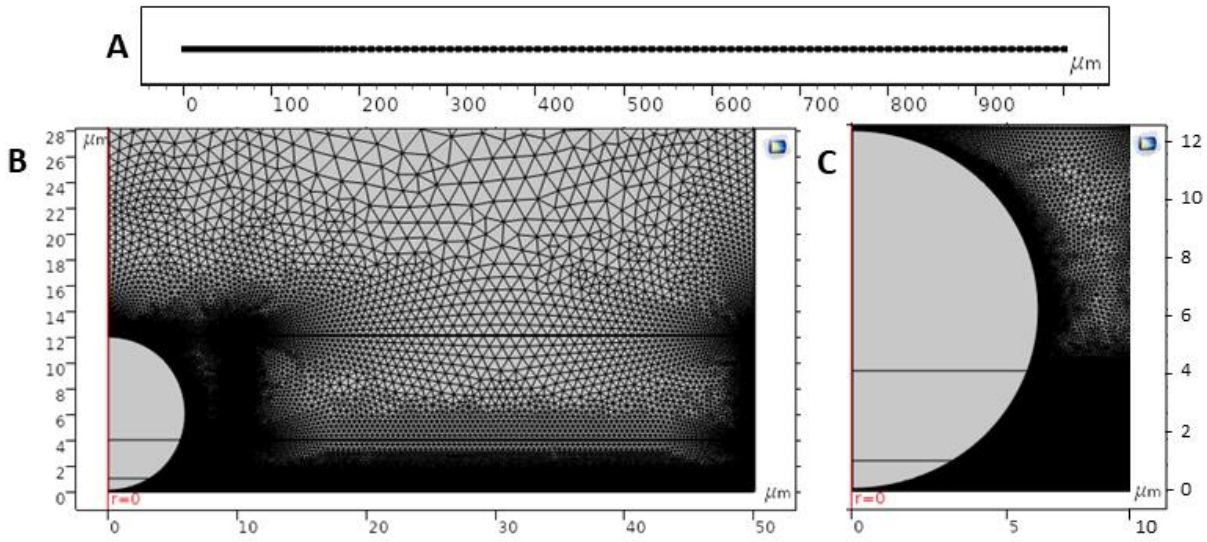

Figure 2.1. Mesh images from **(A)** 1D and **(B, C)** 2D COMSOL models, representing the geometry of the same bead-based ECL system. **(B)** and **(C)** show the mesh of the 2D model at different scales, emphasising the complexity and high density of meshing nodes in the region of interest.

However, the complexity of constructing the simulation mesh and the number of meshing nodes increases drastically with more intricate geometries, increasing the cost in calculation time. Consequently, simulations in multidimensional space are very time-consuming due to the extensive number of nodes in the computational mesh and the multiple species whose concentrations must be computed. Therefore, while 2D simulations can yield accurate results for specific parameter sets, they are unsuitable for exploring the entire parameter space and optimisation of the investigated system because such exploration requires numerous model evaluations under various conditions (distances, concentrations, rate constants, etc.) or model's adaptation for different systems that employ various luminophores or coreactants, which can be extremely computationally demanding and time-consuming. Thus, using a less computationally demanding 1D model is usually preferred for model optimisation and exploratory purposes, especially as it has been demonstrated that 2D simulations can be replaced with quicker 1D simulations without sacrificing the accuracy of the results.[12,25] Additionally, when using COMSOL Multiphysics, following parameter optimisation across the whole parameter space, the 1D model can be easily upgraded to more complex 2D geometries. This is useful when simulating the system under specific and

predefined conditions in more complex experimental setups, such as those employing ECL with beads or biological cells.

2.1.2 Mixed luminophore system

Here, we investigated the ECL system that employs $[Ru(bpy)_3]^{2+}$ as a luminophore and TPrA as a sacrificial coreactant. Being a model system for the majority of ECL applications, it is one of the most studied ECL systems, both experimentally and theoretically, and is, therefore, well characterised (mechanistically and kinetically). The underlying reaction mechanisms, along with necessary kinetic considerations within this coreactant system are described in detail in **Chapter 1 section 1.6.1.2.** Briefly, if both $[Ru(bpy)_3]^{2+}$ and TPrA are freely diffusing in solution, they can undergo heterogeneous oxidation at an appropriate electrode potential and react via an oxidative-reductive mechanism to populate the $[Ru(bpy)_3]^{2+*}$ excited state. However, if the electrode is biased at a potential which is sufficient to oxidise TPrA but not $[Ru(bpy)_3]^{2+}$, or if direct oxidation of $[Ru(bpy)_3]^{2+}$ is obstructed in another way (ie. if $[Ru(bpy)_3]^{2+}$ is used to label an insulating object), generation of ECL will rely on the cascade of reactions involving transient TPrA radicals (**Figure 2.2A**). In this latter case, the efficiency of ECL generation is constrained by the short half-life of $TPrA^{\bullet+}$, thereby limiting the thickness of the ECL-emitting layer and the ECL signal.[26] To overcome this limitation, extensive investigation has been focused on fine-tuning the reaction route, through the development of nanomaterials,[7–10] luminophores,[1–6] or coreactants,[27–30] with improved properties. However, as previously discussed, the success of these optimisation approaches strongly depends on and is complemented by a comprehensive mechanistic understanding of this ECL system.[20,24,25,31–33]

Recently, iridium complexes have emerged as promising luminophores, offering various ECL onset redox potentials and emission colours.[4,6,34–38] In a study by Kerr et al.,[39] ten-fold enhancement of $[Ru(bpy)_3]^{2+}$ ECL emission was reported in the presence of TPrA and the freely diffusing, redox-active tris(2-(2-pyridinyl-κ*N*)-4-sulfonatophenyl-κ*C*)iridium(III) ($[Ir^{III}(sppy)_3]^{3-}$) complex. This enhancement was attributed to the improved efficiency of this mixed coreactant system with $[Ir^{IV}(sppy)_3]^{2-}$ (along with $TPrA^{\bullet+}$) acting as a mediator for oxidative generation of the excited state from $[Ru(bpy)_3]^{+}$ (**Figure 2.2C**). In addition to the increased intensity, the study also reported a shift of $[Ru(bpy)_3]^{2+}$ ECL towards lower

overpotentials. Finally, the $[Ir^{III}(sppy)_3]^{3-}$ ECL emission, generated through the oxidation-reduction mechanism (**Figure 2.2B**), can be used for internal standardisation of the coreactant ECL of $[Ru(bpy)_3]^{2+}$. The chemical structure of this Ir(III) complex is shown in **Figure 2.2E**.

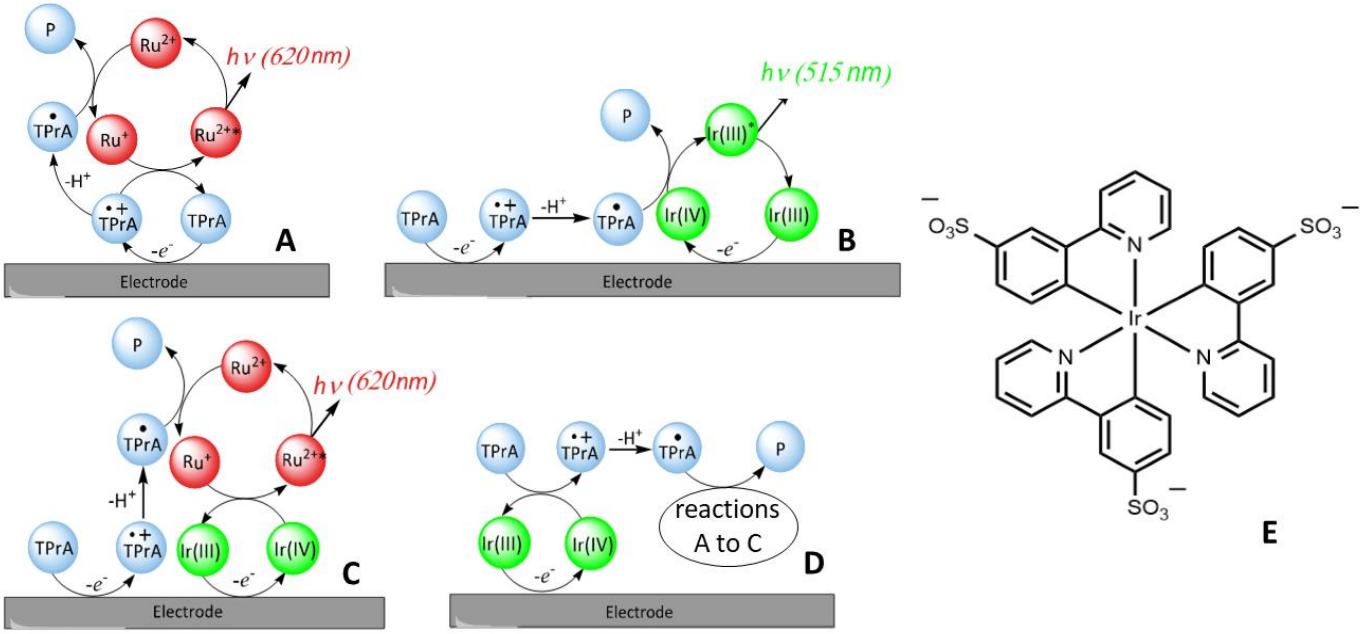

Figure 2.2. Schematics of the **(A)** conventional 'remote' ECL route, **(B)** direct route to $[Ir^{III}(sppy)_3]^{3-}$ ECL, **(C)** enhanced 'redox-mediated' ECL route and **(D)** redox catalysis (catalytic oxidation of TPrA by $[Ir^{IV}(sppy)_3]^{2-}$). Ru^{2+}, Ir(III) and TPrA represent the $[Ru(bpy)_3]^{2+}$ luminophore, the $[Ir^{III}(sppy)_3]^{3-}$ redox mediator and tri-*n*-propylamine, respectively.

The potential of this mixed coreactant system was demonstrated not only in the original publication but also in subsequent studies addressing its value in the context of ECL bioassays[40] and cell imaging[41] (see **Chapter 3**). Furthermore, Fracassa et al.[42] demonstrated experimentally that in such $[Ru(bpy)_3]^{2+}$-immobilized configuration, redox mediators in solution, such as Ir complexes, can modulate the ECL of $[Ru(bpy)_3]^{2+}$/TPrA coreactant system, either by quenching or by enhancing it based on their redox properties. Redox mediators with reduction potentials equal to or more positive than that of $TPrA^{\bullet}$ act as reducing agents, scavenging radical species and quenching ECL, while those with easily accessible oxidation potentials boost ECL by homogenously oxidising $[Ru(bpy)_3]^{+}$ and TPrA (**Figures 2.2C** and **2.2D**, respectively).[40,42,43] This situation is reminiscent of molecular electrocatalysis pathways where a molecular electrocatalyst is used to trigger electrochemical reactions in solution.[44,45]

2.1.3 Molecular catalysis and its role in analysing reaction mechanisms

In general, achieving a satisfactory rate of electrochemical reactions often requires the application of substantial overpotentials. This is particularly true for inner-sphere electron transfer reactions, such as the oxidation of some ECL coreactants (i.e TPrA),[46] or activation of small molecules (typically water, oxygen carbon dioxide or protons).[44,47–49] The kinetics of such reactions heavily depend on the nature of the electrode surface and experimental conditions. Therefore, catalysis of the electrochemical reaction is typically required to increase the reaction rate and, consequently, the current at a potential as close as possible to the equilibrium potential.

This can be achieved through several strategies.[50–52] The most common approach, usually referred to as "electrocatalysis", involves the participation of electrode material in the catalytic process, where substrates (and products) are activated through adsorption at the electrode surface. In this case, the catalyst efficiency is determined by the chemical nature of the electrode surface, its geometry and crystallographic properties and the number and nature of lattice defects (also considering that the material's surface and bulk properties might be different). Thus, applying fundamental molecular concepts to analyse and characterise such electrocatalysis, and to rationally develop similar catalytic systems, is challenging, and often unfeasible.[53]

Another approach to catalysis is to use redox active molecules as catalysts, either dispersed in solution (homogeneous catalysis) or immobilized as a mono-layer or multilayer coating on the electrode surface (heterogeneous catalysis).[51,52] This type of catalysis, termed molecular catalysis, implies that the electrode surface itself is inert and acts as a heterogeneous outer sphere electron acceptor (or electron donor), and the (electro)chemical properties of molecular catalysts determine the catalytic efficiency and electrochemical behaviour within the system.

A typical homogeneous catalysis scheme for the case of oxidation can be represented by equations *2.1* - *2.3*:

$$P \rightleftarrows Q + e^- \qquad (2.1)$$

$$Q + A \xrightarrow{k_{fcat}} P + B \qquad (2.2)$$

$$A \longrightarrow B + e^- \qquad (2.3)$$

Here, P and Q are molecular catalysts, members of a reversible redox couple with a standard potential of $E^0_{P/Q}$ (equation *2.1*). Catalyst Q should facilitate the oxidation of substrate A into product B (equation *2.2*) at lower overpotentials than those required for the direct transformation of A at the electrode surface (equation *2.3*). k_{fcat} represents the rate constant for the forward electron transfer in this catalytic process (equation *2.2*). During the catalytic cycle, the catalyst is regenerated, allowing it to repeatedly participate in the reaction.

Ideally, the standard potential of the catalyst redox couple $E^0_{P/Q}$ should lie between the standard potential of the global electrochemical reaction (in the absence of the catalyst) $E^0_{A/B}$ (equation *2.3*) and the electrode potential E at which the direct oxidation of A occurs. However, catalysis can still proceed when the homogeneous ET is not thermodynamically favourable (i.e. when $E^0_{P/Q}$ is lower but close to $E^0_{A/B}$), in which case reaction *2.2* is equilibrated, with the forward ET rate being lower than the backward rate, but not null. If a subsequent reaction (such as bond breaking or protonation) rapidly transforms the products, this follow-up reaction shifts the equilibrium towards product formation, thereby enhancing the rate of the thermodynamically unfavourable ET step.

Apart from its usefulness on a preparative scale level, molecular catalysis can be used to investigate the properties of electrochemical systems (i.e. electron transfer, mass transport, (electro)chemical characteristics of transient intermediates). Cyclic voltammetry (CV) is usually the preferred technique for probing molecular catalysis, as it is non-destructive and rapid. The usual strategy consists of performing multiple CV experiments with varying scan rates and catalyst-to-substrate concentration ratios. These experiments give rise to a series of CVs with specific peak shapes, positions (potentials) and currents, which reflect the physicochemical properties of the investigated system and allow one to investigate not only the electron transfer, but also the transport of reactants and products to and from the electrode (diffusion), and (in some cases) their chemical reactivity. Thus, analysing such CVs leads to a deeper mechanistic and kinetic understanding of the investigated system, allowing for the determination of the stability of reacting species and reaction intermediates, standard potentials of transient intermediates, and rate constants of (electro)chemical steps.[51,52,54–56]

During this (often complex) analysis, it is helpful that the kinetics (and kinetic treatment) of the simplest reaction schemes are rigorously investigated and compactly described in the form of so-called kinetic zone diagrams. This is illustrated in **Figure 2.3**, which shows the characteristic shapes of CV responses for a catalytic reaction described by equations *2.1–2.3* across different kinetic regimes. It also demonstrates how the change in intrinsic (reaction rates) or operational (scan rate, concentration of catalyst and substrate) parameters causes the system under investigation to pass from one kinetic regime to another.[52,57]

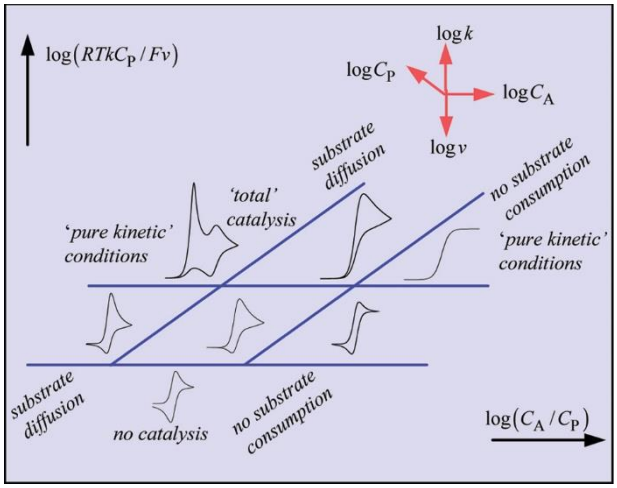

Figure 2.3. Kinetic zone diagram illustrating the characteristic CV response shapes for a catalytic reaction, first-order in both substrate and catalyst, as a function of two dimensionless parameters. Reproduced from [52].

For example, when the catalytic reaction is fast (relative to diffusion), the system is defined by the "pure kinetic conditions" in which, if the catalyst concentration is low, the voltammogram has a characteristic S-shape and the kinetic information can be determined from the steady-state current. Conversely, when increasing the concentration of the catalyst, the CV transitions into the shape characterized by two well-separated waves of which the first one is governed by diffusion of the substrate and its peak potential contains the kinetic information about the catalytic reaction.[52,57]

However, outside of those limiting cases, kinetic analysis of CVs can be complex. Moreover, to quantitatively assess the performance of a catalyst, it is insufficient to consider only the kinetics of the catalytic reaction or the overpotential at which it occurs. Both

parameters must be evaluated together. Therefore, a deeper theoretical analysis is required to benchmark molecular catalysts effectively. In this context, Costentin and Savéant emphasise the significance of expressing a catalyst's intrinsic kinetic properties through catalytic Tafel plots, which correlate turnover frequency (TOF) with the overpotential.[58–60] Notably, TOF is defined as the ratio of the number of product molecules formed per unit time to the maximal number of active catalyst molecules and is directly related to the catalytic reaction rate. Consequently, an efficient catalyst is characterized by a high TOF at a given overpotential, placing its catalytic Tafel plot above and to the left of a less efficient catalyst.[58–60]

Furthermore, extracting accurate kinetic information from CVs is challenging as, besides the solution composition, scan rate and properties of the catalyst, other factors such as ohmic drop, consumption of substrate, catalyst deactivation or inhibition by the product, and direct electrochemical oxidation (reduction) of the substrate profoundly influence the shape of the resulting i-E responce, especially at higher overpotentials. In such cases, it is better to derive the homogeneous kinetics using the low-overpotential portion of the CVs, that is not (or is negligibly) affected by any side phenomena. To do so, Savéant and Costentin have developed a foot-of-the-wave analysis (FOWA) of the CV data, a methodology that is now commonly used to benchmark molecular catalysts of electrochemical reactions.[45,61] FOWA can be expressed by equation *2.4* (where i is the current (in A), i^0_p: anodic peak current of the catalyst in the absence of the substrate (in A), F: the Faraday constant, R: normal gas constant, T: temperature (in K), v: scan rate (in V/s), E: applied potential (in V), and $E°_{P/Q}$: standard potential of the catalyst redox couple (in V)).

$$\frac{i}{i_p^0} = \frac{2.24\sqrt{\frac{RT}{Fv}2k_{fcat}C_A^0}}{1+e^{\left(-\frac{F}{RT}\left(E-E^0_{P/Q}\right)\right)}} \qquad (2.4)$$

Normalising the catalytic current by the catalyst's one-electron peak current, i^0_p, circumvents the requirement for independent determination of the electrode surface area, electron transfer kinetics, and the catalyst's diffusion coefficient. Thus, from equation *2.4*, i/i^0_p is proportional to $1/(1 + \exp[-(F/RT)(E - E^0_{P/Q})])$, within the potential range where the (faradaic) current is independent of the scan rate. Therefore, constructing a plot of i/i^0_p versus

$1/(1 + \exp[-(F/RT)(E - E^0_{P/Q})])$ yields a straight line and the rate constant k_{fcat} can be determined from its slope.

2.1.4 Analysis of the mixed luminophore system - strategy, requirements and aims

Here, we employ $[Ir^{III}(sppy)_3]^{3-}$ as a molecular redox mediator, expecting its electro-oxidized form, $[Ir^{IV}(sppy)_3]^{2-}$, to homogeneously oxidize both the coreactant and $[Ru(bpy)_3]^{+}$. We have shown that the oxidation of $[Ir^{III}(sppy)_3]^{3-}$ at moderate potentials (ca. 0.81 V) effectively enhances the co-reactant ECL of $[Ru(bpy)_3]^{2+}$.[40,42,43] However, a clear contribution of this electrocatalytic path in the mechanism supporting enhanced ECL of $[Ru(bpy)_3]^{2+}$ in the presence of $[Ir^{III}(sppy)_3]^{3-}$ and TPrA remains absent.

Having this in mind, we employ finite element simulations in COMSOL Multiphysics, seeking to investigate the mechanistic and kinetic properties within the mixed luminophore coreactant system involving $[Ru(bpy)_3]^{2+}$, $[Ir^{III}(sppy)_3]^{3-}$ and TPrA and to systematically study the role of Ir(III) electrocatalytic mediator within the total mechanistic scheme. To do so, we construct a numerical simulation model with 1D geometry, using previous knowledge about $[Ru(bpy)_3]^{2+}$/TPrA system and experimentally obtained thermodynamic information on the $[Ir^{III}(sppy)_3]^{3-}$ complex, in which we initially integrate these two electrocatalytic steps and test how they reproduce different electrochemical and ECL experiments. A detailed description of the simulation model is provided in **Section 2.5**.

The constructed numerical model must accurately determine the flux of electroactive species at the electrode surface, which not only allows for the computation of the current but also provides essential numerical data on the electrochemical activation of ECL reactions necessary to compute processes in solution. Additionally, the finite element simulation must precisely resolve the concentration distribution of various species in the solution, particularly the luminophore's excited state, which is critical for assessing the intensity and distribution of the ECL emission. Analysing the accurately simulated concentration profiles of transient species involved in producing the excited state can enhance the overall understanding of the system's reactivity.

In the context of molecular catalysis, we quantify the catalytic (k_{fcat} the forward electron transfer rate of equation *2.5*) homogeneous oxidation rate of TPrA by $[Ir^{III}(sppy)_3]^{3-}$ through Tafel analysis and FOWA of experimental CV plots.

$$[Ir(sppy)_3]^{2-} + TPrA \rightleftarrows [Ir(sppy)_3]^{3-} + TPrA^{\bullet+} \quad (2.5)$$

This assessment serves a dual purpose: i) to determine whether the simulation model can accurately reproduce the subtle electrochemical reactivity that initiates ECL processes, and ii) to evaluate the precision and reliability of the kinetic (and mechanistic) information provided by the numerical simulation model. Moreover, if the information acquired from the numerical simulation are accurate (i.e in agreement with the experiment), the model is potentially useful for predictive mechanistic studies of complex ECL systems employing various redox mediators.

Therefore, our approach relies on i) reproducing the experimentally obtained current vs potential (i-E) and ECL intensity vs potential (I_{ECL}-E) plots, where i is the electrode current, I_{ECL} the ECL intensity and E the electrode potential, to optimise the thermodynamic and kinetic parameters within the simulation model; ii) varying kinetic parameters within the model to explore the properties of this and alternative mixed-luminophore coreactant systems within the reasonably wide parameter space and/or analyse the contribution of specific reaction steps within the total mechanistic scheme and investigate their interplay with the other mechanistic pathways.

2.2 Experimental section

2.2.1 Reagents and apparatus

Reagents and solvents were purchased from commercial suppliers and used without further purification. $[Ir^{III}(sppy)_3]^{3-}$ was purchased from Lumtec as a custom synthesis based on synthetic details previously described.[39,62] Tris(2,2'-bipyridine)ruthenium(II) dichloride hexahydrate ($[Ru(bpy)]_3Cl_2.6H_2O$) was purchased from Strem (USA). Potassium phosphate monobasic and dibasic salt, sodium chloride, TPrA and fac-$Ir(ppy)_3$ were purchased from Sigma-Aldrich Australia.

2.2.2 Electrochemistry and ECL

We used a previously described custom cell design[27] with glassy carbon working electrode, platinum wire counter (CH Instruments) and leakless Ag/AgCl reference (model ET069; eDAQ Australia) to collect all electrochemical and ECL data. The glassy carbon electrode was polished using 1 µm and 0.05 µm alumina polishing powder (CH Instruments) followed by sonication in ethanol prior to each experiment. An Autolab PGSTAT204 or Autolab PGSTAT128N was used for electrochemical measurements and the cell was interfaced with either a photomultiplier tube (PMT, extended-range trialkali S20 PMT, ET Enterprises model 9828B) or charged coupled device (CCD, QEPro, Ocean Optics) for ECL experiments. ECL measurements were conducted in 0.3 M phosphate buffer solution (PBS) with 100 mM TPrA adjusted to pH 6.8 using NaOH or HCl. Cyclic voltammetry was used to generate the ECL emission with a scan rate of 0.1 V/s. Where ECL was captured using a CCD, an integration time of 500 ms was used (i.e. 50 mV interval spectra were obtained). All experiments were collected in triplicate and signals were averaged**.**

2.2.3 Simulation parameters

This numerical simulation model encompasses diffusion-controlled reactions within the solution. The reactive species considered include TPrA (in both its neutral and protonated forms, $TPrAH^+$), its radical cation ($TPrA^{\bullet+}$), the neutral radical ($TPrA^{\bullet}$) and its iminium oxidation product (P), $[Ru(bpy)_3]^{2+}$, and its oxidised and reduced forms ($[Ru(bpy)_3]^{3+}$ and $[Ru(bpy)_3]^{+}$, respectively), as well as $[Ir(sppy)_3]^{3-}$ and its oxidised and reduced states ($[Ir(sppy)_3]^{2-}$ and $[Ir(sppy)_3]^{4-}$, respectively). At the electrode surface, boundary conditions correspond to the oxidation of TPrA (resulting in the generation of $TPrA^{\bullet+}$), the neutral radical $TPrA^{\bullet}$ (resulting in the formation of P), $[Ir(sppy)_3]^{3-}$ (leading to $[Ir(sppy)_3]^{2-}$), and $[Ru(bpy)_3]^{2+}$ (leading to $[Ru(bpy)_3]^{3+}$). Details about the simulation model are provided in **Section 2.5** - Supporting Information.

2.3 Results and Discussion

2.3.1 Methodology

The primary objective of this work is to find the conditions that, when incorporated in the numerical simulation model, replicate the experimental electrochemical and ECL data for: (i) $[Ru(bpy)_3]^{2+}$/TPrA; (ii) $[Ir^{III}(sppy)_3]^{3-}$/TPrA; and (iii) $[Ir^{III}(sppy)_3]^{3-}$/$[Ru(bpy)_3]^{2+}$/TPrA coreactant systems. Subsequent analysis of these conditions can help rationalize different mechanistic pathways involved in the generation of the ECL signal.

ECL presents the advantage of utilizing two experimental descriptors: (i) electrochemical current potential (i-E) curve that provides insights into the kinetics of major reaction steps, and (ii) light emission intensity potential (I_{ECL}-E) curve. Noteworthy, these two descriptors are sensitive to different species or chemical paths (indicated in the SI), which allows a deeper understanding of the whole mechanistic scheme.

In classical ECL experiments where TPrA is used at much higher concentrations than luminophore, the i-E curve is mostly limited by the electrode kinetics of TPrA oxidation. However, the low ECL onset potential in the mixed luminophore coreactant system ($[Ru(bpy)_3]^{2+}$/$[Ir^{III}(sppy)_3]^{3-}$/TPrA) suggests a possible role of $[Ir^{IV}(sppy)_3]^{2-}$ (formed by direct electrooxidation of $[Ir^{III}(sppy)_3]^{3-}$) in the electrocatalytic oxidation of TPrA (equation *2.5*), followed by its regeneration at the electrode surface. This catalytic reaction, with the rate constant k_{fcat}, initiates all homogeneous reactions within the system, effectively altering its reactivity at low anodic overpotentials and as such can be estimated from the electrochemical current. To extract mechanistic information from the current (primarily, to evaluate the efficiency of redox catalysis), we decided to work with lower TPrA concentrations (1 mM, 5 mM and 10 mM) and 1 mM $[Ir^{III}(sppy)_3]^{3-}$. This ensures that both the contributions from direct and mediated TPrA oxidation can be effectively resolved.

However, as the ECL emission of $[Ir^{III}(sppy)_3]^{3-}$ at 515 nm is two orders of magnitude lower than $[Ru(bpy)_3]^{2+}$ (620 nm),[39] a low concentration of $[Ru(bpy)_3]^{2+}$ (500 nM compared to 1 mM $[Ir^{III}(sppy)_3]^{3-}$) needs to be used. In this situation, $[Ru(bpy)_3]^{2+}$ will effectively not contribute to the electrochemistry of the mixed luminophore coreactant system, in which the i-E curve will be equivalent to that of $[Ir^{III}(sppy)_3]^{3-}$/TPrA. Therefore, the mechanistic understanding of the electrochemical (and chemical) steps is obtained by analyzing the TPrA

and $[Ir^{III}(sppy)_3]^{3-}$/TPrA systems (**Figures 2.4** and **2.5**). Conversely, in the mixed luminophore coreactant system, the I_{ECL}-E curve provides insight into the dual $[Ir^{III}(sppy)_3]^{3-}$ and $[Ru(bpy)_3]^{2+}$ ECL emission.

The initial electrochemical characteristics of TPrA and $[Ru(bpy)_3]^{2+}$ are taken from previous simulation works[21,25,63] and changed marginally (for example to account for variations in electrode kinetics and to match simulated and experimental data). The electrochemical characteristics of $[Ir^{III}(sppy)_3]^{3-}$ are estimated directly from the experimental results. However, the model, as proposed, implies the involvement of a range of species and reaction steps. It consists of 10, 9 and 14 species participating in 14, 9 and 24 homogeneous plus interfacial steps in the $[Ru(bpy)_3]^{2+}$/TPrA, $[Ir^{III}(sppy)_3]^{3-}$/TPrA and $[Ir^{III}(sppy)_3]^{3-}$ /$[Ru(bpy)_3]^{2+}$/TPrA coreactant systems, respectively. The model is, therefore, currently under-characterized, requiring knowledge of numerous parameters or rates. The methodology relies on identifying a minimal set of rate-limiting steps, with other steps considered mass-transfer limited. To do so, we focus on reproducing the experimental curves. The impact of these rate-limited steps on the various i or I_{ECL} responses is then systematically explored.

2.3.2 Information extracted from the current

Cyclic voltammetry (CV) has been successfully used to decipher many homogeneous redox catalysis processes where a redox mediator is used to activate in solution the electrochemistry of molecules, such as H^+, O_2, N_2O, and CO_2, to name a few.[44,47–49] In this respect it should be helpful to decipher ECL mechanisms where a redox mediator is used to activate the oxidation of TPrA, as proposed for the $[Ru(bpy)_3]^{2+}$/$[Ir^{III}(sppy)_3]^{3-}$/TPrA system. Although the electrochemistry of each component of this system has been studied individually, this work seeks to understand their behavior as a whole. We anticipate that the electrochemistry of TPrA will predominantly influence this coreactant system. Nevertheless, comparing the electrochemical behavior of TPrA with that of $[Ir^{III}(sppy)_3]^{3-}$/TPrA, at low concentrations of TPrA, can provide valuable insight into subtle changes in the reactivity of the coreactant system, revealing important mechanistic information.

We performed CV experiments in 0.3 M PBS solutions at pH 6.8 containing 10 mM TPrA, and a mixture of 10 mM TPrA and 1 mM $[Ir^{III}(sppy)_3]^{3-}$ (**Figures 2.4A** and **B**, respectively), and subsequently conducted finite element simulations to replicate the experimental results.

The experimental (dashed lines) and the simulated plots (solid lines) are in overall agreement, indicating the numerical simulation model can accurately reproduce the experimental data. Minor discrepancies at high potentials can be attributed to convection and/or water oxidation, the effects of which we did not include in the numerical simulation.

Based on the general good agreement, only the simulated i-E plots, shown in **Figure 2.4C**, of 10 mM TPrA in the presence (in green) and absence (in blue) of 1 mM $[Ir^{III}(sppy)_3]^{3-}$ are discussed**.** Both CVs have a single irreversible peak corresponding to the oxidation of TPrA, reaching a maximum at approximately 0.95 V. However, in the solution containing $[Ir^{III}(sppy)_3]^{3-}$, the onset of oxidation occurs at a lower overpotential and the CV manifests a shoulder in the current at around 0.80 V vs Ag/AgCl. This potential corresponds to the E^0 of the $[Ir^{III}(sppy)_3]^{3-}/[Ir^{IV}(sppy)_3]^{2-}$ redox couple (0.81 V vs Ag/AgCl), determined from experimental and simulated CV plots of 1 mM $[Ir^{III}(sppy)_3]^{3-}$ in the absence of TPrA (**Figure 2.5A**). This points to the involvement of the homogeneous catalysis, or activation, of TPrA oxidation (reaction *2.5*) by $[Ir^{IV}(sppy)_3]^{2-}$, the oxidized form of the molecular catalyst $[Ir^{III}(sppy)_3]^{3-}$, electrogenerated at the electrode.

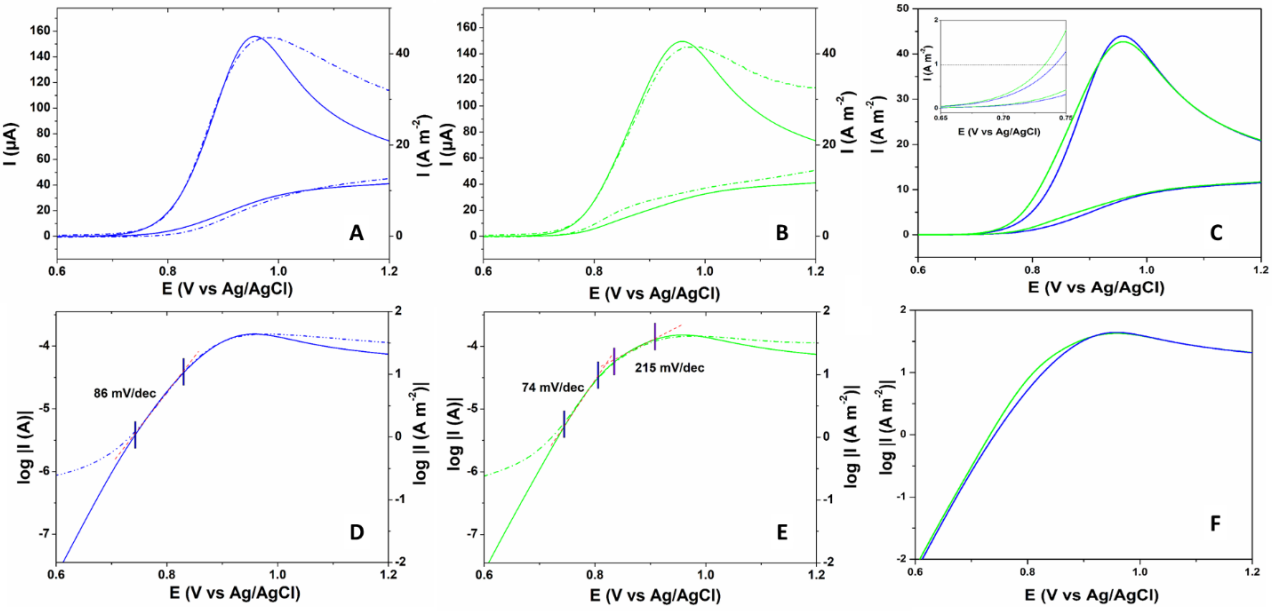

Figure 2.4. Simulated (solid lines) and experimentally obtained (dashed lines) for **(A-C)** CVs and **(D-F)** Tafel plots in 10 mM TPrA solution (blue) and 1 mM $[Ir(sppy)_3]^{3-}$ and 10 mM TPrA solution (green). No baseline subtraction was performed.

Notably, in such homogeneous molecular catalysis framework,[21,44,45,47,48,61,63] here employed to catalyze TPrA oxidation, the redox mediator could have a lower standard potential than the TPrA, making the reaction (*2.5*) disfavored or equilibrated and shifted towards reactants reform. However, the deprotonation of the TPrA radical cation following this homogeneous electron transfer step shifts the reaction (*2.5*) to the right and makes it easier at the potential of the redox mediator oxidation. This is detected as an increase in current for the redox mediator oxidation. In fact, the more the homogeneous step is favored (or the faster the deprotonation), the higher the increase in the redox mediator current.

As shown in **Figure 2.4C**, the difference between the CV responses in the presence and absence of molecular catalysts lies in subtle variations in the foot of the electrochemical waves. To understand the mechanisms at play in this system, it is then important to be able to describe these subtle variations precisely to deduce the contribution of the catalytic reaction. We first used Tafel plots of the CVs constructed by plotting the logarithm of current against the electrode potential. Mechanistic insights are reached from the Tafel plots of the simulated curves of the $[Ir^{III}(sppy)_3]^{3-}$/TPrA system and the TPrA oxidations, shown in **Figure 2.4F**. The shoulder detected in **Figure 2.4C** within the foot of the TPrA oxidation wave is also visible in **Figure 2.4F**: the $[Ir^{III}(sppy)_3]^{3-}$/TPrA system (green line) is characterized by a lower Tafel slope than that of TPrA (blue line). In this potential region, the oxidation of $[Ir^{IV}(sppy)_3]^{2-}$ is probed, which shows faster electrode kinetics than that of TPrA oxidation. At higher overpotentials, a larger Tafel slope is detected as expected for the overlap of both $[Ir^{IV}(sppy)_3]^{2-}$ and TPrA oxidations and mass transfer control. We therefore analyzed the experimental CV curves through such Tafel plots (**Figures 2.4D** and **2.4E**). While the Tafel slope of TPrA exhibits a value of 86 mV/dec, the Tafel plot of $[Ir^{III}(sppy)_3]^{3-}$/TPrA exhibits a lower slope of 74 mV/dec, confirming that the $[Ir^{III}(sppy)_3]^{3-}$ oxidation occurs before the TPrA oxidation.

Beyond the CV simulation, we utilized foot of the wave analysis (FOWA) to quantify the catalytic role of $[Ir^{III}(sppy)_3]^{3-}$ and obtain k_{fcat}, the apparent rate constant of the homogeneous redox catalysis reaction (equation *2.5*). The FOWA analysis was performed on the experimental i-E plots for TPrA concentrations of 1, 5 and 10 mM, yielding three different lines (**Figure 2.5B**). The slopes of the FOWA lines (2.7, 6.0 and 8.5, respectively) were proportional to the square root of the TPrA concentration, as expected from equation *2.4*,

yielding a value of k_{fcat} of $2.8 \times 10^3 \pm 0.05 \times 10^3$ $M^{-1}s^{-1}$. This value is then used as an initial guess to simulate the experimental CVs. The value of k_{fcat} for which the best overlap between the simulated and experimental i-E curves is obtained is 3×10^3 $M^{-1}s^{-1}$, demonstrating the high accuracy of the numerical simulation model and its ability to not only reproduce the experimental data but to give insights into (electro)chemical kinetics within the investigated system.

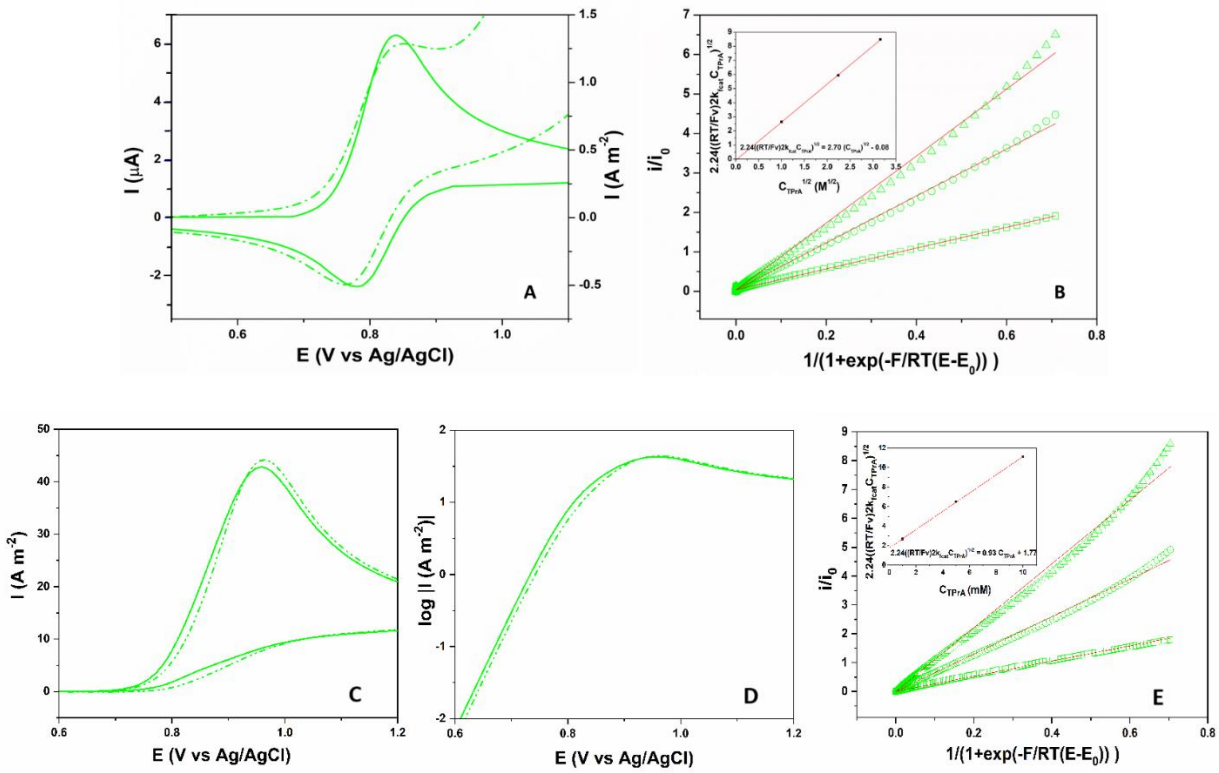

Figure 2.5. **(A)** Simulated (solid line) and experimentally obtained (dashed line) CVs in 1 mM $[Ir(sppy)_3]^{3-}$ solution. **(B)** FOWA analysis of the baseline corrected experimental CVs in 1 mM $[Ir(sppy)_3]^{3-}$ and 1, 5 and 10 mM TPrA solutions, **inset (B)** slope of the FOWA lines against the square root of the TPrA concentration. **(C)** CVs and **(D)** Tafel plots of the simulated data in 1 mM $[Ir(sppy)_3]^{3-}$ and 10 mM TPrA solution, with the redox catalysis incorporated in the model with the rate constant of k_{fcat} = 0 $M^{-1}s^{-1}$ (dashed line) and k_{fcat} = 3000 $M^{-1}s^{-1}$ (solid line). **(E)** FOWA analysis of the simulated CVs in 1 mM $[Ir(sppy)_3]^{3-}$ and 1, 5 and 10 mM TPrA solutions when k_{fcat} = 0 $M^{-1}s^{-1}$, **inset (E):** slope of the FOWA lines against the square root of the TPrA concentration.

Finally, we tested the relevance of the homogenous catalysis reaction relative to the direct oxidation of TPrA by analyzing the simulated plots of the $[Ir^{III}(sppy)_3]^{3-}$/TPrA in the

presence and absence of redox catalysis (k_{fcat} = to 3 $\times$ 10^3 $M^{-1}s^{-1}$ and k_{fcat} = 0 $M^{-1}s^{-1}$, respectively). Owing to the relatively low value of the catalytic reaction rate, one could wonder about its influence on the i-E curves, for example, compared to the direct oxidation of TPrA. We then analyzed the simulated plots of the $[Ir(sppy)_3]^{3-}$/TPrA system under two scenarios: one without redox catalysis (where the k_{fcat} rate constant incorporated in the model is set to 0 $M^{-1}s^{-1}$) and another with k_{fcat} set to 3 10^3 $M^{-1}s^{-1}$ (**Figure 2.5C**). In the absence of redox catalysis, the simulated CV does not present the shoulder at low overpotentials and closely resembles the CV of the TPrA system. This observation is further evident in Tafel plots derived from the simulated CVs (**Figure 2.5D**). The shoulder then highlights the feedback current associated with redox catalytic oxidation of TPrA by the electrooxidized $[Ir(sppy)_3]^{2-}$.

The FOWA further confirms the relevance of this redox catalysis contribution. The simulated i-E curves for 1, 5 and 10 mM TPrA with k_{fcat} = 0 were analyzed within the FOWA formalism (see **section 2.5**). A straight line was also obtained in those cases. This is explained by the close proximity of the direct oxidation of TPrA to that of $[Ir(sppy)_3]^{3-}$. Indeed, at low overpotential, the rising part of the i-E curve for the oxidation of any species would follow a sigmoidal function of the electrode potential (comparable to equation *2.4*). However as observed from the FOWA for k_{fcat} = 0 (see **Figure 2.5E**), the slope of the i/i_p° versus $1/(1 + \exp(-(F/RT)(E - E^0_{Ir}))$ is expected to be proportional to the TPrA concentration or the direct oxidation of TPrA (while it should be proportional to the square-root of TPrA concentration for a redox catalysis scheme, see equation *2.4*). Thus, the primary contribution of $[Ir^{III}(sppy)_3]^{3-}$ to the electrochemical current, at low potentials, arises from the homogeneous catalysis of TPrA.

On a more general note, considering the complexity of the chemical and electrochemical processes involved, various combinations of thermodynamic and kinetic parameters could lead to a satisfactory alignment between the simulated and experimental results. Specifically, factors such as the rate of $TPrAH^+$ deprotonation, oxidation potentials of TPrA and $[Ir^{III}(sppy)_3]^{3-}$ and the rate constants of the corresponding electron transfer steps, deprotonation of $TPrA^{\bullet+}$, rates of homogeneous catalysis and the reaction between the oxidized $[Ir^{IV}(sppy)_3]^{2-}$ and $TPrA^\bullet$, which populates the $[Ir^{III}(sppy)_3]^{3-*}$ excited state can all have a profound influence on the shape of the i-E curves in the mixed luminophore coreactant system. However, previous experimental[46,54] and numerical simulation[21,25,63] studies have

contributed to determining some of these parameters, reducing uncertainty in our model predictions of the current.

2.3.3 ECL of $[Ru(bpy)_3]^{2+}$/TPrA coreactant system

ECL is inherently bound to the homogeneous reactivity of the most reactive transient species, namely the $TPrA^{\bullet}$ radical (as seen in **Figure 2.2**). The ECL light emission then provides a complementary sensitive output that can help decipher further the activity of such transient species in the vicinity of the electrode surface. To gain mechanistic insights, we captured ECL spectra in the range from 350 nm to 1150 nm over a CV scan from 0.1 V to 1.5 V. This approach allowed us to analyze the evolution of ECL intensity with electrochemical potential, while distinguishing the contributions of $[Ir^{III}(sppy)_3]^{3-}$ and $[Ru(bpy)_3]^{2+}$ to the total light emission based on their distinct emission wavelengths (515 nm and 620 nm, respectively).

Figure 2.6A shows the simulated (solid line) and experimental (dashed line) ECL intensity-potential plots at 620 nm, namely $I_{ECL,Ru}$-E, for the 500 nM $[Ru(bpy)_3]^{2+}$ and 10 mM TPrA solution in 0.3 M PBS pH 6.8. To simulate the $I_{ECL,Ru}$-E plot, we integrated all photons that correspond to the emission of $[Ru(bpy)_3]^{2+}$ over the whole volume of solution (at all distances from the electrode surface) and plotted the integrated values against the electrochemical potential. The simulated $I_{ECL,Ru}$ increases with potential in a sigmoidal fashion, with the half wave potential at around 1.08 V vs Ag/AgCl (0.22 V higher than the half wave potential of TPrA oxidation, see **Figure 2.4**) and reaching the maximum at approximately 1.2 V. The ECL emission at low anodic overpotentials is a result of the heterogeneous ("remote") pathway (**Figure 2.2A**). However, at potentials above the E^0 of the $[Ru(bpy)_3]^{2+}/[Ru(bpy)_3]^{3+}$ redox couple (1.04 V vs Ag/AgCl), the mechanistic route including direct oxidation of $[Ru(bpy)_3]^{2+}$ prevails, controlling the steady-state emission. To demonstrate this contribution, we plotted the evolution of the concentrations of TPrA, $[Ru(bpy)_3]^{2+}$, and $[Ru(bpy)_3]^{3+}$ species at the electrode surface with potential (**Figure 2.6B**). All three concentration-potential profiles are sigmoidal, with half-wave potentials of 0.91 V, 1.10 V and 1.10 V, respectively. The half-wave potential of the $I_{ECL,Ru}$-E plot is 1.08 V, indicating the reliance of ECL emission on the generation of $[Ru(bpy)_3]^{3+}$ species at the electrode surface.

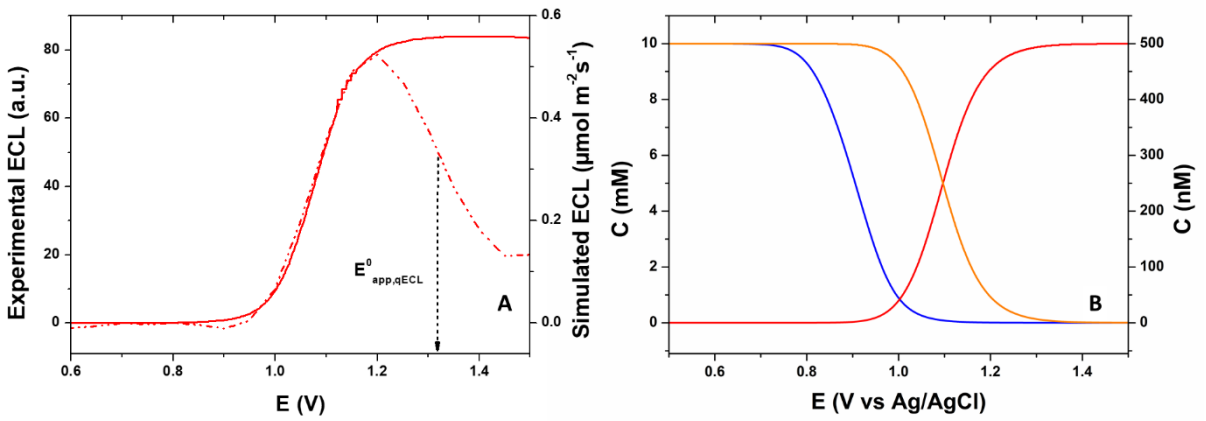

Figure 2.6. **(A)** Simulated (solid line) and experimental (dashed line) ECL intensity at 620 nm in 500 nM $[Ru(bpy)_3]^{2+}$ and 10 mM TPrA solution. **(B)** Evolution of the concentration of TPrA (in blue), $[Ru(bpy)_3]^{2+}$ (in orange) and $[Ru(bpy)_3]^{3+}$ (in red) at the electrode surface with the electrochemical potential (simulated plots).

The described simulated plot (solid line) in **Figure 2.6A** is in agreement with the experimental one (dashed line) within the activation regime (in which $I_{ECL,Ru}$ increases with the potential). However, while the simulation predicts a steady state behavior, the experimental plot exhibits a distinct peak at 1.2 V and ECL depletion at higher potentials. The sigmoidal shape of this ECL signal loss with the electrode potential suggests a potential-induced quenching of the ECL (with the formal potential $E^0_{app,qECL}$ = 2.12 V vs Ag/AgCl). This can be attributed to the electrode surface oxidation influencing electron transfer rates and affecting the $TPrA^{+\bullet}$ deprotonation constant, causing depletion of the TPrA radicals.[64–66] As previously discussed, the oxidation of TPrA involves a proton-coupled electron transfer, initially yielding a radical cation intermediate that rapidly deprotonates forming a neutral radical (equations *2.6 – 2.8*).

$$TPrAH^+ \rightleftarrows TPrA + H^+ \qquad (2.6)$$

$$TPrA \rightarrow e^- + TPrA^{\bullet+} \qquad (2.7)$$

$$TPrA^{\bullet+} \rightleftarrows TPrA^{\bullet} + H^+ \qquad (2.8)$$

The concentration ratio of these radical species determines the dominant ECL pathway, shaping the resulting emission. However, anodically polarized GCE can undergo

surface oxidation, and the formed oxygen-containing functional groups can serve as proton acceptors, facilitating the deprotonation of $TPrA^{\bullet+}$. Consequently, $TPrA^{\bullet}$ radicals form closer to the electrode surface, where they are scavenged before participating in the ECL reactions. Therefore, a decreased lifetime of $TPrA^{\bullet+}$ diminishes the concentration of both TPrA radicals, decreasing the efficiency of the coreactant ECL pathways and leading to ECL quenching. Other possible reasons are the formation of undesired oxidation products, and ECL quenching by electrogenerated species. Given the complexity of these processes, we did not consider them in the numerical simulation and will not further discuss them.

2.3.4 ECL of $[Ir^{III}(sppy)_3]^{3-}$/TPrA coreactant system

The unique redox properties of $[Ir^{III}(sppy)_3]^{3-}$, distinct from those of $[Ru(bpy)_3]^{2+}$, play a pivotal role in the ECL behavior of this coreactant system. Specifically, oxidation potential of $[Ir^{III}(sppy)_3]^{3-}$ ($E^0_{Ir(IV),Ir(III)}$ = 0.81 V) is slightly lower than that of TPrA (E^0_{TPrA} = 0.96 V), enabling its direct electrooxidation followed by the homogenous electron transfer producing TPrA radicals (catalytic route, **Figure 2.2D**). As demonstrated in previous sections, this reaction facilitates all (electro)chemical steps at low anodic potentials, leading to a low ECL onset potential. Moreover, the low reduction potential of this redox mediator (ca. -2.0 V) prevents its reduction by $TPrA^{\bullet}$, limiting $[Ir^{III}(sppy)_3]^{3-}$ ECL generation to only one possible route (**Figure 2.2B**). Therefore, before exploring ECL in the mixed luminophore system, it is imperative to construct a model that accurately replicates the properties of the $[Ir^{III}(sppy)_3]^{3-}$/TPrA coreactant system.

We recorded ECL spectra of the solutions containing 1 mM $[Ir^{III}(sppy)_3]^{3-}$ with 1 mM, 5 mM and 10 mM TPrA in 0.1 M PBS pH 7.4. **Figures 2.7 A** and **B** present the experimental ECL intensity potential, $I_{ECL,Ir}$-E, plots constructed from the spectroscopic ECL evolution recorded at 515 nm.

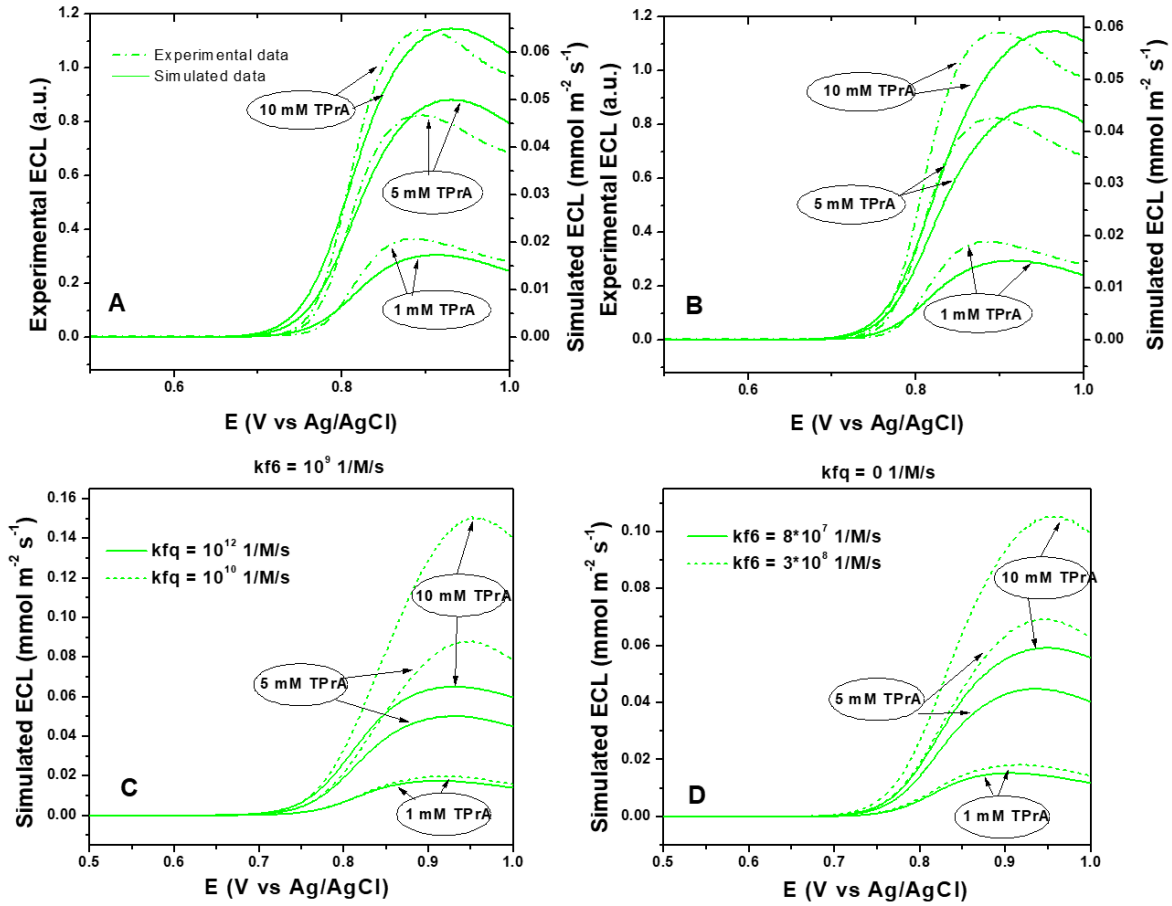

Figure 2.7. Simulated ECL intensities (solid lines) and experimental ECL intensities (dashed lines) at 515 nm for 1 mM $[Ir^{III}(sppy)_3]^{3-}$ and 1 mM, 5 mM, and 10 mM TPrA solutions. Simulated plots are estimated from the model that **(A)** included the oxidative quenching reaction *5.1*, with a rate of $k_{fq} = 10^{12}$ $M^{-1}s^{-1}$ and a rate constant of $[Ir^{III}(sppy)_3]^{3-*}$ excited state production, reaction *5.2*, $k_{f6} = 10^9$ $M^{-1}s^{-1}$ and **(B)** did not include the oxidative quenching and $k_{f6} = 8 \times 10^7$ $M^{-1}s^{-1}$. Simulated ECL intensities **(C)** at constant k_{f6} rate (10^9 $M^{-1}s^{-1}$) and with quenching reaction rate 10^{12} $M^{-1}s^{-1}$ (solid lines) and 10^{10} $M^{-1}s^{-1}$ (dotted lines); and **(D)** without oxidative quenching ($k_{fq} = 0$ $M^{-1}s^{-1}$) at the k_{f6} rate of 8×10^7 $M^{-1}s^{-1}$ (solid lines) and 3×10^8 $M^{-1}s^{-1}$ (dotted lines) at 515 nm in 1 mM $[Ir(sppy)_3]^{3-}$ and 1 mM, 5 mM, and 10 mM TPrA solution.

Subsequently, we employed numerical simulations, starting from the homogeneous catalysis scheme devised above (**Figure 2.2D**), to reproduce the experimental results, **Figures 2.7 A** and **B** (solid lines). It shows that the simulated data follow the general trend observed in the experimental results. Although the CV responses match well (**Figure 2.4B**), the alignment is lower for the ECL responses (**Figures 2.7 A** and **B**) (less than what was seen in the

case of the $[Ru(bpy)_3]^{2+}$ ECL in **Figure 2.6A**). Notably, the experimental ECL onset occurs at low anodic potential values, with a half wave potential at 0.81 V vs Ag/AgCl (which corresponds to the E^0 of the $[Ir^{III}(sppy)_3]^{3-}/[Ir^{IV}(sppy)_3]^{2-}$ redox couple) for all three $[Ir^{III}(sppy)_3]^{3-}$: TPrA concentration ratios, indicating that excited state production requires the oxidation of $[Ir^{III}(sppy)_3]^{3-}$ at the electrode. If the oxidation-reduction route (**Figure 2.2B**) can be postulated, the $TPrA^{\bullet}$ (necessary to populate the excited state) needs to be generated efficiently at low anodic overpotentials compared to the direct heterogeneous oxidation of TPrA, providing further evidence for TPrA oxidation via the homogeneous catalytic mechanism (**Figure 2.2D**).

However, while the ECL intensity, $I_{ECL,Ir}$, increases with the increase in TPrA concentration, this relationship is not linear, suggesting that one of the species involved in the electrochemical oxidation of TPrA is quenching the $[Ir^{III}(sppy)_3]^{3-}$ ECL. As a first possible explanation, it might be due to oxidative quenching of $[Ir^{III}(sppy)_3]^{3-*}$ excited state by $TPrA^{\bullet+}$ (reaction *2.9*), as previously reported for the related $Ir^{III}(ppy)_3$ complex.[67]

$$[Ir(sppy)_3]^{3-*} + TPrA^{\bullet+} \xrightarrow{k_{fq}} [Ir(sppy)_3]^{2-} + TPrA \qquad (2.9)$$

Indeed, taking into account such reaction into the model can reproduce the general experimental trends (simulated data in **Figure 2.7A**). However, to be operative, the rate constant for this reaction needs to be set at $k_{fq} = 10^{12}$ $M^{-1}s^{-1}$, a rate exceeding the bimolecular diffusion limit. As a reference, the simulated plots in **Figure 2.7C** illustrate the difference in ECL under the abovementioned conditions with quenching reaction rate constants of 10^{12} $M^{-1}s^{-1}$ (solid lines) and diffusion-limited value of 10^{10} $M^{-1}s^{-1}$ (dotted lines).

The practically unattainable rate of the oxidative quenching reaction that was necessary to replicate the experimental results indicates it is not the only process that affects the intensity of ECL emission at 515 nm. One possible explanation is that the reaction producing the excited state of $[Ir^{III}(sppy)_3]^{3-*}$ (reaction *2.10*, rate constant k_{f6}), initiated by the oxidation of the $TPrA^{\bullet}$ radical, is rate-limiting rather than diffusion-limited.

$$[Ir(sppy)_3]^{2-} + TPrA^{\bullet} \xrightarrow{k_{f6}} [Ir(sppy)_3]^{3-*} + P \qquad (2.10)$$

This limitation may be due to the comparable values of the TPrA$^{\bullet}$ oxidation potential (*ca*. -1.7 V) to that of the $[Ir^{IV}(sppy)_3]^{2-}/[Ir^{III}(sppy)_3]^{3-*}$ couple: $E^0_{IV/III*} = E^0_{IV/III} - E_{em,Ir} = 0.8 – 2.4 =$ -1.6 V (where $E_{em,Ir}$ is the energy associated to photon emission at 515 nm). If this is true, other reactions, especially redox catalysis, could deplete $[Ir^{IV}(sppy)_3]^{2-}$ species, further decelerating the rate of $[Ir^{III}(sppy)_3]^{3-*}$ excited state formation and limiting the maximum ECL output, affecting the efficiency of this ECL coreactant system. This kinetic control of ECL emission becomes more evident at higher concentrations of TPrA, where the rate of homogeneous catalysis increases, leading to behaviour resembling quenching.

The role of such reaction on $I_{ECL,Ir}$ was also tested through simulation. $I_{ECL,Ir}$-E plots in **Figure 2.7B** were simulated without taking the oxidative quenching into account (reaction *2.9*; $k_{fq} = 0\ M^{-1}s^{-1}$), and considering kinetically-limited reaction *2.10* in the numerical simulation model. The best fit obtained in **Figure 2.7B** is reached for the reaction rate constant of $k_{f6} = 8 \times 10^7\ M^{-1}s^{-1}$. The intensities of as obtained $I_{ECL,Ir}$-E plots (in solid lines) are in agreement with the experimentally obtained maximal ECL intensities (dotted lines), supporting the role of kinetic control over the ECL emission. Noteworthy, as shown in **Figure 2.7D,** for higher k_{f6} values, the $I_{ECL,Ir}$ yields poorer fit as it becomes proportional to the TPrA concentration.

Figure 2.7 demonstrates the borderline cases where the non-linear correlation between the ECL intensity response and TPrA concentration is explained either by oxidative quenching of $[Ir^{III}(sppy)_3]^{3-*}$ excited state by TPrA$^{\bullet+}$ or by the kinetically slow generation of the excited state. In reality, both effects may contribute to this suboptimal ECL output of $[Ir^{III}(sppy)_3]^{3-}$/TPrA coreactant system. More generally, **Figure 2.7** illustrates how this suboptimal ECL output is bound to electron transfer steps between the $[Ir^{IV}(sppy)_3]^{2-}/[Ir^{III}(sppy)_3]^{3-*}$ redox couple with TPrA-related species. Different combinations of the abovementioned reaction rates could provide simulated plots that resemble the experimental ones, and there is no way to estimate the absolute values of all the rate constants without further experimental proof. Nevertheless, the numerical simulation model provides the means to study the mutual dependence of reaction steps, giving insight into their contribution to the electrochemical and ECL behavior of this coreactant system.

Lastly, **Figures 2.7 A** and **B** show a mismatch between the evolution of simulated and experimental ECL intensity with potential. The shift in ECL peak to higher potential values is evident in both figures. This discrepancy is more pronounced in **Figure 2.7B**, where the half-

wave potential for the simulated curves equals 0.83 V. Conversely, the half-wave potential in **Figure 2.7A** matches the experimental one (of 0.81 V), but the ECL onset is shifted to lower overpotentials. This observation suggests that the rate of $[Ir^{III}(sppy)_3]^{3-*}$ excited state generation will influence not only the intensity but also the onset potential of ECL emission. This effect is indirect and involves the interplay of reaction *2.10* with other chemical and electrochemical steps, which will be discussed in the following sections.

2.3.5 Simulating ECL to study reactivity in the mixed $[Ir^{III}(sppy)_3]^{3-}$/$[Ru(bpy)_3]^{2+}$/TPrA system

While systematic study of $[Ru(bpy)_3]^{2+}$/TPrA and $[Ir^{III}(sppy)_3]^{3-}$/TPrA provided insight into the mechanistic schemes of both coreactant ECL systems, to comprehend the reactivity of the $[Ir^{III}(sppy)_3]^{3-}$/$[Ru(bpy)_3]^{2+}$/TPrA system in its entirety, we recognize the need to consider it holistically. Despite its inherent complexity, involving numerous reaction species and steps, constructing a numerical simulation model that encompasses the complete reactivity of the mixed luminophore/coreactant system is feasible. This arises from the possibility of defining the model (or rather reducing the number of unknown variables) by incorporating information obtained during the preliminary analysis of the $[Ru(bpy)_3]^{2+}$/TPrA and $[Ir^{III}(sppy)_3]^{3-}$/TPrA systems, and further refining it by comparing the simulated data with the experimental ECL plots. This strategy allows for discerning the rate-limiting reactions in the system. By discussing the influence of the rates of these reactions on the simulated i-E and I_{ECL}-E plots, we can gain insight that serves both a predictive purpose, if one is able to synthesize other co-redox mediators, and an exploratory one, revealing the intricate interplay between different mechanistic steps.

Figure 2.8A shows simulated CV plots of the mixed luminophore coreactant system upon systematically increasing the rate of $[Ir^{III}(sppy)_3]^{3-*}$ excited state generation. Interestingly, this rate also affects the electrochemical curve, and an increase in k_{f6} leads to a decrease in the peak potentials, seemingly leading to the increase in the rate of electrochemical oxidation of TPrA. This effect can be rationalized by the influence of the rate of reaction *2.10* on the deprotonation of $TPrA^{\bullet+}$ (reaction *2.8,* rate constant $k_{f0} = 10^4\ s^{-1}$). The higher the rate k_{f6}, the faster the consumption of $TPrA^{\bullet}$ (reaction *2.10*), which shifts the equilibrium of $TPrA^{\bullet+}$ deprotonation (equation *2.8*) to the right. This, in turn, accelerates the

rate of TPrA oxidation (equation *2.7*), either from the electrode (direct oxidation) or from the redox catalysis routes, affecting the current response.

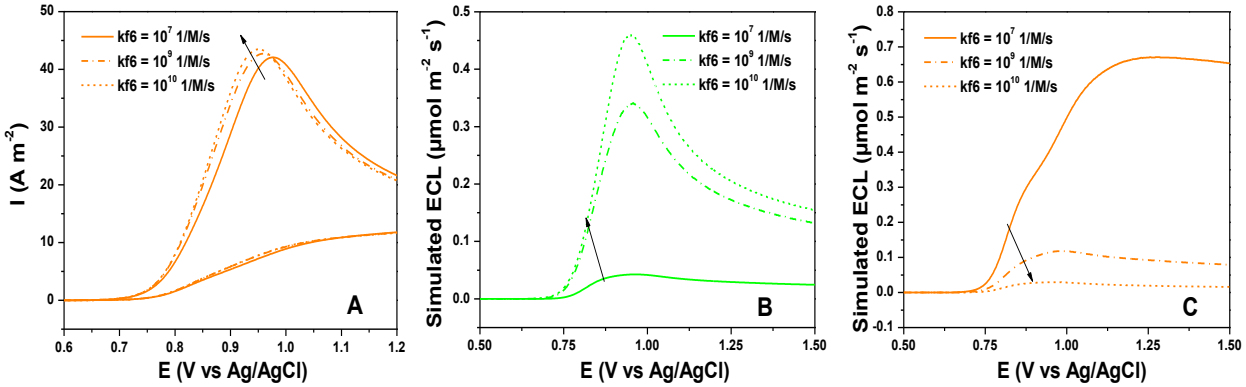

Figure 2.8. Simulated: **(A)** Current; **(B)** ECL intensities at 515 nm; and **(C)** ECL intensities at 620 nm in 500 nm $[Ru(bpy)_3]^{2+}$, 1 mM $[Ir(sppy)_3]^{3-}$ and 10 mM TPrA at different rates of k_{f6}: 10^7 1/M/s (dashed lines), 10^9 1/M/s (solid lines), and 10^{10} 1/M/s (dotted lines).

This rate has even stronger effect on the ECL generation than on the electrode current. **Figure 2.8B** shows the ECL intensity at 515 nm (attributed to $[Ir^{III}(sppy)_3]^{3-}$) increasing with a higher rate constant of $[Ir^{III}(sppy)_3]^{3-*}$ generation. Additionally, the ECL onset potential shifts to lower values with the increase in the k_{f6}, indicating that apart from directly increasing the rate of $[Ir^{III}(sppy)_3]^{3-*}$ formation, an increase in k_{f6} accelerates the formation $TPrA^{\bullet}$ (through reactions *2.7* and *2.8* under the direct and the redox catalytic routes) that is necessary to populate the luminophore's excited state, consequently triggering the ECL emission at low anodic overpotentials.

In contrast, the ECL intensity at 620 nm ($[Ru(bpy)_3]^{2+}$ emission) decreases with the increase in the rate of reaction *2.10* and $I_{ECL,Ru}$ onset shifts to higher potentials (**Figure 2.8C**). The reason for this can be the depletion of the pool of TPrA radicals at high rates of k_{f6}. Since both $TPrA^{\bullet+}$ and $TPrA^{\bullet}$ are necessary for populating the $[Ru(bpy)_3]^{2+*}$ excited state (equations *2.11 – 2.13*), the ECL emission of $[Ru(bpy)_3]^{2+}$ is controlled by the rate of their consumption in reactions *2.10* and *2.8*.

$$[Ru(bpy)_3]^{2+} + TPrA^{\bullet} \rightarrow [Ru(bpy)_3]^{+} + P \qquad (2.11)$$

$$[Ru(bpy)_3]^{+} + TPrA^{\bullet+} \rightarrow [Ru(bpy)_3]^{2+*} + TPrA \qquad (2.12)$$

$$[Ru(bpy)_3]^{3+} + TPrA^{\bullet} \rightarrow [Ru(bpy)_3]^{2+*} + P \quad (2.13)$$

This demonstrates how, although reaction *2.10* initially appears to affect only the intensity of $[Ir^{III}(sppy)_3]^{3-}$ ECL emission, its interplay with other reactions profoundly shapes the reactivity of the entire mixed luminophore coreactant system.

However, this was only explored here in the situation where the homogeneous reduction of $[Ir^{III}(sppy)_3]^{3-}$ by $TPrA^{\bullet}$ (reaction *2.14*) was neglected, due to its thermodynamic unfavourability, since the redox potential of the $TPrA^{\bullet}$/P redox couple (-1.6 V vs Ag/AgCl) is more positive than that of $[Ir^{II}(sppy)_3]^{4-}$/$[Ir^{III}(sppy)_3]^{3-}$ (-2.0 V vs Ag/AgCl), making this reduction reaction unlikely. Noteworthy the reduced form of the $[Ir^{III}(sppy)_3]^{3-}$ is denoted $[Ir^{II}(sppy)_3]^{4-}$ even though formally the electron is borne by the ligand rather than the metal center.

$$[Ir(sppy)_3]^{3-} + TPrA^{\bullet} \rightarrow [Ir(sppy)_3]^{4-} + P \quad (2.14)$$
$$[Ir(sppy)_3]^{4-} + TPrA^{\bullet+} \rightarrow [Ir(sppy)_3]^{3-*} + TPrA \quad (2.15)$$
$$[Ir(sppy)_3]^{4-} + [Ir(sppy)_3]^{2-} \rightarrow [Ir(sppy)_3]^{3-*} + [Ir(sppy)_3]^{3-} \quad (2.16)$$

Nevertheless, its impact on this coreactant system should not be completely disregarded as it can serve for predictive purposes, for example when iridium complexes with different ligand structures are employed.[5,42,68–70] A newly introduced set of reactions is then taken into account. Simulations incorporating these reactions provide insights into the anticipated I_{ECL}-E behaviors. Reaction *2.14* would not only deplete $TPrA^{\bullet}$, thus lowering the rate of reaction *2.10*, but it would also open alternative routes for populating $[Ir^{III}(sppy)_3]^{3-*}$ excited state (equations *2.15* and *2.16*). Overall, this set of reactions decreases the influence of k_{f6} rate constant on the ECL of the Ir species, $I_{ECL,Ir}$.

It further affects the overall ECL in the mixed luminophore coreactant system, and therefore the emission of photons from the Ru species, $I_{ECL,Ru}$. If reaction *2.14* proceeds at high rates, it depletes the pool of $TPrA^{\bullet}$ and localizes them near the electrode surface (**Figure 2.9A**), consequently confining the emission layer of $[Ru(bpy)_3]^{2+}$ ECL (**Figure 2.9B**). Furthermore, with an increase in the rate of reaction *2.14*, the intensity of $[Ru(bpy)_3]^{2+}$ emission decreases and the ECL onset shifts to higher potentials (**Figure 2.9C**). This behavior once again demonstrates the control of $[Ru(bpy)_3]^{2+}$ ECL emission by the concentration of $TPrA^{\bullet}$ (equations *2.11*, *2.12*

and *2.13*). The role of the Ir redox catalyst allows fine-tuning of the potential and spatial distribution of the reactive intermediates TPrA$^{\bullet}$ and TPrA$^{+\bullet}$ and consequently the ECL emissions.

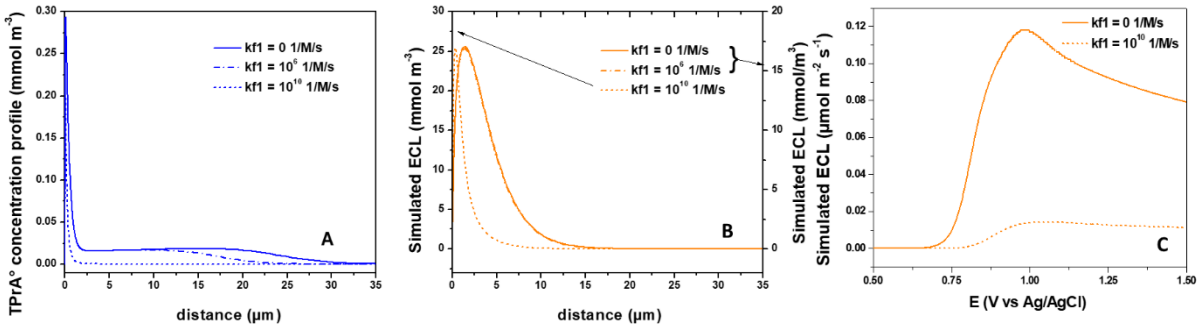

Figure 2.9. Simulated: **(A)** concentration profiles of TPrA radical; **(B)** thickness of the ECL generated photon concentration profiles (at 620 nm) layer in 500 nM $[Ru(bpy)_3]^{2+}$, 1 mM $[Ir(sppy)_3]^{3-}$ and 10 mM TPrA at different rates of homogenous reduction of $[Ir(sppy)_3]^{3-}$ (reaction 7.1), with rate constant k_{f1} = 0 (solid line), 10^6 (dashed line, and 10^{10} $M^{-1}s^{-1}$ (dotted line). **(C)** Simulated ECL intensities at 620 nm, $I_{ECL,Ru}$ in 500 nM $[Ru(bpy)_3]^{2+}$, 1 mM $[Ir(sppy)_3]^{3-}$ and 10 mM TPrA when homogenous reduction of $[Ir(sppy)_3]^{3-}$ (reaction *2.14*) is not included (solid line), and is diffusion-controlled, k_{f1} = 10^{10} $M^{-1}s^{-1}$ (dotted line).

The simulation results indicate that in reaction *2.14*, TPrA$^{\bullet}$ is consumed, affecting the ECL signal by artificially shortening this radical's lifetime. Despite TPrA serving as a sacrificial coreactant in various ECL systems, the lifetime of its neutral radical is unknown. Thus, the numerical simulation treats TPrA$^{\bullet}$ as a long-lived species, propagating here up to 30 µm (**Figure 2.9A**), potentially introducing inaccuracies in the predicted ECL behavior of the system. Given that this highly reactive radical plays a pivotal role in governing ECL reactions and its spatial expansion, it becomes crucial to experimentally determine its stability. For example, based on the predicted spatial light emission profile in **Figure 2.9B**, analyzing the spatial distribution of ECL emission layer, as proposed by Su and co-workers',[18,20] in such a mixed system could help quantify the TPrA$^{\bullet}$ stability. This knowledge not only advances our comprehension of the mixed luminophore ECL system but also contributes to a broader understanding of all coreactant systems involving TPrA or other tri-substituted amines.

While the reaction steps discussed so far provide valuable information on the mutual influence of interconnected mechanistic routes and the way their interplay shapes the ECL of

the investigated coreactant system, we cannot obtain unambiguous information about their influence on the ECL without further complementary experimental evidence. In this context, one must not forget the main aim of this study, which is to comprehend the intricate influence of the incorporation of $[Ir^{III}(sppy)_3]^{3-}$ in the $[Ru(bpy)_3]^{2+}$/TPrA coreactant system has on the $[Ru(bpy)_3]^{2+}$ ECL emission at 620 nm. We initially postulated that the two mechanistic steps responsible for the earlier onset potential and enhanced $[Ru(bpy)_3]^{2+}$ ECL intensity at low anodic overpotentials are the inter-catalyst electron transfer exchange leading to the redox-mediated oxidation of $[Ru(bpy)_3]^{+}$ (reaction *2.17*, rate constant $k_{f,IrRu}$), and the homogeneous catalysis of TPrA oxidation (k_{fcat}, reaction *2.5*).

$$[Ru(bpy)_3]^{+} + [Ir(sppy)_3]^{2-} \rightarrow [Ru(bpy)_3]^{2+*} + [Ir(sppy)_3]^{3-} \qquad (2.17)$$

Therefore, in the final, exploratory part of this study, we simulated the $[Ru(bpy)_3]^{2+}$ ECL emission at 620 nm, $I_{ECL,Ru}$, while systematically varying the rate constants of these reactions (**Figure 2.10**). In an effort to simplify the numerical simulation model, and to adapt to the structure of the present Ir complex, the homogeneous reduction of $[Ir^{III}(sppy)_3]^{3-}$ (reaction *2.14*) will be neglected in all further considerations.

Figure 2.10A depicts simulated $I_{ECL,Ru}$-E plots at 620 nm showing the influence of the kinetics of reaction *2.17*.

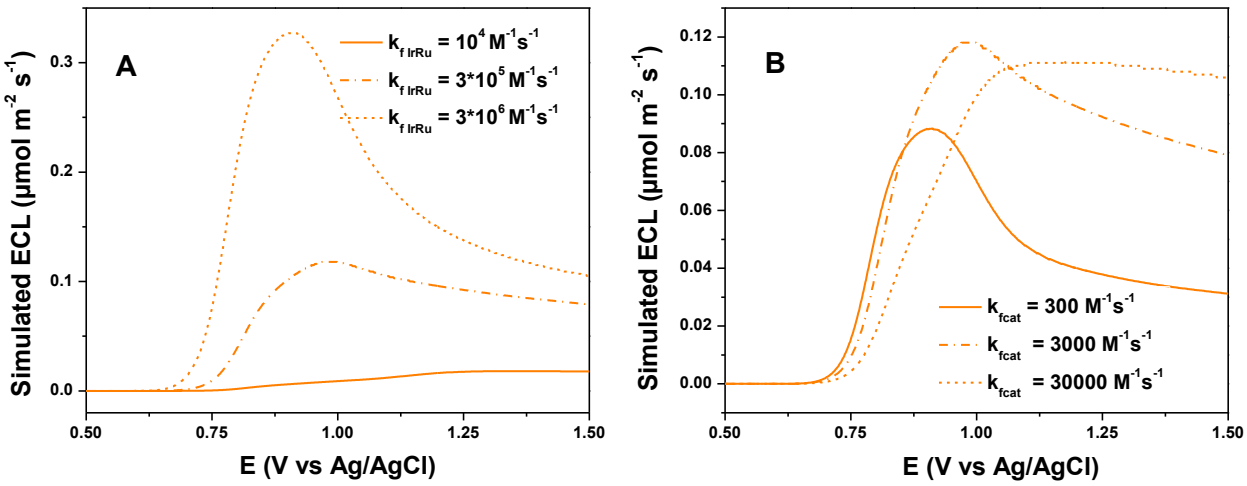

Figure 2.10. Simulated $[Ru(bpy)_3]^{2+}$ ECL intensities at 620 nm, $I_{ECL,Ru}$, in 1 mM $[Ir^{III}(sppy)_3]^{3-}$, 500 nM $[Ru(bpy)_3]^{2+}$ and 10 mM TPrA solution with **(A)** the inter-Ir-Ru species 'redox-mediated' step rate $k_{f,IrRu}$ is 10^4 $M^{-1}s^{-1}$ (solid line), 3×10^5 $M^{-1}s^{-1}$ (dashed line) and 3×10^6 $M^{-1}s^{-1}$ (dotted

line) when k_{fcat} is set to 3×10^3 $M^{-1}s^{-1}$; and **(B)** the rate of redox catalysis 3×10^2 $M^{-1}s^{-1}$ (solid line), 3×10^3 $M^{-1}s^{-1}$ (dashed line) and 3×10^4 $M^{-1}s^{-1}$ (dotted line) when $k_{f,IrRu} = 3 \times 10^5$ $M^{-1}s^{-1}$.

As $k_{f,IrRu}$ increases, the ECL shifts to lower potentials ($I_{ECL,Ru}$ peak transitions from 1.2 V at $k_{f,IrRu} = 10^4$ $M^{-1}s^{-1}$ to 0.90 V at $k_{f,IrRu} = 3 \times 10^6$ $M^{-1}s^{-1}$), accompanied by an elevation in emission intensity. This trend indicates that the introduction of an alternative pathway for $[Ru(bpy)_3]^+$ oxidation enhances the efficiency of $[Ru(bpy)_3]^{2+*}$ excited state generation, consequently amplifying the $[Ru(bpy)_3]^{2+}$ ECL intensity. The high efficiency of reaction *2.17* is rationalized by its driving force of -0.16 V owing to the difference between the E^0 values of the $[Ir^{III}(sppy)_3]^{3-}$/$[Ir^{IV}(sppy)_3]^{2-}$ and $[Ru(bpy)_3]^+$/$[Ru(bpy)_3]^{2+*}$ redox couples (0.81 V and 0.65 V vs Ag/AgCl, respectively). The potential of the $[Ru(bpy)_3]^+$/$[Ru(bpy)_3]^{2+*}$ redox couple is calculated as: $E^0_{+/2+*} = E^0_{+/2+} + E_{em,Ru}$ (where $E_{em,Ru}$ = 2 eV is the energy associated to photon emission at 620 nm). Additionally, the emergence of ECL emission at a lower potential, where only $[Ir(sppy)_3]^{3-}$ can be directly oxidized at the electrode (see **Figure 2.12A**), suggests $TPrA^{\bullet}$ is produced in this potential region, which then generates $[Ru(bpy)_3]^+$. This strongly supports the homogeneous oxidation of TPrA by $[Ir^{III}(sppy)_3]^{3-}$ through reaction *2.5* (**Figure 2.2D**)**.** Moreover, in the absence of the inter-catalyst electron exchange (reaction *2.17*, **Figure 2.2C**), the extent of $[Ru(bpy)_3]^{2+}$ ECL would rely only on the availability of $TPrA^{\bullet}$ and $TPrA^{\bullet+}$, with the luminophores operating independently. The oxidized form of the iridium complex being produced at the electrode, the homogeneous electrocatalysis of TPrA is expected to produce both $TPrA^{\bullet+}$ and $TPrA^{\bullet}$ within the first few micrometres from the electrode. This enables the generation of $[Ru(bpy)_3]^+$ and then ECL emission depending on the efficiency of the inter-catalyst exchange rate and the homogeneous electrocatalysis. On the one hand, the lower the inter-catalyst exchange rate the lower the $[Ru(bpy)_3]^{2+}$ ECL and the more it is shifted towards more positive potential as confirmed by the trend in **Figure 2.10A**.

Therefore, as previously discussed and confirmed here by simulation, in the presence of $[Ir^{III}(sppy)_3]^{3-}$, the $[Ru(bpy)_3]^{2+}$ ECL onset potential observed within the Ir complex oxidation potential region, demonstrates the significant contribution of the redox-mediated route (**Figure 2.2C**) to the overall mechanistic scheme.

As just mentioned, the $[Ru(bpy)_3]^{2+}$ ECL at low potential in the mixed luminophore ECL system also requires the homogeneous oxidation of TPrA by $[Ir^{IV}(sppy)_3]^{2-}$ (reaction *2.5*, rate

constant k_{fcat}); we therefore investigated its influence on the dual ECL emission. We previously estimated the k_{fcat} from the electrochemical currents, and the i-E plots ($k_{fcat} = 3 \times 10^3\ M^{-1}s^{-1}$), but a more in-depth analysis would improve our understanding of the overall reactivity within this coreactant system. Moreover, analyzing the ECL behaviour at different rates of redox catalysis can serve a predictive purpose, if one can synthesize other redox mediators.

Figure 2.10B illustrates simulated $I_{ECL,Ru}$-E plots at 620 nm with varying k_{fcat} values. As k_{fcat} increases, the ECL onset potential becomes more positive. Notably, the plots exhibit a shoulder at low overpotentials, in the $[Ir^{III}(sppy)_3]^{3-}$ oxidation region, attesting the role of the $[Ir^{III}(sppy)_3]^{3-}$/TPrA redox catalysis on the $[Ru(bpy)_3]^{2+}$ ECL. At higher potentials, for lower k_{fcat} values ($3 \times 10^2\ M^{-1}s^{-1}$ and $3 \times 10^3\ M^{-1}s^{-1}$), the $I_{ECL,Ru}$-E plots show peaks (maximum of $I_{ECL,Ru}$), while it is transitioning to a steady-state behavior at higher rate constant values (above $3 \times 10^4\ M^{-1}s^{-1}$). Furthermore, the faster the k_{fcat}, the higher the peak ECL intensity, reaching its highest value for k_{fcat} close to $3 \times 10^3\ M^{-1}s^{-1}$ and decreasing at higher rate constants (where ECL is characterized by steady-state emission).

Reaction *2.5* controls the ECL intensity by controlling the production of $TPrA^{\bullet+}$ (and $TPrA^{\bullet}$ through reaction *2.8*), which is responsible for the population of the $[Ru(bpy)_3]^{2+*}$ excited state (equations *2.11 – 2.13*). Simultaneously, $[Ir^{IV}(sppy)_3]^{2-}$ species are depleted during this reaction. At low concentrations of $[Ir^{IV}(sppy)_3]^{2-}$ the rate of redox-mediated $[Ru(bpy)_3]^{+}$ oxidation (reaction *2.17*) decreases, becoming comparable to the one governed by $TPrA^{\bullet+}$ (reaction *2.12*). These competing reactions impose as steady-state (potential independent) of the concentration of the $[Ru(bpy)_3]^{2+*}$ species. Consequently, the faster k_{fcat} rates cause a transition from the ECL emission controlled by the redox-mediated route (**Figure 2.2C**) to the one controlled by the remote route (**Figure 2.2A**). This phenomenon rationalizes the steady state ECL emission with the higher onset potential (resembling the $I_{ECL,Ru}$-E plot of the $[Ru(bpy)_3]^{2+}$/TPrA system) at faster k_{fcat} rates.

In addition to influencing the ECL intensity, reaction *2.5* also regulates the expansion of TPrA radicals into the solution. Consequently, the rate of homogeneous oxidation should profoundly affect the expansion of the $[Ru(bpy)_3]^{2+}$ ECL layer. We examined this influence by simulating the concentration profiles of $TPrA^{\bullet}$ and $[Ir^{IV}(sppy)_3]^{2-}$, along with the thickness of the ECL layer at 620 nm at different k_{fcat} values (**Figure 2.11**). As expected, an increase in k_{fcat} results in a broader expansion of the $TPrA^{\bullet}$ concentration profile in the solution (**Figure 2.11A**).

However, it simultaneously restricts the diffusion layer of $[Ir^{IV}(sppy)_3]^{2-}$ species due to the redox catalysis process (to only 5 µm at k_{fcat} = 3 × 10^4 $M^{-1}s^{-1}$) (**Figure 2.11B**). While TPrA$^{\bullet}$ governs the production of $[Ru(bpy)_3]^{+}$ in the solution, the concentration and distribution of suitable oxidants (in this case, TPrA$^{\bullet+}$ and $[Ir^{IV}(sppy)_3]^{2-}$) control the generation of the $[Ru(bpy)_3]^{2+}$ ECL. This is reflected in the decreasing thickness of the ECL emitting layer at faster k_{fcat} (**Figure 2.11C**).

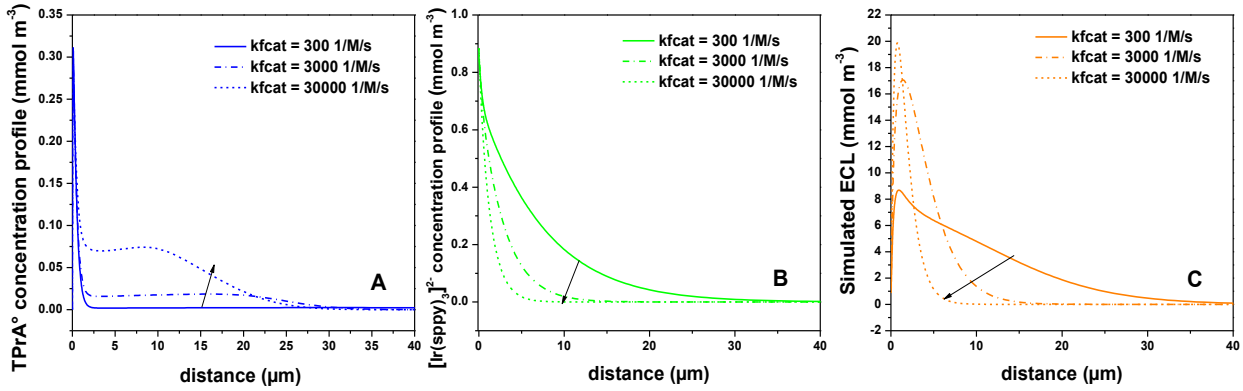

Figure 2.11. Simulated: **(A)** concentration profiles of TPrA radical; **(B)** concentration profiles of $[Ir(sppy)_3]^{3-}$ and **(C)** thickness of the Ru ECL layer (at 620 nm) in 500 nM $[Ru(bpy)_3]^{2+}$, 1 mM $[Ir(sppy)_3]^{3-}$ and 10 mM TPrA at different rates of catalytic reaction *3.1*: 300 $M^{-1}s^{-1}$ (dashed lines), 3000 $M^{-1}s^{-1}$ (solid lines), and 30000 $M^{-1}s^{-1}$ (dotted lines). Arrows show the increase of the k_{fcat} values.

To summarize, **Figure 2.11** illustrates the intricate role of all reaction rates on the spatial distribution of the different intermediates involved. Focusing particularly on the electrocatalytic ECL pathway, at low potentials which relies on the inter-catalyst exchange rate, Ru^{+} species and ECL must be produced in regions rich in both TPrA$^{\bullet}$ and $[Ir^{IV}(sppy)_3]^{2-}$. By increasing k_{cat} the $[Ir^{IV}(sppy)_3]^{2-}$-rich region is more and more confined toward the electrode surface, decreasing its overlap with the TPrA$^{\bullet}$-rich region, which expands in solution. This makes the electrocatalytic pathway for ECL, at low potentials, less efficient with an ECL signal being shifted towards more positive potentials.

2.3.6 ECL of $[Ir^{III}(sppy)_3]^{3-}$/$[Ru(bpy)_3]^{2+}$/TPrA coreactant system

This exploratory study shows how the different homogeneous reactions govern the ECL profiles in terms of intensity, potential and spatial distribution. In the final phase of our study, we conducted numerical simulations aiming to replicate the experimentally observed variations in ECL intensity with potential at 515 nm and 620 nm for the $[Ru(bpy)_3]^{2+}$/TPrA, $[Ir^{III}(sppy)_3]^{3-}$/TPrA and $[Ir^{III}(sppy)_3]^{3-}$/$[Ru(bpy)_3]^{2+}$/TPrA coreactant systems (**Figure 2.12B**). Although the simulated plots do not perfectly match the experimental data, they exhibit a reasonable degree of correlation in terms of onset potential, peak potential, and ECL intensity. However, this correlation is different among the systems. For the $[Ru(bpy)_3]^{2+}$/TPrA the simulation predicts ECL behaviour that is in overall agreement with the experimental results (at least up to the peak potential, as shown in **Figure 2.6A** and red plots in **Figure 2.12B**). It is not the case for the other two systems which, while following the general experimental trends, align less well with the experimental I_{ECL}-E plots in terms of ECL onset and peak potential values.

The simulated $[Ir^{III}(sppy)_3]^{3-}$ ECL intensity, $I_{ECL,Ir}$, versus potential plot at 515 nm (light green) is identical for both the $[Ir^{III}(sppy)_3]^{3-}$/TPrA and $[Ir^{III}(sppy)_3]^{3-}$/$[Ru(bpy)_3]^{2+}$/TPrA coreactant systems. While its ECL onset potential aligns well with the experimental ones, the maximal ECL intensity in the simulated plot is shifted to higher potentials and the overall shape of the ECL intensity versus potential plot deviates from the experimentally obtained ones. This disparity highlights that, while we have a good grasp of the fundamental reaction steps generating $[Ir^{III}(sppy)_3]^{3-}$ ECL, there is a need for a deeper understanding of their kinetics and of any side reactions contributing to the observed differences.

Moreover, it is noteworthy that the $[Ir^{III}(sppy)_3]^{3-}$ ECL intensity at 515 nm differs in **Figures 2.7** and **2.12B**. Initially, in **Figure 2.7**, our simulation predicted a significantly higher ECL intensity than what was observed in the experiment. This points toward the low coreactant efficiency of $[Ir^{III}(sppy)_3]^{3-}$ ECL generation, or might indicate that nonradiative decay plays a more significant role than we originally anticipated. To reproduce the experimentally obtained ECL intensity, we incorporated the reaction for non-emissive decay of the $[Ir^{III}(sppy)_3]^{3-*}$ into the model (reaction *2.18*) with a rate constant of 4.5×10^9 s^{-1}.

$$[Ir(sppy)_3]^{3-*} \rightarrow [Ir(sppy)_3]^{3-} \qquad (2.18)$$

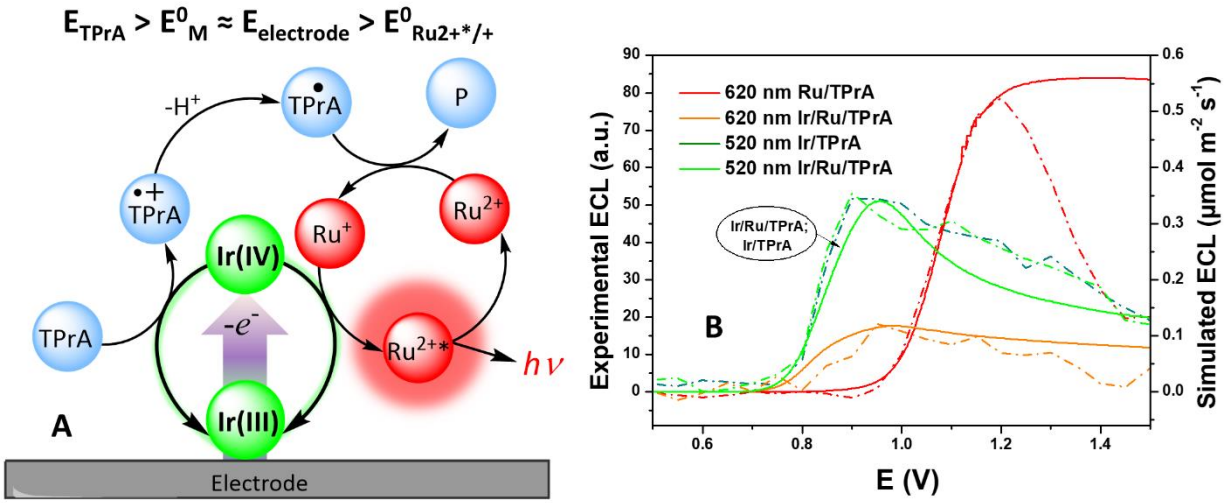

Figure 2.12. (A) Schematic illustrating the role of the Ir(III) electrocatalyst in the oxidation of TPrA and Ru(I) species, leading to amplified $[Ru(bpy)_3]^{2+}$ ECL at low anodic potentials. **(B)** Simulated (solid lines) and experimental (dashed lines) ECL intensities: at 620 nm in 500 nM $[Ru(bpy)_3]^{2+}$ and 10 mM TPrA solution (red lines); at 620 nm in 1 mM $[Ir^{III}(sppy)_3]^{3-}$, 500 nM $[Ru(bpy)_3]^{2+}$ and 10 mM TPrA solution (orange lines); at 515 nm in 1 mM $[Ir^{III}(sppy)_3]^{3-}$and 10 mM TPrA solution (green lines); and at 515 nm in 1 mM $[Ir^{III}(sppy)_3]^{3-}$, 500 nM $[Ru(bpy)_3]^{2+}$ and 10 mM TPrA solution (cyan lines).

Finally, the simulated $I_{ECL,Ru}$-E plot for $[Ru(bpy)_3]^{2+}$ ECL at 620 nm (**Figure 2.12B**, orange plot) in the mixed luminophore/coreactant system is shifted to around 50 mV lower overpotential compared with the experimental one. The ECL generation in this system is complex and depends on multiple chemical steps, as shown in the previous section. While all of them contribute to the final ECL intensity, we reduced the number of reactions responsible for the lower ECL onset potential to only three. As previously discussed, the redox catalysis, the inter-Ir-Ru species redox-mediated $[Ru(bpy)_3]^{+}$ oxidation, and the reaction that generates $[Ir^{III}(sppy)_3]^{3-}$ ECL affect the onset ECL potential of $[Ru(bpy)_3]^{2+}$ in a way illustrated in **Figures 2.10B**, **2.10A** and **2.8C**, respectively. Notably, varying those parameters led to simulated plots that can accurately replicate the experimental results, but further experimental information is needed to fully understand the nature of the reaction steps and their contribution to the chemistry of this complex coreactant system.

In broader terms, the here-developed model provides useful insights into the mechanism of the mixed luminophore coreactant system, but more importantly, it sparks discussion regarding the significance of specific mechanistic steps and the chemical properties of the mediator, particularly its redox properties, which can contribute to future research aimed at improving ECL signals. However, given the complexity of the mechanisms underlying the mixed luminophore system, the model remains under-characterised. In the future efforts to delve into the reactivity and fine interplay of the kinetically limited mechanistic steps, experimentation towards estimating the thickness of the ECL emitting layer,[23,71] especially when varying the ratio of the components within this coreactant system, would greatly aid in this endeavour.

2.4 Conclusion

We have evaluated the crucial role of redox mediators in shaping ECL emission within the $[Ru(bpy)_3]^{2+}$/TPrA coreactant system, highlighting how the rate-limiting processes involving the electrooxidized form of the Ir(III) mediator influence the efficiency of ECL emission, particularly at low electrode potentials. Specifically, we have demonstrated that to effectively enhance $[Ru(bpy)_3]^{2+}$ ECL emission at low anodic potentials, the redox mediator needs to mediate oxidation of both the coreactant and $[Ru(bpy)_3]^{+}$, as depicted in **Figure 2.12A**. The former enables triggering the production of the coreactant reactive intermediates ($TPrA^{\bullet+}$ and $TPrA^{\bullet}$) at electrode potentials lower than those of their direct oxidation. The latter provides a supplemental efficient path to produce the excited $[Ru(bpy)_3]^{2+*}$ luminophore.

For those two mediated oxidations to occur, specific conditions are required regarding the redox properties of the mediator compared to $[Ru(bpy)_3]^{2+}$ and the coreactant (see **Figure 2.12A**). First, typically the mediator should have a standard potential higher than the $[Ru(bpy)_3]^{2+*}/[Ru(bpy)_3]^{+}$ couple and lower then, but close to, the coreactant oxidation. For the $[Ru(bpy)_3]^{+}$/TPrA system it should be between 0.6 and ca. 0.9 V. Secondly, the enhancement of ECL was shown to be more efficient if, unlike the $[Ru(bpy)_3]^{2+}$ luminophore, the redox mediator was not reduced by the $TPrA^{\bullet}$ radical. It is the case here, as the reduction of the $[Ir^{III}(sppy)_3]^{3-}$ redox mediator occurs at – 2.0 V vs Ag/AgCl, 0.4 V more negative than the $TPrA^{\bullet}$ oxidation potential.

In the present study, the redox mediator was also a luminophore, providing a second ECL signature. It was shown that this signature is also related to the redox mediation of the coreactant oxidation, meaning that the $[Ir^{III}(sppy)_3]^{3-}$ ECL takes places during the Ir complex oxidation. The simulation demonstrates that the $[Ir^{III}(sppy)_3]^{3-}$ ECL is also ruled by the redox properties of the $[Ir^{IV}(sppy)_3]^{2-}/[Ir^{III}(sppy)_3]^{3-*}$ couple and how it can participate in the redox conversion of both $TPrA^{\bullet}$ and $TPrA^{\bullet+}$ radical intermediates In particular, the thermodynamically infeasible reduction of $[Ir^{III}(sppy)_3]^{3-}$ restricts the generation of the $[Ir^{III}(sppy)_3]^{3-*}$ excited state to a single pathway: the homogeneous reduction of electrogenerated $[Ir^{IV}(sppy)_3]^{2-}$ by $TPrA^{\bullet}$, thereby limiting the $[Ir^{III}(sppy)_3]^{3-}$ ECL. Furthermore, by highlighting the quenching effect on $[Ru(bpy)_3]^{2+}$ ECL, induced by the oxidant ($[Ir^{IV}(sppy)_3]^{2-}$) scavenging the $TPrA^{\bullet}$ radicals, we suggest that the subsequent free radical reactivity should be further investigated.

Finally, we were able to reasonably reproduce the experimental ECL observations, and provide a mechanistic rationale of why the $[Ru(bpy)_3]^{2+}$ ECL occurs simultaneously with the oxidation of the redox mediator (and therefore at the same time as the $[Ir^{III}(sppy)_3]^{3-}$ ECL). This is of practical and analytical interest for ECL-based biosensors and bioassays because they would depend on the oxidation of an outer-sphere redox mediator, i.e. with a fast electron transfer kinetics, and no longer on the direct oxidation of the coreactant, which is much more dependent on the electrode nature and its passivation. This understanding not only advances our fundamental knowledge of ECL mechanisms but also prompts further experimentation, facilitating the development of ECL systems with tailored properties and improved performance.

2.5 Supporting Information

2.5.1 Model used geometry and mesh

For this study, we used a 1D geometry with boundary conditions where: 0 µm point corresponds to the electrode surface and 1000 µm to the bulk electrolyte. Domains with different mesh dimensions are highlighted in blue in **Figure 2.13** with the corresponding mesh sizes provided in **Table 2.1**. Electrochemical consumption and production of species takes place at at the electrode (flux, at 0 µm), while the species' concentration in the bulk (at 1000

µm) remains constant during the whole experiment and provides an inflow of reactants. Thus, the boundary condition at 1000 µm correspond to the initial solution composition: concentrations of $[Ir(sppy)_3]^{3-}$, $[Ru(bpy)_3]^{2+}$, and TPrA in its protonated and deprotonated form (C_{IrIII}, C_{Ru2+} and C_{TPrAH} and $C_{TPrA)}$. C_{TPrAH} equals to C°Keq/(1+Keq)) with C° the total content of TPrA species and Keq the deprotonation equilibrium based on the pH of the solution and pKA of TPrA (pkA=10; pH = 7, Keq = $10^{(pKA-pH)}$) and C_{TPrA} is C°/(1+Keq); 500 nM $[Ru(bpy)_3]^{2+}$, everything else 0 M), which also corresponds to the initial conditions in the whole volume of the solution (0 - 1000 µm)).

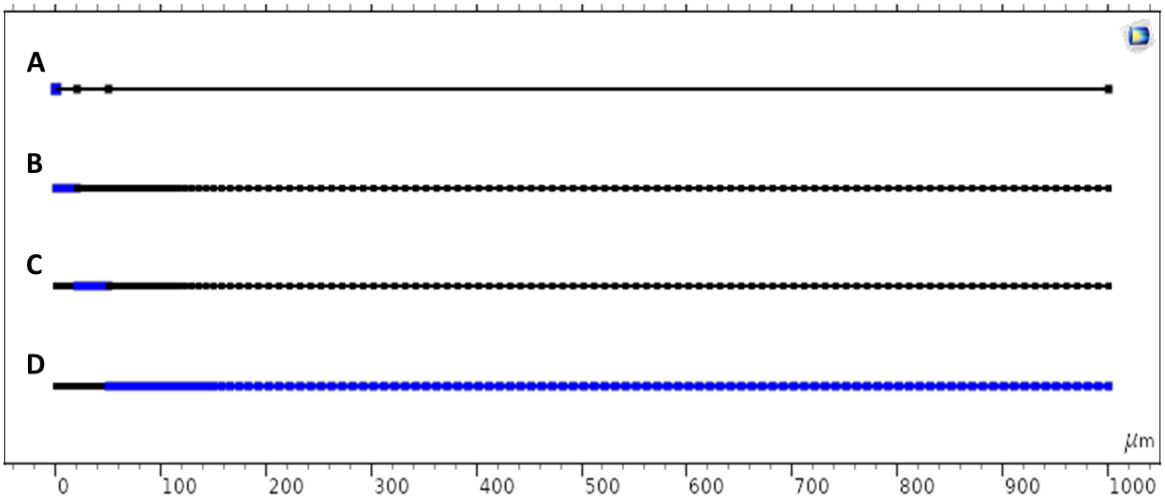

Figure 2.13. Model mesh at different distances from electrode surface: **(A)** 0 µm, **(B)** 0 - 20 µm, **(C)** 20 - 50 µm and **(D)** 50 - 1000 µm.

Domain	A	B	C	D
Maximum element size (µm)	5×10^{-7}	5×10^{-6}	5×10^{-5}	10
Maximum element growth rate	1.05	1.05	1.05	1.05

Table 2.1. Mesh sizes that correspond to the highlighted domains in the model.

2.5.2 Electrochemical and chemical reactivity within the mixed luminophore coreactant system

The upper boundary in the solution defines initial concentrations, to promote diffusion along the x-axis. Solution diffusion is formulated according to the Nernst–Planck equation, assuming that the contribution from the migration and convection is negligible (equations 2.19 and 2.20):

$$\frac{\partial c_i}{\partial t} + \Delta \cdot J_i = R_i \qquad (2.19)$$

$$J_i = -D_i \nabla c_i \qquad (2.20)$$

Here, c_i is the concentration of i^{th} species, t is the time, Δ represents the Laplacian, Di is the diffusion coefficient and J_i the flux of i^{th} species. R_i is the reaction flux necessary to maintain equilibrium.

We approximated the diffusion coefficient to be 10^{-9} m^2/s for TPrAH, TPrA and its radicals, P, $[Ru(bpy)_3]^+$, $[Ru(bpy)_3]^{2+}$, $[Ru(bpy)_3]^{3+}$ and $[Ru(bpy)_3]^{2+*}$; 2.5×10^{-10} m^2/s for $[Ir(sppy)_3]^{4-}$, $[Ir(sppy)_3]^{3-}$, $[Ir(sppy)_3]^{2-}$ and $[Ir(sppy)_3]^{3-*}$; and 10^{-15} m^2/s for hv and hv_r.

Oxidation rates are modelled via Butler-Volmer laws, with sufficiently fast rates to ensure that oxidation proceeds under diffusion control. The simulated curves were solved using a time-dependent solver. The cyclic voltammetry was simulated by estimating the electron transfer equals the flux of the species reacting on the electrode (equation *2.21*), with electrochemical potential dependence on time expressed by the equation *2.22*:

$$I\ (A/m^2) = (J_{TPrA} + J_{TPrA^\cdot} - J_{[Ir(sppy)_3]^{2-}} + J_{[Ir(sppy)_3]^{4-}} - J_{[Ru(bpy)_3]^{3+}} + J_{[Ru(bpy)_3]^{+}}) \cdot F \qquad (2.21)$$

$$E = (E_i + v \cdot t) \cdot (t \leq t_r) + (2 \cdot E_f - E_i - v \cdot t) \cdot (t > t_r) \qquad (2.22)$$

where E_i = 0 V; v = 100 mV/s ; step = 0.01 s ; t_r = 15 s and $t_f = 2 \cdot t_r$

The ECL emission is calculated as the rate of photons emitted by any point of the surface at any computation time (in mol m^{-1} s^{-1}):

$$ECL = \frac{\partial h\nu}{\partial t} \quad (2.23)$$

$$ECL = \frac{\partial h\nu_r}{\partial t} \quad (2.24)$$

Butler-Volmer equations, used to estimate the current, and chemical (and electrochemical) reactions with their corresponding reaction rates (and redox potentials) are given in **Table 2.2** and **2.3**, respectively. We assumed that α = 0.5.

Molecular species	Oxidation rates
TPrA	$-k_0 \cdot \left(TPrA \cdot e^{\left(\alpha\cdot(E-E_0)\cdot\frac{F}{RT}\right)} - TPrA^{\bullet+} \cdot e^{\left(-(1-\alpha)\cdot(E-E_0)\cdot\frac{F}{RT}\right)}\right)$
$TPrA^{\bullet+}$	$k_0 \cdot \left(TPrA \cdot e^{\left(\alpha\cdot(E-E_0)\cdot\frac{F}{RT}\right)} - TPrA^{\bullet+} \cdot e^{\left(-(1-\alpha)\cdot(E-E_0)\cdot\frac{F}{RT}\right)}\right)$
$TPrA^{\bullet}$	$-k \cdot \left(TPrA^{\bullet} \cdot e^{\left(\alpha\cdot(E-E_{0r})\cdot\frac{F}{RT}\right)}\right)$
P	$k \cdot \left(TPrA^{\bullet} \cdot e^{\left(\alpha\cdot(E-E_{0r})\cdot\frac{F}{RT}\right)}\right)$
$[Ir(sppy)_3]^{3-}$	$-k \cdot \left([Ir(sppy)_3]^{3-} \cdot e^{\left(\alpha\cdot(E-E_{0Ir2})\cdot\frac{F}{RT}\right)} - [Ir(sppy)_3]^{2-} \cdot e^{\left(-(1-\alpha)\cdot(E-E_{0Ir2})\cdot\frac{F}{RT}\right)}\right)$
$[Ir(sppy)_3]^{2-}$	$k \cdot \left([Ir(sppy)_3]^{3-} \cdot e^{\left(\alpha\cdot(E-E_{0Ir2})\cdot\frac{F}{RT}\right)} - [Ir(sppy)_3]^{2-} \cdot e^{\left(-(1-\alpha)\cdot(E-E_{0Ir2})\cdot\frac{F}{RT}\right)}\right)$
$[Ru(bpy)_3]^{2+}$	$-k \cdot \left([Ru(bpy)_3]^{2+} \cdot e^{\left(\alpha\cdot(E-E_{0Ru3})\cdot\frac{F}{RT}\right)} - [Ru(bpy)_3]^{3+} \cdot e^{\left(-(1-\alpha)\cdot(E-E_{0Ru3})\cdot\frac{F}{RT}\right)}\right)$ $+k \cdot \left([Ru(bpy)_3]^{+} \cdot e^{\left(\alpha\cdot(E-E_{0Ru1})\cdot\frac{F}{RT}\right)} - [Ru(bpy)_3]^{2+} \cdot e^{\left(-(1-\alpha)\cdot(E-E_{0Ru1})\cdot\frac{F}{RT}\right)}\right)$
$[Ru(bpy)_3]^{3+}$	$k \cdot \left([Ru(bpy)_3]^{2+} \cdot e^{\left(\alpha\cdot(E-E_{0Ru3})\cdot\frac{F}{RT}\right)} - [Ru(bpy)_3]^{3+} \cdot e^{\left(-(1-\alpha)\cdot(E-E_{0Ru3})\cdot\frac{F}{RT}\right)}\right)$
$[Ru(bpy)_3]^{+}$	$-k \cdot \left([Ru(bpy)_3]^{+} \cdot e^{\left(\alpha\cdot(E-E_{0Ru1})\cdot\frac{F}{RT}\right)} - [Ru(bpy)_3]^{2+} \cdot e^{\left(-(1-\alpha)\cdot(E-E_{0Ru1})\cdot\frac{F}{RT}\right)}\right)$

Table 2.2. Oxidation rate equations used in the numerical simulation approach to model the cyclic voltammetry.

Reaction	Constant	Value
$TPrAH^+ \rightleftarrows TPrA + H^+$	k_{fdp}	1000 [1/s]
$TPrA \rightleftarrows e^- + TPrA^{\bullet+}$	k_0; E_0	0.012 [cm/s]; 0.96 [V]
$TPrA^{\bullet+} \rightarrow TPrA^{\bullet} + H^+$	k_{f0}	10000 [1/s]
$TPrA^{\bullet} \rightarrow e^- + P$	k; E_{0r}	0.05 [cm/s]; -1.7 [V]
$TPrA^{\bullet+} + TPrA^{\bullet} \rightarrow TPrA + P$	k_{f5}	10^{10} [1/M/s]
$[Ru(bpy)_3]^{2+} \rightleftarrows e^- + [Ru(bpy)_3]^{3+}$	k; E_{0Ru3}	0.05 [cm/s]; 1.04 [V]
$[Ru(bpy)_3]^{+} \rightleftarrows e^- + [Ru(bpy)_3]^{2+}$	k; E_{0Ru1}	0.05 [cm/s]; -1.35 [V]
$[Ru(bpy)_3]^{2+} + TPrA^{\bullet} \rightarrow [Ru(bpy)_3]^{+} + P$	k_{f1r}	$3 \cdot 10^9$ [1/M/s]
$[Ru(bpy)_3]^{+} + TPrA^{\bullet+} \rightarrow [Ru(bpy)_3]^{2+*} + TPrA$	k_{f2r}	10^6 [1/M/s]
$[Ru(bpy)_3]^{2+*} \rightarrow [Ru(bpy)_3]^{2+} + h\upsilon$	k_{f3r}	10^7 [1/s]
$[Ru(bpy)_3]^{+} + [Ru(bpy)_3]^{3+} \rightarrow [Ru(bpy)_3]^{2+*} + [Ru(bpy)_3]^{2+}$	k_{f4r}	10^{10} [1/M/s]
$[Ru(bpy)_3]^{3+} + TPrA^{\bullet} \rightarrow [Ru(bpy)_3]^{2+*} + P$	k_{f6r}	10^7 [1/M/s]
$[Ru(bpy)_3]^{3+} + TPrA \rightarrow [Ru(bpy)_3]^{2+} + TPrA^{\bullet+}$	k_{fcatr}	k_{bcatr} / K_{catr} *
$[Ru(bpy)_3]^{2+} + TPrA^{\bullet+} \rightarrow [Ru(bpy)_3]^{3+} + TPrA$	k_{bcatr}	3000 [1/M/s]
$[Ru(bpy)_3]^{+} + [Ir(sppy)_3]^{2-} \rightarrow [Ru(bpy)_3]^{2+*} + [Ir(sppy)_3]^{3-}$	k_{flrRu}	$3 \cdot 10^5$ [1/M/s]
$[Ir(sppy)_3]^{3-} \rightleftarrows [Ir(sppy)_3]^{2-} + e^-$	k; E_{0lr2}	0.05 [cm/s]; 0.81 [V]
$[Ir(sppy)_3]^{2-} + TPrA^{\bullet} \rightarrow [Ir(sppy)_3]^{3-*} + P$	k_{f6}	10^9 [1/M/s]
$[Ir(sppy)_3]^{3-*} \rightarrow [Ir(sppy)_3]^{3-} + h\upsilon$	k_{f3}	10^7 [1/s]
$[Ir(sppy)_3]^{2-} + TPrA \rightarrow [Ir(sppy)_3]^{3-} + TPrA^{\bullet+}$	k_{fcat}	3000 [1/M/S]
$[Ir(sppy)_3]^{3-} + TPrA^{\bullet+} \rightarrow [Ir(sppy)_3]^{2-} + TPrA$	k_{bcat}	k_{fcat} / K_{cat}
$[Ir(sppy)_3]^{2-} \rightarrow M$	k_{fside}	0.15 [1/s]
$[Ir(sppy)_3]^{3-*} + TPrA^{\bullet+} \rightarrow [Ir(sppy)_3]^{2-} + TPrA$	k_{fq}	10^{12} [1/M/s]
$[Ir(sppy)_3]^{3-*} \rightarrow [Ir(sppy)_3]^{3-}$	k_{fnr}	$4.5 \cdot 10^9$ [1/s]
$[Ir(sppy)_3]^{3-} + [Ru(bpy)_3]^{3+} \rightarrow [Ir(sppy)_3]^{2-} + [Ru(bpy)_3]^{2+}$	k_{f7}	10^9 [1/M/s]
$[Ir(sppy)_3]^{3-} + TPrA^{\bullet} \rightarrow [Ir(sppy)_3]^{4-} + P$	k_{f1}	/ [1/M/s]
$[Ir(sppy)_3]^{4-} \rightleftarrows e^- + [Ir(sppy)_3]^{3-}$	k; E_{0lr4}	0.05 [cm/s]; -2.0 [V]
$[Ir(sppy)_3]^{4-} + TPrA^{\bullet+} \rightarrow [Ir(sppy)_3]^{3-*} + TPrA$	k_{f2}	10^6 [1/M/s]
$[Ir(sppy)_3]^{4-} + [Ir(sppy)_3]^{2-} \rightarrow [Ir(sppy)_3]^{3-*} + [Ir(sppy)_3]^{3-}$	k_{f4}	10^{10} [1/M/s]

Table 2.3. Homogeneous and heterogeneous reactions and their corresponding rate constants (and electrochemical potentials, where applicable) used in the simulation model to estimate the concentration profiles of solutions species and ECL emission at 515 nm and 620 nm.

References

1 A. Abdussalam and G. Xu, *Anal Bioanal Chem*, 2022, **414**, 131–146.
2 F. Rizzo, F. Polo, G. Bottaro, S. Fantacci, S. Antonello, L. Armelao, S. Quici and F. Maran, *J. Am. Chem. Soc.*, 2017, **139**, 2060–2069.
3 G. J. Barbante, E. H. Doeven, E. Kerr, T. U. Connell, P. S. Donnelly, J. M. White, T. Lópes, S. Laird, D. J. D. Wilson, P. J. Barnard, C. F. Hogan and P. S. Francis, *Eur. J. Chem.*, 2014, **20**, 3322–3332.
4 D. Bruce and M. M. Richter, *Anal. Chem.*, 2002, **74**, 1340–1342.
5 L. Chen, D. J. Hayne, E. H. Doeven, J. Agugiaro, D. J. D. Wilson, L. C. Henderson, T. U. Connell, Y. H. Nai, R. Alexander, S. Carrara, C. F. Hogan, P. S. Donnelly and P. S. Francis, *Chem. Sci.*, 2019, **10**, 8654–8667.
6 M. A. Haghighatbin, S. E. Laird and C. F. Hogan, *Curr. Opin. Electrochem.*, 2018, **7**, 216–223.
7 P. Nikolaou, G. Valenti and F. Paolucci, *Electrochim. Acta*, 2021, **388**, 138586.
8 A. Fiorani, J. P. Merino, A. Zanut, A. Criado, G. Valenti, M. Prato and F. Paolucci, *Curr. Opin. Electrochem.*, 2019, **16**, 66–74.
9 S. Kesarkar, S. Valente, A. Zanut, F. Palomba, A. Fiorani, M. Marcaccio, E. Rampazzo, G. Valenti, F. Paolucci and L. Prodi, *J. Phys. Chem. C*, 2019, **123**, 5686–5691.
10 P. Dai, C. Liu, C. Xie, J. Ke, Y. He, L. Wei, L. Chen and J. Jin, *Anal Bioanal Chem*, 2020, **412**, 1375–1384.
11 A. J. Bard, in *Electrogenerated Chemiluminescence*, CRC Press, 2004.
12 I. Svir, A. Oleinick, O. V. Klymenko and C. Amatore, in *Analytical Electrogenerated Chemiluminescence: From Fundamentals to Bioassays*, ed. N. Sojic, Royal Society of Chemistry, Cambridge, 2019, pp. 134–158.
13 C. Amatore, C. Pebay, L. Thouin, A. Wang and J.-S. Warkocz, *Anal. Chem.*, 2010, **82**, 6933–6939.
14 C. Amatore, O. V. Klymenko and I. Svir, *Anal. Chem.*, 2012, **84**, 2792–2798.
15 C. Amatore, K. Knobloch and L. Thouin, *J. Electroanal. Chem.*, 2007, **601**, 17–28.
16 C. Amatore, C. Pebay, L. Thouin and A. Wang, *Electrochem. Commun.*, 2009, **11**, 1269–1272.
17 C. Amatore, S. Szunerits, L. Thouin and J.-S. Warkocz, *Electrochem. Commun.*, 2000, **2**, 353–358.
18 W. Guo, P. Zhou, L. Sun, H. Ding and B. Su, *Angew. Chem. Int. Ed.*, 2021, **60**, 2089–2093.
19 A. J. Wilson, K. Marchuk and K. A. Willets, *Nano Lett.*, 2015, **15**, 6110–6115.
20 W.-X. Fu, P. Zhou, W.-L. Guo and B. Su, *Adv. Sens. Energy Mater.*, 2022, **1**, 100028.
21 D. Han, D. Fang, G. Valenti, F. Paolucci, F. Kanoufi, D. Jiang and N. Sojic, *Anal. Chem.*, 2023, **95**, 15700–15706.
22 P. Zhou, S. Hu, W. Guo and B. Su, *Fundam. Res.*, 2022, **2**, 682–687.
23 Y. Wang, W. Guo, Q. Yang and B. Su, *J. Am. Chem. Soc.*, 2020, **142**, 1222–1226.
24 O. V. Klymenko, I. Svir and C. Amatore, *ChemPhysChem*, 2013, **14**, 2237–2250.
25 E. Daviddi, A. Oleinick, I. Svir, G. Valenti, F. Paolucci and C. Amatore, *ChemElectroChem*, 2017, **4**, 1719–1730.

26 A. Zanut, A. Fiorani, S. Canola, T. Saito, N. Ziebart, S. Rapino, S. Rebeccani, A. Barbon, T. Irie, H.-P. Josel, F. Negri, M. Marcaccio, M. Windfuhr, K. Imai, G. Valenti and F. Paolucci, *Nat. Commun.*, 2020, **11**, 2668.
27 S. A. Kitte, C. Wang, S. Li, Y. Zholudov, L. Qi, J. Li and G. Xu, *Anal Bioanal Chem*, 2016, **408**, 7059–7065.
28 H. Xing, Q. Zhai, X. Zhang, J. Li and E. Wang, *Anal. Chem.*, 2018, **90**, 2141–2147.
29 C. V. Raju and S. S. Kumar, *Chem. Commun.*, 2017, **53**, 6593–6596.
30 F. Yuan, M. I. Halawa, X. Ma, A. Abdussalam, B. Lou and G. Xu, *ChemElectroChem*, 2020, **7**, 4239–4244.
31 S. Rebeccani, A. Zanut, C. I. Santo, G. Valenti and F. Paolucci, *Anal. Chem.*, 2022, **94**, 336–348.
32 W. Miao, J.-P. Choi and A. J. Bard, *J. Am. Chem. Soc.*, 2002, **124**, 14478–14485.
33 J. Ding, P. Zhou and B. Su, *ChemElectroChem*, 2022, **9**, e202200236.
34 B. D. Muegge and M. M. Richter, *Anal. Chem.*, 2004, **76**, 73–77.
35 S. Zanarini, M. Felici, G. Valenti, M. Marcaccio, L. Prodi, S. Bonacchi, P. Contreras-Carballada, R. M. Williams, M. C. Feiters, R. J. M. Nolte, L. De Cola and F. Paolucci, *Eur. J. Chem.*, 2011, **17**, 4640–4647.
36 A. Kapturkiewicz, *Anal. Bioanal. Chem.*, 2016, **408**, 7013–7033.
37 Q. Zhao, M. Yu, L. Shi, S. Liu, C. Li, M. Shi, Z. Zhou, C. Huang and F. Li, *Organometallics*, 2010, **29**, 1085–1091.
38 E. Kerr, E. H. Doeven, G. J. Barbante, T. U. Connell, P. S. Donnelly, D. J. D. Wilson, T. D. Ashton, F. M. Pfeffer and P. S. Francis, *Eur. J. Chem.*, 2015, **21**, 14987–14995.
39 E. Kerr, D. J. Hayne, L. C. Soulsby, J. C. Bawden, S. J. Blom, E. H. Doeven, L. C. Henderson, C. F. Hogan and P. S. Francis, *Chem. Sci.*, 2022, **13**, 469–477.
40 E. Kerr, S. Knezevic, P. S. Francis, C. F. Hogan, G. Valenti, F. Paolucci, F. Kanoufi and N. Sojic, *ACS Sens.*, 2023, **8**, 933–939.
41 S. Knežević, E. Kerr, B. Goudeau, G. Valenti, F. Paolucci, P. S. Francis, F. Kanoufi and N. Sojic, *Anal. Chem.*, 2023, **95**, 7372–7378.
42 A. Fracassa, C. I. Santo, E. Kerr, S. Knežević, D. J. Hayne, P. S. Francis, F. Kanoufi, N. Sojic, F. Paolucci and G. Valenti, *Chem. Sci.*, 2024, **15**, 1150–1158.
43 S. J. Blom, N. S. Adamson, E. Kerr, E. H. Doeven, O. S. Wenger, R. S. Schaer, D. J. Hayne, F. Paolucci, N. Sojic, G. Valenti and P. S. Francis, *Electrochim. Acta*, 2024, **484**, 143957.
44 C. Costentin, M. Robert and J.-M. Savéant, *Chem. Soc. Rev.*, 2013, **42**, 2423–2436.
45 C. Costentin and J.-M. Savéant, *ChemElectroChem*, 2014, **1**, 1226–1236.
46 F. Kanoufi, Y. Zu and A. J. Bard, *J. Phys. Chem. B*, 2001, **105**, 210–216.
47 M. J. Chalkley, P. Garrido-Barros and J. C. Peters, *Science*, 2020, **369**, 850–854.
48 R. Deeba, S. Chardon-Noblat and C. Costentin, *Chem. Sci.*, 2021, **12**, 12726–12732.
49 D. J. Martin, C. F. Wise, M. L. Pegis and J. M. Mayer, *Acc. Chem. Res.*, 2020, **53**, 1056–1065.
50 L. F. T. Novaes, J. Liu, Y. Shen, L. Lu, J. M. Meinhardt and S. Lin, *Chem. Soc. Rev.*, 2021, **50**, 7941–8002.
51 O. V. Klymenko, I. Svir and C. Amatore, *Mol. Phys.*, 2014, **112**, 1273–1283.
52 J.-M. Savéant, *Chem. Rev.*, 2008, **108**, 2348–2378.
53 A. R. Akbashev, *ACS Catal.*, 2022, **12**, 4296–4301.
54 R. Y. Lai and A. J. Bard, *J. Phys. Chem. A*, 2003, **107**, 3335–3340.
55 C. Costentin, *ACS Catal.*, 2020, **10**, 6716–6725.
56 C. Costentin and J.-M. Savéant, *ACS Catal.*, 2018, **8**, 5286–5297.
57 J. M. Savéant and K. B. Su, *J. Electroanal. Chem. Interf. Electrochem.*, 1984, **171**, 341–349.
58 C. Costentin and J.-M. Savéant, *J. Am. Chem. Soc.*, 2017, **139**, 8245–8250.
59 C. Costentin and J.-M. Savéant, *Nat Rev Chem*, 2017, **1**, 1–8.
60 C. Costentin, *ACS Catal.*, 2021, **11**, 5678–5687.
61 C. Costentin, S. Drouet, M. Robert and J.-M. Savéant, *J. Am. Chem. Soc.*, 2012, **134**, 11235–11242.

62 X. Guo, Y. Okamoto, M. R. Schreier, T. R. Ward and O. S. Wenger, *Chem. Sci.*, 2018, **9**, 5052–5056.
63 M. Sentic, M. Milutinovic, F. Kanoufi, D. Manojlovic, S. Arbault and N. Sojic, *Chem. Sci.*, 2014, **5**, 2568–2572.
64 Y. Zu and A. J. Bard, *Anal. Chem.*, 2000, **72**, 3223–3232.
65 Z. Chen and Y. Zu, *J. Phys. Chem. C*, 2008, **112**, 16663–16667.
66 K. Imai, G. Valenti, E. Villani, S. Rapino, E. Rampazzo, M. Marcaccio, L. Prodi and F. Paolucci, *J. Phys. Chem. C*, 2015, **119**, 26111–26118.
67 E. H. Doeven, E. M. Zammit, G. J. Barbante, P. S. Francis, N. W. Barnett and C. F. Hogan, *Chem. Sci.*, 2013, **4**, 977–982.
68 E. Kerr, E. H. Doeven, D. J. D. Wilson, C. F. Hogan and P. S. Francis, *Analyst*, 2016, **141**, 62–69.
69 J. M. Fernandez-Hernandez, E. Longhi, R. Cysewski, F. Polo, H.-P. Josel and L. De Cola, *Anal. Chem.*, 2016, **88**, 4174–4178.
70 E. Longhi, J. M. Fernandez-Hernandez, A. Iordache, R. Fröhlich, H.-P. Josel and L. De Cola, *Inorg. Chem.*, 2020, **59**, 7435–7443.
71 Y. Wang, J. Ding, P. Zhou, J. Liu, Z. Qiao, K. Yu, J. Jiang and B. Su, *Angew. Chem. Int. Ed.*, 2023, **62**, e202216525.

Chapter III:
Using Redox Mediators for ECL Enhancement in Heterogeneous Systems: Bead-Based Assays and Bimodal Imaging of Cells

Chapter III: Using Redox Mediators for ECL Enhancement in Heterogeneous Systems: Bead-Based Assays and Bimodal Imaging of Cells

3.1 Introduction

The process of diagnosing diseases often begins with the analysis of a patient's bodily fluids, which involves the *in vitro* detection of biomarkers specific to certain illnesses. These biomarkers are typically protein structures such as hormones, enzymes, tumour markers, viral proteins, and antibodies. Accurate and reliable detection of specific biomarkers is crucial for early disease identification and treatment. However, the volumes of patient samples available for biomarker determination are often limited, especially in cases like neonatal blood, where an increasing number of analytes must be identified from a single sample.[1] As the disease progresses, the concentration of biomarkers gradually increases and spreads from the infected area throughout the body, making their concentration in bodily fluids often extremely low. This low concentration can make early-stage disease diagnostics challenging. Medical staff are thus faced with the choice of either performing invasive procedures to obtain samples with potentially higher concentrations of target biomarkers or relying on blood analysis and risk diagnosing the disease at a later stage. Consequently, developing more sensitive methods for biomarker detection is imperative. Additionally, the presence of other biological structures within the sample can cause significant interference, even after sample purification, conditioning the need for using methods selective to specific target biomarkers. Moreover, given the high number of samples processed in commercial biomedical laboratories, rapid analysis is essential, driving the need for multiplexing, faster methods, and advanced laboratory instruments.[1]

Therefore, an ideal method for biomarker determination should be fast, highly sensitive, specific to the target analyte, and capable of analysing multiple analytes from the same sample. Furthermore, the methods' safety and environmental impact are important considerations for commercial implementation in biomedical laboratories.

One method that meets all these criteria is ECL, which can effectively utilise a heterogeneous immunoassay approach. The ECL system at the basis of the design and operation of commercially available ECL instrumentation comprises $[Ru(bpy)_3]^{2+}$ luminophores constrained at the electrode surface (e.g., on magnetic beads) with freely diffusing TPrA. Approximately two billion bead-based ECL immunoassays for the detection of biomarkers in body fluids are conducted worldwide each year.[1] The Cobas system (commercialized by Roche Diagnostics) is a popular benchtop pathology instrument that, coupled with Elecsys immunoassays, enables the sensitive, rapid, and specific detection of over 100 different biomarkers for *in vitro* diagnostics.[1] Elecsys immunoassays predominantly employ a classic bead-based sandwich immunoassay design, where target biomarkers are trapped between a magnetic bead coated with a capture antibody and a detection antibody. A detection antibody is labelled with a $[Ru(bpy)_3]^{2+}$ derivative, and a capture antibody is labelled with a biotin group. These antibodies are combined with the analyte-containing biological sample and allowed to form an immuno-complex, then mixed with streptavidin-coated magnetic microparticles. The immuno-complex-modified magnetic beads are subsequently injected into an electrochemical cell with the working electrode positioned over a magnet to capture the magnetic particles.[1] An electrochemical potential is applied to the cell, and the resulting ECL from the $[Ru(bpy)_3]^{2+}$ label is captured using a photomultiplier tube positioned above the flow cell; the intensity of the ECL signal is proportional to the analyte concentration.[1]

Such assays where the ECL labels are immobilized on an insulating bead and the co-reactant is freely diffusing in solution are termed “heterogeneous,” as opposed to homogeneous (solution-phase) systems. In the “heterogeneous” experimental setup, direct oxidation of $[Ru(bpy)_3]^{2+}$ is impeded as the majority of labels are positioned far from the electrode surface, beyond the electron tunnelling distance of *ca.* 1-3 nm. Consequently, the oxidative-reductive mechanism, involving the electrooxidation of both $[Ru(bpy)_3]^{2+}$ and TPrA followed by an exergonic reaction between a $TPrA^{\bullet}$ radical and $[Ru(bpy)_3]^{3+}$ to produce the excited state $[Ru(bpy)_3]^{2+*}$ of the labels, is not viable. Instead, all the redox reactions leading to ECL emission must be initiated by the electrogenerated TPrA radicals. The heterogeneous oxidation of TPrA yields $TPrA^{\bullet+}$ radical cation, a moderately strong oxidant that undergoes spontaneous and rapid deprotonation, forming a strongly reducing $TPrA^{\bullet}$ radical. Thus, in the

so-called “heterogeneous” or “remote” route, that operates in the bead-based systems, $TPrA^{\bullet}$ reduces $[Ru(bpy)_3]^{2+}$ to $[Ru(bpy)_3]^{+}$, which then reacts with $TPrA^{\bullet+}$ to generate ECL. [2]

Recently, research efforts have focused on analyzing bead-based systems to amplify ECL intensity and enhance assay sensitivity by improving the efficiency of underlying mechanistic pathways and modifying the instrumental setup. One approach involves imaging the spatial distribution of ECL at single beads labelled with the $[Ru(bpy)_3]^{2+}$ luminophore. This reactivity mapping technique provides valuable insights into coreactant efficiency,[3] label stability,[4] ECL emission dynamics,[5] and optical effects resulting from light propagation through the bead.[6] Specifically, ECL intensity and its evolution in time are related to the electrode surface properties (which can be improved by cathodic treatment) and the efficiency of the TPrA oxidation step.[4,5] In general, ECL emission occurs in the micrometric region (*ca.* 3 µm from the electrode) where concentrations of both TPrA radicals are locally the highest, and it is limited by the short half-life of $TPrA^{\bullet+}$ (of *ca.* 200 µs).[3] Thus, the emission intensity and expansion of the luminescent layer can be controlled by optimizing the deprotonation rate of $TPrA^{\bullet+}$. This was achieved by adjusting the pH and ionic strength of the supporting electrolyte, as revealed by ECL imaging.[7] Using ECL microscopy in combination with other analytical techniques, Zanut et al. reported the detection of a transient TPrA radical, formed through cleavage of a C–N bond within close proximity to the electrode surface.[8] This radical contributes to an ECL enhancement of up to 128%. within the $[Ru(bpy)_3]^{2+}$/TPrA bead-based assay. ECL mapping revealed the contribution of a new pathway to ECL generation at distances closer than 1 µm. This additional mechanism exhibits a very high efficiency since it gave a 10 times more intense signal than the one further from the electrode surface (> 1 µm). In addition, enhanced ECL emission was demonstrated through the decrease of bead size and the incorporation of a branched amine additive in the reactant mixture, both aiming to promote the formation of this radical and utilise the resulting additional reaction step.[8] Thus, understanding the mechanisms operating in these heterogeneous ECL applications facilitated the development of new strategies towards ECL enhancement.

Furthermore, proof-of-concept homogeneous ECL experiments are frequently used to demonstrate improvements in analytical sensing before their incorporation into a heterogeneous assay. The examples involve the approaches which aim to enhance ECL generation by utilising gold-coated[9] or carbon nanotubes (CNTs) modified[10] magnetic beads.

The main idea was to extend the ECL emission further from the electrode surface by using conductive materials. The homogeneous light emission observed from the bead surface, regardless of the distance from the electrode, suggests that both the gold coating and the CNTs network facilitate electron transfer reactions, thereby improving the efficiency of the remote route by generating transient TPrA radicals directly at the bead surface. Moreover, $[Ru(bpy)_3]^{2+}$ labels can undergo heterogeneous oxidation at the conductive surface of the bead, introducing an additional pathway for ECL generation. The ECL generation via the "remote" route results in a 21.7-fold increase in the turnover frequency of ECL generation compared to the non-conductive beads. Extending this approach, by decorating beads of different sizes with distinct capture antibodies, offers a means for multiplexed immunosensing of several acute myocardial infarction biomarkers,[9] which eliminates the need for additional fluorescent staining of beads that carry different antibodies.[11] Finally, Feng's group achieved remarkable sensitivity, resolution and specificity in a bead-based ECL bioassay by using ECL imaging to map the spatial distribution of single $[Ru(bpy)_3]^{2+}$-labelled biomarker molecules.[12] This approach enables ultra-sensitive detection and counting of individual target molecules, with a 67-attomolar detection limit. The practical feasibility of this method is subsequently demonstrated by quantification of carcinoembryonic antigen in human serum samples.

Recently, Kerr et al. proposed a novel method of enhancing homogeneous ECL from the $[Ru(bpy)_3]^{2+}$ and TPrA system via the incorporation of $[Ir(sppy)_3]^{3-}$ (where sppy = 2-(2-pyridinyl-κ*N*)-4-sulfonatophenyl-κ*C*, **Figure 3.1A**) to the experimental solution.[13] **Figure 3.1B** shows CVs of solutions containing $[Ir(sppy)_3]^{3-}$, $[Ru(bpy)_3]^{2+}$ and TPrA (commercial ProCell solution). Enhancement of ECL from $[Ru(bpy)_3]^{2+}$ by up to 10.8-fold was observed with the addition of a $[Ir(sppy)_3]^{3-}$ at low anodic potentials (0.85 V vs Ag/AgCl), where $[Ru(bpy)_3]^{2+}$ is not oxidised.

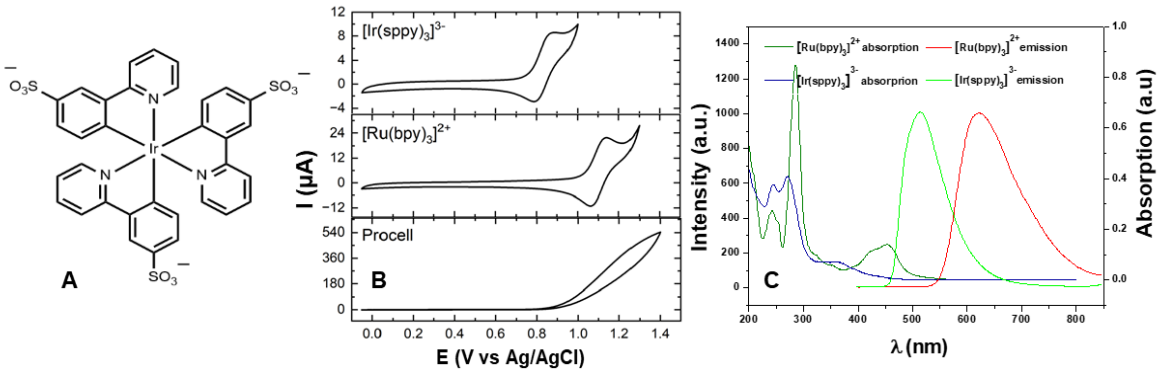

Figure 3.1. **(A)** Structure of $[Ir(sppy)_3]^{3-}$ mediator. **(B)** Cyclic voltammograms of 1 mM $[Ir(sppy)_3]^{3-}$ and 1 mM [Ru(bpy)3]2+ in 0.1 M phosphate buffer, pH 7.5, and of ProCell solution. **(C)** Absorption spectrum of $[Ru(bpy)_3]^{2+}$ (olive plot) and $[Ir(sppy)_3]^{3-}$ (royal blue plot) and normalized photoluminescence emission spectrum of $[Ru(bpy)_3]^{2+}$ (red plot) and $[Ir(sppy)_3]^{3-}$ (green plot). Complex concentration: 10 µM in water at ambient temperature. Reproduced from[13].

Considering the spectral properties of the two luminophores (**Figure 3.1C**), the energy transfer pathway is disfavored. Hence, the authors proposed, along the classic "remote" route (**Figure 3.2A**), a redox-mediated ECL enhancement pathway, outlined in **Figure 3.2B**. Initially, $[Ru(bpy)_3]^{2+}$ is reduced by $TPrA^{\bullet}$ to form $[Ru(bpy)_3]^{+}$. In addition to its reaction with $TPrA^{\bullet+}$, $[Ru(bpy)_3]^{+}$ may also react with $[Ir(sppy)_3]^{2-}$ (produced via direct oxidation of $[Ir(sppy)_3]^{3-}$ at the electrode surface), to form $[Ru(bpy)_3]^{2+*}$ and undergo subsequent radiative decay.[13] Furthermore, the theoretical study in **Chapter 2** suggests a significant role of homogeneous oxidation of TPrA by the electrooxidized $[Ir(sppy)_3]^{2-}$ species (**Figure 3.2C**) in the ECL behaviour of the mixed $[Ir(sppy)_3]^{3-}$/$[Ru(bpy)_3]^{2+}$/TPrA coreactant system within the "homogeneous" (solution-phase) setup.

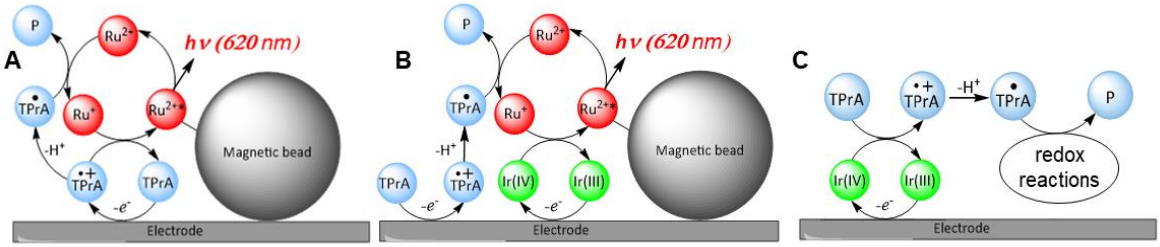

Figure 3.2. Schematics of the **(A)** the conventional heterogeneous ECL route, **(B)** redox-mediated ECL enhanced route in a heterogeneous bead-based ECL sensor format, and **(C)** homogeneous oxidation of TPrA via the electrogenerated $[Ir(sppy)_3]^{2-}$. Ru^{2+} and Ir(III) represent the $[Ru(bpy)_3]^{2+}$ derivative used as an ECL label (denoted below as Ru@PS) decorating the micrometric bead and the $[Ir(sppy)_3]^{3-}$ redox mediator, respectively.

Herein, we evaluate this $[Ir(sppy)_3]^{3-}$-mediated enhancement strategy in a bead-based format using ECL microscopy to determine if this pathway translates to increased ECL signals in a model heterogeneous ECL assay. We demonstrate that the previously observed

enhancement of $[Ru(bpy)_3]^{2+}$ ECL at low oxidation potentials in homogeneous ECL experiments translates to an enhancement in a heterogeneous assay, which has particular promise for improving the sensitivity and reproducibility of analytical ECL systems.[13] Furthermore, we demonstrate the versatility of the $[Ir(sppy)_3]^{3-}$-mediated ECL enhancement approach by examining an alternative co-reactant, 2-(dibutylamino)ethanol (DBAE).[14]

Finally, in line with the recent trends in ECL, we seek to extend the application of the developed "mixed-luminophore" approach to advance the area of ECL imaging. Like in dramatic arts or painting with the "chiaroscuro" technique, ECL microscopy plays with a clever arrangement of light and dark. Two main modes of ECL imaging can be distinguished: "positive"[15–21] and "negative" (or "shadow")[22–25] ECL (**Figure 3.3**). In positive ECL (PECL), the entities under investigation (e.g. micro- or nanoparticles, labelled cells or immunosensing beads) are either electroactive and can directly generate ECL[18,26] or are labelled with an ECL-active luminophore[8,27] in which case ECL generation follows the "remote" route (**Figure 3.2A**). In both scenarios, these entities appear as bright objects against a dark background (**Figure 3.3B**), similar to the images obtained in fluorescence microscopy (**Figure 3.3A**). Conversely, in the negative ECL mode (SECL), both the luminophore and co-reactant are freely diffusing in the solution and the objects to be imaged are deposited on the electrode surface. In this mode, the insulating objects (e.g. cells, organelles, microparticles, or fingerprints) hinder the diffusional flux of the ECL reagents and they are imaged as dark objects against a bright background (**Figure 3.3C**).

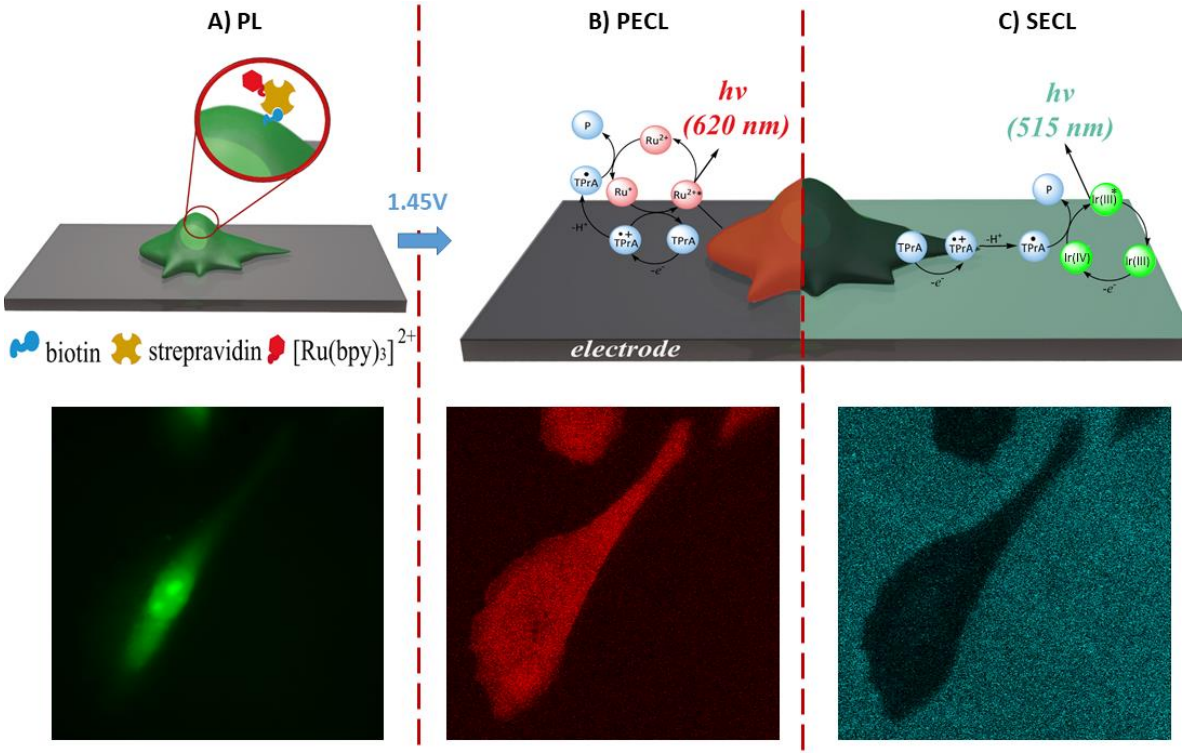

Figure 3.3. (Top) Schematic representation of bimodal imaging of a cell immobilized on a glassy carbon electrode (GCE): **(A)** PL, **(B)** PECL, and **(C)** SECL. Mechanisms of co-reactant PECL (heterogeneous route involving mainly dissolved TPrA and SA@Ru label immobilized on the cell) and SECL (homogeneous route involving only dissolved $[Ir(sppy)_3]^{3-}$ and TPrA) modes. Ru^{2+} and Ir(III) represent the ECL SA@Ru-label and $[Ir(sppy)_3]^{3-}$, respectively. (Bottom) The same single CHO-K1 cell was imaged by **(A)** PL, **(B)** PECL, and **(C)** SECL. Scale bar: 30 µm.

SECL detection principle is somewhat similar to that of the negative feedback mode of scanning electrochemical microscopy (SECM). However, while SECM uses an electrochemical probe to scan the surface of an object under investigation, SECL provides global electrochemical information in a single image, eliminating the need for scanning and its associated drawbacks. The SECL approach is a label-free method and it presents some conceptual similarities with the fluorescence-based label-free microscopies (*e.g.* super-resolution shadow imaging (SUSHI) or some variants of stimulated emission depletion (STED) microscopy), where the diffusible luminophore does not permeate cellular membranes.[28–31]

Both PECL and SECL have been used extensively in ECL imaging.[32] For example, labelling the cellular membrane proteins with $[Ru(bpy)_3]^{2+}$ allows one to image the expression of proteins, membrane transport properties and processes occurring in the vicinity of the

electrode surface using PECL.[17,27,33–35] The diagnostic application of this approach was demonstrated by labelling a plasma receptor overexpressed in tumour cells.[34] The spatial confinement of ECL could be tuned with different experimental strategies[7,8,23,36] and is mainly controlled by the short half-lives of electrogenerated TPrA radicals that react with the luminophore, enabling the formation of the excited state.

The main downside of PECL is the relatively low luminescence intensity, a consequence of the limited number of molecular luminophores attached as labels,[17,27] even if ECL-active nanoparticles may be used to detect single biomolecules.[34,37] The emission intensity further decreases with each applied chronoamperometric pulse due to the depletion of co-reactant in the diffusion layer and surface passivation of the electrode but slightly improves after cathodic surface regeneration treatment.[38] Attempts to perform ultrasensitive ECL analysis, which would enable single-protein detection, required the use of $[Ru(bpy)_3]^{2+}$-doped silica/Au nanoparticle (nanoemitter)-labelled antibodies that can bind to membrane proteins and enhance the intensity of Ru-derived ECL in the presence of TPrA.[34]

Conversely, studying cellular heterogeneity using a negative signal from the unlabeled cell hindering the diffusion of luminophore and co-reactant to the electrode surface – SECL – has been applied to the study of single cells with remarkable spatial resolution,[24] cell-matrix adhesions,[39] morphological changes under oxidative stress,[40] migration of living cells[39] and even sub-cellular entities (i.e mitochondria).[25] Furthermore, by varying the concentrations of freely diffusing luminophore and coreactant, it is possible to tune the thickness of the otherwise electrode surface confined ECL layer to achieve optimal performance and image cell-cell junctions, upper cell membranes and mitochondria.[23,41,42]

This approach not only provides information on the cell shape and dynamic processes of the cellular adhesions but also can spatially resolve objects along the z-axis, which is not easily achievable using PECL. In addition, SECL microscopy can allow the investigation of the transport properties through membranes. However, since SECL is a label-free approach, it can neither distinguish processes occurring on or inside the cellular membrane nor discriminate the proteins or different biological factors in diverse cells. Thus, these two ECL modes (PECL and SECL) are considered complementary, and their combination can give a variety of information on the structure-function properties and processes that occur in the observed system.

To develop a bimodal ECL approach which combines SECL and PECL, we need to resolve – spectrally, potentiometrically, and/or spatially – ECL emitted by a luminophore in solution phase from ECL produced by a luminophore that is immobilized on a cell membrane. This can be achieved by introducing an additional luminophore to the $[Ru(bpy)_3]^{2+}$/TPrA system. This second luminophore must emit light at a wavelength distinct from that of $[Ru(bpy)_3]^{2+}$ (λ_{max} = 620 nm) to facilitate spectral resolution of the emission from the two luminophores. Therefore, Ir(III) emitters, known for their easily tunable electrochemical and spectral properties, are ideal candidates as the secondary luminophore in a combined SECL and PECL imaging strategy. Furthermore, the previously described green emissive and water-soluble $[Ir(sppy)_3]^{3-}$ mediator (λ_{max} = 515 nm), not only acts as an $[Ru(bpy)_3]^{2+}$ ECL enhancer but can be spectrally resolved from the emission of $[Ru(bpy)_3]^{2+}$ (**Figure 3.1C**) in a mixed solution-phase ECL system with $[Ru(bpy)_3]^{2+}$ and TPrA coreactant.[13]

3.2 Experimental Section

3.2.1 Reagents and apparatus

Phosphate-buffered saline (PBS 10×) solution (pH 7.4), streptavidin from Streptomyces avidinii, bis(2',2-bipyridine)-4'-methyl 4-carboxybipyridine-ruthenium *N*-succinimidyl ester bis(hexafluorophosphate) $[Ru(bpy)_2(mcbpy\text{-}O\text{-}Su\text{-}ester)(PF_6)_2]$ (Ru-NHS) and paraformaldehyde (PFA) were purchased from Sigma-Aldrich. CHO-K1 cells were from Public Health England (HPA) Culture Collections and supplied by Sigma (85051005). ProCell solution, containing a 0.3 M phosphate buffer, 0.18 M TPrA and ≤ 0.1% detergent (pH 6.8), was purchased from Roche. $Na_3[Ir(sppy)_3]$ was purchased from Lumtec. Triton X-100 was purchased from Acros Organic. Iscove's modified Dulbecco's medium, fetal bovine serum, PBS 1× pH 7.4, trypsin and penicillin/streptomycin 100 U/mL were purchased from Gibco. Biotin X was purchased from Fisher Scientific. DMSO was purchased from Invitrogen. All the compounds were used as purchased without further purification. Solutions were prepared in ultrapure (Milli-Q) water unless otherwise specified. Amine-functionalized, 12 µm polystyrene (PS) beads were purchased from Kisker Biotech GmbH & Co and functionalized using a previously described procedure.[3] Streptavidin-ruthenium complex (SA@Ru) synthesis and cell labelling followed the same procedure as in our previous work.[27]

3.2.2 Decorating the PS-beads with Ru-label

Briefly, 10 µL of 2.5% PS beads was diluted in 1 mL of 1× phosphate-buffered saline (PBS) and washed using centrifugation (10 min, 10,000 rpm) prior to resuspension in 1 mL of 1× PBS. Bis(2,2'-bipyridine)-4'-methyl-4- carboxybipyridine-ruthenium N-succinimidyl ester bis- (hexafluorophosphate) ($[Ru(bpy)_2(mbpy\text{-}NHS)]^{2+}$) (1 mg) was dissolved in 100 µL of dimethylsulfoxide and added to the suspension. This suspension was stirred for 3 h at 4 °C. The resulting $[Ru(bpy)_3]^{2+}$ derivative-functionalized PS beads via a peptide bond (noted Ru@PS) were washed 10 times using centrifugation, resuspended in 1 mL of 1× PBS, and stored at 4 °C.

3.2.3 Cell culture, labeling and permeabilization

Iscove's modified Dulbecco's medium (IMDM) supplemented with 10% fetal bovine serum and penicillin/streptomycin 100 U/mL was used to grow cells in an incubator. CHO-K1 cells were trypsinized, plated on a glassy carbon electrode and incubated for 48 h with a culture medium at 37°C, 5% CO_2. Before the ECL experiment, CHO-K1 cells were fixed for 10 min with PFA (4%), permeabilized for 10 min with Triton X-100 (0.1%), labelled with biotin X (11 µM) (1 h incubation step) and 0.1 mg/mL streptavidin-ruthenium complex solution (SA@Ru) for 45 min.

3.2.4 Electrochemistry and ECL

For this work, we used an an a-Clipse C custom-designed electrochemical cell. The cell is designed and produced in our laboratory and is now commercially available at www.idylle-labs.com. The cell housed the working electrode (WE, 3 mm diameter, glassy carbon), reference electrode (RE, Ag/AgCl, 3.5 M KCl), and counter electrode (CE, Pt wire). All potentials are referenced versus Ag/AgCl.

For the bead-based experiments, working electrodes were prepared by drop-casting a small volume (3−6 µL) of polystyrene beads in 1× PBS onto the working electrode surface and allowing the solution to evaporate at room temperature in dark-room conditions. PL micrographs were collected using an FITC-LP filter (Leica, 11525302) of beads at the working electrode (WE) surface prior to applying an electrochemical potential. A single chronoam-perometric (CA) pulse to the designated potential was applied to the WE (versus the RE

potential), and the length of the pulse was varied to ensure the obtained signals were within the linear range of the EM-CCD detector: for top-view experiments in Procell, a 4 s CA pulse to 0.9 V or a 1 s CA pulse to 1.2 V was used; for side-view experiments in Procell, a 2 s CA pulse to 1.2 V was used; for experiments using DBAE as a co-reactant, a 15 s CA pulse was used. Three consecutive measurements were collected at each WE, and the ECL signal was calculated as an average response from the three consecutive measurements.

For bimodal ECL experiments, the potential applied to the working electrode was 1.45 V *vs* Ag/AgCl (KCl, 3 M). PL, SECL and PECL micrographs were collected using FTIC_LP (Leica, number 11525302), FTIC (Leica, number 11525307) and Y5 (Leica, number 11525312) filter cubes, respectively. For multimodal images acquisition 0.3 s, 10 s and 10 s exposure times were used for PL, SECL, and PECL, respectively.

For microscopic imaging, an inverted epifluorescence microscope from Leica (DMI6000, Leica Microsystems) equipped with an ultrasensitive Electron-Multiplying Charge Coupled Device camera (EM-CCD C9100-23B from Hamamatsu, Hamamatsu Japan) was used for all measurements.[17,27] The integrated system also included a potentiostat from Metrohm (PalmSens) suitable to apply the required potential to generate ECL. The exposure time of the EM-CCD camera was set to 1 s longer than the aforementioned CA pulse time, to ensure all ECL emission was captured. A 63× objective (Leica, 11506279) was used for all top-view measurements, and a 40× objective (Leica, 11506155) was used for all side-view measurements.

3.3 Results and Discussion

3.3.1 ECL signal enhancement in the bead-based immunoassays

To examine the effect of the dissolved $[Ir(sppy)_3]^{3-}$ mediator on heterogeneous bead-based ECL assays, we used covalently labelled 12 µm polystyrene (PS) beads functionalized with a $[Ru(bpy)_3]^{2+}$ derivative (denoted Ru@PS beads) as a model system (**Figures 3.2** and **3.4**). Previous research has demonstrated that the ECL observed in such a Ru@PS bead system is an accurate model for that of a heterogeneous bead-based ECL sandwich immunoassay.[3,4,11,36,43] Both photoluminescence (PL) and ECL micrographs (**Figure 3.4**) of single Ru@PS beads exhibited a typical pattern for top-view microscopy experiments (**Figure**

3.4G). ECL profiles were determined using ImageJ software; a detailed image analysis procedure is provided in the **Section 3.5** - Supporting Information.

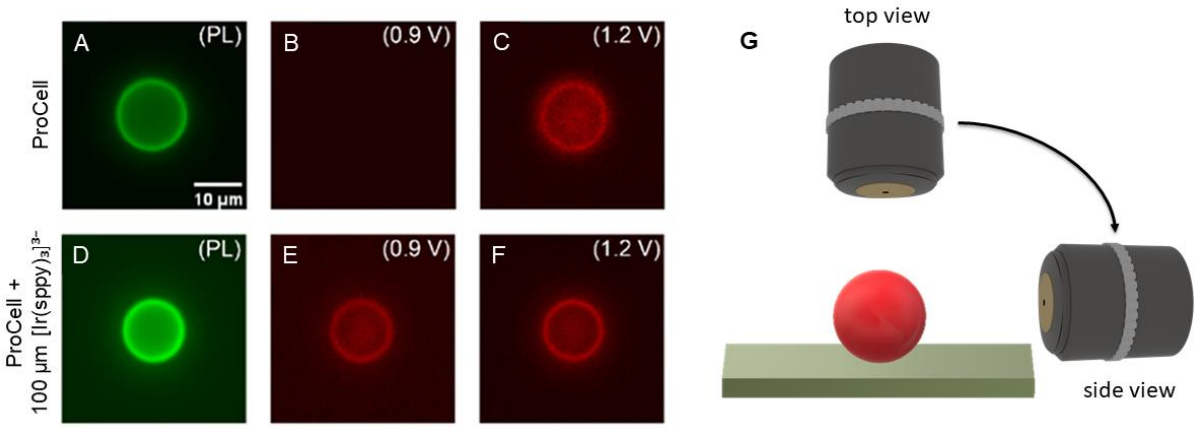

Figure 3.4. Representative micrographs, top-view configuration, of single 12 µm Ru@PS beads using PL (**(A** and **D)**, contrast scale 0–65,000) and ECL mode (**(B** and **C)**, contrast scale 0–12,000, **(E** and **F)**, contrast scale 0 to 45,000). **(A–C)** Obtained in Procell, **(D–F)** obtained in Procell with 100 µM $[Ir(sppy)_3]^{3-}$: **(B** and **E)** 0.9 V, **(C** and **F)** 1.2 V. **(G)** Schematic representation of top and side view configurations used in ECL microscopy.

PL micrographs showed a uniform distribution of $[Ru(bpy)_3]^{2+}$ labels, but in ECL micrographs, nonuniform emission was instead observed across the surface of the bead. The pattern of ECL recorded in top-view experiments with bright ECL at the centre and edges of the bead is primarily due to the optical pathway through the PS bead.[3,6] The ECL from Ru@PS beads in Procell solution at 0.9 V vs Ag/AgCl, below the oxidation potential of $[Ru(bpy)_3]^{2+}$ ($E^{0'}$ = 1.1 V vs Ag/AgCl) but above the oxidation potential of TPrA ($E^{0'}$ ≈ 0.83−0.95 V vs Ag/AgCl)[2,44,45] was barely visible (**Figure 3.4B**). However, the addition of 100 µM $[Ir(sppy)_3]^{3-}$ to the Procell solution, besides contributing to an overall increase of the background luminosity (due to the Ir-based homogeneous ECL), brought about a clear enhancement of the ECL from the Ru@PS beads (**Figure 3.4E**). At 1.2 V vs Ag/AgCl, the ECL from both the conventional and $[Ir(sppy)_3]^{3-}$- mediated systems were visible due to the increased availability of electro-oxidized TPrA radicals at this potential (**Figure 3.1B**). However, the ECL from Ru@PS was significantly brighter with the addition of 100 µM $[Ir(sppy)_3]^{3-}$ (**Figure 3.4C** and **F**). To obtain a quantitative representation of the ECL emission, we extracted the ECL profiles (**Figure 3.5A** and **B**) from each image. The significant increase in the background ECL when 100 µM

$[Ir(sppy)_3]^{3-}$ was added to the solution results from ECL emission from $[Ir(sppy)_3]^{3-*}$; generated via the direct oxidative-reductive pathway with TPrA (**Figure 3.3C**). To examine the effect of the addition of $[Ir(sppy)_3]^{3-}$ on the ECL from the $[Ru(bpy)_3]^{2+}$ derivative labels, we subtracted the background ECL from the raw profiles and calculated the maximum ECL intensity from the resulting background-subtracted profile, which was attributed only to emission from Ru@PS. When 100 µM $[Ir(sppy)_3]^{3-}$ was added to the experimental system, we observed a dramatic 70.9-fold enhancement of ECL from the Ru@PS beads at 0.9 V and a 2.9-fold enhancement at 1.2 V (**Figure 3.5C**). Both values were significantly higher than the ECL enhancement observed in the previous corresponding solution-phase experiments (10.8- and 1.5-fold in the solution phase respectively).[13] The reported approach provides a new strategy for the production of bright ECL signals in the heterogeneous format, which opens new possibilities for ECL sensing and imaging.

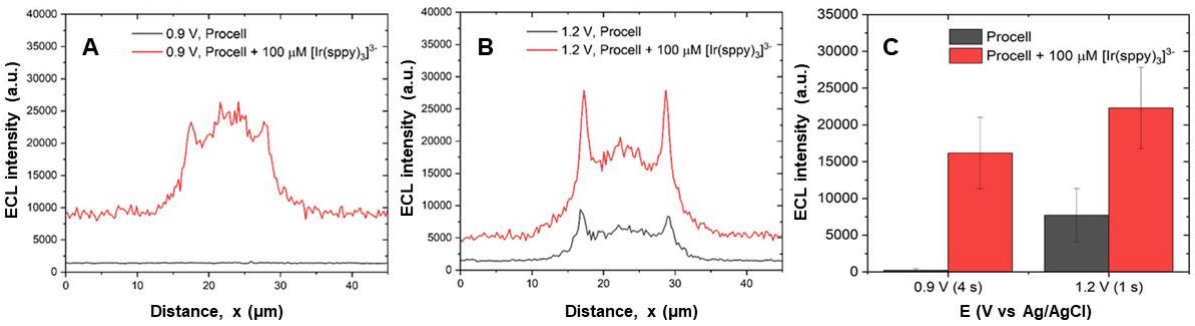

Figure 3.5 (A) and **(B)** Representative profiles of ECL intensity of Ru@PS beads in Procell without and with 100 µM $[Ir(sppy)_3]^{3-}$ at **(A)** 0.9 V, extracted from micrographs **(B)** and **(E)** in **Figure 3.4.** and 1.2 V **(B)**, extracted from **Figure 3.4**, images **(C)** and **(F)**. **(C)** ECL intensities, top-view configuration, n = 6 electrodes, in Procell (grey columns) and Procell with 100 µM $[Ir(sppy)_3]^{3-}$ (red columns) at 0.9 and 1.2 V. Same experimental conditions as in **Figure 3.4**.

The ability to conduct ECL at low oxidation potentials is particularly important for biosensors and cell imaging, where high potentials can cause (i) oxygen evolution reaction (i.e., bubbles at the electrode surface), (ii) ECL background emission, (iii) damage to biological recognition elements or cleavage of the biological recognition elements from solid supports, and (iv) damage to the microfabricated electrode in miniaturized sensing systems due to high currents and/or potentials.[46–49] Furthermore, recent research has demonstrated that the application of high potentials in ECL experiments can lead to an increase in electrode

passivation and deleterious side reactions, both of which decrease the analytical sensitivity of the technique.[4,50] The advantage of being able to conduct ECL at low oxidation potentials, combined with the signal enhancement observed in the $[Ir(sppy)_3]^{3-}$-mediated heterogeneous model assay compared to the standard $[Ru(bpy)_3]^{2+}$ and TPrA system, indicates the promise of this strategy for the development of ultrasensitive heterogeneous ECL assays.

To further investigate the effects of adding 100 µM $[Ir(sppy)_3]^{3-}$ to the ECL system, we used an orthogonal side-view configuration (see **Figure 3.4G**), which can yield information on the width of the ECL-emitting layer (i.e., how far away from the electrode surface ECL can be observed). Considerable research has been conducted in recent years to precisely define and modify the thickness of the ECL-emitting layer.[3,7,36,42,43] The stability of the $TPrA^{\bullet+}$ is a determining factor.[2,3,8] Fiorani et al. demonstrated that by modifying the buffer concentration, the deprotonation rate of $TPrA^{\bullet+}$ could be controlled, enabling the modulation of the concentration profiles of both $TPrA^{\bullet}$ and $TPrA^{\bullet+}$ in the experimental solution and, therefore, the precise modulation of the thickness of the ECL emission layer.[7,51] This approach enables both the improvement of the ECL signal in conventional systems and the examination of substrates of different heights.[7] Furthermore, researchers have exploited the catalytic ECL route to significantly extend the ECL-emitting layer, owing to the comparatively high stability of the $[Ru(bpy)_3]^{3+}$ species compared to $TPrA^{\bullet+}$.[36,42] Based on this research, it could be reasonably hypothesized that the comparatively high stability of the $[Ir(sppy)_3]^{2-}$ species might induce a similar increase in the length of the ECL emissive layer. However, the high local concentration and reactivity of both TPrA radicals should also be considered because they confine the ECL reaction at the electrode surface due to their short lifetimes. Side-view ECL microscopy allows the examination of this phenomenon in the $[Ir(sppy)_3]^{3-}$- mediated ECL system (**Figure 3.6**). These micrographs showed a typical side-view profile, with two visible ECL-emitting regions, one close to the electrode surface, due to ECL emission from Ru@PS, and the second at the top of the bead, due to the optical paths and focusing effect of the bead as previously described.[3,6]

The reflection of the bead on the electrode surface was also clearly visible in both the PL and ECL profiles; ECL emissions at positive z values ($z > 0$) result from luminophores in the solution ($[Ir(sppy)_3]^{3-*}$) or on the bead ($[Ru(bpy)_3]^{2+*}$), and those at negative z values ($z < 0$) result from the reflection of ECL on the electrode surface. Interestingly, when 100 µM

$[Ir(sppy)_3]^{3-}$ was added to the solution, a distinct "shadow" region from ~1.6 to 4.4 µm from the electrode surface was visible in the ECL micrograph (**Figure 3.6D**). This visual effect is, however, attributed to an artifact, likely resulting from tilting of the microscope objective with respect to the bead, which may cause the lower half of the bead to be slightly more visible than the upper half. Furthermore, the bead modifies the pathway of photons emitted by $[Ir(sppy)_3]^{3-}$ luminophores located behind the bead, which propagate through the bead via complex refraction pathways that may alter the emission profile. Outside of the range of the bead, the EM-CCD collects all ECL emission from $[Ir(sppy)_3]^{3-}$ luminophores within the depth of field centred at the focal plane, and this effect, combined with the altered angle of the microscope objective relative to the Ru@PS bead, may account for the observed shadow region. Thus, the observed shadow region may be attributed to the combined effects of bead blocking and the tilting of the microscope objective. This was supported by an examination of the ECL of bare (unlabeled) PS beads. (**insets** in **Figures 3.6B** and **C**). After accounting for both the blocking effect of the bare beads and the angle of the objective, side-view profiles revealed that there is no significant extension in the ECL emissive layer in Procell solutions when $[Ir(sppy)_3]^{3-}$ is added (**Figures 3.6E** and **F**). This could result from inaccuracies in the method of correction for the blocking effect of the beads or the fact that the high concentration of phosphate buffer in Procell (0.3 M) limits the lifetime of $TPrA^{\bullet+}$ and, therefore, propagation of $TPrA^{\bullet}$ into the solution, restricting the distance from the electrode at which reactions essential for ECL emission via the heterogeneous pathway (**Figure 3.2**) can occur.[7]

Despite there being no significant change in the distance-dependent profile of the ECL emission with the addition of $[Ir(sppy)_3]^{3-}$, significant enhancement of the ECL signal from Ru@PS is also observed in the side-view configuration (2.4-fold, **Figure 3.6G**). This enhancement is consistent with the results obtained in the top-view configuration. The similar ECL patterns and the limited extension of the ECL-emitting region observed with and without $[Ir(sppy)_3]^{3-}$ suggest that radiative energy transfer between $[Ir(sppy)_3]^{3-*}$ and Ru@PS is not the dominant process occurring in the heterogeneous bead-based format. It is important to note that, in addition to the previously discussed redox-mediated pathway (**Figure 3.2B**), catalytic generation of $TPrA^{\bullet+}$ by electro-oxidized $[Ir(sppy)_3]^{2-}$ (**Figure 3.2C**), suggested by a simulation of the underlying reaction mechanisms in the homogeneous (solution-phase) system (**Chapter 2**), may also play a role in the ECL enhancement in the heterogeneous ECL systems.

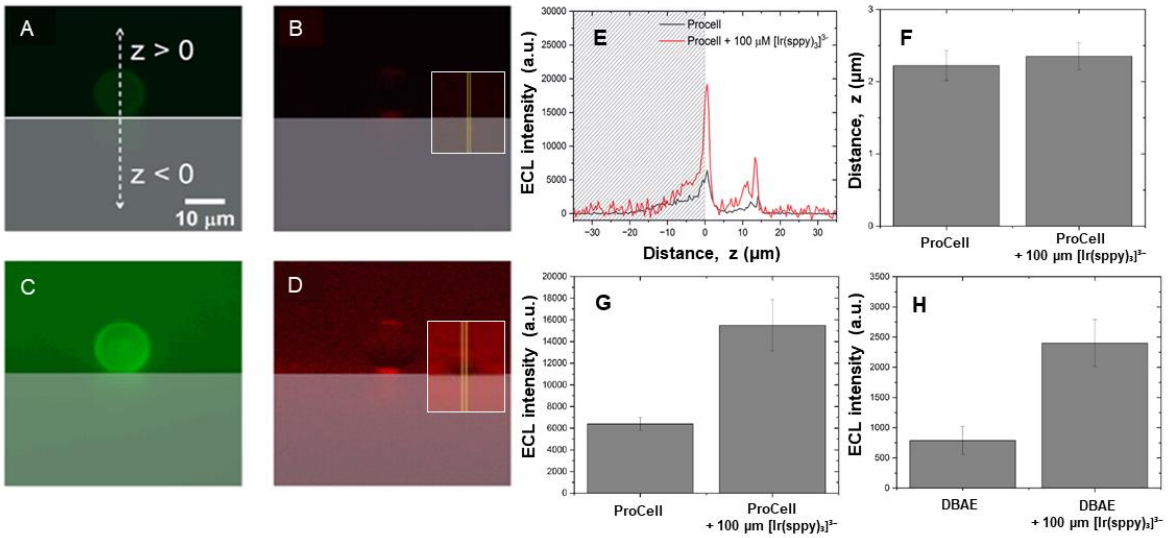

Figure 3.6. Side-view micrographs of 12 µm Ru@PS beads in **(A)** and **(C**) photoluminescence (PL) mode and **(B)** and **(D**) electrochemiluminescence (ECL) mode, with a contrast scale of 0–30,000. The solid horizontal line in **(A)** represents the electrode surface, while the intersecting dashed line indicates the ECL profile. Emission at z > 0 arises from ECL from Ru@PS or $[Ir(sppy)_3]^{3-}$ in solution, and emission at z < 0 is due to the reflection of ECL at the glassy carbon working electrode surface (shaded zone in each micrograph). **(A)** and **(B)** show results obtained in ProCell, while **(C)** and **(D)** show results in ProCell with 100 µM $[Ir(sppy)_3]^{3-}$. Insets in **(B)** and **(D)** display representative ECL micrographs of unlabelled PS beads under the same conditions. **(E)** Representative background-subtracted ECL intensity profiles of Ru@PS beads at 1.2 V in ProCell, with and without 100 µM $[Ir(sppy)_3]^{3-}$. The hatched zone indicates the reflection of ECL on the electrode surface (z < 0 µm). **(F)** ECL intensities and **(G)** thickness of the ECL emission layer in ProCell and ProCell with 100 µM $[Ir(sppy)_3]^{3-}$ at 1.2 V, side-view configuration (n = 4 electrodes). Same experimental conditions as in **(B)** and **(D)**. **(H)** ECL intensities at 1.2 V in 0.1 M, pH 7.4 phosphate buffer with 20 mM DBAE (n = 6 electrodes).

Xu and coworkers first demonstrated homogeneous ECL (i.e., with both ECL reagents dissolved in solution) of $[Ru(bpy)_3]^{2+}$ with DBAE, an alternative amine coreactant.[14] The authors observed ~10 times higher ECL with DBAE as a coreactant compared to TPrA in the solution-phase system at gold electrodes.[14] However, when Sentic et al. examined DBAE as a coreactant in a heterogeneous Ru@PS bead-based model, lower ECL from Ru@PS was observed when using DBAE compared to TPrA.[3] This was attributed to the poor (~10 times

lower) stability of $DBAE^{\bullet+}$ compared to $TPrA^{\bullet+}$, reducing the distance to which DBAE radicals can diffuse into the solution and decreasing the distance from the electrode surface at which ECL can occur.[3] Unlike the solution-phase system examined by Xu et al., where both the direct and the catalytic pathways may contribute to the ECL emission, such routes are unavailable in a heterogeneous bead-based system where the $[Ru(bpy)_3]^{2+}$ label is immobilized on the surface of a bead (**Figure 3.2A**), thus resulting in significantly weaker emissions. When DBAE was combined with $[Ir(sppy)_3]^{3-}$, however, the ECL observed from Ru@PS was 3.1-fold higher compared to DBAE alone at 1.2 V (**Figure 3.6H**). This would suggest that a similar $[Ir(sppy)_3]^{3-}$-mediated enhancement mechanism occurs with both TPrA and DBAE as a co-reactant.

As a rule of thumb, the catalytic generation of both amine radical cations by electro-oxidized $[Ir(sppy)_3]^{2-}$ (**Figure 3.2C**) should occur at rates comparable with the values reported for the electro-oxidized $[Fe(bpy)_3]^{3+}$.[44] Furthermore, since both redox mediators have comparable $E^{0'}$ and similar ligand structures, they would likely have similar outer-sphere-type self-exchange electron transfer. Expected values for the rate constants of these electron transfers (mediating the oxidation of amine and $[Ru(bpy)_3]^{+}$) would be in the range of 10^4 to 10^5 M^{-1} s^{-1}, sufficient to explain the ECL enhancement at the $[Ir(sppy)_3]^{3-}$ oxidation potential. Indeed, based on a finite element simulation and foot of the wave analysis of the experimental CV plots (see **Chapter 2**), the rate constants of these homogeneous oxidations are $3 \cdot 10^3$ M^{-1} s^{-1}, and $3 \cdot 10^5$ M^{-1} s^{-1}, which is in line with the expected values.

It is important to note that the ECL intensity observed from the DBAE system was much lower than that observed in Procell; for DBAE, a 15 s pulse time was needed to obtain a substantial ECL signal at 1.2 V, compared to 1 s for Procell. Similarly, the ECL from a heterogeneous ECL format was 7-fold lower when using DBAE as a co-reactant compared to TPrA.[3] Nevertheless, the consistency of the enhancement of ECL from Ru@PS with both TPrA and DBAE as a co-reactant demonstrates the versatility of the $[Ir(sppy)_3]^{3-}$-mediated ECL approach.

3.3.2 Bimodal and bicolour imaging of cells

As discussed above, the redox characteristics of $[Ir(sppy)_3]^{3-}$ allow it to mediate the homogeneous oxidation of TPrA and $[Ru(bpy)_3]^{+}$, thereby enhancing the ECL emission from $[Ru(bpy)_3]^{2+}$. However, unlike other redox mediators such as $[Fe(bpy)_3]^{3+}$,[44] $[Ir(sppy)_3]^{3-}$ is both

luminescent and ECL active, with distinct spectral properties compared to $[Ru(bpy)_3]^{2+}$ (**Figure 3.1C**). If $[Ir(sppy)_3]^{3-}$ is present in a solution along with TPrA as a sacrificial coreactant, the excited state of $[Ir(sppy)_3]^{3-}$ can be populated at low anodic potentials (*ca.* 0.85 V vs Ag/AgCl) through the classic oxidative-reductive route (**Figure 3.3C**). The radiative decay of this excited state emits green light with a maximum of approximately 515 nm, which can be distinguished from the emission of $[Ru(bpy)_3]^{2+}$ (λ_{max} = 620 nm) using appropriate filters or diffraction grids.

Additionally, since ECL in the $[Ru(bpy)_3]^{2+}$/TPrA system can occur without the direct electrooxidation of $[Ru(bpy)_3]^{2+}$ (see **Figure 3.2A**), $[Ru(bpy)_3]^{2+}$ can be used to label insulating objects on the electrode surface, as shown previously with polystyrene beads. In this scenario, the emission from $[Ru(bpy)_3]^{2+}$ labels and $[Ir(sppy)_3]^{3-}$ in solution are spatially separated and highlight different regions of the electrode: $[Ru(bpy)_3]^{2+}$ labels illuminate the surface of objects under investigation (**Figure 3.3B**), while $[Ir(sppy)_3]^{3-}$ produces ECL confined to the bare electrode surface, avoiding the regions where its diffusion is obstructed by the imaged objects (**Figure 3.3C**).

Here, we resolve the ECL emissions of the $[Ru(bpy)_3]^{2+}$ and $[Ir(sppy)_3]^{3-}$ both spectrally and spatially to develop a bimodal (combined SECL and PECL) approach for imaging single cells, thereby enhancing the information obtained from biological ECL imaging. In developing this approach, the adherent CHO-K1 cells were grown on the GCE surface. The cells were permeabilized with Triton X-100 as classically performed in immunofluorescence or Western blot methods[27,52,53] and the SA@Ru labels were attached to membrane proteins using the well-known streptavidin-biotin interactions. Biotin unselectively binds to the primary amino groups of membrane proteins, which enables attachment of the SA@Ru to the entire cell membrane. This type of labelling was chosen as a proof-of-concept approach to demonstrate the complementarity of information obtained in two ECL modes – SECL and PECL – and the applicability of SA@Ru (PECL) and $[Ir(sppy)_3]^{3-}$ (SECL) emissions to image distinct features, that may be difficult to observe using traditional PL imaging strategies (primarily the morphology of the cell, cell-surface adhesions, cell-cell junctions transport and transport through the permeabilized membrane). The electrodes decorated with cells were immersed in a custom-made electrochemical cell suitable for microscopy,[17,27] containing 100 µM $[Ir(sppy)_3]^{3-}$ in a commercially available ProCell buffer solution (0.18 M TPrA).

We used a wide-field microscope to obtain a PL image of the cells immobilized on the non-transparent GCE surface in a reflection mode and through the solution (**Figure 3.3**). For the PL microscopy, a filter set suitable to detect the emission from the $[Ru(bpy)_3]^{2+}$ luminophore was chosen. In other words, PL images show the SA@Ru labelling sites on the whole surface of the cellular membrane, proving that there are no unlabeled regions. The background PL signal, already high due to the autoluminescence and the excitation light scattering by the non-transparent GCE surface, is increased owing to the presence of the $[Ir(sppy)_3]^{3-}$ luminophore in the solution. Turning off the excitation light and applying a constant 1.45 V potential pulse resulted in ECL imaging of the identical location using the emission of $[Ru(bpy)_3]^{2+}$ and $[Ir(sppy)_3]^{3-}$ complexes. The luminescence of the two is discriminated using suitable bandpass emission filters (see experimental section) to create two complementary ECL images: PECL derived from $[Ru(bpy)_3]^{2+*}$ (i.e. SA@Ru*) and SECL derived from $[Ir(sppy)_3]^{3-*}$ (**Figures 3.3** and **3.7**). As previously discussed, ECL emission of SA@Ru follows the cascade of reactions initiated by the oxidation of TPrA and $[Ir(sppy)_3]^{3-}$ (see **Figures 3.2** and **3.3B**), to produce its excited state at the level of the plasma membrane, leading *in fine* to the local ECL emission at 620 nm.[2,3,13,54] In brief, these mechanisms (i.e. the remote, redox-mediated[13] and electrocatalytic pathways) may occur with different prevalence in the case of PECL microscopy resulting in the emission at 620 nm. For SECL with light emission at 515 nm, the excited state $[Ir(sppy)_3]^{3-*}$ results from the oxidation of TPrA and $[Ir(sppy)_3]^{3-}$ at the electrode surface and their subsequent reaction in the homogeneous phase (**Figure 3.3C)**. More complex mechanisms with competitive pathways, described in **Chapter 2**, are possible as well[2,13].

Regardless of the underlying ECL mechanism, both PECL and SECL images enable visualization of a larger area of the plasma membrane in comparison to PL, showing finer membrane details and extended cellular structures such as different cell-electrode adhesions along the cell margin (**Figure 3.3**). Similarly, **Figure 3.7** displays two cells during the mitosis process (i.e. cell division). The PECL image reveals the entire surface-confined area of the cells, which is in good agreement with the PL image, except for the two dark regions in the middle of the nuclei. Notably, visualization of the cells by PECL is possible only when their membranes are permeabilized, allowing TPrA to diffuse to the electrode surface.[27] Since the PL micrograph clearly shows that the whole plasma membrane was labelled, the observed dark areas in the

PECL image do not indicate the absence of the luminophore in these zones but rather the local hindrance of the TPrA diffusion to the electrode, which affects the PECL but not the PL mode. As previously described in the literature,[27] the reason for this diffusional hindrance is the presence of nucleoli: RNA-producing structures in mammalian cell nuclei. These organelles have a membrane that is less susceptible to the influence of surfactants and to the permeabilization procedure. Thus, the membrane of the nucleoli remains impermeable, blocking the diffusion of the coreactant and its subsequent oxidation at the electrode surface. As a result, the ECL reaction cascade is not triggered in these regions, causing them to appear darker than their surroundings.[27]

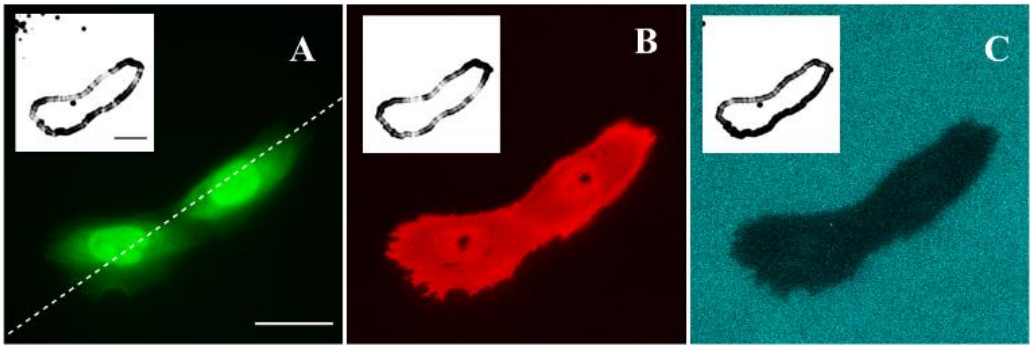

Figure 3.7. (A) PL, **(B)** PECL (showing only SA@Ru ECL emission) and **(C)** SECL (showing only $[Ir(sppy)_3]^{3-}$ emission) micrographs of the same cells. The images are recorded in Procell with 100 µM $[Ir(sppy)_3]^{3-}$. Dotted line denotes a direction in which PL and ECL intensity profiles were extracted. **Inset A**: PL to SECL, **inset B**: PL to PECL, and **inset C** SECL to PECL difference SSIM maps. Scale bar: 30 µm.

Conversely, SECL imaging mode relies on the cells hindering the diffusion of one or both ECL reagents to the electrode. Therefore, if the iridium complex cannot diffuse through the plasma membrane, the SECL micrograph should ideally be the opposite of the PECL one. Indeed, **Figure 3.7** shows that, except for the nucleoli, both ECL modes uncover the total area of the cells, but with inverted bright and dark regions. The comparison of both ECL modes (PECL *vs* SECL) indicates that the TPrA coreactant can diffuse through the permeabilized plasma membrane, as evidenced by the cells being visible in PECL. Conversely, the diffusion of the $[Ir(sppy)_3]^{3-}$ complex is hindered under the reported experimental conditions, resulting in the cells remaining dark in SECL due to the membrane blocking the $[Ir(sppy)_3]^{3-}$ diffusion. This

is important because it demonstrates that the transport through the cell membranes of different molecules involved in the ECL process can be discriminated by combining SECL and PECL. While its size can contribute to the slower diffusion of the Ir(III) complex, other parameters may also affect transport through the cell membranes and thus the final SECL signal. Indeed, other iridium complexes have been successfully used for cell staining.[55–57] It was reported that the charge, amphiphilicity and protein binding characteristics of the iridium complexes are crucial for their distribution and staining performance.[55] Since the reported complexes are positively charged and have different polarity than $[Ir(sppy)_3]^{3-}$, they may have distinct transport properties through the net negatively charged cellular membrane and SECL microscopy could allow resolving such differences.

By further analysing the cells in **Figure 3.7**, one can observe they are at the last stage of mitosis. The nuclei are well-separated, but the plasma membranes of each cell are not completely disconnected. In this region, the cell-cell contacts of the plasma membranes are visible in PL in **Figure 3.7A** but with a low contrast. On the other hand, this thin inter-cell region of the plasma membranes is easily visualized in both PECL and SECL micrographs. It emits a strong ECL emission in PECL and remains completely dark in SECL. Indeed, ECL is a surface-confined process triggered by an initial electron-transfer reaction. The thin cell-cell junction blocks the ECL process, leading to strong positive or negative signals, which are easy to detect in both PECL and SECL modes, respectively.

To confirm these observations and provide more details about the information revealed using different modes, we constructed structure similarity index measurement (SSIM) maps (**insets Figure 3.7**). SSIM maps depict morphological differences between images obtained using PL and SECL (**Inset Figure 3.7A**), PL and PECL (**Inset Figure 3.7B**) and SECL and PECL (**Inset Figure 3.7C**), with SSIM indexes being 0.925, 0.94 and 0.91, respectively. These indexes are numbers scaled from 0 to 1, describing the level of similarity between the two images, with 1 being a perfect match. The high index values (above 0.9) obtained for all combinations of the images confirm that the areas displayed on all of them are the same, with the distinct regions on the cell periphery indicating the above-mentioned differences in the ability of PL and ECL to resolve fine structural details and disparities of the thin cell-electrode adhesions and cell-cell junctions. Furthermore, SSIM difference maps for PL/SECL and PECL/SECL show several pixels near the edge of the image and one on the top border of the

cell. This difference is due to slight variations in the SSIM map generation process. Namely, to create the maps, it is necessary to threshold the original microscopic images and to condense the total information about the intensities of pixels to only two: black and white. Consequently, depending on the contrast and the occurrence of incidentally brighter/darker pixels in each mode, the chosen threshold will not be identical, additionally contributing to the differences in the ISSM maps and indexes.

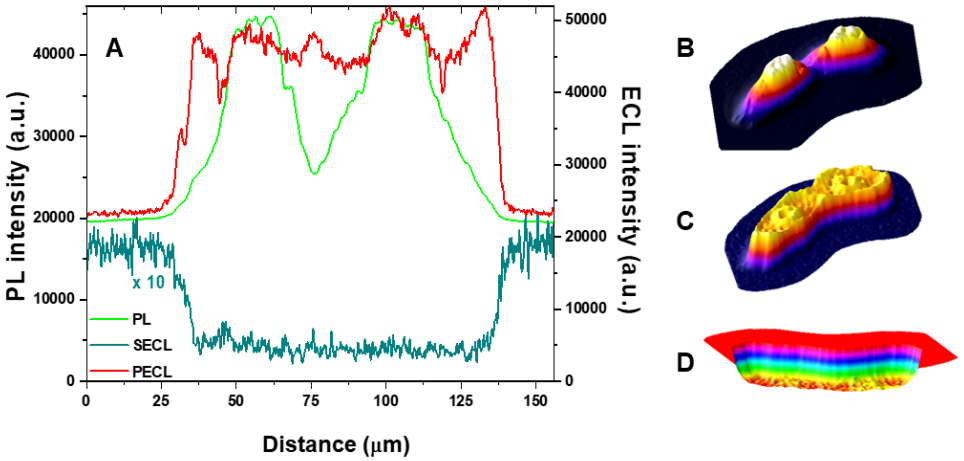

Figure 3.8. PL, SECL and PECL intensity profiles of the cells extracted along the dashed line on **Figure 3.7A**. **(B-D)** 3D intensity profiles extracted from the **(B)** PL, **(C)** PECL, and **(D)** SECL micrographs in **Figure 3.7**.

Moreover, to further investigate the PL/ECL imaging capabilities, we extracted the PL and ECL intensity profiles (**Figure 3.8A**) along the section indicated by a dotted line in **Figure 3.7A**. The intensity of the PL profiles is the lowest at the periphery of the cells, increases in the proximity of the nuclei and reaches two distinct maxima at the nuclei centres. In PL mode, both $[Ru(bpy)_3]^{2+}$ and $[Ir(sppy)_3]^{3-}$ are excited and emissions from the two luminophores are observed simultaneously. Furthermore, all the luminophores labelling the cellular membrane are excited simultaneously. Thus, the thicker regions of the cell contain more labels and appear brighter in the PL image. Conversely, since ECL emission is confined near the electrode surface due to the short half-life of TPrA radicals, the focal plane of ECL is closer to the electrode compared to the focal plane of PL.[27] Therefore, in a first-order approximation, we do not expect to observe differences in ECL intensity in the regions that have different thicknesses. Indeed, PECL and SECL profiles look like mirror images of each other, showing the outline of the basal cell membrane without discriminating the areas based on the thickness of

the membrane or cell-cell junctions (**Figure 3.8A**). Furthermore, dark spots visible in the centres of the nuclei in the PECL image in **Figure 3.7B** can be seen in the PECL profile as slight drops in intensity, confirming that co-reactant diffusion is hindered but not completely blocked in those regions. As a visual confirmation of the described differences between PL, SECL and PECL, we extracted the 3D intensity profiles of the same cells (**Figures 3.8B-D**). They illustrate the variation in PL and ECL intensities across the entire surface of the cells. The similarities in the PECL and SECL patterns – considered positively or negatively – may indicate that the same part of the cell is imaged in the reported experimental conditions. It further points to the probable dominant role of the lifetime of TPrA radicals, which determines the ECL-layer thickness in both ECL processes. Thus, tuning the ECL-layer thickness along the z-axis by changing the respective concentrations of TPrA and $[Ir(sppy)_3]^{3-}$ constitutes an appealing prospect for bimodal imaging of the 3D morphology of biological objects, as demonstrated previously for the $[Ru(bpy)_3]^{2+}$ luminophore.[23,36]

Finally, despite having a high quantum yield (Φ = 0.73),[58] $[Ir(sppy)_3]^{3-}$ exhibits weaker coreactant ECL intensity compared to $[Ru(bpy)_3]^{2+}$. This is attributed to its poor energetics with the TPrA coreactant,[13] resulting in SECL intensity being over an order of magnitude lower than PECL intensity. This could potentially be improved by analyzing alternative Ir(III) complexes that retain the benefits of $[Ir(sppy)_3]^{3-}$ but generate more intense ECL with TPrA.[59–62]

3.4 Conclusion

This chapter is focused on ECL heterogeneous systems: beads and then cells. We first present a new approach for the enhancement of $[Ru(bpy)_3]^{2+}$ ECL in a conventional, heterogeneous assay format where the $[Ru(bpy)_3]^{2+}$ labels are attached to micrometric beads, as in classic ECL bead-based immunoassays. The addition of $[Ir(sppy)_3]^{3-}$ to the experimental solution yielded a significant increase in ECL from the $[Ru(bpy)_3]^{2+}$ labels. This enhancement was particularly pronounced at low oxidation potentials (0.9 V vs Ag/AgCl), below the oxidation potential of $[Ru(bpy)_3]^{2+}$ (1.1 V vs Ag/AgCl). The ability to produce bright ECL signals at low oxidation potentials is particularly important for improving the versatility, sensitivity, and reproducibility of heterogeneous ECL assays because the lower applied potential for analysis avoids the oxygen evolution reaction with the formation of bubbles and local pH gradients. Moreover, it enables (i) a decrease of electrode surface passivation by TPrA, (ii) a

reduction of the incidence of interfering side reactions, (iii) ECL analysis at potentials lower than that required to cleave biological recognition elements that are covalently linked to the electrode surface, and (iv) the creation of miniaturized ECL sensing devices by reducing current generation and subsequent electrode degradation. Furthermore, we demonstrate the versatility of the $[Ir(sppy)_3]^{3-}$-mediated ECL enhancement approach by examining the system using DBAE an alternative co-reactant. These results demonstrate that $[Ir(sppy)_3]^{3-}$ can induce enhancements of ECL from $[Ru(bpy)_3]^{2+}$ in different analytical systems.

Second, since the ECL of the $[Ru(bpy)_3]^{2+}$ and TPrA system is widely used in imaging, incorporating $[Ir(sppy)_3]^{3-}$ in this system constitutes an appealing opportunity to develop ECL microscopy with improved sensitivity and increased complexity. Here, we demonstrate a new, bimodal and bicolour, approach in ECL microscopy by exploiting the simultaneous ECL emissions of $[Ru(bpy)_3]^{2+}$ and $[Ir(sppy)_3]^{3-}$. Because $[Ru(bpy)_3]^{2+}$ is used to label the cells and $[Ir(sppy)_3]^{3-}$ is dissolved in solution, their signals can be spatially resolved, while their distinct emission wavelengths (620 and 515 nm, respectively) enable simple spectral resolution by applying suitable emission filters to obtain micrographs in two modes: PECL (for $[Ru(bpy)_3]^{2+}$ emission) and SECL (for $[Ir(sppy)_3]^{3-}$ emission). Both images depict the same area of interest with the same cell, but the regions emit opposite ECL intensity at different wavelengths. In this way, the reported approach provides complementary information about the observed system: PECL imaging shows the distribution of the SA@Ru labels on the cell membrane, while SECL reflects the diffusional hindrance of the ECL reagents by the cell membranes. Comparing both images, we show that TPrA can diffuse through the permeabilized plasma membranes, whereas diffusion of a larger $[Ir(sppy)_3]^{3-}$ molecule is blocked. Due to the low coreactant ECL efficiency of $[Ir(sppy)_3]^{3-}$, the intensity of the SECL signal is comparatively low. However, replacing this luminophore with similar Ir(III) complexes that give higher ECL intensity would improve contrast in SECL mode.

This innovation in ECL imaging opens prospects in imaging distinct proteins or cellular structures, membrane transport properties, or single molecules at the level of a cellular membrane using enhanced PECL, while simultaneously observing the outline of the cell and its morphological changes using SECL. The bimodal approach possesses numerous advantages compared to traditional imaging techniques and could contribute not only to ECL microscopy but also to the development of more sensitive and reproducible ECL bioassays. Both PECL and

SECL modes alleviate issues of photobleaching and phototoxicity associated with classical microscopy techniques. Furthermore, because it provides more information about the imaged objects, this approach could contribute to the fundamental studies of different biological systems, processes, and reactions using bimodal ECL imaging.

3.5 Supporting Information

3.5.1 Image Analysis

3.5.1.1 ECL enhancement in the bead-based system

Fiji (ImageJ) software was used for all micrograph analyses. Where unspecified, contrast is automatically adjusted by ImageJ. False color was applied to micrographs using Green (for PL) and Red (for ECL) look up tables in ImageJ. For each micrograph, a 180×4 pixel rectangle, centered at the base (side-view, 71.4×1.6 μm) or center (top-view 45.7×1.0 μm) of the bead, was used to generate the emission profile using the default profile settings of the ImageJ software; the average pixel intensity of the width of the rectangle (four pixels) was plotted over a 180 pixel window. For top-view experiments, background-subtracted ECL intensities were calculated by subtracting the maximum emission from the first 10 pixels (where no emission from the bead was observed) from the maximum ECL signal from the entire ECL profile (**Figure 3.9**).

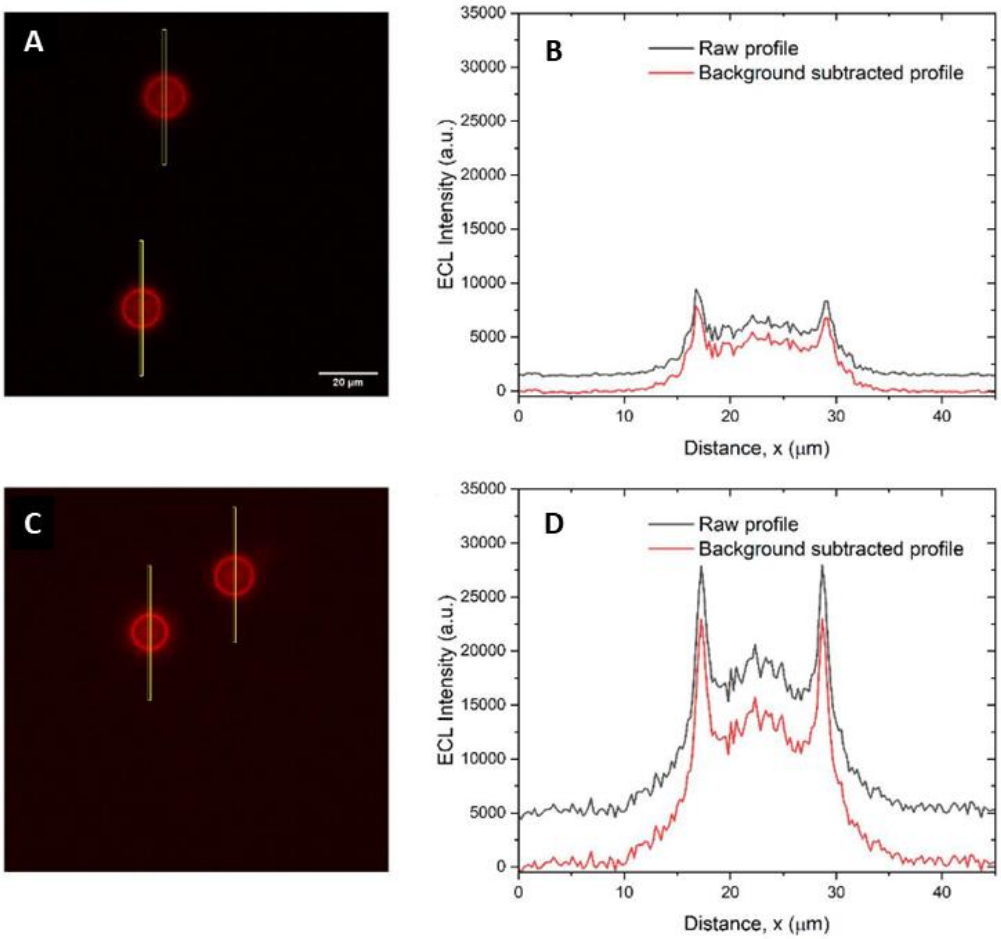

Figure 3.9. Representative ECL micrographs (top-view configuration) obtained in Procell **(A)** and Procell with 100 µM $[Ir(sppy)_3]^{3-}$ **(B)**, including 180×4 pixel rectangles (shown in yellow) used to generate ECL emission profiles (b and d respectively), 1.2 V, 1 s CA pulse, 2 s EM-CCD exposure time. To generate the background subtracted profiles (red lines, **B** and **D**) the maximum of the first 10 pixels (~2.54 µm) of ECL emission (where no emission from Ru@PS was observed) was subtracted from the raw profile (black lines, **B** and **D**).

The distance dependent background ECL profile of the emission from $[Ir(sppy)_3]^{3-}$ complicated the calculation of the ECL emission profile from Ru@PS beads in the side-view orientation. This is due to the 'blocking' effect of the PS beads, angle of the microscope objective and optical effects influencing the light propagating trough the bead. To accurately compensate for the change in ECL emission from $[Ir(sppy)_3]^{3-}$, both with distance from the WE surface and in the presence of the Ru@PS beads, we determined the $[Ir(sppy)_3]^{3-}$ emission profile from a 'bare' (unfunctionalized) PS bead in the presence of $[Ir(sppy)_3]^{3-}$ (**Figure 5.4**) The

profile was then normalized to the intensity of each micrograph using a procedure described in detail in **Figure 3.10**.

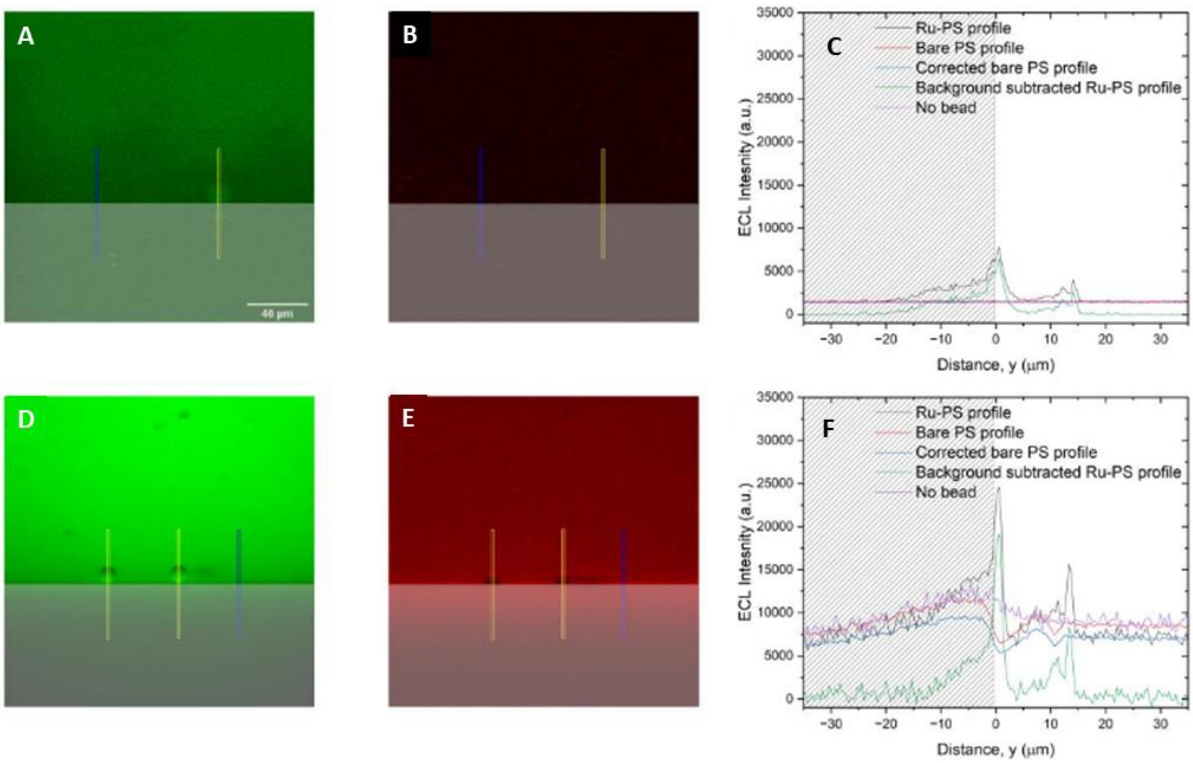

Figure 3.10. Representative side-view configuration PL micrographs **(A** and **D)** and corresponding ECL micrographs **(B** and **E)** obtained in Procell **(A** and **B)** and Procell with 100 μM $[Ir(sppy)_3]^{3-}$ **(D** and **E)** including shaded zone representing reflection of ECL on the electrode surface (z < 0 μm) 180×4 pixel rectangles (shown in yellow) used to generate ECL emission profiles (**C** and **F**, respectively) of unlabeled PS beads in side-view configuration at 1.2 V (2 s CA pulse, EM-CCD exposure 3 s), hatched zone represents reflection of ECL on the electrode surface (z < 0 μm). Blue rectangles, away from the PS spheres, show the background ECL profile; i.e. from $[Ir(sppy)_3]^{3-}$ in solution only (purple lines in figures **C** and **F**). To generate the background subtracted profiles (green lines, **C** and **F**) the maximum of the first 10 pixels (~3.97 μm) of ECL emission (where no emission from Ru@PS was observed) was calculated for both Ru@PS (black lines) and bare PS (red lines) profiles. A correction factor was applied to the bare PS profile (blue lines) to normalize the bare PS profile to the Ru@PS profile. This corrected bare PS profile was then subtracted from the raw Ru@PS profile to generate the background subtracted Ru@PS profile (green lines).

We also collected the emission profiles from bare beads in top-view configuration and found that this effect did not substantially impact the ECL intensity profiles in this configuration (**Figure 3.11**).

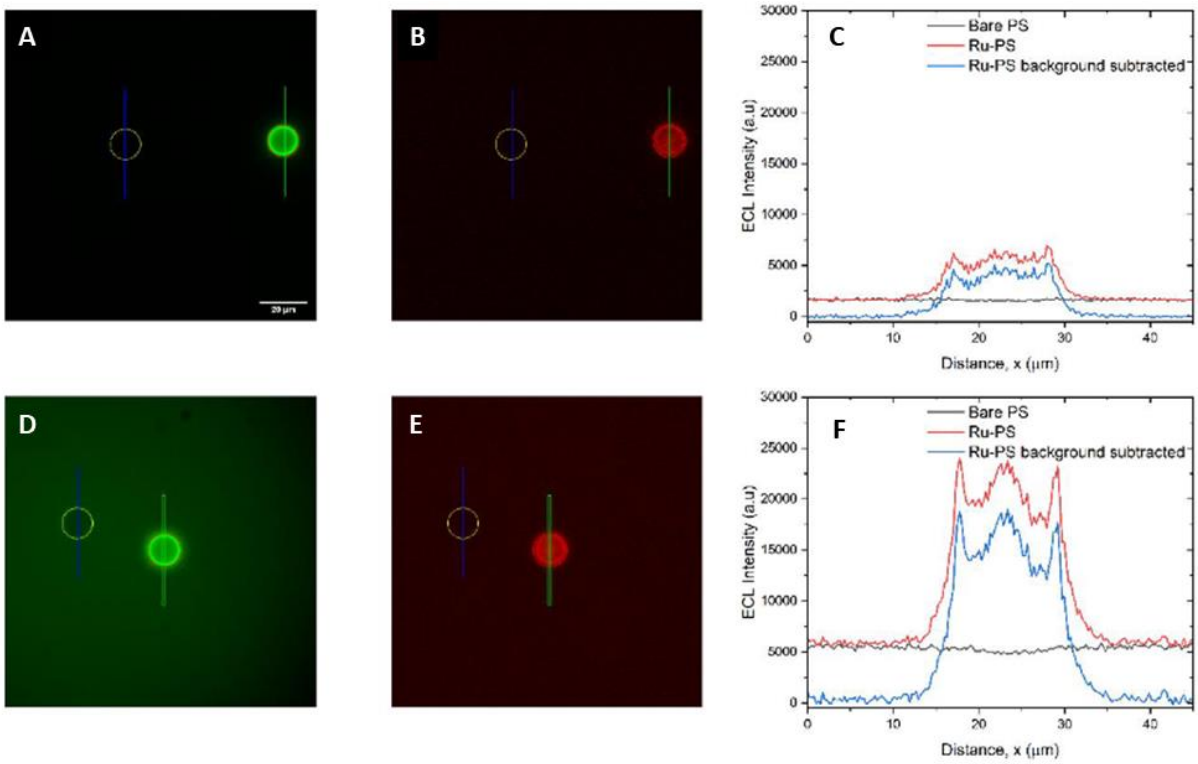

Figure 3.11. Representative top-view configuration PL micrographs **(A** and **D)** and ECL micrographs **(B** and **E)** obtained in Procell **(A** and **B)**, and Procell with 100 µM $[Ir(sppy)_3]^{3-}$ **(D** and **E)** including 180×4 pixel rectangles (shown in blue and green) used to generate ECL emission profiles **(C** and **F**, respectively) of bare PS beads (circled in yellow) and Ru@PS beads (circled in red) 1.2 V, 1 s CA pulse, EM-CCD exposure 2 s. To generate the bare-PS background subtracted profiles (blue lines, **C** and **F**) the bare PS profile (black lines, **C** and **E**) was subtracted from the raw Ru@PS profile (red lines, **C** and **F**).

3.5.1.2 Bimodal ECL imaging of single cells

ImageJ was used to process all the micrographs. Micrographs of the cells were false-colored: green for PL, red for PECL and cyan for SECL using default ImageJ lookup tables. Rectangular regions of interest were used to extract PL and ECL intensity profiles of the imaged cells. The profiles were reduced to the same baseline and the SECL intensity values were multiplied by a factor of 10 to improve the visibility and to enable easier interpretation of the

profiles. It is important to note that PL and ECL profiles are on distinct scales because the images are taken using different cameras (CCD for PL and EM-CCD for ECL). Furthermore, all intensity values are in arbitrary units, so the range of a specific profile is more informative than the absolute intensity values, which is why reducing the profiles to the same baseline does not influence their interpretation.

To examine the information revealed using different microscopy modes (PL, PECL and SECL), we constructed structure similarity index measurement (SSIM) maps. SSIM is a method used to measure the similarity between two images. It is calculated by dividing the images into smaller blocks and comparing the quality factors for each block between the images. The SSIM method takes into account three different image quality factors: luminance, contrast, and structure. Luminance represents the total brightness of the object (which is a product of the illumination and the reflectance) and is calculated as the mean value of pixel intensity. Contrast is a measure of the difference between the light and dark pixels, determined as a standard deviation of the intensity. Structure properties are all properties of the image unrelated to the lighting conditions (for example textures, edges, and shapes). Structure properties are expressed mathematically as signals normalized by their standard deviation. While these factors are relatively independent, the SSIM index is calculated by one equation which is a combined function of luminance, contrast and structure functions.[63]

Considering the differences in lighting and intensity between PL and ECL, as well as the complementarity of the PECL and SECL approach, here we wanted to avoid measuring the difference in luminance and contrast and concentrate on the structural differences between the micrographs. For this reason, to create the maps, it was necessary to threshold the original micrographs (ImageJ - Image - Adjust - Threshold) to condense the total information about the intensities of pixels to only two - black and white. The SSIM maps with corresponding indexes are automatically generated from the downsampled (thresholded) images using a plugin in ImageJ (ImageJ - Plugins - SSIM index created by Gabriel Prieto Renieblas from Complutense University Madrid, Spain, https://imagej.nih.gov/ij/plugins/ssim-index.html).

References:

1 E. Faatz, A. Finke, H.-P. Josel, G. Prencipe, S. Quint and M. Windfuhr, *Analytical Electrogenerated Electroluminescence*, 2019, 443–470.

2 W. Miao, J.-P. Choi and A. J. Bard, *J. Am. Chem. Soc.*, 2002, **124**, 14478–14485.

3 M. Sentic, M. Milutinovic, F. Kanoufi, D. Manojlovic, S. Arbault and N. Sojic, *Chem. Sci.*, 2014, **5**, 2568–2572.
4 P. Dutta, D. Han, B. Goudeau, D. Jiang, D. Fang and N. Sojic, *Biosens. Bioelectron.*, 2020, **165**, 112372.
5 D. Han, D. Fang, G. Valenti, F. Paolucci, F. Kanoufi, D. Jiang and N. Sojic, *Anal. Chem.*, 2023, **95**, 15700–15706.
6 D. Han, D. Jiang, G. Valenti, F. Paolucci, F. Kanoufi, P. C. Chaumet, D. Fang and N. Sojic, *ACS Sens.*, 2023, **8**, 4782–4791.
7 A. Fiorani, D. Han, D. Jiang, D. Fang, F. Paolucci, N. Sojic and G. Valenti, *Chem. Sci.*, 2020, **11**, 10496–10500.
8 A. Zanut, A. Fiorani, S. Canola, T. Saito, N. Ziebart, S. Rapino, S. Rebeccani, A. Barbon, T. Irie, H.-P. Josel, F. Negri, M. Marcaccio, M. Windfuhr, K. Imai, G. Valenti and F. Paolucci, *Nat. Commun.*, 2020, **11**, 2668.
9 X. Yang, J. Hang, W. Qu, Y. Wang, L. Wang, P. Zhou, H. Ding, B. Su, J. Lei, W. Guo and Z. Dai, *J. Am. Chem. Soc.*, 2023, **145**, 16026–16036.
10 S. Rebeccani, C. Wetzl, V. A. Zamolo, A. Criado, G. Valenti, F. Paolucci and M. Prato, *Chem. Commun.*, 2021, **57**, 9672–9675.
11 F. Deiss, C. N. LaFratta, M. Symer, T. M. Blicharz, N. Sojic and D. R. Walt, *J. Am. Chem. Soc.*, 2009, **131**, 6088–6089.
12 W. Zhu, J. Dong, G. Ruan, Y. Zhou and J. Feng, *Angew. Chem. Int. Ed.*, 2023, **62**, e202214419.
13 E. Kerr, D. J. Hayne, L. C. Soulsby, J. C. Bawden, S. J. Blom, E. H. Doeven, L. C. Henderson, C. F. Hogan and P. S. Francis, *Chem. Sci.*, 2022, **13**, 469–477.
14 X. Liu, L. Shi, W. Niu, H. Li and G. Xu, *Angew. Chem. Int. Ed.* , 2007, **46**, 421–424.
15 H. Zhu, D. Jiang and J.-J. Zhu, *Chem. Sci.*, 2021, **12**, 4794–4799.
16 C. Ma, S. Wu, Y. Zhou, H. Wei, J. Zhang, Z. Chen, J. Zhu, Y. Lin and W. Zhu, *Angew. Chem. Int. Ed.*, 2021, **60**, 4907–4914.
17 G. Valenti, S. Scarabino, B. Goudeau, A. Lesch, M. Jović, E. Villani, M. Sentic, S. Rapino, S. Arbault, F. Paolucci and N. Sojic, *J. Am. Chem. Soc.*, 2017, **139**, 16830–16837.
18 A. J. Wilson, K. Marchuk and K. A. Willets, *Nano Lett.*, 2015, **15**, 6110–6115.
19 J. Zhou, G. Ma, Y. Chen, D. Fang, D. Jiang and H. Chen, *Anal. Chem.*, 2015, **87**, 8138–8143.
20 Y. Chen, D. Zhao, J. Fu, X. Gou, D. Jiang, H. Dong and J.-J. Zhu, *Anal. Chem.*, 2019, **91**, 6829–6835.
21 J. Dong, Y. Xu, Z. Zhang and J. Feng, *Angew. Chem. Int. Ed.*, 2022, **61**, e202200187.
22 L. Xu, Z. Zhou, C. Zhang, Y. He and B. Su, *Chem. Commun.*, 2014, **50**, 9097–9100.
23 H. Ding, P. Zhou, W. Fu, L. Ding, W. Guo and B. Su, *Angew. Chem. Int. Ed.*, 2021, **60**, 11769–11773.
24 J. Dong, Y. Lu, Y. Xu, F. Chen, J. Yang, Y. Chen and J. Feng, *Nature*, 2021, **596**, 244–249.
25 Y. Ma, C. Colin, J. Descamps, S. Arbault and N. Sojic, *Angew. Chem. Int. Ed.*, 2021, **60**, 18742–18749.
26 M.-J. Zhu, J.-B. Pan, Z.-Q. Wu, X.-Y. Gao, W. Zhao, X.-H. Xia, J.-J. Xu and H.-Y. Chen, *Angew. Chem. Int. Ed.*, 2018, **57**, 4010–4014.
27 S. Voci, B. Goudeau, G. Valenti, A. Lesch, M. Jović, S. Rapino, F. Paolucci, S. Arbault and N. Sojic, *J. Am. Chem. Soc.*, 2018, **140**, 14753–14760.
28 J. Tønnesen, V. V. G. K. Inavalli and U. V. Nägerl, *Cell*, 2018, **172**, 1108-1121.e15.
29 Y. M. Sigal, R. Zhou and X. Zhuang, *Science*, 2018, **361**, 880–887.
30 N. T. Urban, K. I. Willig, S. W. Hell and U. V. Nägerl, *Biophys J*, 2011, **101**, 1277–1284.
31 U. V. Nägerl, K. I. Willig, B. Hein, S. W. Hell and T. Bonhoeffer, *Procl. Nat. Acad. Sci.*, 2008, **105**, 18982–18987.
32 Z. Zhang, C. Ma, Q. Xu and J.-J. Zhu, *Analyst*, 2022, **147**, 2884–2894.
33 M. Sentic, F. Virgilio, A. Zanut, D. Manojlovic, S. Arbault, M. Tormen, N. Sojic and P. Ugo, *Anal. Bioanal. Chem.*, 2016, **408**, 7085–7094.

34 Y. Liu, H. Zhang, B. Li, J. Liu, D. Jiang, B. Liu and N. Sojic, *J. Am. Chem. Soc.*, 2021, **143**, 17910–17914.
35 H. Al-Kutubi, S. Voci, L. Rassaei, N. Sojic and K. Mathwig, *Chem. Sci.*, 2018, **9**, 8946–8950.
36 W. Guo, P. Zhou, L. Sun, H. Ding and B. Su, *Angew. Chem. Int. Ed.*, 2021, **60**, 2089–2093.
37 B. Li, X. Huang, Y. Lu, Z. Fan, B. Li, D. Jiang, N. Sojic and B. Liu, *Adv. Sci.*, 2022, 2204715.
38 D. Han, B. Goudeau, D. Jiang, D. Fang and N. Sojic, *Anal. Chem.*, 2021, **93**, 1652–1657.
39 H. Ding, W. Guo and B. Su, *Angew. Chem. Int. Ed.*, 2020, **59**, 449–456.
40 H. Gao, W. Han, H. Qi, Q. Gao and C. Zhang, *Anal. Chem.*, 2020, **92**, 8278–8284.
41 J. Descamps, C. Colin, G. Tessier, S. Arbault and N. Sojic, *Angew. Chem. Int. Ed.*, **n/a**, e202218574.
42 C. Ma, M.-X. Wang, H.-F. Wei, S. Wu, J.-R. Zhang, J.-J. Zhu and Z. Chen, *Chem. Commun.*, 2021, **57**, 2168–2171.
43 D. Han, B. Goudeau, V. Lapeyre, V. Ravaine, D. Jiang, D. Fang and N. Sojic, *Biosens. Bioelectron.*, 2022, **216**, 114640.
44 F. Kanoufi, Y. Zu and A. J. Bard, *J. Phys. Chem. B*, 2001, **105**, 210–216.
45 R. Y. Lai and A. J. Bard, *J. Phys. Chem. A*, 2003, **107**, 3335–3340.
46 S. Kirschbaum-Harriman, M. Mayer, A. Duerkop, T. Hirsch and A. J. Baeumner, *Analyst*, 2017, **142**, 2469–2474.
47 M. C. Rodríguez and G. A. Rivas, *Talanta*, 2009, **78**, 212–216.
48 D.-Y. Liu, Y.-Y. Xin, X.-W. He and X.-B. Yin, *Analyst*, 2011, **136**, 479–485.
49 S. Senthil Kumar and A. J. Bard, *Anal. Chem.*, 2013, **85**, 292–295.
50 A. Fiorani, G. Valenti, Irkham, F. Paolucci and Y. Einaga, *Phys. Chem. Chem. Phys.*, 2020, **22**, 15413–15417.
51 E. Daviddi, A. Oleinick, I. Svir, G. Valenti, F. Paolucci and C. Amatore, *ChemElectroChem*, 2017, **4**, 1719–1730.
52 B. D. Gomperts and J. M. Fernandez, *Trends Biochem. Sci.*, 1985, **10**, 414–417.
53 S. Watkins, *Curr. Protoc. Cytom.*, 2009, **48**, 12.16.1-12.16.10.
54 S. Rebeccani, A. Zanut, C. I. Santo, G. Valenti and F. Paolucci, *Anal. Chem.*, 2022, **94**, 336–348.
55 Y. You, *Curr. Opin. Chem. Biol.*, 2013, **17**, 699–707.
56 G. Zhang, H. Zhang, Y. Gao, R. Tao, L. Xin, J. Yi, F. Li, W. Liu and J. Qiao, *Organometallics*, 2014, **33**, 61–68.
57 Q. Zhao, M. Yu, L. Shi, S. Liu, C. Li, M. Shi, Z. Zhou, C. Huang and F. Li, *Organometallics*, 2010, **29**, 1085–1091.
58 M. R. Schreier, X. Guo, B. Pfund, Y. Okamoto, T. R. Ward, C. Kerzig and O. S. Wenger, *Acc. Chem. Res.*, 2022, **55**, 1290–1300.
59 E. Kerr, E. H. Doeven, G. J. Barbante, T. U. Connell, P. S. Donnelly, D. J. D. Wilson, T. D. Ashton, F. M. Pfeffer and P. S. Francis, *Eur. J. Chem.*, 2015, **21**, 14987–14995.
60 L. Chen, D. J. Hayne, E. H. Doeven, J. Agugiaro, D. J. D. Wilson, L. C. Henderson, T. U. Connell, Y. H. Nai, R. Alexander, S. Carrara, C. F. Hogan, P. S. Donnelly and P. S. Francis, *Chem. Sci.*, 2019, **10**, 8654–8667.
61 J. M. Fernandez-Hernandez, E. Longhi, R. Cysewski, F. Polo, H.-P. Josel and L. De Cola, *Anal. Chem.*, 2016, **88**, 4174–4178.
62 B. Newman, L. Chen, L. C. Henderson, E. H. Doeven, P. S. Francis and D. J. Hayne, *Front. Chem.*
63 Z. Wang, A. C. Bovik, H. R. Sheikh and E. P. Simoncelli, *IEEE T. Image Process.*, 2004, **13**, 600–612.

Chapter IV
Enhanced electrochemiluminescence at the gas/liquid interface of bubbles propelled into solution

Chapter IV: Enhanced electrochemiluminescence at the gas/liquid interface of bubbles propelled into solution

4.1 Introduction

It has been demonstrated that rates of bimolecular reactions can be significantly (by several orders of magnitude) enhanced at the gas/liquid and liquid/liquid interfaces of microscopic bubbles and droplets.[1–3] For example, organic reactions performed in water, where hydrophobic reagents are emulsified rather than dissolved in organic solvent, benefit from decreased reaction times and improved yields,[4] while enzymatic reactions in micro- and nanometric water droplets proceed at enhanced rates compared to the same reactions in bulk solutions.[5] Furthermore, chemical species' redox reactivity and stability seem to be different at phase interfaces than in bulk, as evidenced by spontaneous oxidation and reduction processes that take place at the surface of aqueous micro/nanodroplets.[6,7] Therefore, studying the reactivity at interfaces is of fundamental interest in different fields of science and industry.

When discussing (electro)chemical reactivity within submicrometric droplets adsorbed at the electrode surface, it can be helpful and intuitive to consider such droplets as micro/nanoreactors which introduce a high level of confinement into the investigated system. (Electro)chemical reactivity within those droplets (or in confined spaces in general) is enhanced due to the fast mass transport of reactants and products and the increased probability of reactants colliding with each other and the electrode surface and adsorbing to the electrode surface and/or droplet interface.[1,8,9] This is especially true since the reaction volumes in such droplets often range from several attoliters to several microliters. Consequently, the transport of reactive species to the electrode surface is almost instantaneous, allowing the use of stochastic electrochemistry to study the reactivity within individual droplets filled with electroactive and/or electrocatalytic species upon their collisions with the surface of a microelectrode.[5,10–12]

Notably, as droplet size decreases, reaction rates within the droplets increase due to higher levels of confinement. Additionally, smaller droplets have a larger surface area-to-volume

ratio, maximising the contribution of reaction steps occurring at the droplet interface rather than in its centre. Since the physicochemical properties of the system (e.g., dielectric constant, electric field, solvation and orientation of molecules)[1–3] differ at the interface compared to the bulk, confined environments where reactions preferentially occur at the interface can profoundly influence the thermodynamics and kinetics of (electro)chemical processes, leading to significantly enhanced reaction rates.

For example, the increased efficiency of some organic reactions (e.g., the Diels-Alder reaction) when performed in water (or "on water") instead of in organic solvent can be attributed to lowered reaction activation energies due to more favourable interactions of the transition state (or activated complex) with the surrounding water molecules compared to the interactions of the reactants with water. Depending on the nature of these interactions, the enhanced reaction kinetics can be attributed to the hydrophobic effect, hydrogen bonding, the polarity effect, or a combination of all of these factors.[4,13]

On the other hand, reaction acceleration in aqueous droplets can be ascribed to the defects in the water hydrogen bonding structure, partial solvation of reactants, adsorption of reactants and products on the interface, and the existence of electric fields and pH gradients at the interface between water and oil or air.[1–3] All of these effects influence, to a certain extent, the chemical environment of the reactants, transition state and products, resulting in accelerated reaction rates. Defects in the water hydrogen bonding structure lead to the accumulation of charge on water molecules with an odd number of hydrogen bonds, causing a charge buildup at the interface where water is more self-ionised.[2,7,14] Those unsolvated H_3O^+ or OH^- groups can align across the droplet's surface, sticking into the gas or oil phase and causing local super acidity (or super basicity).[3,15,16] This phenomenon could explain the acidic character of aerosols or the accumulation of negative charge (OH^- ions) at the air side of water droplets and air bubbles.[17,18,18] The as-generated pH gradient near the phase interface can catalyse chemical reactions by altering the protonation of solute molecules.[19]

Furthermore, at the interface, where water molecules are highly ordered, incomplete coordination of solutes by water molecules can occur. This frustrated hydration leads to enhanced energy gap fluctuations, reducing the reorganization energy (λ) and facilitating electron transfer

in the normal Marcus regime, thereby enhancing the reaction kinetics.[20,21] On top of that, the energy requirements to overcome the solvent interactions are lower for the reactants that are not fully solvated than in the bulk, which facilitates the formation of transition states and lowers the reaction enthalpy.

Apart from the altered structure and properties of the surface water molecules, the interfacial reactivity significantly depends on the surface activity of solutes. Adsorption of reactants at the interface increases their local concentrations and aligns them at the interface, indirectly facilitating the reaction kinetics.[22] Additionally, factors such as the timescale (rate constants) of adsorption/desorption processes, the surface-to-volume ratio of microcompartments (i.e. droplets' radii), and the initial concentration of dissolved molecules all contribute to the enhancement of the surface reactivity.[22,23] Furthermore, Ben-Amotz demonstrated theoretically that the adsorption free energy of the products and/or activated complex directly correlates with the reaction free energy.[24] Thereby, the formation of surface-active products facilitates the forward reaction by decreasing its energy requirements. This adsorption-based model explains the increase in the interfacial reactivity with the increase in product size and decrease in product polarity, aromaticity, and charge. Additionally, it rationalises the high interfacial reactivity of small or charged molecules when the reaction products can specifically interact with the interface (i.e. through hydrogen bonding or charge transfer interactions).

Finally, strong electric fields are observed at the interface of media with different dielectric constants (i.e. water/air or water/oil), causing the formation of electric double layers, attraction or repulsion of charged species, and the formation of ion gradients.[25,26] Electric fields likely contribute to lower reaction barriers and stabilize redox species, facilitating spontaneous redox reactions such as the accumulation of hydroxyl radicals and the formation of hydrogen peroxide at the water/air interface of microdroplets.[27,28]

This complex view of accelerated reactivity within submicrometric droplets extends beyond the effects of confinement and accentuates the influence of interfacial effects on global reactivity enhancement. Thus, similar considerations might apply to the local reactivity at the interface of gas bubbles in aqueous solutions.

Bubble formation at electrodes is highly relevant in the industrial production of gases such as hydrogen and oxygen by electrochemical water splitting, and chlorine in the chlor-alkali process.[29] In the latter, chloride ions are oxidized at an anode, forming gaseous chlorine, one of the most important products of the chemical industry. However, bubbles have a notoriously bad press in electrochemistry because the generation of adherent bubbles at the electrode surface affects the efficiency of most electrochemical reactions. Indeed, bubbles block the electrode surface, preventing electron-transfer reactions and leading to drops in faradaic current and process efficiency losses. Therefore, gas bubbles are generally considered detrimental in electrochemistry, particularly in electroanalysis.

However, opposite to the traditional view, gas bubbles in water do not always have a negative impact on the electrochemical reactivity. Even though they hinder the electrode surface, bubbles are not inert entities as they introduce additional interfaces into the electrochemical system (gas/liquid and gas/solid). As discussed above, these interfaces can lead to complex and often enhanced chemical reactivity by influencing the electric fields, pH gradients and adsorption of solvated species. Thus, during the formation of gas bubbles, there is a trade-off between positive effects (enhanced reactivity at the phase interface) and negative effects (decrease of the electrode's active surface area). Better understanding and control of these contributions through probing the interfacial reactivity of bubbles is vital for understanding and improving electrochemical processes that involve formation of gas products at the electrodes.

Among the electrochemical techniques, ECL is a light emission phenomenon confined to the immediate vicinity of an electrode surface.[30] ECL is a very sensitive analytical technique based on orthogonal principles with an electrochemical trigger and an optical readout. Electrogenerated radicals react homogeneously in solution through a redox reaction with a luminophore and populate its excited state. Therefore, ECL is very efficient for *operando* studies of chemical reactivity near electrode surfaces,[31–40] in confined spaces,[41–46] at interfaces[47–51] and catalytic sites.[52–57] and as such represents an ideal method for investigating the mechanistic and kinetic aspects of formation and evolution of gas bubbles at the electrodes.

Unfortunately, ECL is limited by relatively low light intensities, rapid signal decay, and spatial confinement to the micrometric region near the electrode surface.[58,59] The limited lifetime

of the electrogenerated species limits the spatial extension of the ECL-emitting layer.[31,44,60,61] In this context, apart from investigating the electrochemical environment and interfacial reactivity of electrochemically generated gas bubbles, the purpose of this study is to utilise the enhanced chemical reactivity at the bubble's surface to improve the ECL method by amplifying the ECL emission and extending its duration in space and time.

Here, we focus on the coreactant system typically used for bioanalysis, employing a derivative of luminol, 8-amino-5-chloro-2,3-dihydro-7-phenyl-pyrido[3,4-d]pyridazine-1,4-dione (L-012) [62,63] as a luminophore, and hydrogen peroxide as a coreactant. Luminol (and its derivatives) emits light upon oxidation in the presence of H_20_2 in alkaline aqueous solutions. The luminescence intensity is linearly dependent on the H_2O_2 concentration.[64–69] The mechanism of this ECL generation is complex, involving luminol oxidation to yield diazaquinone radicals ($L^{\bullet-}$).[37,70] These radicals subsequently react with hydrogen peroxide anion (HO_2^-) or other reactive oxygen species (ROS), namely hydroxyl radicals ($OH^\bullet$) and superoxide radicals ($O_2^{\bullet-}$), produced during H_2O_2 decomposition, water oxidation,[71,72] or reduction of dissolved oxygen,[70,73] ultimately populating the excited state and emitting blue light upon decay.[37,70,74]

Enhancing the ECL intensity, duration, and spatial extension in the luminol/H_2O_2 coreactant system depends significantly on understanding the underlying mechanisms for ECL generation.[37,59] Common strategies for modulating the luminol ECL response involve designing more efficient ECL emitters such as substituted luminol derivates,[62,75–77] employing materials[70–73,78] and experimental conditions[37,79] that facilitate the generation of radical intermediates and using reagents that lead to prolonged ECL generation.[77,80] However, as already discussed, another approach toward accelerating the rates of chemical reactions and improving their efficiency involves conducting the reactions within confined environments,[42,78,81,45] such as micropores,[37,82,83] droplets,[49,50,84] or interface[85] of bubbles,[47,51,86] which leads to enhanced ECL intensities. Moreover, within microscopic bubbles and droplets, which possess a high surface-to-volume ratio, interfacial effects can significantly stimulate chemical reactivity.[9,47,51] For instance, Ciampi and co-workers demonstrated that the elevated self-ionization constant of water at the gas-water interface leads to the accumulation of hydroxide ions, resulting in the electrically

charged corona of the bubble-promoting oxidative processes (specifically ROS generation) at the electrode-gas-water interface.[47]

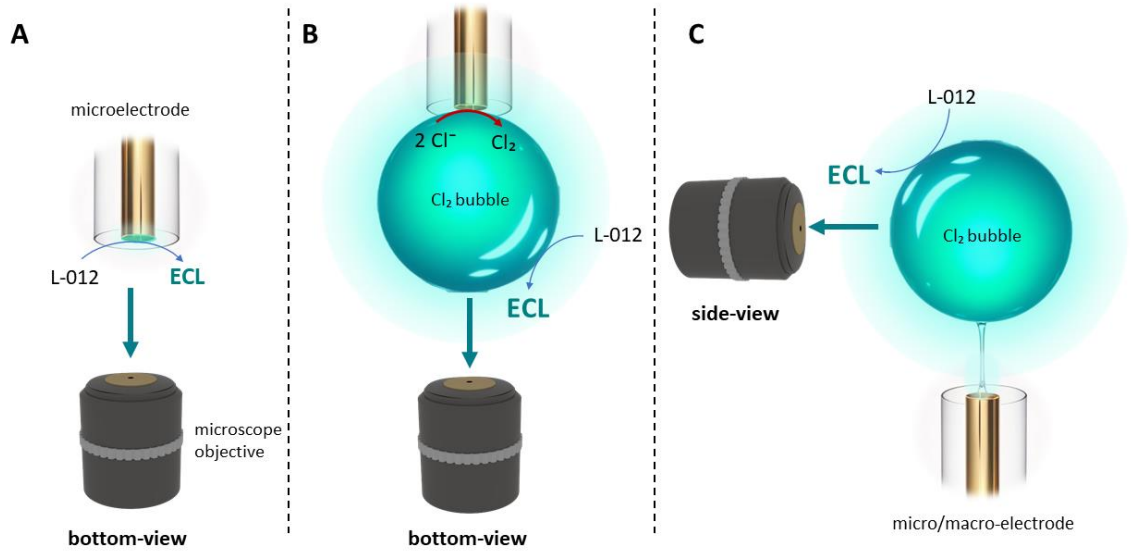

Figure 4.1. Schemes illustrating the L-012 ECL emission process: **(A)** at the surface of a gold microelectrode, **(B)** at the interface between the Cl_2 bubble (gas phase) electrogenerated by a microelectrode and the aqueous phase before, and **(C)** after the Cl_2 bubble detaches from the electrode surface. To study the ECL enhancement at the gas/liquid interface and the spatial extension (and propagation) of the ECL-emitting layer after bubble detachment, imaging experiments were performed in **(B)** bottom-view and **(C)** side-view configurations with the electrode positioned **(A, B)** above or **(C)** below the Cl_2 bubble.

In this work, we implemented a simple experimental approach involving the electrochemical generation of chlorine gas bubbles on the surface of an anode to enhance the ECL emission of L-012 (**Figure 4.1**). In chloride-containing solutions, these bubbles predominantly consist of chlorine, which undergoes a reaction with water, yielding hypochlorite (ClO^-). Hypochlorite present at the interface between the aqueous phase and the electrochemically generated bubbles can homogeneously oxidize L-012[65,87]. Simultaneously, the bubble corona effect [7,47] elevates the oxidation reaction rates at the electrode/gas/electrolyte interface, ensuring the generation of an abundant supply of ROS. ROS then react with the oxidized L-012, producing its excited state and resulting in an enhanced and long-lasting ECL emission at the

bubble's surface. This emission, driven by the *in situ* (electro)chemical generation of oxidants, can extend up to 5 mm from the electrode surface after bubble detachment. While ECL is typically confined to processes within the immediate vicinity (a few micrometers) of the electrode, our method extends its application to phenomena occurring far away (up to several millimeters) from the electrode surface. In prospect, this remotely generated and long-lasting ECL can be used to analyze dynamic processes in the bulk that are inaccessible to traditional ECL methods.

4.2 Experimental Section

4.2.1 Regents and apparatus

Reagents and solvents were purchased from commercial suppliers and used without further purification. L-012, hydrogen peroxide, glucose oxidase, α-D-glucose, benzoic acid, sodium dihydrogen phosphate dihydrate, disodium hydrogen phosphate, potassium chloride and potassium nitrate were purchased from Sigma-Aldrich and used as received.

All solutions were prepared with milliQ water of resistivity not less than 18 MΩ cm. A 25-µm gold disk microelectrode (ItalSens, PalmSens, NL) was used for single bubble imaging experiments, while 1.5-mm gold, 1.5-mm platinum and 3-mm glassy carbon disk electrodes from BASi (IN, US) were used for ECL imaging and experiments with a photomultiplier tube (PMT). All working electrodes were polished using 0.05 µm alumina polishing powder, followed by sonication in ethanol before each experiment.

4.2.2 Electrochemistry and ECL

The experiments were performed in custom-made electrochemical cells with a glass slide window for collecting ECL signals. All the cells used a three-electrode configuration, in which a gold 25-µm disc microelectrode, a gold 1.5-mm disc electrode, a platinum 1.5-mm disc electrode or a glassy carbon (GC) 3-mm disc electrode acted as a working electrode, Ag/AgCl ($LiCH_3COO$ 0.1 M) or Ag/AgCl/KCl 3M as reference electrodes, and a Pt wire as a counter-electrode.

For ECL and bright field microscopies, an epifluorescence microscope from Leica (DMI6000, Leica Microsystems) equipped with an ultrasensitive Electron-Multiplying Charge Coupled Device camera (EM-CCD C9100-23B from Hamamatsu, Hamamatsu Japan) was used with

an inverted 10 × microscope objective (10 × /0.25, 17.6 mm; Leica, number 11506260). The integrated system also included a potentiostat (PalmSens 4) suitable to apply the required potentials to generate ECL. All micrographs were collected without using filter cubes.

An Autolab PGSTAT101 (Metrohm-DropSens) controlled by NOVA 2.1 was used for all other electrochemical measurements and the custom-made electrochemical cells were interfaced with either a photomultiplier tube (PMT, Hamamatsu R5070, with a Hamamatsu C9525 high-voltage power supply and a Keithley 6485 Picoammeter) or an Honor Magic 4 Lite 5G smartphone with an attached 12 x/ 24x macro lens (Apexel, Amazon, ES). Videos were recorded in RAW format using MotionCam Pro for Android.

ECL measurements were conducted in 0.2 M phosphate buffer solution (PBS) at pH 8 with 0.05 M KCl or KNO_3 supporting electrolyte, 0.5 M H_2O_2, and 0.42 mM L-012. The pH was adjusted using NaOH or H_3PO_4 to obtain the desired value. Cyclic voltammetry from 0 V to 3 V with a scan rate of 0.1 V s^{-1} or chronoamperometry (CA) at 0.7 V, 2.4 V or 3 V were used to generate the ECL emission. ECL was captured using an EMCCD with an integration time of 0.1 s or 1 s.

4.2.3 Image analysis

ImageJ was used to process all the micrographs. All the micrographs were false-colored: yellow for PL and cyan for ECL using default ImageJ lookup tables. Rectangular regions of interest were used to extract PL and ECL intensity profiles of the imaged cells and background-subtracted ECL intensities were calculated by subtracting the maximum emission from the first 10 pixels (where no ECL emission was observed) from the maximum ECL signal from the entire ECL profile.

4.3 Results and discussion

4.3.1 Electrochemical and ECL characterizations

The main aim of this study is to extend and improve the performance of ECL and to achieve more efficient emission without relying on nanomaterials or specific experimental setups to boost the ECL signal. To accomplish this objective, our approach relies on microelectrodes to electrogenerate Cl_2 microbubbles, which surface triggers an intense ECL emission (Figure 1). First, we investigated the electrochemical reactivity of the L012/H_2O_2 system, especially at high anodic

potentials, which are usually overlooked in electrochemical analysis. Figures S1A-C show the voltammetric responses in 50 mM KNO_3 (red curves) or KCl (blue curves) supporting electrolyte in PBS (pH 8) at the surface of glassy carbon (GC), Au and Pt electrodes, respectively. At the GC electrode, electrolysis starts approximately at 0.1 V lower potential in KCl than in KNO_3 supporting electrolyte (**Figure 4.2A**), indicating the involvement of two parallel processes in KCl: water oxidation and chloride oxidation[88], as opposed to a single process: water oxidation, that takes place in KNO_3. Conversely, at the Au and Pt electrodes, anodic reactions are shifted to more positive potentials in the KCl-containing solution (**Figures 4.2B** and **4.2C**). This is a consequence of the strong adsorption of chlorides at the electrode surface, which hindered OH^- adsorption and shifted gold and platinum oxidation to more positive potentials,[88,89] while also promoting chlorine evolution at higher overpotentials. Thus, biasing Au, Pt and GC electrodes to high anodic potentials leads to oxygen evolution (OER) in the KNO_3 electrolyte solution, whereas a dominant reaction in 50 mM KCl solution is chlorine evolution (CER).[88] Under the same experimental conditions, we evaluated the influence of the supporting electrolyte on the oxidation of L-012 (**insets** in **Figures 4.2A**-**C**). L-012 oxidation resulted in a sharp peak with a half-wave potential of 0.65 V vs Ag/AgCl (all the potentials of this study are reported *versus* this reference electrode) in KNO_3 and 0.85 V in KCl-containing solution, at both GC and Au working electrodes.

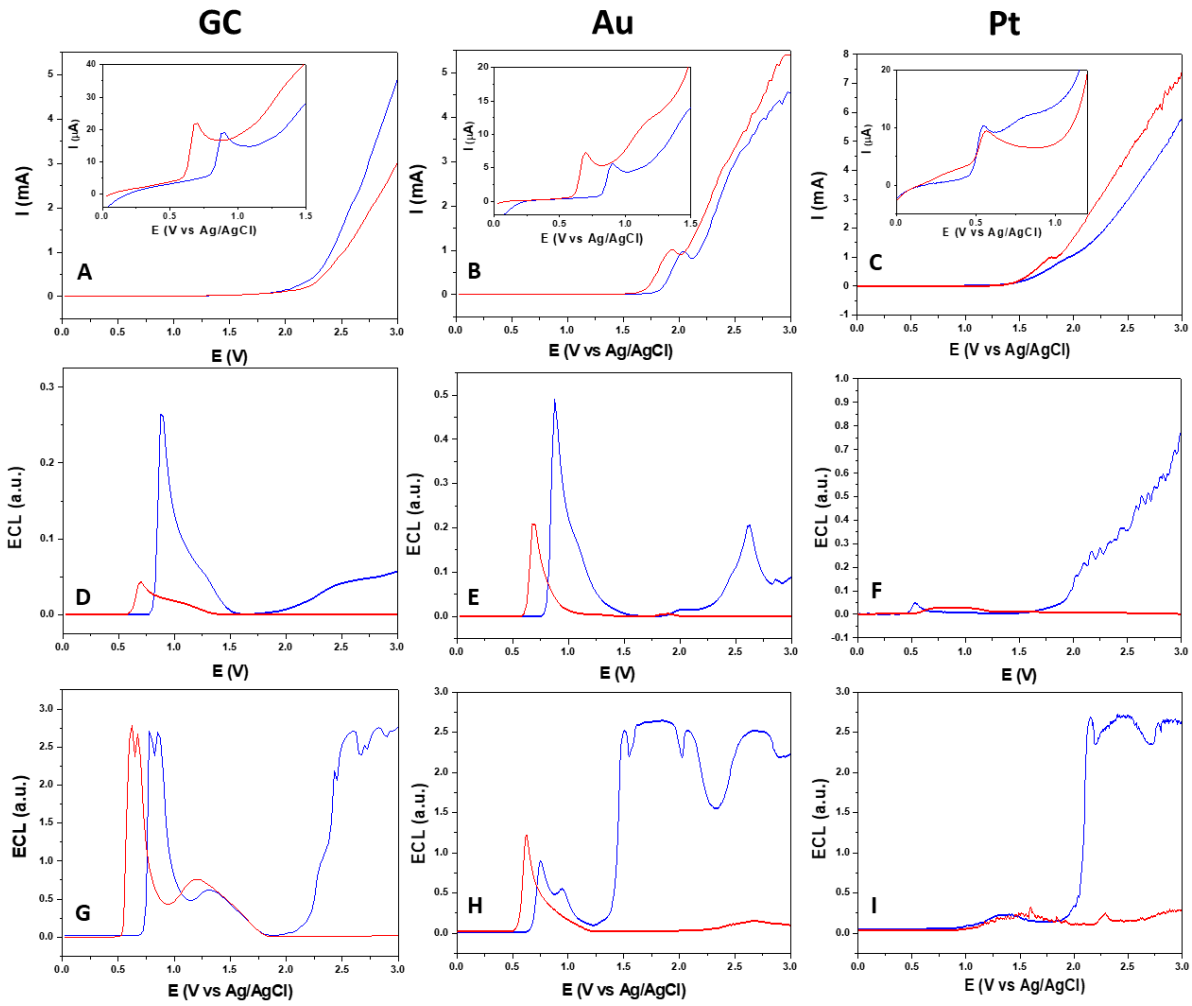

Figure 4.2. **(A-C)** Linear sweep voltammograms at 0.1 V s^{-1} from 0 V to 3.0 V in 0.2 M PBS (pH = 8) with 50 mM KNO_3 (red) and KCl (blue) on **(A)** GC electrode, **(B)** Au electrode, **(C)** Pt electrode. Insets **(A-C)** show the electrochemical oxidation of L-012 in KNO_3 (red) and KCl (blue) supporting electrolytes on different working electrodes. **(D-I)** Corresponding evolution of the ECL intensity with electrode potential during a linear potential sweep at 0.1 V s^{-1} from 0 V to 3.0 V in 0.2 M PBS (pH = 8), 0.42 mM L-012, 50 mM KNO_3 (in red) or KCl (in blue) and **(D-F)** 0 M H_2O_2 or **(G-I)** 0.5 M H_2O_2 on **(D** and **G)** GC electrode, **(E** and **H)** Au electrode, **(F** and **I)** Pt electrode.

The previously discussed chloride adsorption prevented the adsorption of other reactive species, in this case L-012, and caused this anodic shift, accompanied by a small decrease in the observed peak current. Conversely, L-012 oxidation does not seem to be significantly affected by

the adsorption of chlorides on the Pt electrode. However, a comparison of current-potential plots in KNO_3 (red lines) and KCl (blue lines) supporting electrolytes containing 0.42 mM (solid lines) or no (dashed lines) L-012 (**Figure 4.3A**) shows that oxide layer formation at the platinum electrode shifts to higher potentials in the presence of chloride ions (from ca. 0.36 to ca. 0.61 V). Thus, L-012 oxidation effectively takes place at different electrode surfaces in KNO_3 and in KCl.

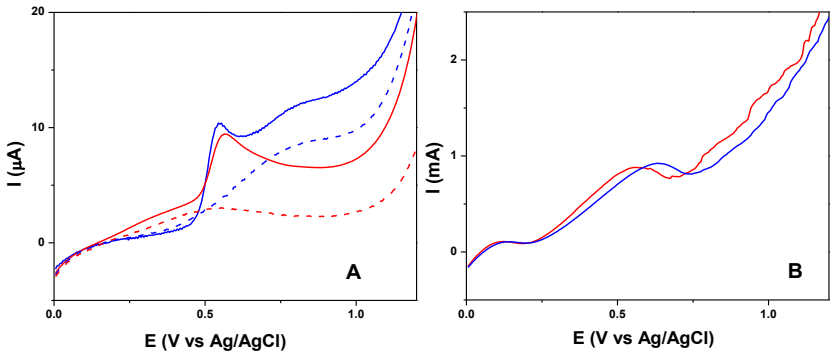

Figure 4.3. Linear sweep voltammograms at Pt electrode at 0.1 V s^{-1} from 0 V to 1.2 V in 0.2 M PBS pH 8 with 50 mM KNO_3 (red) and KCl (blue) **(A)** containing 0 mM L-012 (dashed lines) and 0.42 mM L-012 (solid lines) and **(B)** containing 0.42 mM L-012 and 0.5 M H_2O_2.

Moreover, under the same experimental conditions, **Figures 4.2D-F** show the evolution of ECL intensity with the working electrodes' potential. They demonstrate that the low-potential ECL emission at GC and Au electrodes shifts anodically in the presence of chloride, which is consistent with the observed change in L-012 oxidation potential in different supporting electrolytes (**inset** in **Figures 4.2A** and **4.2B**). Furthermore, the low-potential ECL intensity is enhanced 5.4-fold and 2.4-fold in the presence of chlorides at the GC and Au electrodes, respectively. This enhancement is likely caused by the electrochemically produced OER and CER intermediates facilitating the homogeneous oxidation of the ECL species, leading to enhanced emission. This is evidenced by an increase in the faradaic current at potentials above ca. 1 V (**insets** in **Figures 4.2A-C**), where, although kinetically sluggish, OER and CER reactions are thermodynamically feasible.[88,90] Thus, the enhanced ECL emission in the Cl^--containing solutions indicates the involvement of chlorine species in the mediation of the ECL reactions. Additionally, at the Pt working electrode, a sharp, peak-shaped L-012 emission arises at ca. 0.55 V in the KCl solution (red line, **Figure 4.2F**).

Conversely, in the absence of chloride ions, a low-intensity ECL emission persists over a broad potential range (ca. from 0.6 V to 1.25 V). This result is consistent with an anodically shifted oxidation of Pt electrode surface in KCl (**Figure 4.3A**), supporting the crucial role of adsorption and oxidation of chloride ions on the (electro)chemical and surface properties of Pt electrode and, consequently, ECL behaviour of luminol-based ECL systems.

Similar conclusions can be drawn from the ECL emission at high anodic potentials (i.e., above 2 V), where CER and OER proceed at significant rates. Regardless of the working electrode's material, high-potential ECL arises in the KCl-containing solutions but is absent when KNO_3 is used as the supporting electrolyte. This clearly indicates that inorganic chlorine species are involved in the underlying mechanism of ECL generation by homogeneously oxidizing L-012 and its intermediates. Differences in high-potential ECL intensities at GC, Au, and Pt electrodes can be attributed to the distinct kinetics of CER at different electrode surfaces.

Finally, we probed the ECL signal of the L-012/H_2O_2 system at GC, Au and Pt electrodes. We scanned the potential from 0 V to 3 V in the 50 mM KNO_3 (red curvess) or 50 mM KCl solution (blue curves) (**Figures 4.2G-I**, respectively). Notably, ECL emission intensities in the presence of H_2O_2 are increased by ca. an order of magnitude, relative to the same conditions in the absence of H_2O_2. At both GC and Au electrodes, the onset of low potential ECL shifted to ca. 200 mV higher values in the KCl solution compared to the KNO_3 solution. This shift is attributed to differences in the oxidation potential of L-012 in different supporting electrolytes (**insets** in **Figures 4.2A** and **4.2B**). Conversely, regardless of the electrolyte composition, only a faint low-potential ECL, shifted to higher overpotentials, was observed over a wide potential range at the Pt working electrode. This is likely due to the earlier onset of Pt oxidation in the presence of H_2O_2, which, as previously discussed, results in altered electrode surface properties and reduced reactivity toward L-012 oxidation.

At high electrode potentials, where Cl_2 and O_2 evolution reactions take place, strong ECL emission was detected at all three electrodes when using KCl as a supporting electrolyte. This high-potential ECL emission is comparable to the low-potential ECL observed at the GC electrode and is 2.2 and 3 times higher than the low-potential ECL emission at the gold electrode in the KNO_3 and KCl supporting electrolytes, respectively. In contrast, when using KNO_3 as a supporting

electrolyte, no high-potential ECL was observed at the GC electrode, while a low level of light emission emerged from the Au and Pt electrodes. This difference is due to the electrogenerated Cl_2 reacting with water to produce ClO^-, a potent oxidant that efficiently mediates the homogenous oxidation of L-012, resulting in strong ECL emission in solution. Conversely, while hydroxyl and superoxide radicals formed during water oxidation generate strong ECL upon reacting with L-012 radicals,[71] they do not efficiently promote the oxidation of L-012. Moreover, the evolution of O_2 competes with the electrochemical oxidation of L-012, quenching the high potential ECL by decreasing the concentration of electrogenerated L-012 radicals. Thus, ECL at high electrode potentials in the L-012/H_2O_2 system highlights the crucial role of electrogenerated Cl_2 in mediating oxidation reactions that produce ECL radical intermediates.

Consequently, ECL can be generated by oxidizing L-012 at the electrode surface at moderate anodic potentials (ca. 0.7 V) and on the surface of the gas bubbles produced by chloride oxidation at high potentials (above 2.0 V). In the latter case, electrogenerated oxidants (Cl_2 and ROS) mediate the ECL production at the surface of the bubbles by homogenously oxidizing the ECL reagents.

4.3.2 Imaging spatial and temporal reactivity: ECL emission produced at the electrode surface *versus* at the gas/liquid interface of single bubbles

Capturing the ECL signal with an optical microscope allowed us to spatially resolve the light distribution at different distances and in various phases from the electrode surface. The resulting optical information can then be correlated to the electrochemical responses. First, we recorded the ECL emission generated at the level of the surface of a microelectrode with a microscope in a bottom-view configuration (**Figure 4.1A**). Micrographs in **Figure 4.4** show the ECL emission of L-012 in PBS solution (pH 8) containing KNO_3 (**Figure 4.4A-C**) or KCl (**Figure 4.4D-F**) as supporting electrolytes. The gold microelectrode was biased (from left to right) at 0.7 V, 2.4 V and 3 V. **Figures 4.4A** and **4.4D** show micrographs in KNO_3 and KCl supporting electrolytes, respectively, when the potential of the working electrodes was set to 0.7 V. Both images were captured during the application of a constant potential with an exposure time of 1 s for the CCD camera. Applying such a moderate anodic potential resulted in the generation of stable ECL

signals confined to the surface of the microelectrode. The size of the ECL-emitting layer corresponds to the dimension of the microelectrode. At this potential, no bubble was produced in either electrolyte. The mean ECL intensities were 2317 arbitrary scale units (a.u.) and 467 a.u. in KNO_3 and in KCl, respectively (see histogram in **Figure 4.4G**). The brighter ECL emission in the KNO_3 electrolyte can be explained by the more efficient oxidation of L-012 at 0.7 V in the absence of chloride ions (see inset in **Figure 4.2B**).

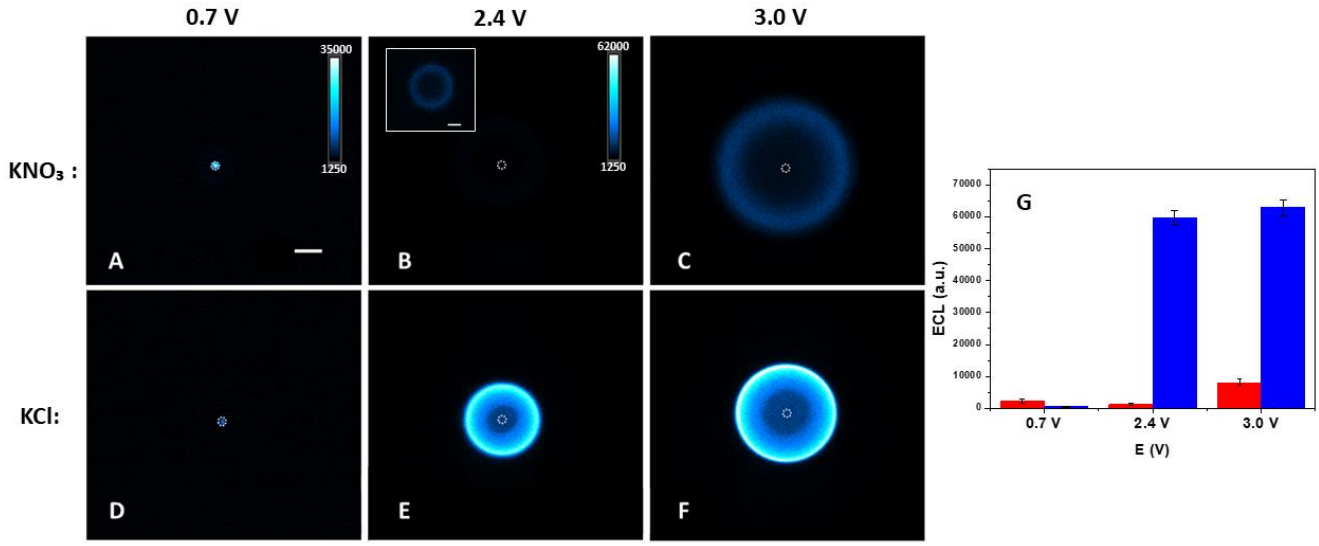

Figure 4.4. Bottom-view images of the ECL emission at the gold 25-µm disc microelectrode in the 0.2 M PBS solution (pH 8) containing 0.5 M H_2O_2, 0.42 mM L-012 and 50 mM **(A-C)** KNO_3 or **(D-F)** KCl. Electrode potential was set to **(A** and **D)** 0.7 V, **(B** and **E)** 2.4 V and **(C** and **F)** 3 V vs Ag/AgCl for 20 s. Images **A** and **D** were recorded with a 1-s exposure time, upon applying the electrochemical potential for 1 s. Images (**B**, **C**, **E** and **F**) were taken with a 0.1-s exposure time, upon applying the potential for 5 s (when the Cl_2/O_2 bubbles were fully formed). False-color ECL images (**A** and **D**) and (**B**, **C**, **E** and **F**) were coded with the light intensity scales 1200-35000 (shown in **A**) and 1200-62000 (shown in **B**), respectively. The inset image in **Figure 4.4B** was coded with the intensity range 1200-10000. The dashed circle materializes the gold disc microelectrode. Scale bar: 50 µm. **(G)** The mean ECL intensity in the presence of 50 mM KNO_3 (in red) and 50 mM KCl (in blue) supporting electrolyte upon applying chronoamperometric pulses of 0.7 V, 2.4 V and 3 V vs Ag/AgCl. The values in the histograms represent the mean of experiments per conditions as

shown in micrographs **(A-F)** performed in triplicate in the presence (in blue) and absence of Cl^- (in red).The error bars indicate ±1 standard deviation from the mean.

Biasing the microelectrode at higher anodic potentials resulted in the generation of gas bubbles at its surface. We imaged the ECL signal across the solid/liquid/gas interface of a single electrogenerated bubble, before and after its detachment from the microelectrode surface (**Figures 4.1B** and **4.1C**, respectively). First, to analyze the bubble evolution on the electrode surface (**Figure 4.1B**), the working electrode faces downward and is imaged through a coverslip glass using the epifluorescence microscope. This configuration allowed us to analyze a single electrogenerated gas bubble, which remained stable at the electrode surface throughout the experiment, by looking from the bottom of the bubble during and after its formation, as electrostatic and buoyancy forces kept it attached to the microelectrode. Electrogenerated bubbles grow on the electrode surface until the rate of gas formation and that of its diffusion back into the solution equilibrate. After this, bubbles dissolve by diffusion which, in the case of pinned bubbles, is slowed down due to the presence of the electrode on one side.[91]

Water oxidation in absence of chloride ions generates an O_2 bubble whereas a Cl_2 bubble is produced in the electrolyte containing KCl. Both bubbles were visualized by bright field microscopy (**Figures 4.5B** and **4.5D**). ECL images were captured with an exposure time of 0.1 s, 5 s after imposing the potential in PBS solution (pH 8) containing H_2O_2, L-012 and either 50 mM KNO_3 (**Figures 4.4B** and **4.4C**) or 50 mM KCl (**Figures 4.4E** and **4.4F**). All micrographs recorded at high anodic potentials (i.e. **Figures 4.4B**, **4.4C**, **4.4E**, **4.4F**) are displayed with intensity scales adjusted to 1200-62000 colour levels, except for the **inset** image in **Figure 4.4B**, which has the intensity range set to lower values of 1200-10000. This adjustment was necessary to visualize the ECL emission in the inset of **Figure 4.4B**. **Figures 4.4B** and **4.4C** depict the ECL generated at the gas/liquid interface of the oxygen bubbles produced by applying electrode potentials of 2.4 V and 3 V, respectively. The substantial increase in the ECL intensity with the increase in electrode potential, from 1149 a.u. at 2.4 V to 8083 a.u. at 3 V (see **Figures 4.4B**, **4.4C,** and histogram in **Figure 4.4G**) suggests the dependence of the produced ECL on the rate of the oxygen evolution reaction (OER). Comparing a micrograph captured in the ECL conditions (**Figure 4.5A**) with a

corresponding bright field image of the same bubble (**Figure 4.5B**) clearly shows that ECL emission arises from the gas/liquid interface, suggesting the involvement of chemical reactions at the bubble surface. Indeed, the size of the bubble observed in bright field mode corresponds to the size of the ECL-emitting bubble, even if the ECL intensity is low and the intensity scale has to be adjusted to be visualized. These ECL-producing reactions likely include homogeneous oxidation of L-012 mediated by hydroxyl radicals[70], followed by its subsequent reaction with the superoxide radicals to populate the excited state. Since both $OH^{\bullet}$ and $O_2^{\bullet-}$ radicals are OER intermediates, their involvement in the ECL generation rationalizes the increasing emission intensity with the increase in electrode potential. Furthermore, the corona effect of the bubble promotes the generation of $OH^{\bullet}$ radicals at the electrode/bubble/electrolyte interface, possibly further enhancing ECL generation through the homogenous oxidation of L-012.[47]

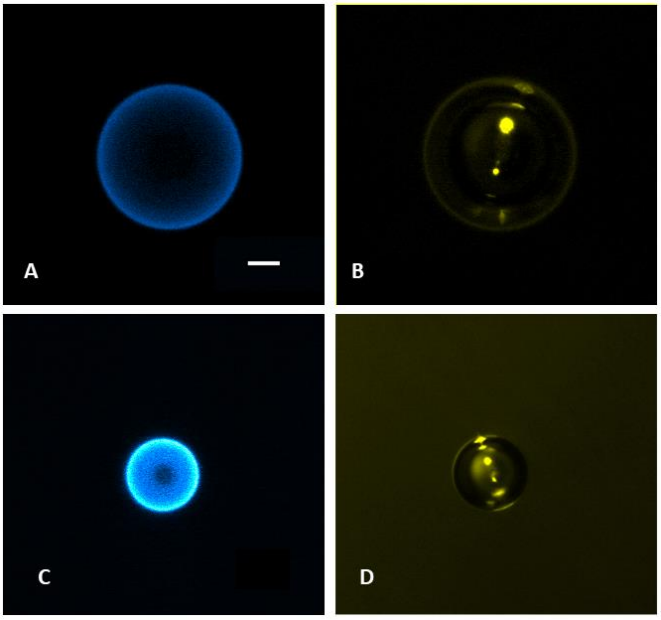

Figure 4.5. Top view micrographs of the ECL emission **(A** and **C)** and brightfield images **(B** and **D)** of the gas bubbles (O_2 for **(A-B)** and Cl_2 for **(C-D)**) generated at the gold microelectrode in the 0.2 M PBS solution pH 8 containing 0.5 M H_2O_2, 0.42 mM L-012 and 50 mM **(A-B)** KNO_3 and **(C-D)** KCl. Images were taken with the 0.1 s exposure time upon applying a 2.4 V potential pulse. The intensity scales were set to **(A)** 1200-3500 and **(C)** 1200-58000 grey levels. The scalebar is set to 50 µm.

Next, we tested the influence of the presence of chloride and the potential generation of Cl_2 bubbles on the ECL emission. We recorded both bright field and ECL images of the Cl_2 bubbles electrogenerated at 2.4 V and 3 V in the PBS solution, containing KCl supporting electrolyte, H_2O_2 and L-012 (**Figures 4.4E** and **4.4F**, respectively). The mean ECL intensities of the obtained micrographs were 59585 a.u. at 2.4 V and 62900 a.u. at 3 V (**Figure 4.4G**). Thus, in the presence of electrogenerated chlorine, we observed 51.8-fold (at 2.4 V) and 7.8-fold (at 3 V) ECL enhancements relative to the signals produced in the same conditions in the solution containing KNO_3 supporting electrolyte, and a 127.6-fold enhancement (at 2.4 V) compared to the low potential ECL (at 0.7 V) in the same electrolyte solution (**Figure 4.4G**). **Figures 4.5C** and **4.5D,** showing ECL and bright field micrographs of the same electrogenerated bubble, demonstrate that the ECL emission is produced by oxidizing L-012 (and H_2O_2) at the bubble/electrolyte interface according to the well-established mechanism of ECL generation in the presence of dissolved chlorine species.[87] Briefly, dissolved Cl_2 reacts with hydroxide ions (or water) to generate hypochlorite, a potent oxidant that efficiently mediates the oxidation of L-012. Oxidized L-012 then reacts with hydrogen peroxide or ROS, triggering consecutive chemical transformations that populate the excited state of the luminophore.

Similar considerations can be applied to the ECL emission in the absence of H_2O_2 (see **Figure 4.6**). Upon biasing the microelectrode to the potential of 0.7 V, ECL emission confined to the surface of the electrode was observed in both KNO_3 and KCl supporting electrolytes (see **Figures 4.6A** and **4.6D**) with ECL intensities of 21 a.u. and 48 a.u., respectively (histogram in **Figure 4.6G**). Thus, although visible, this ECL response is two and one ranges of magnitude lower in KNO_3 and KCl supporting electrolyte, respectively, when compared to the same conditions in the presence of H_2O_2. Furthermore, when biasing the microelectrode at high anodic potentials, the resulting ECL emission appeared at the outlines of the produced O_2 and Cl_2 gas bubbles (**Figures 4.6B, 4.6C, 4.6E** and **4.6F**) with the intensities of 19 a.u. and 42 a.u. in KNO_3 and 81 a.u. and 64 a.u. in KCl supporting electrolyte at 2.4 V and 3.0 V, respectively (histogram in **Figure 4.6G**). The enhanced ECL at the interface can be attributed to the increased production of hydroxyl radicals at the gas/solid/liquid interface due to charge separation at the surface of the bubble. There are reports of this reaction occurring spontaneously at the gas/liquid interface of microdroplets,

ultimately producing H_2O_2 through the recombination of hydroxyl radicals produced at the interface.[27,28] Furthermore, as previously discussed, the gas/solid/liquid interface at the anodically polarized electrodes further enhances the production of ROS,[47] demonstrating the importance of the interface effects on the reactivity within this heterogeneous system. The ECL intensity at the bubble's interface was more significantly enhanced in the presence of chloride ions, further confirming the key role of electrogenerated chlorine for the L-012 ECL enhancement, while the enhanced ECL emission with the increase of electrode potential in KNO_3 supporting electrolyte confirmed the importance of OER intermediates (i.e ROS) in producing the electrochemically excited state of L-012. Finally, the ECL intensity at high anodic potentials in the absence of H_2O_2 is lower by three and four orders of magnitude in KNO_3 and KCl supporting electrolytes, respectively, compared to the same experimental conditions in the presence of 0.5 M H_2O_2. Thus, ECL in the absence of H_2O_2 would not interfere with any potential analytical application of such ECL measurements as it is in the acceptable error range and the ECL intensity of L-012 demonstrates high dependence on the concentration of H_2O_2.

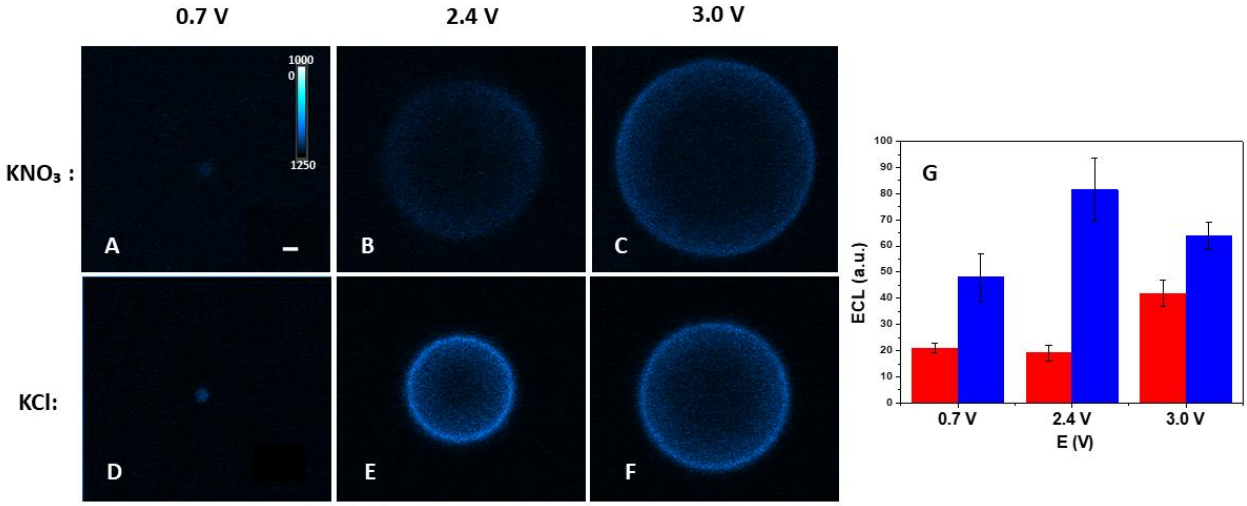

Figure 4.6. Bottom-view images of the ECL emission at the gold 25-µm disc microelectrode in the 0.2 M PBS solution (pH 8) containing 0.42 mM L-012 and 50 mM **(A-C)** KNO_3 or **(D-F)** KCl. Electrode potential was set to **(A** and **D)** 0.7 V, **(B** and **E)** 2.4 V and **(C** and **F)** 3 V vs Ag/AgCl for 20 s. Images **A** and **D** were recorded with a 3-s exposure time, while applying the electrochemical potential for 3 s. Images (**B**, **C**, **E** and **F**) were taken with a 1-s exposure time, upon applying the potential for 5 s (when the Cl_2/O_2 bubbles were fully formed). False-color ECL images were coded with the light

intensity scales 1200-10000 (shown in **A**). Scale bar: 25 µm. **(G)** The mean ECL intensity in the presence of 50 mM KNO_3 (in red) and 50 mM KCl (in blue) supporting electrolyte upon applying chronoamperometric pulses of 0.7 V, 2.4 V and 3 V vs Ag/AgCl. The values in the histograms represent the mean of experiments per conditions as shown in micrographs **(A-F)** performed in triplicate in the presence (in blue) and absence of Cl^- (in red). The error bars indicate ±1 standard deviation from the mean.

Moreover, in the general case, ECL generation is confined to the immediate vicinity of the electrode surface, due to the limited lifetime of the electrogenerated species in solution, typically a few micrometres, depending on luminophore type, the experimental conditions and the operating ECL mechanisms.[31,33,34,37,44,60,92–94] However, the here-reported approach demonstrates the possibility of extending the ECL-emitting region far from the electrode. Indeed, the sizes of the ECL-emitting bubbles shown are 138 µm and 186 µm (**Figures 4.4E**, and **4.4F**, respectively). This is an important result because it considerably extends the ECL-active region using electrochemical reactions that are generally considered detrimental.

Besides emission intensity, the generated signal stability and its duration are also important to most ECL applications. We analyzed the ECL intensity in KNO_3 or KCl supporting electrolytes (in the presence of L-012 and H_2O_2) when the Au microelectrode was biased at 2.4 V for 20 s (**Figure 4.7A** and **4.7B**, respectively). To ensure a good temporal resolution, we recorded a video during the 20 s potential pulse, at a rate of 8 frames per second. We then analyzed each frame by extracting intensity profiles of a rectangular region along the diameter of the electrogenerated bubbles (as shown in **Figure 4.8A**) and plotted the obtained profiles against time (**Figures 4.7A** and **4.7B**). This allowed the analysis of ECL intensity during the bubble evolution at the electrode surface. **Figure 4.7A** shows that the ECL intensity initially increases with an increase in the diameter of the electrogenerated oxygen bubble, to reach a maximal value of ca. 3400 a.u., 5 s after initiating a potential pulse at 2.4 V, followed by a sharp decrease of the ECL emission with the increase in the bubble size, reaching the level of background noise at around 13 s after the potential pulse. Conversely, while ECL emission in KCl solution expresses a maximum of 90000 a.u. 5 s after imposing the potential, the decrease in the light intensity with the increase in the Cl_2

bubble size is less pronounced, with the emission reaching a steady state at an emission intensity of ca. 40000 a.u. after 7 s, which lasted to the end of the 20 s chronoamperometric pulse (**Figure 4.7B**).

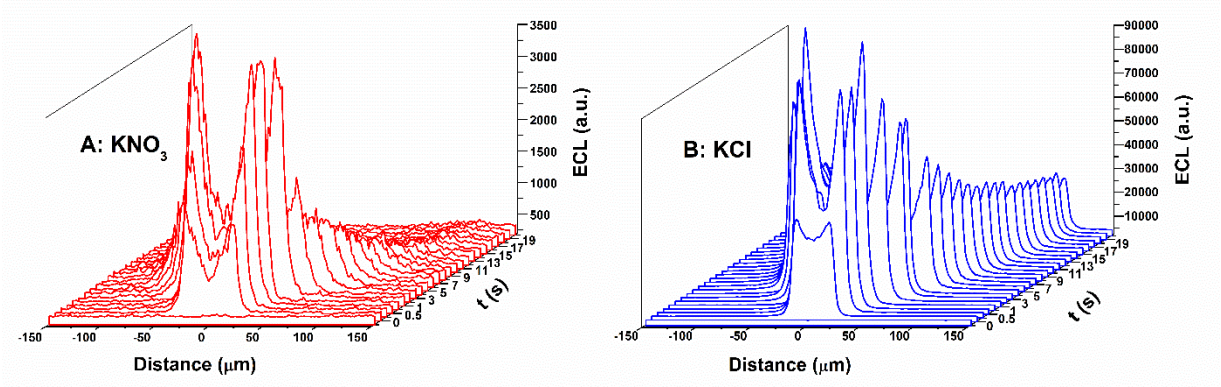

Figure 4.7. Evolution with time of the ECL intensity profiles at the interface of the O_2 and Cl_2 gas bubbles produced at the surface of a gold microelectrode. The electrode was immersed in the 0.2 M PBS solution (pH 8), containing 0.5 M H_2O_2, 0.42 mM L-012 and 50 mM of **(A)** KNO_3 or **(B)** KCl and the potential of 2.4 V vs Ag/AgCl was applied for 20 s.

The increase in ECL intensity observed during the initial 5 s of the potential pulse, followed by an ECL decrease, is noteworthy as it indicates a common underlying phenomenon controlling ECL emission during bubble formation in both KCl and KNO_3 electrolytes. Since the gas evolution reactions at 2.4 V are expected to selectively generate chlorine and oxygen in KCl and KNO_3, respectively, this trend is not attributed to a shared reaction step in the two electrolyte solutions. Rather, it is linked to a general increase in electrochemical reactivity at the solid/gas/liquid interface, driven by the corona effect of the bubble.[47] Initially, elevated reactivity at the interface compensates for the decrease in electrode surface area that is covered by the gas bubble. However, after the bubble reaches a certain size (at 5 s), the enhancement in electrochemical reactivity can no longer compensate for the large portion of the microelectrode isolated from the solution. Consequently, ECL generated at the surface of the O_2 bubble rapidly decreases as ROS are no longer efficiently produced. In contrast, ECL at the Cl_2 bubble reaches a plateau, as electrogenerated chlorine species can effectively mediate all the redox reactivity in the system, sustaining ECL emission even in the absence of ROS.

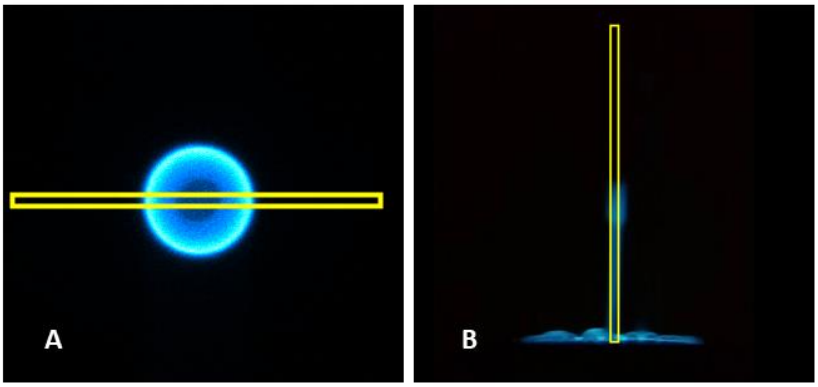

Figure 4.8. Representative examples of the micrographs with shown rectangular regions of interest used to extract ECL intensities for the plots in **(A)** Figure 2 (bottom-view) and **(B)** Figure 4 (side-view).

Several works have been devoted to the development of chemiluminescent and ECL systems that produce luminescence for a long-lasting time.[77,80] Indeed, in the ECL field, since the species producing the excited state are electrogenerated, stopping their production ends the ECL emission instantly. Therefore, developing a long-lasting ECL emission can be considered as a challenging task. To investigate the temporal characteristics of the reported approach, we followed the ECL emission after stopping the imposition of the anodic potential (**Figure 4.9**). As expected, no ECL was observed in the KNO_3 supporting electrolyte after stopping the application of the anodic potential (**Figure 4.9A**), and the system returned to its background value immediately. The behaviour is completely different in the presence of KCl: ECL emission persists at the interface of the Cl_2 bubble even when the potential is no longer applied to the microelectrode (**Figures 4.9B**-**4.9D)**. The intensity of this "afterglow" ECL exponentially decreases over time, vanishing after approximately 145 s (**Figure 4.9E**). This very long-lasting ECL is a very important result because the ECL process is based on a different mechanism involving the production of Cl_2 bubbles. Moreover, the observed ECL emission layer expands into the solution, following the diffusion pattern of dissolved Cl_2. We observed complex ECL patterns with bright ECL rings that are visible inside the Cl_2 bubble in **Figures 4.9B-4.9D**. Dick and co-workers reported the reflection of ECL light (generated at the electrode surface) by CO_2 bubbles located far away.[51] The ECL patterns that we observed might be related to the reflection of the ECL emitted in

solution by the glass insulating the Au microelectrode tip, and not from the ECL emission inside the bubble.

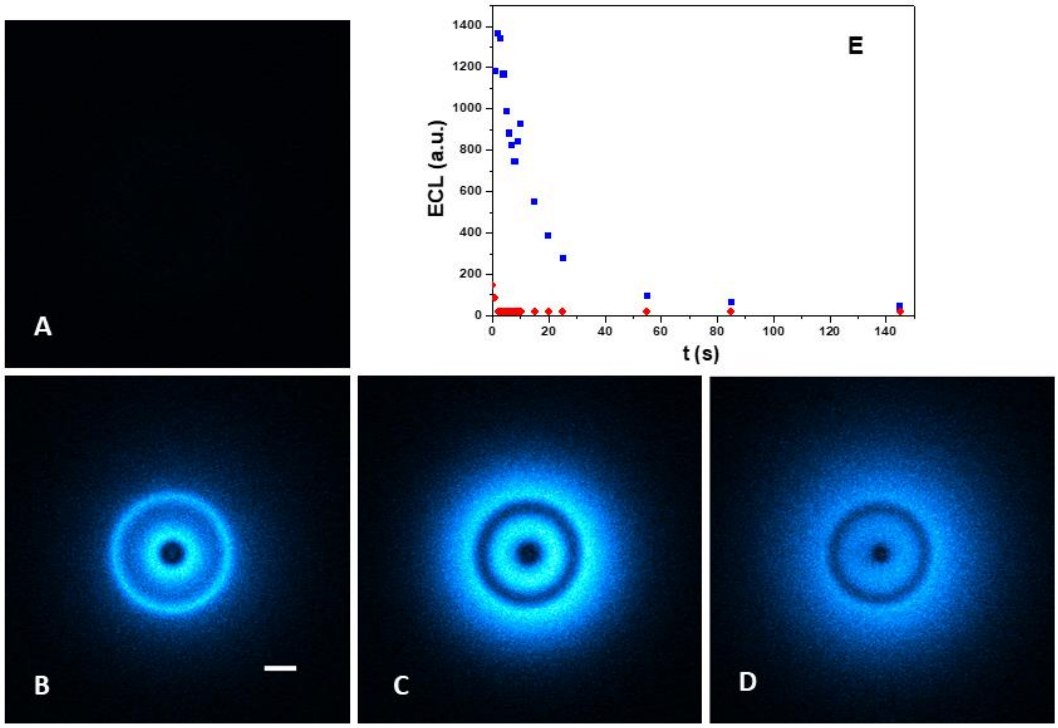

Figure 4.9. **(A-D)** Top view micrographs of the ECL emission at the gold microelectrode in the 0.2 M PBS solution pH = 8 containing 0.5 M H_2O_2, 0.42 mM L-012 and 50 mM **(A)** KNO_3 and **(B-D)** KCl. Images were captured with a 1 s exposure time, 1 s **(A** and **B)**, 3s **(C)** and 7 s **(D)** after stopping the CA potential pulse of 2.4 V. The intensity scale is set to the range of 1200-15500 units of grey value. The scalebar is set to 50 µm. **(E)** Evolution of the mean ECL intensity with time in the presence of 50 mM KNO_3 (in red) and 50 mM KCl (in blue) supporting electrolyte. Solution composition and electrochemical conditions are consistent with **(A-D)**.

4.3.3 ECL in bulk: mapping spatial ECL extension

As discussed above, bubble effects can significantly enhance the electrochemical reactivity on the solid/gas/liquid interface, amplifying drastically the resulting ECL intensity and its duration. In addition, once the Cl_2 bubble is generated, ECL is emitted at the gas/liquid interface with the solution even in the absence of the applied potential. Consequently, after detaching from the electrode, the bubble is likely a reservoir for oxidizing species, initiating redox

reactions and producing ECL emission while travelling through the solution. To confirm this, we followed the bubble formation and its subsequent detachment from the electrode in an upright experimental setup (**Figure 4.1C**). In other words, the working electrode faced upwards in an electrochemical cell and ECL was imaged through a coverslip glass window on the side of the cell. In this arrangement, the buoyancy force propelled the bubble upward through the solution. To monitor the bubble evolution in solution and the volumic extension of the ECL-emitting zone at the bubble from the side, we changed the angle of observation with an orthogonal side-view configuration (**Figure 4.1C**). It supplements the bottom-view configuration with a 2D ECL imaging approach normal to the electrode surface and allows the exploration of events occurring away from the electrode surface.

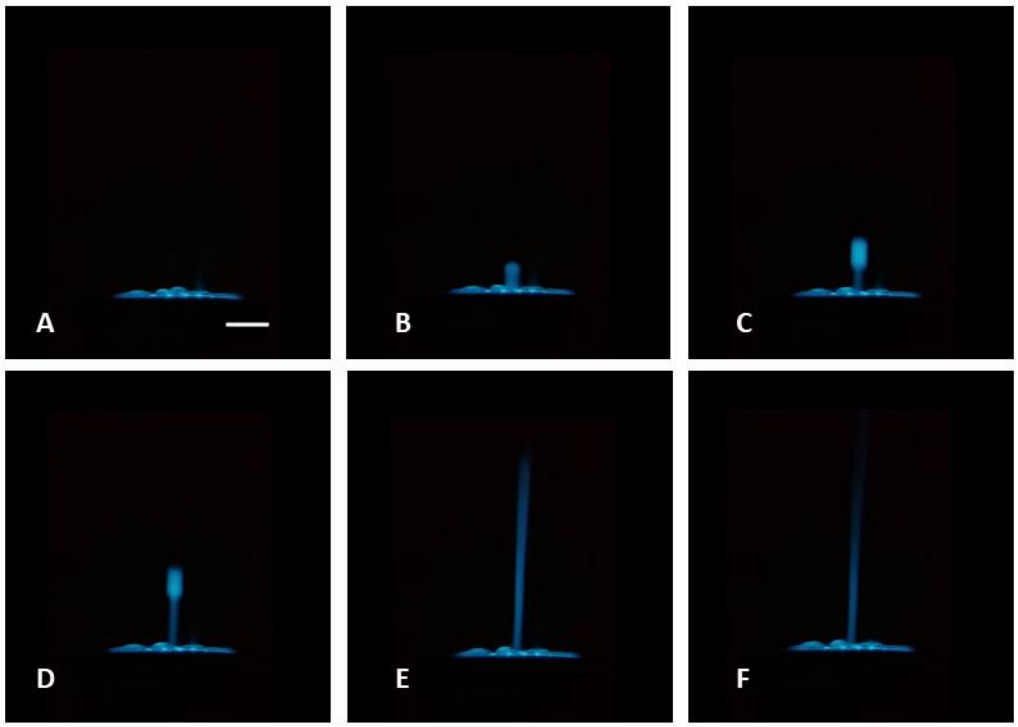

Figure 4.10. Side-view ECL images **(A-F)** depict the trajectory of a single electrochemically generated Cl_2 bubble at different times (**A-F**: 0, 33 ms, 67 ms, 100 ms, 233 ms, and 367 ms, respectively) after detachment from the surface of the glassy carbon electrode. These images were extracted from a video provided in the SI, recorded during a cyclic voltammetry scan from

0 V to 3 V at a scan rate of 0.1 V s^{-1} in a 0.2 M PBS solution (pH 8), containing 0.5 M H_2O_2, 0.42 mM L-012, and 50 mM KCl. Scale bar: 1 mm.

We used a 3-mm GC disc electrode, which ensured the bubbles would grow unrestrained by the limited electrode surface area of a microelectrode. This arrangement allowed us to observe the growth of the electrogenerated bubbles to their critical size and to track their path as the buoyancy force propelled them upward through the solution. We recorded a video (see SI) at 30 frames per second, while scanning the potential imposed on the working electrode from 0 V to 3 V at 0.1 V s^{-1}. The frames in **Figures 4.10A-4.10F** show the vertical movement of a single Cl_2 bubble from the electrode surface where it is electrogenerated into the bulk solution. These images reflect the change in size and velocity of the chlorine bubble. Furthermore, they show the diffusion pattern of dissolved chlorine (luminescent regions tracing the bubble's path). Thus, the evolution of chlorine at high anodic potentials not only extends the ECL emission of L-012 far from the electrode surface, but it provides a means of visualizing the dissolution of gases, diffusion of chemical species, and reactions at phase interfaces and in solution.

Furthermore, we evaluated how ECL intensity varied with distance from the electrode after the bubble shown in **Figure 4.10** was propelled into the solution. This involved analyzing ECL intensity profiles along rectangular regions extending from the electrode surface into the bulk solution (see **Figure 4.8B**). Subsequently, we plotted these intensity profiles against time, as illustrated in **Figure 4.11**. The profiles from 0 s to 100 ms correspond to the images in **Figure 4.10A-4.10D**. They show that the front of ECL emission follows the bubble propagation, with strong intensity concentrated on the bubble's surface and comparable intensity values in the solution between the bubble and electrode. In other words, considering the electrogenerated bubble, the maximum ECL intensity is located in the regions far from the electrode, where the bubbles propel and meet “fresh” reactants. It indicates that ECL emission results from reactions occurring with chlorine without any additional involvement of the electrode reactions. However, after 100 s, the dissolution of chlorine caused the bubble to collapse, resulting in the strong ECL emission in solution and the disappearance of the sharp emission front. This ECL in solution reached a maximum distance of 5 mm from the electrode surface at 233 ms. At this point, the

bubble was completely dissolved (**Figure 4.10E**). As the dissolved chlorine species were consumed, the ECL front gradually decreased until the ECL emission was no longer visible.

It is noteworthy that this is the first example of generating ECL emission a few millimetres from the electrode surface. As already mentioned, the ECL phenomenon is usually confined to the micrometric region in the immediate vicinity of the electrode surface.[31,33,34,37,44,60,92–94] The reported approach allows analyzing processes occurring far away from the electrode surface. Finally, while examples of ECL emission at the interface of two immiscible liquids exist in the literature,[48,49] this study presents the first example of ECL produced at the gas/liquid interface.

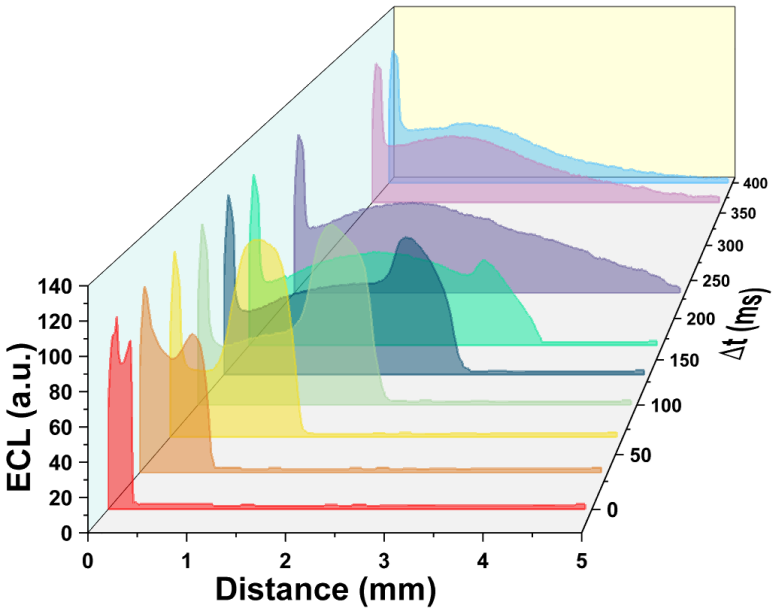

Figure 4.11. Spatial extension of the ECL emission following a detachment of a Cl_2 bubble from the electrode surface (corresponding images are shown in **Figure 4.10**). The propagation of ECL up to 5 mm from the electrode indicates the possibility for delayed formation of the reactive radical species upon dissolution of the gas entrapped inside the bubble.

4.3.4 High potential ECL toward enhanced biosensing performance

One of the key analytical applications of the luminol/H_2O_2 system is in biosensing, [42,95–98] primarily due to the direct correlation of its ECL intensity with the concentration of hydrogen peroxide. Since H_2O_2 is commonly produced in enzymatic reactions involving oxidase enzymes, ECL emission by luminol can be used to effectively quantify substrates of such enzymes (e.g.

cholesterol and glucose), or to study the kinetics of enzymatic reactions.[67,99] Consequently, we anticipate that the enhanced ECL at the surface of the electrogenerated chlorine bubble, observed in here-investigated approach, would lead to a decrease in the detection limit in oxidase-based enzymatic sensors. Moreover, this robust ECL emission could enable the at-home monitoring of glucose using disposable ECL sensing devices, with detection facilitated by a smartphone camera.

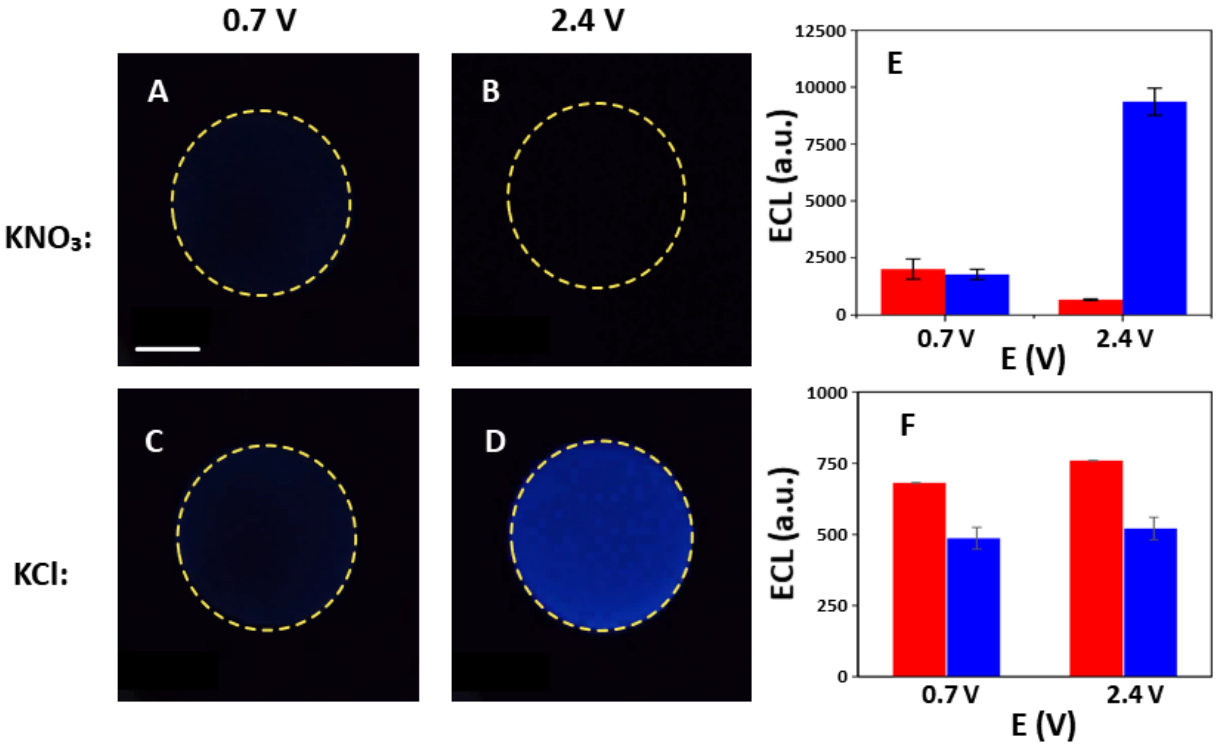

Figure 4.12. ECL detection of glucose. ECL emission on GC electrode in a 0.2 M PBS solution (pH 8) containing 0.42 mM L-012, 1 mg ml^{-1} glucose oxidase, and 1 mM glucose, with 50 mM **(A-B)** KNO_3 or **(C-D)** KCl supporting electrolyte upon applying a 10 s potential pulse at **(A** and **C)** 0.7 V and **(B** and **D)** 2.4 V. Scale bar: 1 mm. **(E-F)** Histograms showing the mean ECL Intensity extracted from the experiments performed in triplicate under experimental conditions as in **(A-D)** in the presence (in blue) and absence of Cl^- (in red) at different potentials in the **(E)** presence or **(F)** absence of glucose. The error bars indicate ±1 standard deviation from the mean.

In this proof-of-principle study, we used a phone camera to record the ECL emission in 0.2 M PBS solutions containing 0.45 mM LO12 and 1 mM glucose, immediately upon adding 1 mg ml^{-1} glucose oxidase. The images were captured when the working electrode was biased at 0.7 V (**Figures 4.12A** and **4.12C**) and 2.4 V (**Figures 4.12B and 4.12D**) for 10 s, while 50 mM KNO_3 (**Figures 4.12A** and **4.12B**) or KCl (**Figures 4.12C** and **4.12D**) served as the supporting electrolytes. **Figures 4.12A** and **4.12C** show that the ECL produced at low electrode potentials is not significantly influenced by the nature of the supporting electrolyte, and it exhibits average intensities of 2040 a.u. and 1803 a.u. (**Figure 4.12E**) in KNO_3 and KCl supporting electrolytes, respectively. Conversely, upon applying a potential of 2.4 V to the working electrode, no ECL was detected in the KNO_3-containing solution (**Figure 4.12B**), while bright ECL emission with an intensity of 9396 a.u. emerged from the KCl-containing solution (**Figure 4.12D** and histogram in **Figure 4.12E**). Thus, the ECL signal at 2.4 V was 5.2-fold higher than that observed at 0.7 V (**Figure 4.12C**), potentially facilitating more sensitive glucose detection and quantification. Moreover, **Figure 4.12D** reveals non-uniform ECL distribution at the electrode surface, with brighter regions corresponding to the localization of electrogenerated bubbles, further emphasizing the crucial contribution of chlorine bubble formation in the enhanced ECL for enzymatic detection of glucose.

Control experiments performed under the same conditions, but in the absence of glucose show that ECL response is low and similar in all experimental conditions regardless of the value of applied potential or the composition of the supporting electrolyte (**Figure 4.12F**). The intensity of such ECL signal in the KCl-containing solution at 2.4 V is 17.8 lower than in the same conditions in the presence of 1 mM glucose. This indicates that, while the effects of gas/liquid interface (including bubble corona effect) have a significant influence on (electro)chemical reactivity and mechanism of ECL generation in the L-012/H_2O_2 system, they do not introduce significant background noise to the measurement. Furthermore, the low standard deviation of the measurements, along with enhanced ECL intensity (increased sensitivity), of the high-potential measurements in the presence of chloride ions, renders this method suitable for quantitative measurements.

4.4 Conclusion

Bubble formation is usually avoided in electroanalysis and in ECL because it introduces variability and decreases the reliability of electrochemical measurements. However, chlorine bubbles, formed at an electrode in a solution containing chloride ions, extend the spatial and temporal range of ECL events. ECL is a highly localized phenomenon normally restricted to a few micrometers from the electrode surface.

In this work, we have shown that bubble formation enhanced ECL emission of luminol and its derivatives trough two parallel effects: (i) the corona effect of the bubble, which consists of the buildup of reactive oxygen species such as hydroxyl radicals at the gas/liquid interface; (ii) the release of chlorine into the solution, which readily oxidizes luminol in the presence of H_2O_2. While the corona effect also triggered ECL in the absence of chloride ions, the second effect only occurred following the oxidation of chloride into chlorine gas bubbles at high anodic potentials (i.e above 2 V). The subsequent release and dissolution of chlorine in the solution (producing hypochlorite) generated an intense ECL emission at the gas/liquid interface. In addition, bubbles that grow large enough to detach from the electrode surface, continue emitting light during their movement as long as they contain chlorine. Remarkably, we have observed ECL emission from these bubbles up to a remarkable distance of 5 mm away from the electrode surface.

Moreover, the intensity of this bubble-enhanced ECL recorded at 2.4 V was 127.6 times higher than that of the ECL emission recorded at the commonly used potential of 0.7 V. In terms of ECL duration, the emissions recorded at 0.7 V vanished immediately after stopping the electrode polarization. In the case of the electrogenerated bubbles, ECL emissions that lasted for up to 145 s have been observed after electrode polarization. This long-lasting ECL emission is an unusual behavior in the ECL field.

Last, we have shown the utility of this approach for the detection of glucose. Again, the enzymatic detection of glucose performed at 2.4 V in the presence of chloride was 5.2 times higher than that at the same electrode polarized at 0.7 V. This is highly significant in the field of interfacial chemistry and electroanalysis, not only because it provides enhanced signals, but mainly because it represents the first example of ECL produced at the gas/liquid interface, which

opens the technique to the study of the dissolution of gases, diffusion of chemical species, and reactions at phase interfaces and in solution.

References

1 K. J. Vannoy, M. Q. Edwards, C. Renault and J. E. Dick, *Annu. Rev. Phys. Chem.*, 2024, **17**, 149–171.
2 Z. Wei, Y. Li, R. G. Cooks and X. Yan, *Annu. Rev. Phys. Chem.*, 2020, **71**, 31–51.
3 M. F. Ruiz-Lopez, J. S. Francisco, M. T. C. Martins-Costa and J. M. Anglada, *Nat Rev Chem*, 2020, **4**, 459–475.
4 R. N. Butler and A. G. Coyne, *Chem. Rev.*, 2010, **110**, 6302–6337.
5 K. J. Vannoy, I. Lee, K. Sode and J. E. Dick, *Proc. Natl. Acad. Sci.*, 2021, **118**, e2025726118.
6 J. K. Lee, D. Samanta, H. G. Nam and R. N. Zare, *J. Am. Chem. Soc.*, 2019, **141**, 10585–10589.
7 L. Qiu and R. G. Cooks, *Angew. Chem. Int. Ed.*, 2024, **63**, e202400118.
8 J. Wordsworth, T. M. Benedetti, S. V. Somerville, W. Schuhmann, R. D. Tilley and J. J. Gooding, *Angew. Chem. Int. Ed.*, 2022, **61**, e202200755.
9 S.-M. Lu, K. J. Vannoy, J. E. Dick and Y.-T. Long, *J. Am. Chem. Soc.*, 2023, **145**, 25043–25055.
10 J. E. Dick, E. Lebègue, L. M. Strawsine and A. J. Bard, *Electroanalysis*, 2016, **28**, 2320–2326.
11 W. Cheng and R. G. Compton, *Angew. Chem. Int. Ed.*, 2015, **54**, 7082–7085.
12 W. Cheng and R. G. Compton, *Angew. Chem. Int. Ed.*, 2016, **55**, 2545–2549.
13 Y. Jung and R. A. Marcus, *J. Am. Chem. Soc.*, 2007, **129**, 5492–5502.
14 D. Ben-Amotz, *Science*, 2022, **376**, 800–801.
15 J. S. Hub, M. G. Wolf, C. Caleman, P. J. van Maaren, G. Groenhof and D. van der Spoel, *Chem. Sci.*, 2014, **5**, 1745–1749.
16 P. B. Petersen and R. J. Saykally, *Chem. Phys. Lett.*, 2008, **458**, 255–261.
17 G. Zheng, H. Su, S. Wang, M. O. Andreae, U. Pöschl and Y. Cheng, *Science*, 2020, **369**, 1374–1377.
18 L. Cohen, M. I. Quant and D. J. Donaldson, *ACS Earth Space Chem.*, 2020, **4**, 854–861.
19 K.-H. Huang, Z. Wei and R. Graham Cooks, *Chem. Sci.*, 2021, **12**, 2242–2250.
20 R. K. Bhullar, M. J. Zdilla, M. L. Klein and R. C. Remsing, *J. Mater. Chem. A*, 2021, **9**, 6924–6932.
21 R. C. Remsing, I. G. McKendry, D. R. Strongin, M. L. Klein and M. J. Zdilla, *J. Phys. Chem. Lett.*, 2015, **6**, 4804–4808.
22 A. Fallah-Araghi, K. Meguellati, J.-C. Baret, A. E. Harrak, T. Mangeat, M. Karplus, S. Ladame, C. M. Marques and A. D. Griffiths, *Phys. Rev. Lett.*, 2014, **112**, 028301.
23 K. R. Wilson, A. M. Prophet, G. Rovelli, M. D. Willis, R. J. Rapf and M. I. Jacobs, *Chem. Sci.*, 2020, **11**, 8533–8545.
24 D. Ben-Amotz, *J. Chem. Phys.*, 2024, **160**, 084704.
25 C. F. Chamberlayne and R. N. Zare, *J. Chem. Phys.*, 2020, **152**, 184702.
26 A. G. Volkov, D. W. Deamer, D. L. Tanelian and V. S. Markin, *Prog. Surf. Sci.*, 1996, **53**, 1–134.
27 J. K. Lee, K. L. Walker, H. S. Han, J. Kang, F. B. Prinz, R. M. Waymouth, H. G. Nam and R. N. Zare, *Proc. Natl. Acad. Sci.*, 2019, **116**, 19294–19298.
28 M. A. Mehrgardi, M. Mofidfar and R. N. Zare, *J. Am. Chem. Soc.*, 2022, **144**, 7606–7609.
29 L.-N. Zhang, R. Li, H.-Y. Zang, H.-Q. Tan, Z.-H. Kang, Y.-H. Wang and Y.-G. Li, *Energy Environ. Sci.*, 2021, **14**, 6191–6210.
30 Z. Liu, W. Qi and G. Xu, *Chem. Soc. Rev.*, 2015, **44**, 3117–3142.
31 M. Sentic, M. Milutinovic, F. Kanoufi, D. Manojlovic, S. Arbault and N. Sojic, *Chem. Sci.*, 2014, **5**, 2568–2572.
32 J. E. Dick, C. Renault, B.-K. Kim and A. J. Bard, *Angew. Chem. Int. Ed.*, 2014, **53**, 11859–11862.

33 Y. Wang, W. Guo, Q. Yang and B. Su, *J. Am. Chem. Soc.*, 2020, **142**, 1222–1226.
34 A. Zanut, A. Fiorani, S. Canola, T. Saito, N. Ziebart, S. Rapino, S. Rebeccani, A. Barbon, T. Irie, H.-P. Josel, F. Negri, M. Marcaccio, M. Windfuhr, K. Imai, G. Valenti and F. Paolucci, *Nat. Commun.*, 2020, **11**, 2668.
35 N. S. Adamson, A. G. Theakstone, L. C. Soulsby, E. H. Doeven, E. Kerr, C. F. Hogan, P. S. Francis and L. Dennany, *Chem. Sci.*, 2021, **12**, 9770–9777.
36 A. Fracassa, C. I. Santo, E. Kerr, S. Knežević, D. J. Hayne, P. S. Francis, F. Kanoufi, N. Sojic, F. Paolucci and G. Valenti, *Chem. Sci.*, 2024, **15**, 1150–1158.
37 P. Zhou, S. Hu, W. Guo and B. Su, *Fundam. Res.*, 2022, **2**, 682–687.
38 M. Belotti, M. M. T. El-Tahawy, M. Garavelli, M. L. Coote, K. S. Iyer and S. Ciampi, *Anal. Chem.*, 2023, **95**, 9779–9786.
39 M. Belotti, M. M. T. El-Tahawy, L.-J. Yu, I. C. Russell, N. Darwish, M. L. Coote, M. Garavelli and S. Ciampi, *Angew. Chem. Int. Ed.*, 2022, **61**, e202209670.
40 H. M. Rodriguez, M. Martyniuk, K. S. Iyer and S. Ciampi, *J. Am. Chem. Soc.*, 2024, **146**, 10299–10311.
41 P. A. Defnet and B. Zhang, *ChemElectroChem*, 2020, **7**, 252–259.
42 Y. Wang, R. Jin, N. Sojic, D. Jiang and H. Chen, *Angew. Chem. Int. Ed.*, 2020, **59**, 10416–10420.
43 P. Nikolaou, G. Valenti and F. Paolucci, *Electrochim. Acta*, 2021, **388**, 138586.
44 W. Guo, P. Zhou, L. Sun, H. Ding and B. Su, *Angew. Chem. Int. Ed.*, 2021, **60**, 2089–2093.
45 H. Al-Kutubi, S. Voci, L. Rassaei, N. Sojic and K. Mathwig, *Chem. Sci.*, 2018, **9**, 8946–8950.
46 M. Wang, J. Liu, X. Liang, R. Gao, Y. Zhou, X. Nie, Y. Shao, Y. Guan, L. Fu, J. Zhang and Y. Shao, *Anal. Chem.*, 2021, **93**, 4528–4535.
47 Y. B. Vogel, C. W. Evans, M. Belotti, L. Xu, I. C. Russell, L.-J. Yu, A. K. K. Fung, N. S. Hill, N. Darwish, V. R. Gonçales, M. L. Coote, K. Swaminathan Iyer and S. Ciampi, *Nat. Commun.*, 2020, **11**, 6323.
48 M. W. Glasscott and J. E. Dick, *J. Phys. Chem. Lett.*, 2020, **11**, 4803–4808.
49 M. W. Glasscott, S. Voci, P. J. Kauffmann, A. I. Chapoval and J. E. Dick, *Langmuir*, 2021, **37**, 2907–2912.
50 S. Voci, K. J. Vannoy and J. E. Dick, *J. Colloid Interface Sci.*, 2024, **661**, 853–860.
51 B. R. Layman and J. E. Dick, *J. Am. Chem. Soc.*, 2024, **146**, 707–713.
52 Y. Chen, D. Zhao, J. Fu, X. Gou, D. Jiang, H. Dong and J.-J. Zhu, *Anal. Chem.*, 2019, **91**, 6829–6835.
53 M.-M. Chen, C.-H. Xu, W. Zhao, H.-Y. Chen and J.-J. Xu, *Chem. Commun.*, 2020, **56**, 3413–3416.
54 M.-M. Chen, C.-H. Xu, W. Zhao, H.-Y. Chen and J.-J. Xu, *J. Am. Chem. Soc.*, 2021, **143**, 18511–18518.
55 H. Zhu, D. Jiang and J.-J. Zhu, *Chem. Sci.*, 2021, **12**, 4794–4799.
56 J. Dong, Y. Xu, Z. Zhang and J. Feng, *Angew. Chem. Int. Ed.*, 2022, **61**, e202200187.
57 J.-W. Xue, C.-H. Xu, W. Zhao, H.-Y. Chen and J.-J. Xu, *Nano Lett.*, 2023, **23**, 4572–4578.
58 C. Ma, Y. Cao, X. Gou and J.-J. Zhu, *Anal. Chem.*, 2020, **92**, 431–454.
59 S. Rebeccani, A. Zanut, C. I. Santo, G. Valenti and F. Paolucci, *Anal. Chem.*, 2022, **94**, 336–348.
60 W. Miao, J.-P. Choi and A. J. Bard, *J. Am. Chem. Soc.*, 2002, **124**, 14478–14485.
61 J. Hu, N. Zhang, P.-K. Zhang, Y. Chen, X.-H. Xia, H.-Y. Chen and J.-J. Xu, *Angew. Chem. Int. Ed.*, 2020, **59**, 18244–18248.
62 Y. Nishinaka, Y. Aramaki, H. Yoshida, H. Masuya, T. Sugawara and Y. Ichimori, *Biochem. Biophys. Res. Commun.*, 1993, **193**, 554–559.
63 A. Kielland, T. Blom, K. S. Nandakumar, R. Holmdahl, R. Blomhoff and H. Carlsen, *Free Radic. Biol. Med.*, 2009, **47**, 760–766.
64 N. Harvey, *J. Phys. Chem.*, 1929, **33**, 1456–1459.
65 J. Arnhold, S. Mueller, K. Arnold and E. Grimm, *J. Biolumin. Chemilumin.*, 1991, **6**, 189–192.

66 H. Cui, W. Wang, C.-F. Duan, Y.-P. Dong and J.-Z. Guo, *Eur. J. Chem.*, 2007, **13**, 6975–6984.
67 M. Guo, D. Du, J. Wang, Y. Ma, D. Yang, M. A. Haghighatbin, J. Shu, W. Nie, R. Zhang, Z. Bian, L. Wang, Z. J. Smith and H. Cui, *Chem. Biomed. Imaging*, 2023, **1**, 179–185.
68 F. Han, H. Jiang, D. Fang and D. Jiang, *Anal. Chem.*, 2014, **86**, 6896–6902.
69 R. He, H. Tang, D. Jiang and H. Chen, *Anal. Chem.*, 2016, **88**, 2006–2009.
70 W. Xu, Y. Wu, X. Wang, Y. Qin, H. Wang, Z. Luo, J. Wen, L. Hu, W. Gu and C. Zhu, *Angew. Chem. Int. Ed.*, 2023, **62**, e202304625.
71 M. Xi, Z. Wu, Z. Luo, L. Ling, W. Xu, R. Xiao, H. Wang, Q. Fang, L. Hu, W. Gu and C. Zhu, *Angew. Chem. Int. Ed.*, 2023, **62**, e202302166.
72 W. Liang, M. Wang, C. Ma, J. Wang, C. Zhao and C. Hong, *Small*, 2024, **20**, 2306473.
73 N. Gao, G. Ren, M. Zhang and L. Mao, *J. Am. Chem. Soc.*, 2024, **146**, 3836–3843.
74 H. Xia, X. Zheng, J. Li, L. Wang, Y. Xue, C. Peng, Y. Han, Y. Wang, S. Guo, J. Wang and E. Wang, *J. Am. Chem. Soc.*, 2022, **144**, 7741–7749.
75 M. Mayer, S. Takegami, M. Neumeier, S. Rink, A. Jacobi von Wangelin, S. Schulte, M. Vollmer, A. G. Griesbeck, A. Duerkop and A. J. Baeumner, *Angew. Chem. Int. Ed.*, 2018, **57**, 408–411.
76 S. Rink, A. Duerkop and A. J. Baeumner, *Anal. Sens.*, 2023, **3**, e202200111.
77 Y. Liu, W. Shen, Q. Li, J. Shu, L. Gao, M. Ma, W. Wang and H. Cui, *Nat Commun*, 2017, **8**, 1003.
78 X. Li, Y. Du, H. Wang, H. Ma, D. Wu, X. Ren, Q. Wei and J.-J. Xu, *Anal. Chem.*, 2020, **92**, 12693–12699.
79 H. Zhu, J.-L. Zhou, C. Ma, D. Jiang, Y. Cao and J.-J. Zhu, *Anal. Chem.*, 2023, **95**, 11526–11534.
80 L. Chen, X. Zhu, J. Wei, L. Tian, C. Hu, X. Xiang and S.-F. Zhou, *Anal. Chem.*, 2023, **95**, 2917–2924.
81 M. Jaugstetter, N. Blanc, M. Kratz and K. Tschulik, *Chem. Soc. Rev.*, 2022, **51**, 2491–2543.
82 S. Voci, A. Ismail, P. Pham, J. Yu, A. Maziz, F. Mesnilgrente, L. Reynaud, T. Livache, P. Mailley, A. Buhot, T. Leichle, A. Kuhn, L. Leroy, A. Bouchet-Spinelli and N. Sojic, *J. Electrochem. Soc.*, 2020, **167**, 137509.
83 N. Wang, H. Ao, W. Xiao, W. Chen, G. Li, J. Wu and H. Ju, *Biosens. Bioelectron.*, 2022, **201**, 113959.
84 K. J. Vannoy, M. Q. Edwards, C. Renault and J. E. Dick, *Annu Rev Anal Chem (Palo Alto Calif)*, , DOI:10.1146/annurev-anchem-061622-030919.
85 J. Li, Y. Xia, X. Song, B. Chen and R. N. Zare, *Proc. Natl. Acad. Sci.*, 2024, **121**, e2318408121.
86 S. Mohsen Beladi-Mousavi, G. Salinas, L. Bouffier, N. Sojic and A. Kuhn, *Chem. Sci.*, 2022, **13**, 14277–14284.
87 U. Isacsson, J. Kowalewska and G. Wettermark, *J. Inorg. Nucl. Chem.*, 1978, **40**, 1653–1656.
88 J. G. Vos and M. T. M. Koper, *J. Electroanal. Chem.*, 2018, **819**, 260–268.
89 O. Kasian, N. Kulyk, A. Mingers, A. R. Zeradjanin, K. J. J. Mayrhofer and S. Cherevko, *Electrochim. Acta*, 2016, **222**, 1056–1063.
90 T. Lim, J. Kim and S. H. Joo, *J. Electrochem. Sci. Technol*, 2023, **14**, 105–119.
91 J. H. Weijs and D. Lohse, *Phys. Rev. Lett.*, 2013, **110**, 054501.
92 W.-X. Fu, P. Zhou, W.-L. Guo and B. Su, *Adv. Sens. Energy Mater.*, 2022, **1**, 100028.
93 X. Yang, J. Hang, W. Qu, Y. Wang, L. Wang, P. Zhou, H. Ding, B. Su, J. Lei, W. Guo and Z. Dai, *J. Am. Chem. Soc.*, 2023, **145**, 16026–16036.
94 Y. Wang, J. Ding, P. Zhou, J. Liu, Z. Qiao, K. Yu, J. Jiang and B. Su, *Angew. Chem. Int. Ed.*, 2023, **62**, e202216525.
95 A. Chovin, P. Garrigue and N. Sojic, *Electrochim. Acta*, 2004, **49**, 3751–3757.
96 J. Xu, P. Huang, Y. Qin, D. Jiang and H. Chen, *Anal. Chem.*, 2016, **88**, 4609–4612.
97 B. Haghighi, S. Bozorgzadeh and L. Gorton, *Sens. Actuators B Chem.*, 2011, **155**, 577–583.
98 D. Tian, C. Duan, W. Wang and H. Cui, *Biosens. Bioelectron.*, 2010, **25**, 2290–2295.

99 C. Cui, R. Jin, D. Jiang, J. Zhang and J.-J. Zhu, *Anal. Chem.*, 2020, **92**, 578–582.

Conclusions and prospects

Conclusions and Prospects

Owing to the orthogonality of its electrochemical trigger and optical output, the ECL method can sensitively report on the (electro)chemical reactivity and its local and global changes, providing multidimensional information on the investigated system. As such, it has become invaluable in different fields of science and technology, driving constant advancements not only in fundamental research but also in the areas of sensing, material science, biology, and imaging. However, the low efficiency of processes that populate the luminophore's excited state often limit the maximal ECL intensity and the method's usefulness for practical applications. Thus, the success of strategies for improving ECL emission relies on a fundamental understanding of its underlying reaction mechanisms. This PhD work focuses on developing novel approaches toward enhancing the intensity, duration, and spatial extension of electrochemiluminescence emission through understanding and improving its underlying mechanistic pathways.

After a general introduction in Chapter I, Chapter II explores the role of redox mediators in facilitating ECL systems by developing a comprehensive theoretical framework that supports, generalizes, and rationalizes mechanistic pathways borrowed from molecular electrocatalysis. Specifically, it investigates the electrocatalytic amplification of coreactant ECL within the $[Ru(bpy)_3]^{2+}$/TPrA system when utilizing a water-soluble redox-active Ir(III) complex as an electrocatalyst. Through electrochemical methods, spectroscopy, and finite element simulation, we demonstrate that amplified low-potential ECL emission in this system is governed by three kinetically limited reactions, which modulate the concentration ratio of radical species. Namely, homogeneous oxidation reactions facilitated by the electrooxidised Ir(IV) lead to the production of TPrA radicals and excited $[Ru(bpy)_3]^{2+*}$ states, enhancing ECL intensity. Conversely, Ir(IV) reacting with $TPrA^{\bullet}$ radicals results in ECL quenching.

Further exploration of the interplay between these key reaction steps provides predictive insights into ECL behavior, underscoring the mediator's redox potential as pivotal in determining ECL onset and peak potential, maximal intensity, and spatial extension of the light-emitting layer. Therefore, the redox mediators (alternatives for Ir(III) complex) should fulfil specific redox requirements to enhance (and not quench) the resulting ECL. First, to efficiently mediate the

homogeneous oxidation of both coreactant and luminophore, their oxidation potential should be lower but close to the potential of the TPrA/TPrA$^{+\bullet}$ redox couple and higher than the one of the $[Ru(bpy)_3]^{+}$/$[Ru(bpy)_3]^{2+*}$ redox couple. Second, to avoid scavenging TPrA$^{\bullet}$ radicals that causes ECL quenching, their reduction potential should be more negative than the potential of the TPrA$^{\bullet}$/P redox couple.

This refined understanding opens up exciting future prospects for developing advanced ECL systems. The finite element simulation model enhances our ability to predict and interpret ECL dynamics in the presence of redox mediators of varying redox properties, revealing how these mediators can catalytically enhance coreactant ECL. This is particularly important for constructing more efficient ECL-based biosensors and bioassays, as it shifts focus from the direct oxidation of coreactants, affected by electrode surface properties and passivation, to the faster electron transfer kinetics of outer-sphere redox mediators. Additionally, this simulation model not only deepens our fundamental understanding of ECL mechanisms but also paves the way for the rational design of redox mediators, luminophores, and coreactants with specific redox characteristics, potentially enabling the creation of ECL systems with tailored properties and enhanced performance. Looking forward, this has the potential to transform ECL research as it offers a framework for optimizing not only the $[Ru(bpy)_3]^{2+}$/TPrA system but also a range of other coreactant systems, significantly improving ECL applications across analytical, imaging, and biomedical fields.

Chapter III further investigates the application of Ir(III) mediator in heterogeneous ECL systems –where $[Ru(bpy)_3]^{2+}$ labels are immobilized on the surface of polystyrene beads and single cells. In those systems, $[Ru(bpy)_3]^{2+}$ cannot undergo direct oxidation at the electrode surface and the ECL generation relies on the mechanisms that operate through homogeneous redox reactions of $[Ru(bpy)_3]^{2+}$ with TPrA radicals and/or Ir(III) mediator. The first part of this chapter uses a bead-based sandwich design, commercially employed in immunoassays, where target biomarkers are trapped between a magnetic bead coated with a capture antibody and a detection antibody labelled with the $[Ru(bpy)_3]^{2+}$ emitter. In this bead-based setup, we achieved a remarkable 70.9-fold enhancement in $[Ru(bpy)_3]^{2+}$ ECL at low (0.9 V), and 2.9-fold enhancement at moderate (1.2 V) anodic potentials when the redox-active $[Ir(sppy)_3]^{3-}$ complex was introduced

into the TPrA-containing supporting electrolyte solution. We explored the potential mechanistic pathways that contribute to the observed signal enhancement by using ECL imaging to map the intensity and spatial distribution of the emission at individual polystyrene beads, thus experimentally confirming that the electrocatalytic amplification of $[Ru(bpy)_3]^{2+}$ ECL, involving homogeneous oxidation of both TPrA and $[Ru(bpy)_3]^{+}$ label by the Ir(III) mediator, is feasible in the heterogeneous ECL setup.

Such catalytically enhanced ECL in heterogeneous systems, particularly at low oxidation potentials, offers significant perspectives for improving current ECL assays and ECL-based microscopy. Employing an outer sphere complex (Ir(III) mediator) as a molecular catalyst reduces the reliance of ECL reactions on the heterogeneous oxidation of TPrA and provides an alternative oxidant which can populate the $[Ru(bpy)_3]^{2+*}$ excited state, increasing the efficiency of ECL processes and allowing them to operate at lower potentials. Thus, this approach not only amplifies the ECL intensity but also addresses key challenges in ECL sensing by reducing electrode surface passivation and minimizing deleterious side reactions. In prospect, ECL systems employing redox mediators hold the potential to significantly enhance the sensitivity and reproducibility of commercial ECL immunoassays. Such improvement could lead to lower detection limits, facilitating earlier and less invasive disease diagnostics and broadening the application of ECL technologies in clinical and research settings.

The second part of Chapter III extends the application of the $[Ir(sppy)_3]^{3-}$ /$[Ru(bpy)_3]^{2+}$/TPrA system to enable bimodal cell imaging. This involves capturing simultaneous positive ECL (PECL) and shadow ECL (SECL) images of single cells, resulting from the concurrent red luminescence of $[Ru(bpy)_3]^{2+}$ used for membrane labelling (light-emitting object on a dark background - PECL) and green luminescence of $[Ir(sppy)_3]^{3-}$ mediator in solution (non-emissive object shadowing the background luminescence - SECL). By spectrally and spatially resolving the ECL emission, we recorded the images of the same cells in both PECL and SECL modes using the $[Ru(bpy)_3]^{2+}$ (λ_{max} = 620 nm) and $[Ir(sppy)_3]^{3-}$ (λ_{max} = 515 nm) luminescence, respectively. PECL shows the distribution of the $[Ru(bpy)_3]^{2+}$ labels attached to the cellular membrane, whereas SECL reflects the local diffusional hindrance of the ECL reagents by each cell. The high sensitivity and surface-confined features of this approach are demonstrated by imaging cell-cell contacts

during the mitosis process. Furthermore, the comparison of PECL and SECL images demonstrates the differential diffusion of TPrA and $[Ir(sppy)_3]^{3-}$ through the permeabilized cell membranes.

In prospect, this bimodal ECL imaging could provide a more detailed understanding of biological systems. Potentially, it can offer insights into cellular morphology, adhesions, and movements through SECL imaging, while simultaneously revealing the distribution of specific membrane proteins or other intracellular entities labelled with Ru-dye via PECL imaging. Additionally, comparing SECL and PECL images could provide valuable information on membrane permeability and transport properties, providing insight into cellular dynamics.

Chapter IV explores the enhancement of the (electro)chemical reactivity, and consequently ECL, at the gas/liquid phase interface. It demonstrates that ECL emission of luminol/H_2O_2 system is enhanced up to 127.6 times at the surface of a chlorine bubble, produced at high anodic potentials (i.e. 2.4 V), relative to the ECL recorded at the commonly used potential of 0.7 V (where no bubbles are produced). Furthermore, this emission is long-lasting and can extend up to several millimetres away from the electrode, which is not the case in the commonly used, low-potential conditions, where short lifetimes of ECL species restrict ECL to the micrometric region at the vicinity of the electrode.

The mechanisms behind this bubble-enhanced ECL were investigated by following the evolution of current and ECL intensity with potential and by using ECL imaging to map ECL distribution at an Au microelectrode in chloride-containing and chloride-free electrolyte solutions. We discovered that ECL emission at the gas/liquid interface is driven by two parallel effects. First, the bubble corona effect facilitates the generation of hydroxyl radicals capable of oxidizing luminol while the bubble is attached to the surface. Second, hypochlorite produced from the electrogenerated chlorine sustains luminol emission for over 20 seconds and extends the ECL emission range up to 5 mm into the solution, following bubble detachment. While the corona effect also triggered ECL in the absence of chloride ions (at the surface of an electrogenerated oxygen bubble), the second effect only occurred following the formation of a chlorine bubble, demonstrating the significance of the dissolved chlorine species in ECL generation. Finally, we tested the practical applicability of this new approach, showing that it can increase the emission intensity of luminol-based assays five-fold compared to the conventional

method. This is demonstrated through a glucose bioassay, using a mid-range mobile phone camera for detection.

Overall, this study provides noteworthy advancements in the fields of interfacial chemistry and electroanalysis. The method developed in this work not only achieves enhanced signal intensities, but also represents the first demonstration of ECL at the gas/liquid interface. This significantly expands the potential applications of ECL by allowing it to probe the interfacial reactivity of bubbles and droplets. Furthermore, triggering ECL reactions at the interface of an electrogenerated gas bubble extends the effective range of its traditionally transient and surface-confined light emission in both time and space. Thus, this novel approach towards ECL generation opens up new opportunities for studying reaction dynamics at interfaces, both in the electrode's proximity and in the bulk. Furthermore, spatially resolved ECL at the surface of gas bubbles could potentially serve to investigate the generation, consumption and dissolution of gases and diffusion of chemical species.

Aknowledgements

First, I would like to thank my academic supervisor, Prof. Neso Sojic, for the countless opportunities he provided for my personal and professional development. I am also thankful for his patience and constant help and support that exceeded those of his duty as a supervisor and for all the valuable advice he has given me during these three years. Finally, his dedication, hard work, scientific curiosity, and enthusiasm for research have inspired me to do my best.

I would also like to thank Dr. Frédéric Kanoufi for his kindness and the generosity with which he shared his time and knowledge with me. I would like to thank him for welcoming me to ITODYS lab, for working with me, being an excellent teacher, for always being available when I needed help and for the great scientific discussions from which I am constantly learning.

My thanks also go to the other partners of the ANR ELISE project: Dr. Jasmina Vidić, for her friendliness, support, and understanding, even when experiments did not go as planned; Dr. Yann Percherancier, for his dedication, optimism, and tireless efforts on the transfection experiments; and Prof. Gilles Tessier, for his hospitality and contributions during our project meetings.

I would like to acknowledge the members of the jury who evaluated this thesis. I am especially grateful to Dr. Frédéric Kanoufi and Dr. Laurent Bouffier for their ongoing support and advice throughout my PhD. I thank Prof. Federico Polo and Prof. Jeffrey Dick, not only for their role as referees, but also for being approachable, kind, friendly, and always ready to engage in a scientific discussion. I thank Dr. Corinne Lagrost for investing her time and effort into evaluating my thesis manuscript.

I also wish to thank everyone I collaborated with and learned from during my thesis, especially Prof. Francesco Paolucci and Dr. Giovanni Valenti from the University of Bologna, Prof. Paul Francis and Dr. Emily Kerr from Deakin University and Dr. Javier del Campo from BCMaterials.

Special thanks to Dr. Bertrand Goudeau for his generosity and kindness in teaching me the critical skills in biology and microscopy, which were essential for the completion of my thesis. His passion for science and willingness to help are a constant source of inspiration.

I would also like to thank Dr Stéphane Reculusa, Patrick Garrigue and Véronique Lapeyre for their positive attitude and help in the lab. I thank Prof. Alexander Kuhn, Prof. Valérie Ravaine, Dr. Laurent Bouffier, Dr. Adeline Perro, Dr. Guillaume Longatte and Dr. Gabriel Loget for all the kindness they have shown, all the advice they gave me and the help they provided, making my time in the lab truly enjoyable.

My thanks also go to the essential administrative staff—Laetitia, Cécile, and Olivier—who were always ready to help with any issues that arose.

I am grateful to all the PhDs and postdocs that I encountered at NSySA. Thank you Dr. Kostia, Dr. Tatjana, Dr. Youness, Dr. Julie, Lea, Magda, Dr. Jerry, Dr. Marta, Dr. Tomasso, Dr. Rémi, Miaoxia, Dongni, Ruchao, Xiaodan, Best, Dr. Titapong, Ljuba, Dr. Mohsen, Guillaume, Lilian, Marine, Leslie, Kelly, Benjamin, Wanmai, Zikawas for the good times, laughter, friendships, and support.

I also thank my friends Michele, Robin and Eleftheria, for all the lunch breaks, board game nights, walks, trips and picnics, and for all the joyous and hard moments of our PhDs. I also thank Alexis, Alex, and Sercan for all the fun we had, for being my hosts and guides, for our bouldering/climbing sessions and above all, for their friendship.

A special thanks goes to the Belgrade team, especially Dr. Dalibor Stanković and Prof. Dragan Manojlović, for all their support during my education. I am forever grateful for their advice and for the solid foundation in electrochemistry they provided.

In the end, I thank my friends for believing in me and cheering me on from Serbia. I thank my parents, Vesna and Milija, for their unconditional love and support. Iako često niste razumeli ono što radim, uvek ste se trudili da budete tu za mene i da me podržite. Hvala vam na tome. I thank my brother Dušan, for being a great sibling. I also thank Nada, Ivica, Milica and Nikola, as well as the rest of my extended family for their help and support. Finally, I thank Filip for being there for me and believing in me troughout the years. Thank you for all your love and support.